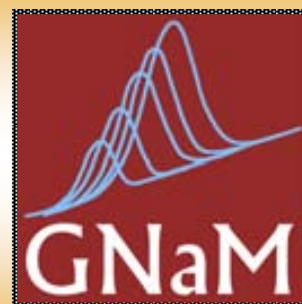
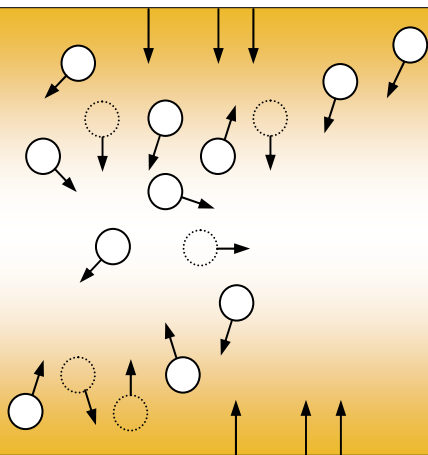


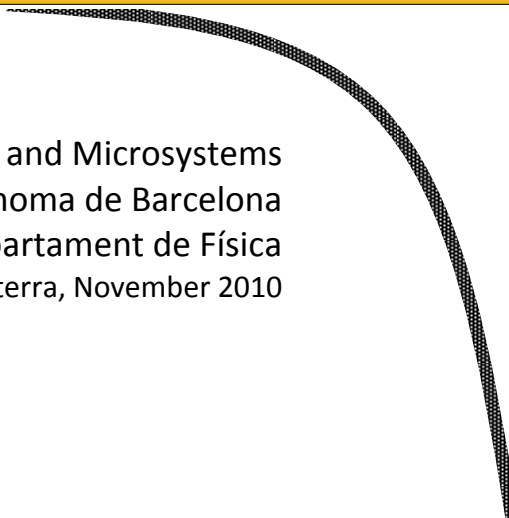
Nanocalorimetric studies of several kinetic phenomena over a wide range of heating rates

Alfonso Sepúlveda Márquez



Ph.D. Thesis in Material Science

Group of Nanomaterials and Microsystems
Universitat Autònoma de Barcelona
Departament de Física
Bellaterra, November 2010



Dr. Javier Rodríguez Viejo, profesor titular de Física Aplicada en la Facultad de Ciencias de la Universidad Autónoma de Barcelona.

CERTIFICA:

Que Alfonso Sepúlveda Márquez, Licenciado en Ingeniería Electrónica y Comunicaciones por el Instituto Tecnológico y de Estudios Superiores de Monterrey, México; y en posesión del Máster Oficial en Micro y Nanoelectrónica por la Universidad Autónoma de Barcelona, ha realizado bajo su dirección el trabajo que lleva por título "*Nanocalorimetric Studies of Several Kinetic Phenomena Over a Wide Range of Heating Rates*", el cual se recoge en esta memoria para optar al grado de Doctor en el programa de Ciencia de Materiales por la Universidad Autónoma de Barcelona.

Dr. Javier Rodríguez Viejo
Bellaterra, Noviembre 2010

Nanocalorimetric studies of several kinetic phenomena over a wide range of heating rates

Thesis Submitted by
Alfonso Sepúlveda Márquez
to apply for the degree of Doctor in Material Science

Thesis supervisor: Dr. Javier Rodríguez Viejo



Grup de Nanomaterials i Microsistemes
Departament de Física
Universitat Autònoma de Barcelona
Bellaterra, November 2010

“Sólo hay un bien, el conocimiento;
sólo hay un mal, la ignorancia.”

Sócrates

Index

Acknowledgments	IX
Summary	XI
Chapter I	
Nanomaterials and Microsystems	
1.1 Introduction	1
1.2 Thesis objectives	3
Chapter II	
Calorimetry	
2.1 Introduction: Conventional Calorimetry	5
2.1.1 Adiabatic calorimetry	6
2.1.2 Power compensated	7
2.2 Membrane-based Calorimetry	10
2.2.1 Introduction: Nanocalorimetry	10
2.2.2 Modeling	10
2.2.3 Experimental measure of temperature profiles	21
2.2.4 Microfabrication	25
2.3 Device Operation	28
2.3.1 Quasi-Adiabatic	29
2.3.2 Power Compensation	35
2.3.3 Power Losses	48
Chapter III	
Hydrogen Storage Systems	
3.1 Introduction: Metal Hydrides	53
3.2 Metal Hydride Thin Films	55
3.3 Thermodynamic characterization	57
3.4 Experimental Setup	59
3.4.1 Control Development	62
3.5 Sample Deposition and Results	67
3.5.1 Mg, Mg/Al and Mg/Ti depositions: individual and combinatorial	68
3.5.2 Mg and Mg/Al characterization results	70
3.5.3 Mg _x Ti _{1-x} characterization results	72
3.6 Surface Micrography Analysis	75
3.6.1 Mg-based thin films	75
3.6.2 Mg/Al library compositions	76
3.6.3 MgTi coevaporated samples	76

Chapter IV

Glass forming liquids

4.1 General Introduction	79
4.1.1 Strong and fragile liquids	81
4.1.2 Thermodynamics and kinetics	84
4.1.3 The Kauzmann entropy crisis	90
4.1.4 Aging and cooling rate effect on the glass	92
4.1.5 Polyamorphism	95
4.1.6 Toluene and ethylbenzene	96
4.2 Stable glasses by vapor deposition	98
4.3 Experimental description	102
4.3.1 Thermal treatments on thin film organic glasses	104
4.4 Results and discussions	106
4.4.1 Influence of deposition temperature	106
4.4.2 Cooling rate effect	107
4.4.3 Temperature effect on aging: isochronal experiments	115
4.4.4 Aging of ethylbenzene and toluene glasses obtained from the liquid: Influence of thickness	117
4.4.5 Isothermal aging of bulk organic glasses above T_g of the normal liquid ($T_g = 117$ K)	123

Chapter V

Amorphous Solid Water

5.1 General Introduction	131
5.1.1 Crystallization: nucleation and growth	135
5.1.2 ASW and crystalline ice sublimation rates	138
5.1.3 The glass transition in water	140
5.2 Experimental Procedure	142
5.2.1 Thermal treatments on amorphous glassy water	143
5.3 Results and discussions	145
5.3.1 Mass estimation	145
5.3.2 Crystallization kinetics	147
5.3.3 Glass transition in amorphous water	157

Chapter VI

Conclusions	169
-------------	-----

Appendix

Multiparallel dehydrogenation analysis: preliminary example	173
---	-----

Bibliography	179
--------------	-----

Acknowledgments

First of all and more sincerely I would like to thank my supervisor Dr. Javier Rodríguez-Viejo for giving me the opportunity to make part of the scientific staff of the *Group of Nanomaterials and Microsystems* (GNaM) at the Universitat Autònoma de Barcelona. His scientific guidance and fruitful discussions helped me acquired a fundamental research ability and extend my knowledge to other fields. Special thanks to Prof. Maria Teresa Mora Aznar for her support, enthusiasm and enjoyable company in the group meetings. I appreciate her assistance in the modeling of the crystallization kinetics of amorphous solid water and for her productive discussions in all this time I have spent here. I also would like to express my gratitude to Dra. Gemma Garcia Alonso for her pleasant talks, her day-to-day understanding, motivation and guidance throughout this thesis project.

I am grateful to all the GNaM members for their availability on helping me out in any circumstances. I would like to thank Dra. Marta Gonzalez-Silveira for her sympathy and for always putting a smile in my face. To Dr. Aitor Lopeandía-Fernández for his long lasting discussions. Thanks to Iris Moder for her constant willingness to help. Manel Molina for the interesting conversations and all the relief sessions including the time spent playing squash. To old group members: Thanks to Dr. Joan Torrens i Serra for sharing his knowledge and experience; and helping me with the teaching laboratory; Dr. Edgar León-Gutierrez for all the patience and help that he has offered me throughout the years, especially for all the fruitful explanations in glass forming liquids and all his teaching in vacuum equipment. Thanks to Dr. Jaime Alvarez Quintana, Dr. Roger Doménech-Ferrer, Jordi Higuera Guisset and José Valenzuela.

I acknowledge the *Laboratori de Capes Primes*, in particular Dr. Francesc Pi for the infinite sample depositions with the e-beam evaporator and his enormous work provided to the group and me. The *Centro Nacional de Microelectrónica de Barcelona* for the microfabrication of the devices. To the *Consejo Nacional de Ciencia y Tecnología de México* (CONACYT) for the financial support granted to the development of this thesis. I would also like to recognize my admiration to Prof. Mark Ediger from the University of Madison, Wisconsin for his fruitful discussions on glass stability.

Thanks to all my friends in Mexico for their long distance support. Despite your friendship solitude in the past couple of years; the time will come for the long awaited reunion. To my friends in Europe, thank you very much for turning the entertainment outside the university so delightful and for making my integration to this new and different life style so easy.

Certainly, I would like to express my most honest appreciation to my family for their unconditional love. Without their support this thesis and all my accomplishments in life would not have been possible. I am mostly grateful to them for always being there in times of need. I will always be in debt to them.

Finally I would especially like to show my appreciation to the one person I admire the most and which I have the pleasure to share each and every moment. For all the infinite patience, support, advice, inspiration, respect, laughs, tears and unlimited love, thank you very much Ylenia.

Thanks to every person who has been part of this experience.

Summary

To understand essential properties of materials it is necessary to dispose of an experimental countenance with a high accurate thermodynamic measurement system. Custom-made and commercial types of nanocalorimeters are available for different kind of applications. Membrane-based nanocalorimetry is an important tool for thermo-physical analysis since this technique can achieve pJ/K resolution and characterize the presence of possible unknown nano-phases in modern materials. Some new class materials may be complicated to produce in large size samples and can just be available in small quantities or thin films. Examples of attractive applications of novel calorimetric techniques include high-throughput synthesis and screening of thin films and metal hydrides for hydrogen storage [1,2], the study of quantum effects and phase transitions in magnetic systems [3,4], in nano-scale systems to investigate synthetic and/or organic glasses [5,6] above room temperature and below. Adiabatic conditions become more complicated to be satisfied when the temperature and sample dimension decreases. Accurate measurements of low temperature heat capacities become thus more difficult because small heat fluxes from the surroundings can lead to significant errors.

Power compensated calorimetry: Slow heating regime

With the goal of measuring the heat released or absorbed during phase transitions occurring in small samples, we have developed a *power compensated membrane-based calorimeter* that can maintain linear heating rates spanning 1–1000 K/s under non-adiabatic conditions. The device works in the intermediate range of heating rates between conventional, $\beta < 5$ K/s, and thin film, $\beta > 10^3$ K/s, scanning calorimeters. Active control in real time during heating/cooling experiments is achieved using the NI-7833 FPGA card, which includes a 3M field programmable array with a control loop timer of 20 μ s. An improvement of the existing methodology [7] achieved by minimizing control action through the use of predefined temperature profiles is also demonstrated. With $\sim 1\mu$ J energy sensitivity, this is a very sensitive scanning calorimeters working in power-compensation mode [8]. In addition, we highlight the suitability of the thin film membrane-based calorimetric technique to measure kinetically limited phase transitions such as the dehydrogenation of metallic hydrides and provide a first insight into the development of a multiparallel high-throughput screening technique. We analyzed the dehydrogenation reaction in several metallic hydrides (pure Mg, Mg/Al and MgTi) thin films. We determine the influence of the alloy composition on the onset dehydrogenation temperature [9].

Adiabatic Calorimetry: Rapid heating regime

Glassy films of organic molecules grown by physical vapor deposition at temperatures slightly below the glass transition temperature behave as stable glasses compared to those cooled directly from the liquid. Higher stability is achieved when depositing at 0.8T_g [10,11]. By means of nanocalorimetry we can monitor the behavior of the samples and determine their kinetic and thermodynamic stability.

Glassy toluene, ethylbenzene and water films were directly deposited using a home-made evaporator design in an ultra high vacuum chamber [12] onto the SiNx membrane of the microcalorimetric chips at temperatures above liquid-nitrogen. Calorimetric scans are done *in situ* with a high sensitivity calorimetric setup with scanning rates up to 10^5 K/s. In quasi-adiabatic treatment ultrafast heating rates are applied for samples from 5 to 100 nm thickness. Thinner films dispose of a less kinetic stability while increasing their thermodynamical stability. Aging a glass will modify its physical properties and approach the sample to more stable configurations. Physical aging effects are erased by heating the glass above its glass transition. The optimal aging temperature will correspond to fictive temperature (T_f) of the corresponding AD film.

Kinetic effects on several transitions such as crystallization are of high interest. With nanocalorimetry it is possible to study this type of phenomena. With pulse-heating we can apply fast (15000 K/s) and ultra fast (40000 K/s) heating rates and characterize different size samples. Although in some cases these complex kinetic events may have to be supported with proper and high-quality modeling.

Chapter I

Nanomaterials and Microsystems

1.1 Introduction

This Thesis work has been carried out in the Group of Nanomaterials and Microsystems¹ of the Physics Department at the Universitat Autònoma de Barcelona. GNaM's work mainly focuses in the study of thermal properties in low dimensional systems. New tools are developed within the group to foster the analysis of thin films down to few nm thick. Downsizing produces remarkable changes in the properties of materials and one of GNaM's objective is to understand those changes in order to use such nanostructures in novel applications and devices.

The characterization, further analysis and possible applications of nanomaterials configure one of the most exciting emerging fields of research. A great deal of work and investigation still remains to be done as to increase the knowledge and usability of new materials. However, the analysis of new materials at the nanoscale may not be that obvious since it confronts severe limitations in apparatus resolution and proper instrumentation. In addition, property characterization of nanomaterials is challenging because of the difficulties in manipulating structures of such small size. New methods and methodologies are being developed to quantify the properties of individual nanostructures.

Membrane based micro-devices have developed into one of the most promising designs for new heating/sensing techniques. The main inspiration of nanocalorimeters is to reduce the heat capacity of the addenda by using very thin membrane support. This way the sensitivity of the sensor is highly increased and information such as enthalpies or kinetic parameters in phase transitions can be easily accessed. Devices microfabricated for nanocalorimetry are capable to provide quantitative data to support the development of ultrafast thermal anneal processes that are inaccessible with conventional calorimetry. With nanocalorimetry, samples in the order of nanograms or even below can be studied with the aid of the proper measurement procedure.

¹ <http://gnam.uab.es>

The nanocalorimetry field has experienced a very significant evolution in the past 15 years making of this technique an important method for the characterization of nanomaterials. However, it is not mature enough for being considered a generalized methodology in the scientific community. Few research groups focus in nanocalorimetric studies of several phenomena. Groups have attained nanocalorimetry as a potential ex-situ and/or in-situ technique for thin films, size effect studies, glass transition, crystallization dynamics, magnetic transitions,... [13-18].

In *chapter II* we describe in more detail the state-of-the-art of nanocalorimetry and the recent developments of the GNaM group, which are at the basis of the present work. We also present a brief explanation on the microfabrication process and the several characterization procedures of the nanodevices. Since it is very important to understand the performance of the nanoheaters over a wide range of temperatures and pressures, we dedicate an extensive explanation to the modeling of this micofabricated structures.

In *chapter III* we show the suitability of the thin film membrane-based calorimetry working in power compensation mode to measure kinetically limited phase transitions such as the dehydrogenation of several Mg-based metallic hydrides. The main advantages of this outcome is to exploit the use of vapor phase deposition techniques for material preparation and the possibility to use nanocalorimetry in parallel with other optical methods which makes this approach to be considered as a first step towards a combinatorial deposition methodology coupled with other high-throughput characterization technique to facilitate the discovery of new materials for hydrogen storage. The sample masses studied in this section are lower than 5 μg , 1000 times smaller than typically used in conventional calorimetric experiments. Slow heating rates (10 K/min) are required to completely finish the de/hydrogenation process in these thin film samples. This small value in mass and the slow temperature evolution in time set a compelling demand on the system sensitivity which will interact with controller performance and associated instrumentation.

In *chapter IV* we present results obtained from quasi-adiabatic scanning nanocalorimetry at ultrafast heating rates (~ 35000 K/s) on very thin films of glasses obtained from the vapor, either using organic molecules of toluene and ethylbenzene. A special setup that enables in-situ measurements has been used to vapor deposit thin film organic glasses in the active area of the nanodevice. This methodology permits growth of a large variety of thin films (1-100 nm) and to quickly measure the heat capacity of the material over a wide range of temperatures starting from

liquid nitrogen temperature. The recent discovery that films grown from the vapor are most stable than films cooled from the liquid has boosted interest in the field and the in-situ setup is an ideal tool for the study of these materials.

In *chapter V* we present the use of quasi-adiabatic nanocalorimetry to study the crystallization kinetics of amorphous solid water of very thin films ($4 - 100 \text{ nm}$) obtained from the vapor phase. The heat capacity of the amorphous and crystalline phases are measured and analyzed in detail. Also, we show calorimetric evidence of a change in the heat capacity of the amorphous sample just before crystallization and demonstrated that this upswing can be designated as the glass transition in water since none of the possible contributions affecting the calorimetric trace, i.e. amorphous desorption; explain this effect.

1.2 Thesis objectives

The basic objective of this thesis is to explore systems that had not been yet studied with nanocalorimetry. From utilizing this technique in power compensation mode for slow heating treatments to the quasi-adiabatic state for fast heating processes we can measure the heat capacity and reveal phase transformations that may occur in nanostructures and which are sightless to conventional calorimetry. With this main idea we look forward to expand the interest for the investigation of new phenomena.

The general features of this Thesis are:

The use of membrane-based calorimeters working in power compensation mode to analyze the dehydrogenation behavior of metal hydride thin films. The dehydrogenation of Mg, Mg/Al and $\text{Mg}_x\text{Ti}_{(1-x)}$ hydrides thin films has been analyzed at heating rates of 10 K/min.

The use of quasi-adiabatic nanocalorimetry to study the kinetic and thermodynamic stability of thin film organic glasses. Toluene and ethylbenzene thin films (5-100 nm) grown from the vapor phase and cooled from the liquid were studied by using heating rates around 35000 K/s. Calorimetric traces obtained by this technique will provide information on the nature of the glass and some of its properties.

The use of quasi-adiabatic nanocalorimetry to study the crystallization kinetics of amorphous solid water and the possible presence of a glass transition. Water is a very interesting system, which has been widely studied. However, a controversial on its glass transition temperature exists and the crystallization kinetics of amorphous solid water has not been detailed sufficiently. A model of the crystallization kinetics along with experimental evidence can provide some information to understand other of its possible properties and anomalies.

Chapter II

Calorimetry

2.1 Introduction: Conventional calorimetry

Calorimetry is the technique that measures the heat and rate of the heat exchange with the surroundings. Calorimetric techniques measure the heat that can be generated, consumed or dissipated. The processes are called exothermic and endothermic for generated and consumed energies respectively. Therefore, calorimetry is a suitable technique to characterize kinetic and thermodynamic properties of materials. A simple classification of calorimeters divides them in adiabatic (*no heat exchange with the surroundings*) or isoperibol (*the temperature of the surroundings is maintained constant*). Adiabatic calorimetry represents the ideal tool to measure the heat capacity of a sample that is simply the ratio between the input power and the heating rate. However, adiabatic conditions are very difficult to fulfill and isoperibol calorimeters are of common use. Among those Differential Scanning Calorimetry is one of the most established methods to analyze phase transitions in organic or inorganic materials over a wide range of temperatures.

Differential Scanning Calorimeters in power compensation mode maintain a constant heating rate even during phase transformations by means of a compensation scheme that measures the differential power with respect to a reference side. The control system establishes a nearly zero temperature difference between the substance sample and the inert reference. There are two main types of DSC's systems that are of common use [1]: i) Those based on heat flux measurement and ii) Power compensation DSC. The heat flux DSC belongs to the class of heat-exchanging calorimeters. In heat flux, the reference and the sample are both heated by the oven through a thermal resistance. The heat flux DSC consists of a low resistance heat path connected to both sample and reference specimens in a single furnace chamber. Enthalpy or heat capacity changes in the sample cause a difference in its temperature. This temperature difference is recorded and then plotted to relate the enthalpy change. Due to the good sample/reference thermal contact, the resulting heat flow is small compared with that in Differential Thermal Analysis. In commercial heat-flux DSC's, the well-defined heat conduction path is realized in

different ways; with the measuring system begin sufficiently dominating. This technique is based in the heat measurement during time. These measurements are typically held for samples in the mg range, the lower limit for bulk samples. On the other hand, the power compensation DSC operates maintaining a constant temperature ramp in both sample and reference at the expense of providing different power to both cells. Since this is the methodology of choice for our compensation scheme it will be analyzed in depth in section 2.3.2.

2.1.1 Adiabatic calorimetry

No calorimeter is strictly adiabatic; some heat is lost by the sample to the surroundings. In adiabatic calorimetry a substantial effort is devoted to build thermal shields that maintain the same temperature as the sample cell to minimize heat exchange with the surroundings. This calorimetric technique results in high absolute accuracy of the heat capacity of the samples under study. However, suffers from technical difficulties that prevent its generalized use. Heat capacity values can be assessed very easily from adiabatic conditions, since we can assure that:

$$dH(t) = Cp(t)dT(t) \quad 2.1$$

where $dH(t)$ is the *induced power*, heat capacity Cp and the temperature variation $dT(t)$. Experimentally we can determine the power given to the calorimetric cells and the variation of the temperature as a function of time. Since having both identical reference and sample calorimeters placed in series the subtraction of both input powers is necessary to attain the heat capacity of the studied sample following the next equation:

$$Cp(t) = \frac{P_S}{\beta} - \frac{P_R}{\beta} \quad 2.2$$

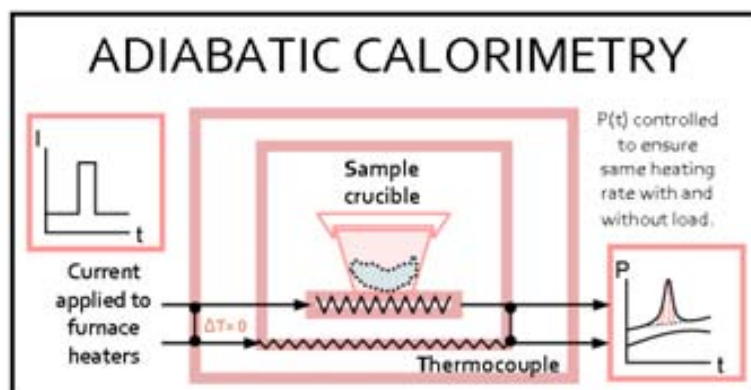


Fig. 2.1: Schematic representation of an adiabatic calorimeter working in non-differential mode. A current pulse passes through the heaters with and without the sample.

2.1.2 Power Compensated

In power compensation a heater is placed within the vessel to sustain a constant temperature. The supplied energy required to maintain the calorimetric cell at constant temperature or with a constant heating rate can be varied and the calorimetric signal is purely derived from the electrical power input. The power compensation DSC belongs to the class of heat-compensating calorimeters. With this technique, the temperatures of the sample and reference are controlled independently using separate but identical furnaces. The temperatures of the sample and reference are made identical by varying the power input to the two furnaces. The heat measured is compensated with electric energy, by increasing or decreasing the amount of power dissipated by Joule effect. The necessary energy to make the equality between temperatures is a measure of the enthalpy or heat capacity changes in the sample. The commercial power compensation DSC, being the most widely used the one of Perkin-Elmer's, is an instrument with isoperibol (*surroundings at identical temperature along the calorimetric scan*) mode of operation.

For isothermal treatments, the enthalpy is calculated by:

$$\Delta H = \left[\int \frac{dQ}{dt} \text{sample} - \int \frac{dQ}{dt} \text{reference} \right] dt \quad 2.3$$

For continuous heating:

$$\Delta H = \int \frac{1}{\beta} \left[\frac{dQ}{dt} \text{sample} - \frac{dQ}{dt} \text{reference} \right] dt \quad 2.4$$

where, β is the heating rate.

Energy calibration may be carried out by using either known heats of fusion for metals, commonly indium or zinc or known heat capacities. Synthetic sapphire is used as a reference to calibrate the system due to its heat capacity standard. The absolute accuracy for measurements of heat capacity and transformation enthalpies are more often limited by a lack of appropriate standards, and difficulties in assigning a baseline construction, than by limitations of the instrument itself. In the study of irreversible processes, the baseline (*reference*) is obtained by making a second measure over the sample in the same heating conditions. Both Differential Thermal Analysis (*DTA*) and Differential Scanning Calorimetry (*DSC*) are concerned with the measurement of energy changes in materials. They are thus the most generally applicable of all thermal analysis methods, since every physical or chemical change involves a change in energy. Compared with heat flux DSC's, the power compensation DSC offers a short heat conduction path between samples and heater and the relatively small masses of the micro-furnaces allow an almost instantaneous response to a sample reaction. Reaction heat flow rates are rapidly and to a large extent compensated by electrical heating power. As a result, only small temperature differences ΔT occur between the micro-furnaces of sample and reference. The total compensating energy is equal to the reaction heat or heat of transition. We have to keep in mind

that the temperature difference between the two micro-furnaces is not totally compensated for in commercial power compensation DSC's. During the peak there is still a temperature difference ΔT proportional to the reaction heat flow rate. The power compensation DSC can be considered a kind of a DTA instrument with a ΔT as the measurement signal, but with a ΔT which is much smaller than that developed in a heat flux DSC measuring system. All the attributes of heat flux DSC systems which depend on this temperature difference can also be found in the real power compensation DSC, but in a minor degree. The calibration factor in particular is not a constant figure but depends in principle on temperature, heat flow rate, heating rate and peak area.

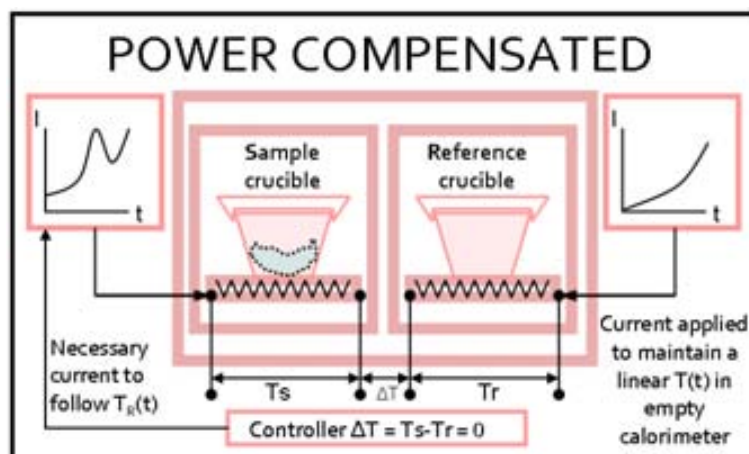


Fig. 2.2: Schematic representation of a calorimetric system in power compensation mode. Two separate current sources provide the necessary power to attain linear heating rates for both sample and reference crucibles. Since the sample crucible contains the sample of interest it will need of more or less power to compensate the transition taking place. A controller monitors the temperature difference between both cells ($T_S - T_R$) and provides the power compensation to maintain the linear heating rate.

2.2 Membrane-based Calorimetry

2.2.1 Introduction: Nanocalorimetry¹

When the purpose of the study is to measure phase transitions in very small samples (*thin films, quantum dots,...*) conventional calorimetry cannot be applied due to its insufficient resolution and sensitivity to detect with accuracy very small energy changes. In some cases the use of a multilayer configuration is implemented to surpass the problem [2, 3], but this approach lacks generality. The key to measure small samples is to reduce the heat capacity of the calorimetric cell. Since the calorimetric signal is proportional to the total addenda², reducing the addenda enables measurements on even smaller samples increasing sensitivity and signal-to-noise ratio. The design of new devices has to consider this concept and other several important requirements (*materials, current density, temperature limits, etc.*) to improve flexibility and to reduce the thermal link with the surroundings.

The arrival of the micro-electro-mechanical system (*MEMS*) technology has enabled the development of calorimeters which can operate with considerably smaller sample sizes. In a microfabricated nanocalorimeter all the required components are included on one substrate as a single integrated structure (*heater/sensor elements, sample holder*). MEMS promise to revolutionize nearly every product category by bringing together silicon-based electronics with micromachining technology, making possible the realization of complete systems-on-a-chip. Nanocalorimeters often use a thin membrane as substrate or sample support. This way both calorimetric cell addenda and thermal link are dramatically reduced which increases the sensitivity. Nanocalorimeters are, essentially, physically small with low internal heat capacities so that they can be used with small sample volumes preserving required sensitivities without the calorimeter dominating the thermal process.

2.2.2 Modeling

The simulation of microstructures is very important to understand and/or predict the behavior of the devices already fabricated and to support the imagination of new designs by reproducing the possible performance. We have used COMSOL Multiphysics to model the thermal

¹ The term “nanocalorimetry” is used to describe the sensitivity of the instrument rather than the dimensions of the device used in this technique.

² Sample heat capacity plus the calorimetric cell heat capacity.

behavior of the different microheaters employed along this thesis work in the slow and fast heating rates regimes. The thermal profile across the active area of the devices is critical given that the presence of a non-homogenous temperature can adversely affect calorimetric traces. Due to the reduced SiN_x membrane thickness, from 180 to 480 nm, the temperature difference between the heater and sample is less than 0.02 K at high heating rates. Therefore, we assume that the temperature does not depend on the vertical coordinate z on a 3D representation. So, modeling can be treated as a 2D system in the membrane plane. However, out-of-plane behavior is considered in the simulation to take into account the possible convective and radiative losses which are represented by parameters of the membrane surrounding.

To accomplish a finite model³ it is necessary to divide the entire device into discrete elements by creating a mesh⁴ and apply an energy balance equation for each one of the individual structures to analyze the various degrees of freedom. The model of the two main geometries can be observed in the following figure corresponding to a mesh of 19264 elements (Fig. 2.3).

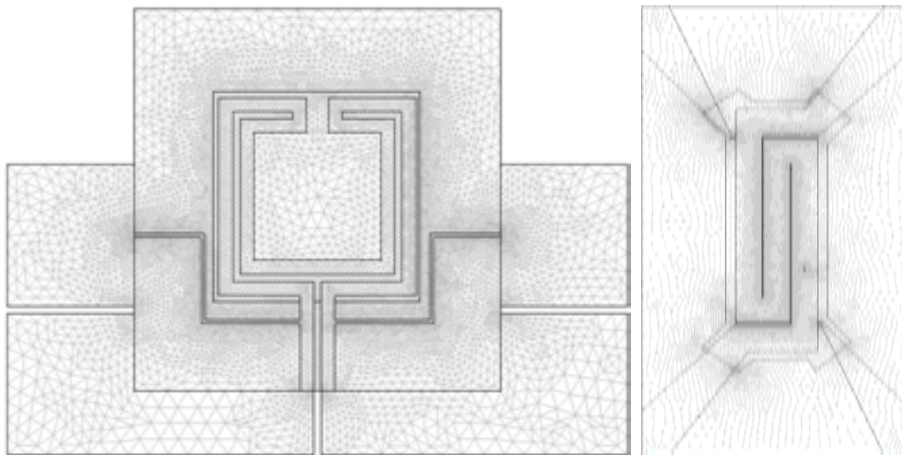


Fig. 2.3: Mesh visualization of the U and S-shaped micro-calorimeters. Creating a mesh in the geometry structure of these devices is a previous step to generate a simulation result. To produce a smoother solution would be to refine the mesh to estimate the accuracy. In this case, heat transfer recreation is obtained by the representation of the temperature field across the calorimetric cell. The mesh layer will basically define the ΔT present within the microdevice.

³ A *mesh element* together with a set of *shape functions* and corresponding *degrees of freedom*.

⁴ A subdivision of the domains of a geometric model into, for example, triangles (2D) or tetrahedrons (3D).

COMSOL Multiphysics® has the simulation capabilities to model heat transfer via conduction, convection, and radiation, as well as the ability to couple these to other physical phenomena. From the modeling standpoint, heat transfer in MEMS is similar to the macroscale heat transfer conditions. Also, thermal expansion coupling is an important phenomenon in MEMS modeling since it can be helpful to determine maximum supported temperatures to avoid structure damage. In this model, the three methods of heat transfer have been included since the experimental analyses are carried out in several different environments (*vacuum, H, Ar, He*).

As a result of the material electric resistance, the current heats up the structure by joule effect; the heat dissipates by conduction through the membrane or through the metal leads into the silicon frame or into the atmosphere (*Ar, He, H₂*) by convection. When using Pt as heater/sensor the relationship between electrical resistance and temperature is approximately linear over a wide range of temperature following:

$$R = R_0[1 + \alpha(T - T_0)] \quad 2.5$$

Where α is the Temperature Coefficient of Resistance of the thermometer. For the recreation of the input current that heats the device we induce a potential difference between the heater leads which produces a linear ramp in temperature. By changing the predefined variable potential, different heating rates of the calorimetric cell can be induced and its effect on the thermal profile within the active area visualized.

Internal energy or heat is principally the kinetic energy of the molecules vibrating in the material. This kinetic motion increases as the temperature is raised. The entire kinetic activity will be uniform if the whole material is at one uniform temperature. The principle of conduction is the transfer of kinetic activity between the faster moving molecules and the slower ones when a hot material comes into contact with a colder material. The heat transfer is inversely proportional to the thickness of the material and it also depends on the type of material. The Thermal Conductivity, defined by k , is the property of a material which indicates its ability to conduct heat. The Thermal Conductivity of a material is defined as:

$$k = \frac{H}{A} \frac{d}{\Delta T} \quad 2.6$$

where, H is the heat flow rate, A is the total cross sectional area of the conducting surface, d is the thickness of the conducting surface separating the difference temperatures ΔT . The units of the thermal conductivity are: $\text{W}\cdot\text{K}^{-1}\cdot\text{m}^{-1}$. The Thermal Conductivity values for each element making part of the nanocalorimeter are as follows:

	k (W·K⁻¹·m⁻¹)
Pt	73
Si_xN_y	2.6
Ag	420
Al₂O₃	8

Table 2.1: Thermal conductivities at room temperature of the materials forming part of the microdevice. Obtained from reference [6] and therein.

Convection is the heat transfer by the physical movement of a heated medium. It is a property of liquids and gases. It occurs because when a liquid or gas gets hot, it tends to rise above the rest of the body. The heat transfer rate depends on the thermal conductivity of the fluid in contact with the surface and the volumetric expansion properties of the fluid. The flow of particles over a surface is a major issue in fluid mechanics and the work on boundary layers which are consider inside the modeling algorithm. Under the statement that the experiments are performed in vacuum the equation of state will be:

$$\delta \cdot \rho \cdot Cp(dT / dt) + \nabla \cdot (-k\Delta T) = Q \quad 2.7$$

where δ is a time scaling coefficient, ρ is the density, k is the thermal conductivity, Cp is the heat capacity, Q is the heat power source. For a steady-state problem, the temperature does not change over time and the first term disappears. This equation is executed in the internal algorithm for each of the membrane elements formed in the model mesh. Under high vacuum conditions convection heat transfer can be neglected due to the fact that no particles are present in the medium. It has been already demonstrated that for this type of microdevices convection does not occur to any appreciable extent below 10^{-6} mbar of pressure. Radiation losses can also be neglected if working at heating temperatures below 500 K. The conductive losses through the thermal link between the calorimetric cell and the Si frame are limited due to the 180-480 nm SiN_x membrane.

In conduction the only direct path linked to this heat transfer mechanism will be the metal strip (*Pt*) making part of the device and its neighbor materials (*SiN*, *Al₂O₃*). By applying a current, heat can be transferred between these materials by the presence of Joule effect heating in the metal Pt strip. Although the electrical resistivity is temperature dependent, it can be used at a given temperature to calculate the resistance of a given geometry. If we consider the total length of the strip heater for the U-shaped device, $L = 20\ 200\ \mu\text{m}$, the area of the cross-section (A) is equal to $200\ \mu\text{m}$ (*width*) \times $100\ \text{nm}$ (*thickness*). The electrical resistivity (ρ) of Pt films was experimentally determined by previously calibrations resulting $2.54\text{e-}7\ \Omega\cdot\text{m}$. These parameters directly determine the value of the heater resistance, equal to $254\ \Omega$, since:

$$R = \rho \frac{L}{A(\Omega)} \quad 2.8$$

The heat generated in the Pt strip can be obtained with Joule's first law, which is defined by:

$$Q = I^2 \cdot R \cdot t \quad 2.9$$

where Q is the heat generated by a constant current I flowing through a conductor for a corresponding time t . The conductor material will have an electrical resistance R , which could be obtained from equation 2.8. The inverse of the electrical resistivity is called electrical conductivity. The use of conductivity is more convenient in some cases. The electrical conductivity values used in the conductive media parameters for each conductor element forming the nanocalorimeter are as follows:

	σ (S·m ⁻¹)
Pt	8.9×10^6
Si_xN_y	INSULATOR
Ag	6.30×10^7
Al₂O₃	INSULATOR

Table 2.2: Electrical conductivities at room temperature of the materials forming part of the microdevice.

The calorimeter model generated for the simulations has a very thin structure on one of its geometry dimensions ($dz = 180 \text{ nm}$) (see Figure 2.4) and it is very efficient to reduce the model geometry to 2D or even 1D and use the out-of-plane heat transfer mechanism. This way we apply a 2D model due to the small thickness of the membrane (180-480 nm). Therefore, a 2D coordinate system is implemented to obtain reliable results comparable to those in experimental analyses for these ultra-thin structures.

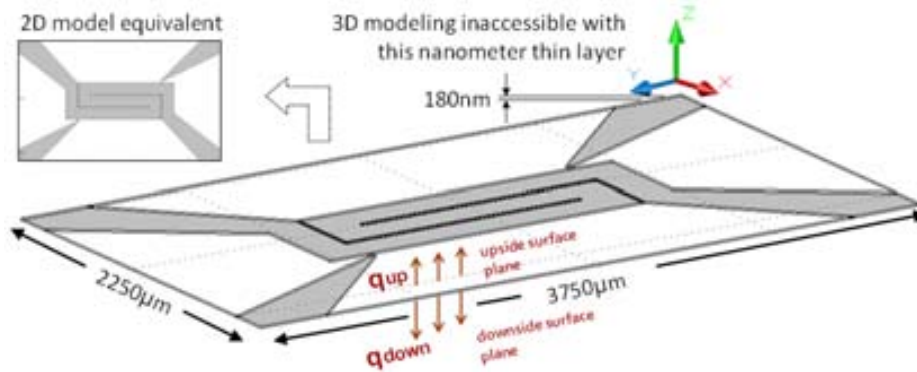


Fig. 2.4: Representation of the microdevice considered as a 3D dimensional model in which due to membrane thickness heat transfer modelling is inaccessible. A geometry reduction from 3D to a 2D model representation will be necessary to achieve good quality simulations.

The working atmosphere, i.e. type of gas and pressure, is an important parameter in the simulations since directly affects the input power and the thermal profile in the active area of the device. The different behavior of the heater in different atmospheres represents a change of parameters for conduction heat transfer and the addition of the out-of-plane conditions in the modeling for convection and radiation phenomena. The mathematical model for heat transfer by conduction is represented by equation 2.7. Most practical applications combine convective and conductive heat transfer. In the case of operating in a vacuum environment the convection heat transfer was ignored, but changing pressures by working in other medium i.e. air, Ar, He the convection losses would have to be considered. We obtain the mathematical model for heat transfer by conduction and convection by adding a convective term to the heat equation for conduction. The resulting equation is as follows:

$$\delta \cdot \rho \cdot C_p (dT / dt) + \nabla \cdot (-k \Delta T) = Q - \rho C_p v \cdot \Delta T \quad 2.10$$

where δ is a time scaling coefficient, ρ is the density, k is the thermal conductivity, C_p is the heat capacity, Q is the heat power source and v is the velocity field vector.

The convection and conduction heat equation currently given appears in its non-conservative form. That form assumes that the continuity equation for the velocity field $\Delta u = 0$ is fulfilled. An alternative is the conservative formulation for the conduction and convection equation:

$$\delta \cdot \rho \cdot C_p (dT / dt) + \nabla \cdot (-k \Delta T + \rho C_p v T) = Q \quad 2.11$$

Up to now we have discussed the heat transfer of the model by means of conduction and convection. The third mechanism is radiation, which denotes the stream of electromagnetic waves emitted from a body at a certain temperature. In vacuum, radiative transfer is the dominant mechanism since conductive heat transfer will only occur between objects that are physically in contact and convection will not exist without any presence of a liquid or gas. Thermally isolated objects in vacuum can only get rid of heat through radiative heat transfer. Typically in our devices, this term is significant for temperatures above 500K. Working in other media besides vacuum and at higher temperatures imposes to consider the radiative heat transfer mechanisms. Below 500 K radiative heat transfer does not have an impact on the heat equation for the modeling system since the only main mechanism in a 2D model will be conduction. The reduced geometry in 2D does not strictly represent the upside and downside surfaces of the plate as boundaries. Instead, by using out-of-plane heat transfer, the reduced model takes into account heat transfer through these boundaries by using an integrated version of the heat equation (*see Figure 2.4*). The following equation shows the heat expression for a 2D heat transfer setback that includes conduction and out-of-plane heat transfer corresponding, in this case, to the convection and radiative heat transfers. Mathematically this is the heat equation integrated along the thickness of the full 3D geometry where dz represents the thickness of each mesh structure.

$$\delta \cdot d_z \cdot \rho \cdot C_p (dT / dt) + \nabla \cdot (-d_z \cdot k \Delta T) = d_z \cdot Q + h(T_{ext} - T) + \epsilon \sigma (T_{amb}^4 - T^4) \quad 2.12$$

where T is the temperature, δ is a time scaling coefficient, ρ is the density, k is the thermal conductivity, Cp is the heat capacity, Q is the heat power source. The first out-of-plane term represent the convective heat flux ($T_{ext}-T$), where h is the heat transfer coefficient, and T_{inf} is the external bulk temperature which in this case will represent the Si frame temperature. The value of h depends on the geometry and the ambient flow conditions, therefore:

$$h(T_{ext} - T) = h_{up} (T_{ext,up} - T) + h_{down} (T_{ext,down} - T) \quad 2.13$$

where:

- . h_{up} is the heat transfer coefficient for the upside,
- . h_{down} is the heat transfer coefficient for the downside,
- . $T_{ext,up}$ is the external temperature for the upside, and
- . $T_{ext,down}$ is the external temperature for the downside.

In addition, the second out-of-plane term represent the heat flux due to surface-to-ambient radiation. Corresponding to the radiation effect of the whole calorimetric cell to the chamber ambient surroundings, this is:

$$\varepsilon\sigma(T_{amb}^4 - T^4) = \varepsilon_{up}\sigma(T_{amb,up}^4 - T^4) + \varepsilon_{down}\sigma(T_{amb,down}^4 - T^4) \quad 2.14$$

where:

- . ε_{up} is the surface emissivity for the upside,
- . ε_{down} is the surface emissivity for the downside,
- . σ is the Stefan-Boltzmann constant,
- . $T_{amb,up}$ is the ambient temperature for the upside, and
- . $T_{amb,down}$ is the ambient temperature for the downside.

In a first approximation, we tried to use this model with lumped parameters to simulate the behavior of the microcalorimeter when is fed by a constant current pulse, fitting the parameters (Kth , ε , h) with experimental data. Several previous conditions were imposed over

each parameter to simplify the fitting and keep its physical meaning: 1) h was fixed to zero, since under vacuum conditions convection losses can be neglected in comparison with the other terms, 2) we used ϵ as a radiation constant which over 500 K turns to be the most important channel for heat losses and finally, 3) the thermal conductance was chosen with a linear dependence with temperature. In figure 2.5 we show the corresponding modeling of the calorimetric cell in vacuum up to 10^{-6} mbar. The heater has a current input equal to the one in the experimental measurements. The final simulating temperature is equivalent to the final real temperature, given us a good reliability on the simulation results. Also, the temperature profile of the sensing area is visualized. It is important to reveal that the temperature gradient around the calorimetric cell varies with a high difference, mainly for the U-shaped design. This is the main reason why a thermal plate was added for the experiments.

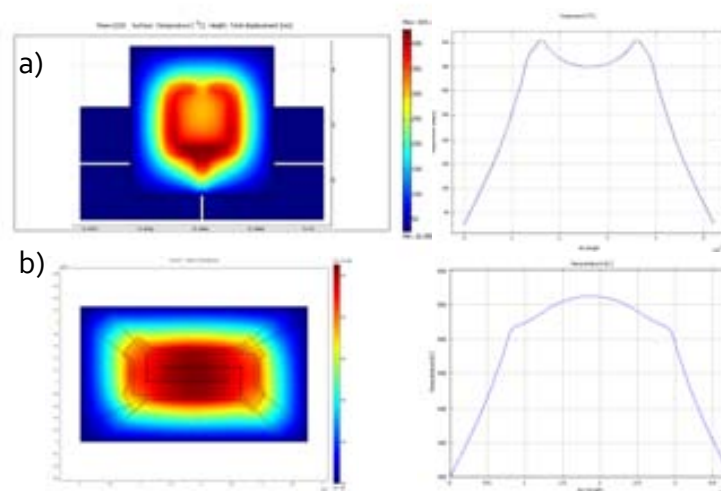


Fig.2.5: U and S-shaped heater temperature profiles at a heating rate of 10 K/min in vacuum environment. We assume that the thermal conductivity, emissivity and convection coefficients are independent of temperature. These parameters are fitted to satisfy the previously experimentally determined ratio between the input power through the heater and the average heater temperature. In vacuum, the calorimetric cell temperature distribution stands within 15 K of the averaged experimental temperature

Some of the analyses we have investigated are carried in other environments besides vacuum, i.e. H_2 , Ar. It is important to understand the profile across the calorimetric cell and the difference with the one in vacuum conditions. The next figure corresponds to the modeling carried out in air surroundings. Again, the final simulating temperature was equal to the real temperature reached in these conditions.

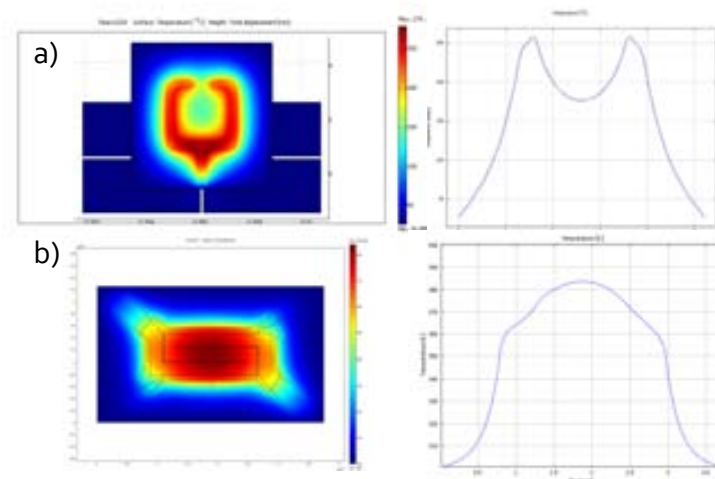


Fig.2.6: U and S-shaped heater temperature profiles at a heating rate of 10 K/min at atmospheric pressure. This simulation shows that temperature differences become more pronounced because of the high thermal conductivity of the gas, which withdraws heat from the center zone.

Visualizing both simulations, we observe that the temperature profile in the calorimetric cell clearly deteriorates in the presence of a gas. In air, convection losses are present in the membrane due to the air flux in the upper and bottom side, causing the temperature to reduce deteriorating the profile across the calorimetric cell. To improve the temperature profiles an Ag thermal layer of 50 nm was deposited allowing a homogeneous heating in the microcalorimetric cell. Further simulations were made adding the same thermal plate in the modeling. The results are present in the figures below for both vacuum and air conditions, respectively. The profiles for both conditions improve significantly by adding this type of thermal plate.

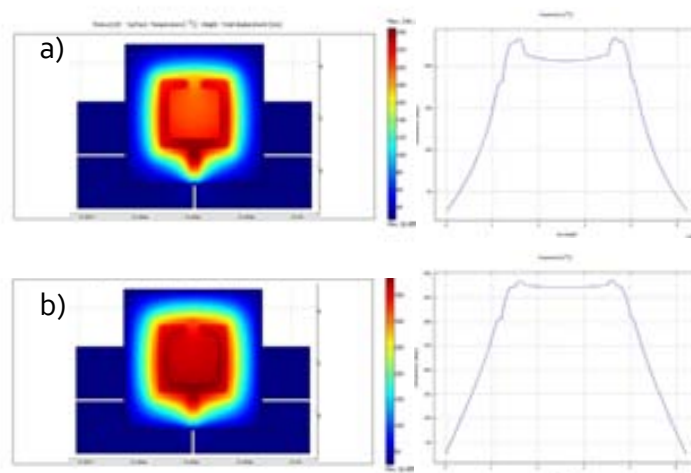


Fig.2.7: U-shaped heater with Ag thermal plate temperature profiles at a heating rate of 10 K/min at a) atmospheric pressure and b) vacuum. The large area required to improve sensitivity imposes severe restrictions on the heater design in order to achieve reasonable temperature variations across the calorimetric cell. The use of an Ag thermal plate below the heater significantly improves the temperature distribution in the device active area.

2.2.3 Experimental measure of temperature profiles

InfraRed thermography can be a suitable technique to determine temperature profiles across the calorimetric cell. Measurements in several of the microcalorimeters available in the Si wafer were tested to analyze their single thermal profile and the behavior of calorimetric resistance due to the microfabrication process. By using a VarioCAM InfraTec thermal imaging camera, which detects the radiation in the infrared range of the electromagnetic spectrum it is possible to identify the thermal profiles of the microdevices and compare these results to the ones obtained with previous simulations.

According to the black body radiation law, infrared radiation is emitted by all objects above room temperature. The amount of radiation emitted by an object increases with temperature; therefore, thermography allows to track variations in temperature. For bodies other than black, the heat radiated depends upon the type of surface which is normally defined by the emissivity of the materials at the surface, ϵ . The radiation emitted from the sample follows the Stefan-Boltzmann law:

$$W_b = \sigma \varepsilon T^4 \quad 2.15$$

where W is the power radiated per unit surface at a temperature T for a body with emissivity ε ; being σ the Boltzman constant= $5.7 \cdot 10^{-8} \text{ Wm}^{-2}\text{K}^{-4}$. The radiated power is proportional to the 4th power of the temperature and varies linearly with the emissivity.

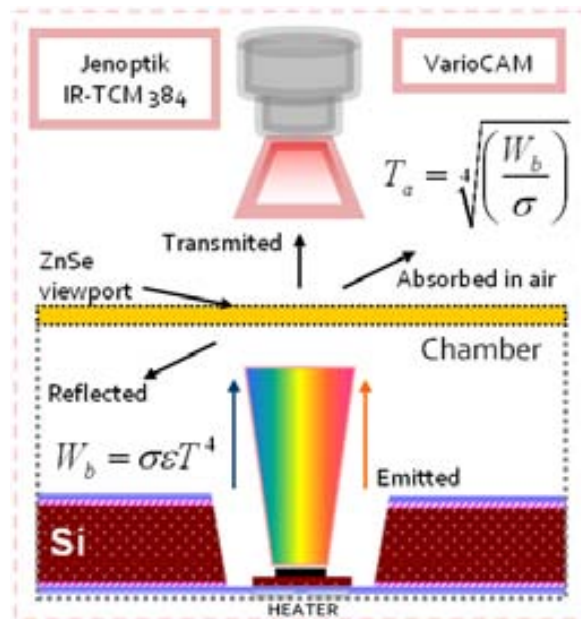


Fig. 2.8: Schematic representation of the infrared configuration. The radiation arriving to the camera does not correspond exactly to the radiation emitted from the heater due to the presence of several radiation losses and external contributions.

Evidently, due to power losses in the calorimetric cell, the power input varies from medium-to-medium. These power losses affect directly the temperature profile of the calorimetric membrane degrading the accuracy of the measurement. If we take, for instance, hydrogen-to-vacuum powers the immense differences in convective power losses produce important changes in the temperature profiles and limits the maximum temperature that can be achieved with a given power, i.e. with an input power of 60 mW the system attains temperatures up to 400°C in vacuum, while only 50°C in hydrogen.

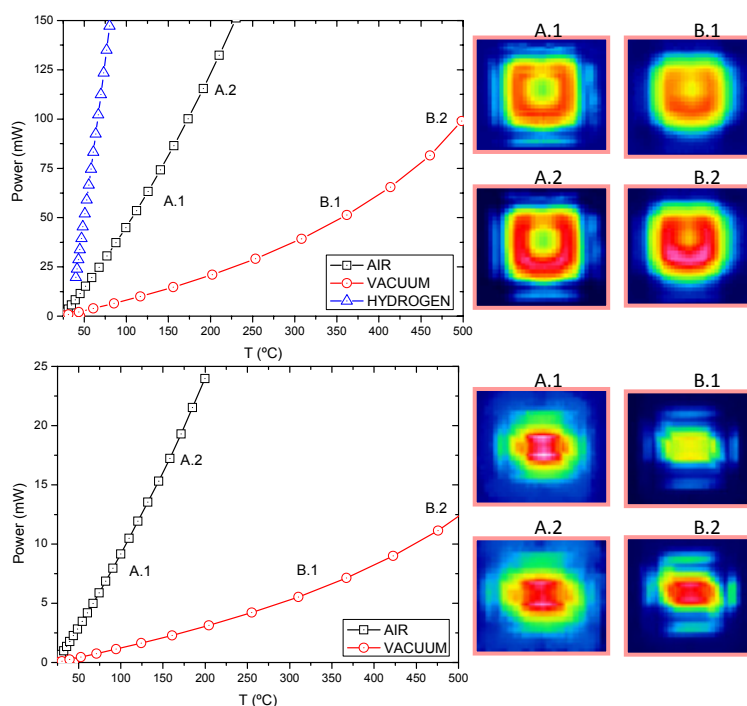


Fig. 2.9: Characterization of the U and S-shaped type of heaters. The graphics show the evolution of the necessary power over temperature at atmospheric pressure, vacuum and hydrogen. Several IR images were acquired when the heaters were fed with a value of an isothermal current. Unfortunately, the pixel resolution of the VarioCAM infrared camera is not sufficient enough to obtain in detail a good ΔT estimation. Nevertheless with this experiment we can link the simulation results with the real temperature behavior of the membrane. The profile of the temperature distribution in the calorimetric cell for different average temperatures is evidenced.

Although it is difficult to extract an accurate value of the absolute temperature from the IR mapping, it is very instructive to visualize temperature differences across the membrane in stationary conditions and to view the thermal performance in the range of the supported current densities of the microdevices. Figure 2.10 shows a comparison of a section of the calorimeter wafer and simulation results. Several calorimeters were heated by inducing a constant current; the heaters are connected in series so the temperature in each device, ideally, will be equal discarding the temperature changes due to resistance value deviations. The thermal profiles formed in different calorimetric cells are in agreement with the corresponding simulation results.

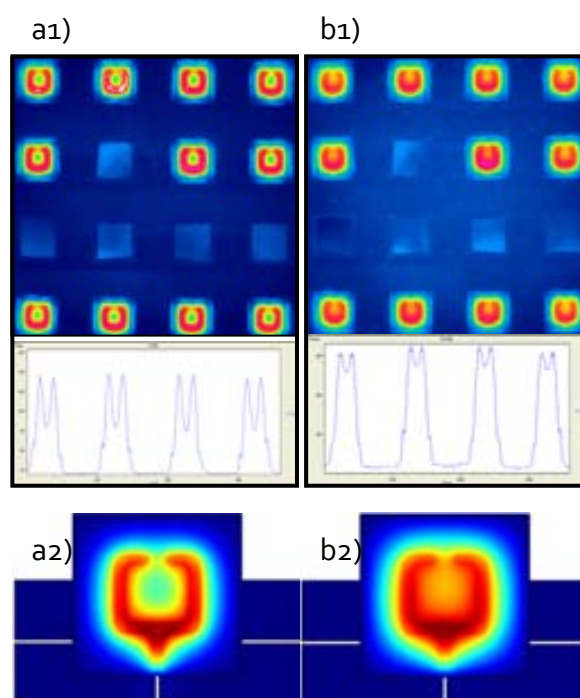


Fig.2.10: IR images of the U-shaped type of heater recorded in a.1) vacuum and b1) atmospheric pressure. We show the temperature profile simulation results of the U-shaped type of heater in a2) vacuum and b2) atmospheric pressure. It is evident that the simulation results are in good agreement with what we obtain experimentally.

It is worth to point out that the S-shaped heater is primarily intended for ultrafast measurements where the temperature variation across the active area of the calorimetric cell is much lower than in stationary conditions. Strip type heaters give suitable profiles at fast heating rates, but an isotropic introduction of heat in the sensing area and the thermal link of the wide platinum wire with the Si frame tend to produce marked parabolic profiles in steady state preventing those devices to be used at lower heating rates. In a U-shape design the thermal profiles are not that of good quality and give an M type of profile in the sensing area, but with the presence of a thermalization layer, the temperature gradient can be drastically reduced. Thermal modeling illustrates the necessity to use suitable thermal layers to improve temperature homogeneity.

2.2.4 Microfabrication

Microfabrication methods based on silicon technology have paved the way for the development of miniature reactors through the use of thin film heaters and thermometers and recent advances in membrane technology. A significant effort has been devoted to build sensitive calorimeters to measure phase transitions in ultra-small systems [4, 5]. A detailed explanation of the development of such devices has been reported elsewhere [6]. Measurements at heating rates spanning 0.1-to- 10^5 K/s are feasible. The variety of rates that can be effectively achieved with enough resolution depend on the power electronics and the sensitivity of the device. Slow heating can be realized after implementing a severe electronic system specially designed to work in *Power Compensation* mode with the aid of a high speed controller algorithm that can provide the current changes needed to balance the power to $\Delta T \sim 0$ and obtain a reliable calorimetric trace. Also, a simpler configuration in which DTA measurements can be done is also possible with this system going up to 1000 K/s. Independent scanning for each cell or differential measurements can also be realized. For the power compensated calorimetric technique it is more suitable to use larger devices to increase the amount of energy released during a specific transformation since due to the electronics associated to active control the noise is typically higher than in non-controlled systems (*Fig. 2.11a*). Calorimetry working in pulse heating has demonstrated to be a powerful technique to measure small systems with great resolution, however, ultrafast scanning calorimetry might not be well suited for analyzing thermal phenomena in kinetically limited processes, such as hydrogen absorption/desorption in metallic hydrides or intermetallic formation in multilayers. In those systems, heating rates need to be greatly reduced at the expense of decreasing power resolution. Microfabrication of larger calorimeters was considered to enhance the power-to-noise ratio by having a much larger surface area. This way, the required heating rates (*K/min*) produce calorimetric traces with sufficient energy resolution to distinguish slow kinetic transitions. The U-shaped calorimeters consist of a 480 nm thick low-stress Si rich SiNx membranes and a ring square-shaped heater with an active area of 6 mm². The microfabrication procedure is analogous to the one used for the S-shaped calorimetric cells, (*Fig. 2.11b*). Recently, it has been shown that power compensation could be adapted to membrane-based calorimeters enabling measurements in the sub-microgram range [7]. The microreactors were fabricated at the Microelectronic National Center in Barcelona using standard microfabrication techniques.

A *Quasi-Adiabatic* technique has been developed to complete the task for the high-speed analysis. Also, a complete electronic configuration is required for the voltage amplifications and

signal coupling. The use of ultrafast rates have been already reported for a variety of studies enabled for ex and in-situ experiments [4,8]. Heating rates of 5×10^4 K/s can be easily achieved with this configuration which permits to study a wide variety of systems in the nano-range with good accuracy and reproducibility. The fast scanning devices have an active area of 2 mm^2 with a centered-serpentine type of heater (Fig. 2.11b). This type of microdevices are composed of a 180 nm thick low-stress Si rich SixNy, a 75-100 nm thick Pt film which was selectively deposited on the membrane by e-beam evaporation using a 5-10 nm thick Ti adhesion layer. The heaters were designed to provide good thermal uniformity across the membrane at fast heating rates (see modeling section).

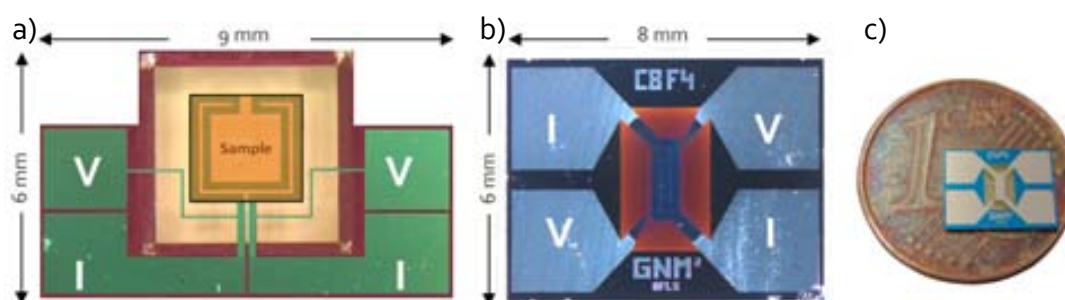


Fig. 2.11: U-shaped type of Heater with an active area of 6 mm^2 showing the paths in with voltage sensing and current feeding is made. b) S-shaped type of heater with an active area of $\sim 1 \text{ mm}^2$ showing the paths in with voltage sensing and current feeding is made. c) S-shaped type of heater visualized on top of a 1 cent of Euro for scaling purposes.

After the lift off process the devices were thermally stabilized by annealing at a temperature of 900 K. KOH etching defined the final size of the membrane. Figure 2.12 shows the evolution of the KOH attack of the last remaining $5 \mu\text{m}$ of Si. The surface roughness of the Si layer is typically high. Under the typical conditions of concentration and temperature, the KOH chemical etch is quite vigorous and creates hydrogen bubbles [9], which hinder the transport of the fresh solution to the silicon surface, causing a sort of micro-masking and hillock formation. The optimum selected process to remove the $5 \mu\text{m}$ Si layer was found to be an attack at room temperature with KOH solution at 60% wt. To etch the individual microcalorimeters a micropipette is used to leave a

drop of the chemical solution, in the hole defined in the silicon by the previous KOH attack. This attack typically lasts around 8-10 hours, and highly improves the smoothness of the final surface while not significantly affecting the SiO₂ layer beneath the Si since the etching rate of SiO₂ is smaller than 0.81 nm/h [9].

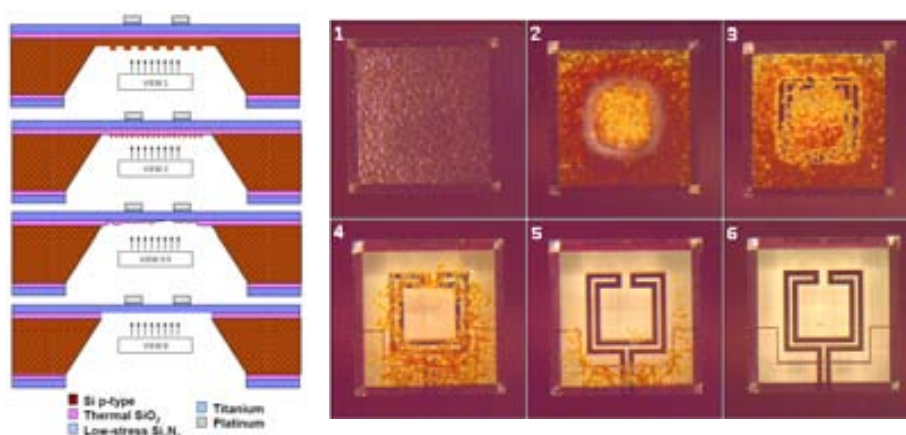


Fig. 2.12: Typical micro-fabrication history of the devices at the last stage of the etching process. The last remaining $\sim 5 \mu\text{m}$ Si layer is removed with a KOH solution at 60 % wt. A drop is directly placed in to the devices with a micropipette. This last process of etching takes around 10 hours following a typical etching rate of $0.5 \mu\text{m/hr}$. The etching procedure will attack the Si layer without affecting the SiO₂ layer since the etching rate for this component is significantly lower. A well defined etching process is critical to obtain identical calorimetric devices, thus making possible to work in differential mode and increase sensitivity.

The level of stress depends on the membrane thickness and influences the resistance value of the heater. Therefore, a suitable control of the etch process is critical to obtain identical calorimetric cells with the aim to measure in differential mode. Several wafers with 5x5 and 4x4 mm² membranes were produced. The largest size was difficult to handle and on average around 10% of the membranes did not survive the final etching process. Improvements on the etching procedure are being developed to increase the mechanical strength of the membranes.

2.3 Device operation

The operation of the microdevices is essentially based on resistive heating by Joule effect. The microcalorimeters are fed with a current through the Pt strips, which will cause a heating in the active surfaces of the membrane due to the electric current passage through the resistive element. By varying the current through the resistor, that is using different powers, various heating rates can be achieved, following equation 2.9. The heater incorporates two leads to measure the voltage drop (V) in the active area of the calorimetric cell (*see Fig. 2.13*) in a four-point configuration. It permits direct calculation of the resistance (V/I) and the power released ($V \cdot I$) in the active area of the heater without considering the thermal leads. From the temperature dependence of the heater resistance (*equation 2.5*) obtained in an independent furnace in a previous calibration, the temperature at a certain point of current value can be obtained as follows:

$$T(t) = \frac{R(t) - R_0}{\alpha \cdot R_0} + T_0 \quad 2.16$$

Where R_0 is the resistance at temperature T_0 and α is the Temperature Coefficient of Resistance (TCR).

Because of the reduced thickness of the different elements forming the calorimetric cell, the temperature of the membrane and the metallic heater can be assumed to be equal, independent of the heating rate. This assumption is especially important at fast heating rates because no thermal lag corrections are required in the calorimetric traces.

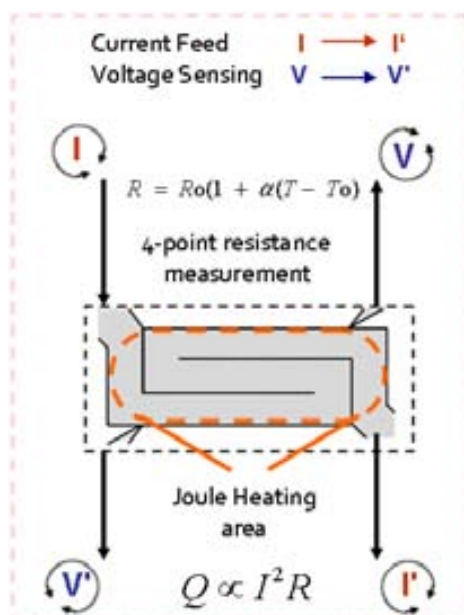


Fig. 2.13: Schematic representation of the micro-calorimeter operation. The calorimetric experiments are performed inside specially designed high-vacuum chambers. Electrical connections to the on-chip bond pads are made using gold coated pogo-pins in a four-point probe configuration. The contact is performed by adjusting the micro-fabricated heaters to a probe card containing the pogo-pins.

2.3.1 Quasi-Adiabatic

Quasi-adiabatic thin film scanning calorimetry is a technique that employs very fast heating rates on a thermally isolated sample to minimize heat losses with the surroundings. The pulse of current, some mA within milliseconds, ensures quasi-adiabatic conditions in our membrane-based devices.

Most of these nanocalorimetric techniques are based on thin films and use experimental conditions necessary to attain adiabatic conditions. The methodology at heating rates up to 500

K/s was created by Hager [10] and a more recent development by Allen et al. [11] permits heating rates up to 10^7 K/s in high vacuum for chips with very small heat capacity addenda. The resolution and energy sensitivity are good enough to permit the analysis of phase transitions in ultrathin films [11-15]. Schick and co-workers have proposed a variant technique under non-adiabatic conditions which consists of inducing a predefined saw-tooth-shaped pulse in low pressure helium atmosphere to accomplish nearly constant scanning rates in a range from 10^2 to 10^5 K/s during both heating and cooling [16,17]. However, important corrections for heat losses have to be considered decreasing absolute accuracy. In general, the quasi-adiabatic technique is essentially important for the study of the thermodynamic properties of very small materials over a wide range of temperatures (crystallizations, glass transition temperatures, melting points, magnetic or superconducting transitions, sublimation, etc.).

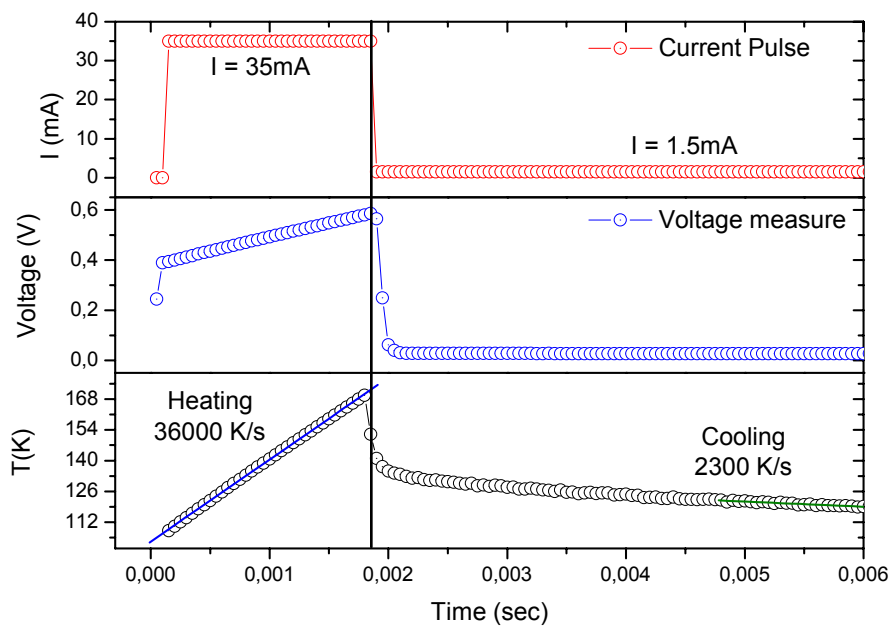


Fig. 2.14: Experimental data as a function of time corresponding to the current pulse, voltage and temperature signal in experiments where cooling is also required. The initiation of the pulse up to 35 mA over a millisecond range will heat up the device with a rate of ~ 36000 K/s. The end of the pulse is lowered to a few mA to acquire the voltage data proportional to the time constant of the device achieving cooling rates about 2000 K/s.

Microcalorimeter design has to be an important consideration for this type of technique since it is necessary to scale down the physical size of the calorimeter in order to measure small amounts of thermal energy and to achieve the smallest fraction as possible of power losses involved while heating at fast rates. The quasi-adiabatic behavior is illustrated in the schematic figure 2.14 where the time needed to reach a temperature T from a base temperature T_0 is much smaller than the time required to cool down to the initial temperature T_0 . Under these conditions measurements are considered quasi-adiabatic and direct values of the heat capacity can be obtained. When using identical calorimetric cells for the reference and sample cells power losses are even lower and absolute accuracy in the C_p measurement can be reached. Under adiabatic conditions the relation between input power and heat capacity is given by:

$$C_p(T)dT = V(t)I(t)dt = P(t)dt \quad 2.17$$

The heat capacity of the reference and sample cells is therefore given as

$$C_p^{reference.cell}(T_R(t)) = \frac{V_R(t)I_R(t)}{\beta_R(t)} \quad 2.18$$

$$C_{P_{empty}}^{sample.cell}(T_S(t)) = \frac{V_S(t)I_S(t)}{\beta_S(t)} \quad 2.19$$

where $C_p^{reference.cell}$ is the heat capacity of the reference cell and $C_{P_{empty}}^{sample.cell}$ the heat capacity of the sample cell without any load. With equations 2.18 and 2.19 it is possible to determine the initial difference between the sample and reference cell prior to depositing any sample to the sample cell. By subtracting these equations it results as follows:

$$\Delta C_{P_{init}}(T_S) = C_{P_{empty}}^{sample.cell}(T_S(t)) - C_p^{reference.cell}(T_R(t)) \quad 2.20$$

The heat capacity of the loaded sample can be obtained by evaluating the increase of the difference in heat capacities before and after deposition. After sample load the heat capacity of the sample cell will contain the heat capacity of the sample and the heat capacity of the addenda (the empty calorimeter before deposition of the sample).

$$C_p^{sample}(T_S) = \Delta C_{P_{load}}(T_S) - \Delta C_{P_{init}}(T_S) \quad 2.21$$

where:

$$\Delta C_{P_{load}}(T_S) = C_{P_{loaded}}^{sample.cell}(T_S(t)) - C_P^{reference.cell}(T_R(t)) \quad 2.22$$

The consideration mentioned in equation 2.22 is valid for an individual calorimeter analysis with sample. The non-differential measurement in quasi-adiabatic conditions is often preferred when the heat capacity of the sample is larger than the heat capacity of the addenda. For example, a typical value of heat capacity at room temperature of a 2 mm² S-shaped empty nanocalorimeter is 100 nJ/K. This value can be reduced to 60 nJ/K with an etching process. After the deposition of 50 nm Ag plate in the central part of the channel the heat capacity rises to 200 nJ/K. When dealing with very small samples in the range of ng this approach does not provide enough sensitivity and the differential approach is preferred. In the differential configuration the current input is equal for both reference and sample cells $I_S(t) = I_R(t)$. If we consider that

$T_S(R) = T_R(R)$ and that $\frac{V_S(t)}{V_R(t)} \approx 1$, we can write the heat capacity of the sample as a function

of the differential voltage $\Delta V(t)$:

$$C_{P_{sample}}(T(t)) = \frac{V_R(t)}{(dT/dt)^2 (dR/dT)|_t} \frac{d\Delta V}{dt} \quad 2.23$$

where $dT/dt = \beta(t)$ and $\Delta V(t) = V_S(t) - V_R(t)$. This procedure presents a much better signal-to-noise ratio compared to the non-differential measurement because for nearly identical cells ΔV is a very small signal that can be heavily amplified [18].

The presence of the sample can modify the heating rate between sample and reference. As the differential voltage is obtained in the time domain a correction on the raw data has to be performed. This behavior in fact establishes a restriction in the amount of mass which can be analyzed in differential mode. In general we use the differential approach for samples with thickness below 100 nm to avoid this type of non-adiabaticity. Single scans show a resolution ($\Delta C/C$) around 5×10^{-2} , i.e. 0.5 nJ/K for a heat capacity signal of 10 nJ/K. Those values can be greatly improved after applying statistical averaging over hundreds of scans through a raw data box averaging procedure (see Figure 2.15). A resolution ($\Delta C/C$) of the order of 2×10^{-3} , i.e. around 20 pJ/K for a heat capacity signal of 10 nJ/K, is routinely achieved in a large temperature range. The following figure shows the general process to obtain the heat capacity from the measured data acquired experimentally.

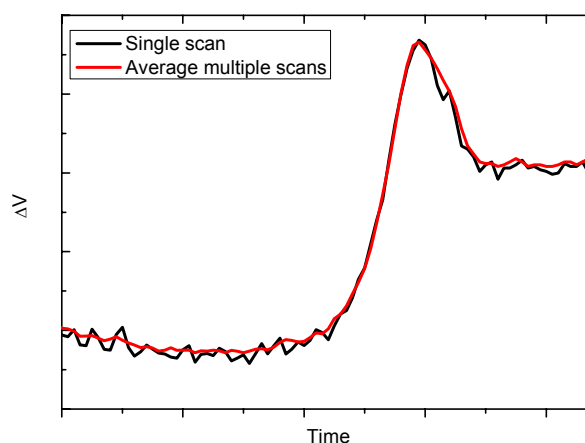


Fig. 2.15: Voltage differential signal where the glass transition of a 50 nm thin film of glycerol is observed. The difference of resolution for the ΔV signal from a single scan and the average of 100 scans is noticeable.

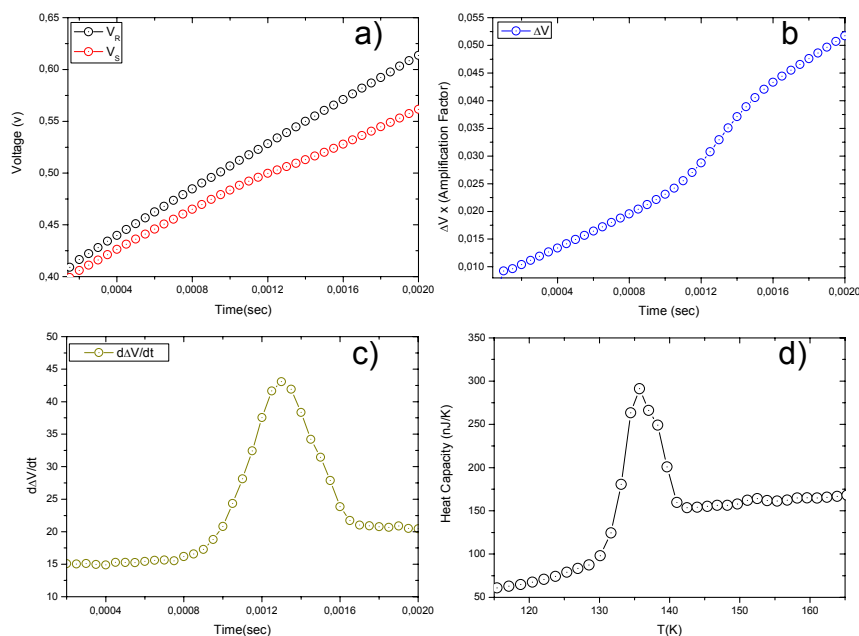


Fig. 2.16: Typically experimental data obtained from the quasi-adiabatic technique to study glass forming liquids. This data has been previously treated with statistics of hundreds of scans and box averaging. a) Shows the voltage evolution as a function of time of both reference and sample cells when the input step of current is applied. b) Voltage difference between reference and sample micro-devices as a function of time. c) Time derivative of the voltage difference $d\Delta V/dt$ signal as a function of time. d) Shows the final result of the heat capacity C_p of a 75 nm thin film of ethylbenzene obtained from cooling the liquid. The result is obtained by using equation 2.23.

The resolution and therefore sensitivity of the measurements in ultrathin films depend largely on the choice of identical calorimeters for sample and reference cells. Therefore, twin chips with similar heat capacity and temperature coefficient of resistance of the Pt heater/thermometer are identified within the wafer to be used in differential mode (Fig 2.16d). The limit of the amplification stage is mainly related to the initial difference between the two calorimetric cells. That is why almost identical pair of calorimeters are needed to obtain high-quality resolution in measured data and increase system capabilities.

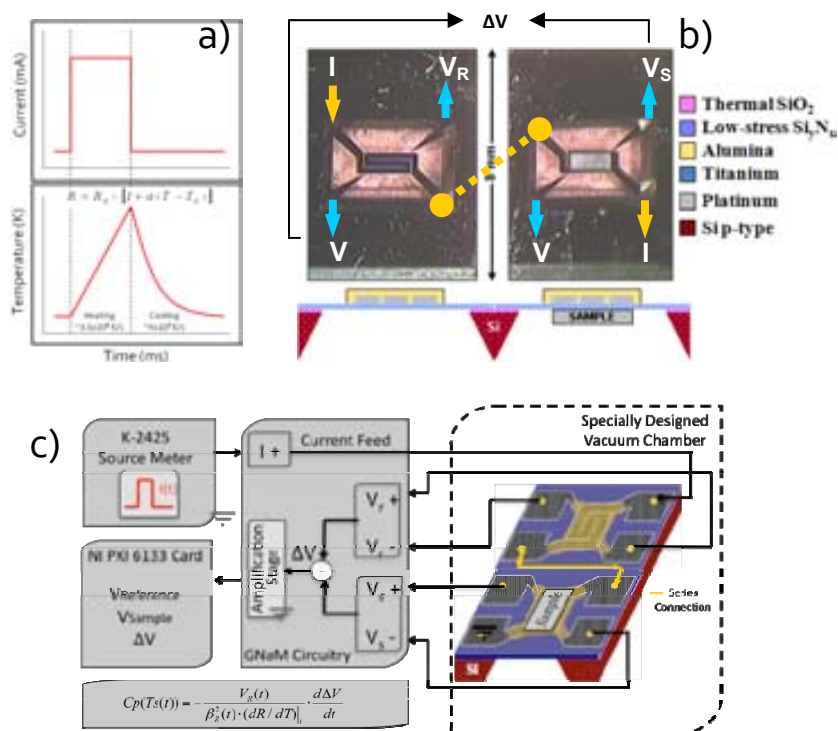


Fig: 2.17: a) Typical current feed as a function of time and temperature response in the millisecond range corresponding of high heating rates around 35000 K/s, b) Differential configuration of twin calorimeters. The micro-devices are connected in series passing the same pulse current in both devices. c) Quasi-adiabatic configuration system which mainly consist of amplificatory stages for single (V_S | V_R) and differential (ΔV) voltage amplification.

2.3.2 Power Compensation

Controlled-based calorimetry has become a key technique to understand and to analyze several material properties and to work as a rapid thermal annealing method in several manufacturing procedures replacing conventional annealing approaches that requires typical heating rates from 1-100 K/s [19]. It is essentially important to develop a technique which could overcome current limitations, such as energy resolution and heating rates imposed in conventional DSC. In those calorimeters heating rates can not be increased due to unwanted thermal lags between sample and sensor and small samples can not be measured since the heat capacity of the addenda dominates the calorimetric signal. For this purpose, membrane-based calorimetry

working in power compensation mode offers enhanced capabilities compared to traditional calorimeters. The challenge is to achieve fast heating rates ($\sim 1-10^3$ K/s) under controlled conditions and to measure the heat released or absorbed by small samples during a phase transition. Although sensitivity limit is well enhanced by using membrane-based calorimeters, control response in this technique needs constant improving to attain linear heating rates at high experimental speeds.

Calorimetry in power compensation mode relies on controller performance since it provides the correction in current that will be induced to the sample calorimeter. If maintaining linear heating rates is necessary independent of the transition taking effect, the implementation of an active control is preferable because it enables direct heat flow measurements. If no controller is present the scanning rate can change dramatically during a phase transition if the energy involved is comparable or larger than the addenda ($1 \mu\text{J/K}$). Additionally, the quantitative determination of the enthalpy implicated in kinetically limited phenomena need slower heating rates than those accomplished in pulse-heating mode under quasi-adiabatic conditions. For this purpose we have developed a power compensation thin film calorimetric system that can attain heating rates spanning 1-to-1000 K/s achieving a dynamic sensitivity below $1 \mu\text{J}$ [7,20]. The use of digital controllers provides more flexibility and greater robustness and speed compared to analogical control systems. However, some disadvantages in control action may arise such as incomplete control response at very fast rates, presence of oscillations or uncompensated thermal effects.

The power compensation calorimetric approach developed in this work is based on a differential arrangement of a pair of twin calorimeters working independently but suffering the same heating rate treatment throughout the entire experiment. This configuration has slight changes and improvements compared with the technique previously developed by the GNaM group [7] since the heating/cooling rates are obtained directly from a predefined current profile which is programmed directly on a Keithley 6221 current source. The two calorimeters have to be almost identical to diminish errors in the measurements. The heating/cooling ramp is accomplished by the inducement of the necessary current to define a linear rate in time.

A well suited version of a power compensation differential scanning calorimeter was created by PerkinElmer [25]. This setup measures the energy difference required to keep both sample and reference cell at the same temperature while computing. When a transformation

occurs, the energy released or absorbed by the sample is compensated by an increase or decrease energy input to the sample cell to maintain a zero temperature difference with respect to the reference side. This configuration is based on two separate control loops: 1) In charge of the control of the average temperature of both cells. This feedback controller compares the temperature of individual cells to the programmed temperature and corrects the electrical power if any deviations are detected. 2) The control of the temperature differences between cells by using a differential temperature amplifier. The amplifier output will adjust the power difference fed to the reference and sample crucibles to maintain the same temperature. The heat of transition is not provided by the differential controller but by the average controller since the same power involved in the sample side during a transition is fed by the differential controller to the reference cell to keep a strict symmetry of the measuring system. This is a very sophisticated apparatus involving good hardware electronics. The main drawback is that it works up to 10 K/s analyzing milligram samples. No higher rates can be implemented with this type of system since controller performance with rapid response is required and cannot correct deviations for fast transformation involved in nanogram samples.

Pursuing this concept we attempted to develop a new high sensitive power compensation scheme working with higher heating rates to analyze nanogram samples. The main purpose of this new development is to reduce noise and control oscillations during the measurements. The action of controlling the current values to obtain linear heating ramps has been removed by implementing two-parallel Keithley 6221 DC Current Sources in charge of inducing a predefined-user current profile to generate, by Joule effect, a linear heating ramp into a twin differential system of calorimetric cells (sample and reference). With this approach we can obtain high heating rates up to 10000 K/s without the implementation of a digital controller although monitoring of current profile for variable rates has to be previously studied. The Keithley® Model 6221 consists in a low current level power-efficient electronic circuit with high sourcing accuracy and built-in point-by-point control functions. It can provide customizable waveforms with an arbitrary waveform generator (*ARB*) at frequencies ranging from 1 MHz to 100 kHz with an output update rate of 10 MS/s. This is of high interest in our application since we can program up to 64000 points of current values achieving high accuracy and low noise levels in the order of nA and eliminating control oscillations generated from the set-point heating ramp. The control loop structure proposed to implement the differential nanocalorimetric setup is divided into four different blocks. i) The first is devoted to the digital calculations performed within a Field Programmable Gate Array card (*FPGA*)

during a reaction. FPGA characteristics and advantages will be described later on in section 3.4.1.

ii) Another block contains the necessary circuitry (current driver, current and voltage sensing with instrumentation amplifiers), iii) the block that includes the acquisition and storage of raw data, iv) and finally the current predefinition block with the Keithley 6221 Current Sources. As the FPGA is loaded with the controller algorithm, the acquisition and storage of all the signals involved in the calorimetric measurements are performed with the National Instruments® PXI 6123 card, which permits acquisitions up to 500 kHz per channel. This strategy releases memory and also accelerates the control loop in the FPGA, since the communication between the FPGA card and the computer is limited to the starting trigger. Both cards, the FPGA NI 7833R and acquisition card NI PXI 6123, are mounted in a NI PXI-8187 computer rack with a Windows-based LabView® installed inside. A host program permits introduction *a priori* of the parameters that define the FPGA controller action and also synchronization of the triggers for the initialization of the raw data acquisition and mainly of the two external Keithley® 6221 Current Sources. The parallel FPGA control action is monitoring the entire measurement and will act upon a signal transition eliminating previous oscillations. The programming of the FPGA is performed with the LabVIEW® FPGA module. It permits defining of the various tasks (*digital operations, analogue inputs and outputs*) in a high-level graphical programming language and afterwards compilation of it in the FPGA to use the NI 7833R card as a dedicated hardware. A detailed explanation of the control development of the system will be discussed in the next chapter

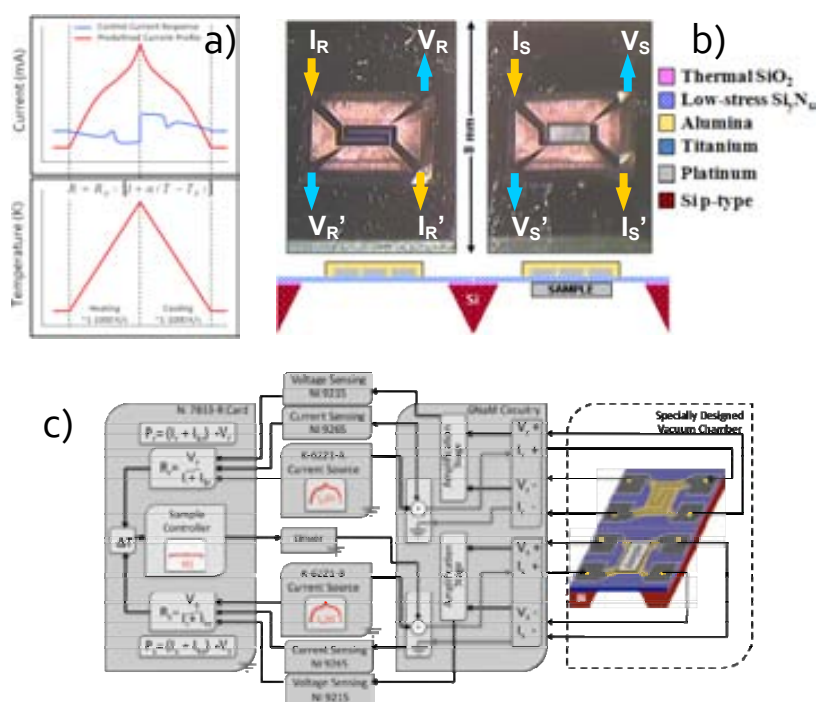


Fig. 2.18: Power Compensated Calorimetry configuration scheme. a) Typical current feed as a function of time and temperature response corresponding of heating and cooling rates from 1K/min to a maximum of 1000 K/s, b) Differential configuration of twin calorimeters. The micro-devices are connected separately. Each device is connected to a current source and to a current PID feeding stage. The current source is the one in charge of applying a predefined current profile corresponding to a linear heating rate in both cells. The PID feeding in the reference cell will be null and will act only in the sample cell upon any evidence of transition phenomena. c) Power compensated configuration system which consist of amplificatory stages for single (V_S | V_R) and differential (ΔV) voltage amplification. Current detection stage for the current source and for the PID feeding and a LabView® PID controller with a control loop of 20 μ s.

While the injection of the current in both microcalorimeters (*reference and sample*), heats up the devices by Joule effect, the other current injection coming from the FPGA differential controller will help correct deviations to adjust the current of the sample to the adequate heating/cooling rate from the control action with respect to the reference temperature. The reference temperature will follow the programmed temperature with the aid of the current profile and the corrections coming from a non-differential PI controller. The FPGA controller only acts during the transformation when $\Delta T \neq 0$. Once the controller calculates the correct compensated control action, it provides the required power in the form of current using home made circuitry based on MOSFET drivers; or the National Instruments 9265 module which has 4 analogical

simultaneous outputs of 100 kS/s with an output range from 0-20 mA for 16 bit resolution. Each output channel comprises individual digital-to-analog converters which produces the current signal coming from control action of the FPGA loop. Each channel also has overvoltage and short-circuit protection. The maximum load supported for this module is 600 Ω which is enough for our system configuration since individual calorimetric load for the centered-serpentine heater ranges from 20 to 60 Ω . Working with maximum channel coverage we would have an upper limit load of approximately 250 Ω . The output current value from the NI 9265 module is added to the predefined current that describes the heating ramp. The sum of the two current signals (heating ramp with Keithley 6221 and FPGA control action) gives the total current necessary to heat the calorimetric cell and act upon heat reaction obtaining the required power for the experiment (See Fig 2.19 for current module output).

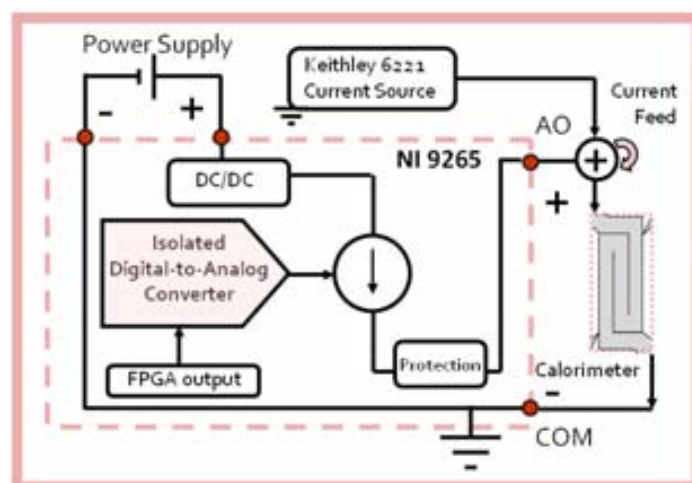


Fig. 2.19: Current module configuration scheme of the calorimetric system working in power compensation mode. Basically the micro-device acquires current coming from two sources. 1) A Keithley® 6221 AC/DC current source which offers tools for defining current ramps and stepping through predefined sequences of up to 65536 output values using. It supports linear, logarithmic, and custom sweeps. 2) A National Instruments® 9265 current module capable of synchronizing with an FPGA logarithm. The maximum of current supplied is 20 mA with a 250 Ω of charge.

During the realization of this thesis work, a prototype of a nanocalorimetric system with analog controllers that attains fast heating rates up to 10^5 K/s in heating and cooling working with a differential scanning power compensated scheme has been proposed and tested with the study of melting and crystallization of metals [21-23]. They use two separate control loops 1) A slow but precise PID controller for the reference temperature control and 2) A high sensitive and fast proportional controller for the sample temperature control. The acquisition of several signals is necessary to determine the power difference between sample and reference cell. A differential power compensation setup using equal sensors provides a direct heat flow rate into the sample which simplifies heat capacity calculation [23]. This system allows investigating very fast processes on heating and cooling up to 10^5 K/s with a reliable temperature measurement with an uncertainty of ± 3 K with some established procedures. This system is the evidence of the correct operation of analog amplifiers and controllers. A Stanford Research Systems with the Small Instrumentation Module was utilized in Schick's et al. development [24]. This is a ready-to-use system with adjustable parameters and PC communication interface. This configuration is a good quality setup which can help for further improvements in the power compensation technique utilizing this kind of fast analog device; however, we have chosen a digital control solution because it provides several advantages over analogical control, such as more flexibility, low cost, greater facility of implementation, and better robustness (sensitivity to parameter variations). The control block used in this power compensation scheme is seen in figure 2.20.

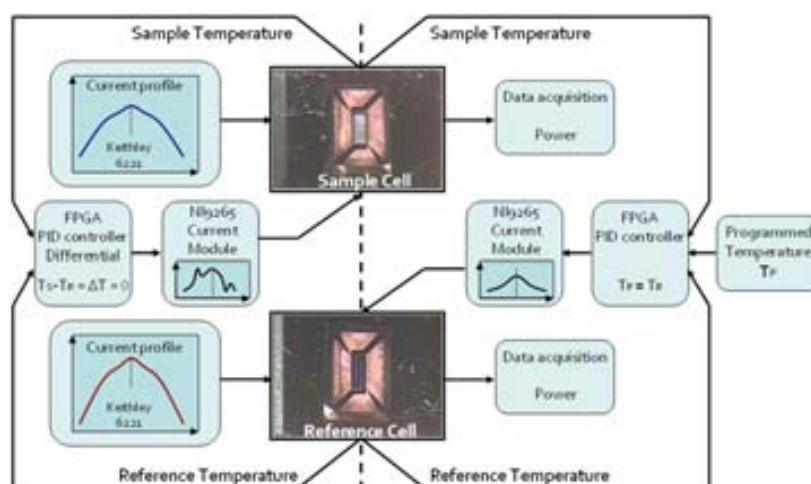


Fig. 2.20: Power compensation scheme for the operation at high scanning rates. Separated modules for the control loop and the heating/cooling set-point

The procedure of the measurements consists on applying the current profile generated by the Keithley current source to produce the heating and cooling rates. A current variable of the FPGA will be attending the transition point of the particular studied sample to act upon reaction. The sum of the both currents will yield the power involved.

To work with a differential power compensated scheme we first measure the power differences between empty calorimetric cells. Then, the sample of interest is placed in the sample cell and the same treatment procedure is applied. The initial difference with empty calorimeters can be expressed as a correcting baseline ΔP_0 which reduces the possible errors introduced, obtaining by two measurements the power employed only to heat the sample (*Fig. 2.21d*). The expression is as follows:

$$Cp_{SAMPLE} \cdot \frac{dT(t)}{dt} = \Delta P - \Delta P_0 \quad 2.24$$

where ΔP_0 is the power difference between empty calorimetric cells and ΔP is the power difference between the sample cell with load and the reference cell. The reason for applying two equal procedures with and without sample using the same calorimetric cells for both measurements is to prevent the possible heat capacity difference due to the conductive losses through the membrane which may change with sample loading.

The data obtained in our typical power compensated measurement are shown in figure 2.21. Every signal with prefix (1) correspond to the involved data acquisition in the first scan to determine ΔP_0 ; subscript (2) refers to the signals acquired in the second scan to define ΔP . The signals (I_{SK1} , I_{SK2} , I_{RK1} , I_{RK2}) correspond to the current profile previously programmed in the Keithley 6221 current sources for a heating rate of 10 K/s. This current profile normally is the same for sample and reference calorimetric cells even though it could be different if calorimeter resistance highly differs between both devices. The currents coming from the NI9265 module coupled with the FPGA control are I_{S1} , I_{S2} , I_{R1} and I_{R2} . We can observe a constant current (I_{R1} , I_{R2}) that correspond to the reference signals in the first and second measurement, respectively. Given that there is no control action for this cell in the two scans since there are no perturbations that can affect the

induced power, the reference current value will be the same through out the experiment for both scans. In the sample side we distinguish the currents I_{S1} and I_{S2} . The first scan is heating/cooling treatment without sample load in which only the change in sample current to adjust the rate to attain $T_{reference}$ can be distinguished (I_{S1}). By using I_{S1} we can define the initial power difference $\Delta P_0 = P_{S1} - P_{R1}$ between empty cells. The second scan corresponds to heating/cooling treatment with the sample loaded in the calorimetric cell. The sample unit will follow the temperature obtained in reference cell by changing the current output of the PI controller (I_{S2}) to correct the treatment rates with respect of the reference temperature and create power compensation $\Delta P = P_{S2} - P_{R2}$ during transition (Fig 2.21 c).

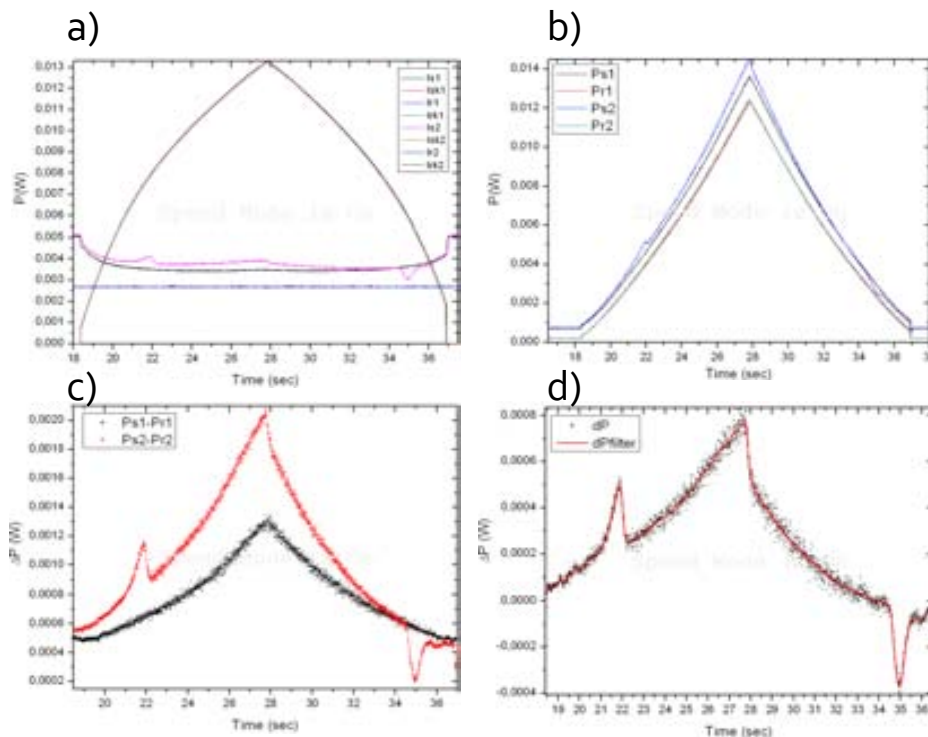


Fig. 2.21: Typically raw experimental data obtained from the power compensation technique to study the melting of a High Density Polyethylene Film (HDPE). a) Shows the power evolution as a function of time of the reference and sample cells for both current sources. Each power is monitored with and without sample. I_{S1}/I_{S2} =Current coming from the NI 9265 to the sample cell without/with sample; I_{Sk1}/I_{Sk2} =Current coming from the Keithley 6221 to the sample cell without/with sample; I_{R1}/I_{R2} =Current coming from the NI 9265 to the reference; I_{Rk1}/I_{Rk2} =Current coming from the Keithley 6221 to the reference cell b) Power evolution as a function of time for the reference/sample cells without/with sample. P_{S1} =Power of the sample cell without sample load; P_{S2} =Power of the sample cell with sample load; P_{R1} = P_{R2} =Power of the reference cell c) Differential individual power evolution as a function of time d) Shows the final result in power compensation mode of a 10 μm HDPE film.

To verify the performance of the S-shaped calorimeter working in power compensation mode we have studied the melting of a 10 μm thick high density polyethylene (HDPE) film corresponding to an approximate mass of $\sim 4 \mu\text{g}$. HDPE is chosen as a reference material since it is well known and provides a severe test for the microdevices. Prior to acquiring the data, the sample is held isothermally at 400 K to completely melt the film and improve the thermal contact between sample and surface with the aim to minimize thermal lags at fast heating rates. The HDPE film is a poor thermal conductor and very thick compared to the surface of the calorimeter and thermal gradients along the thickness of the film could develop at very fast heating rates. In fact, this phenomenon adds an important constraint to the calorimeter behavior. The measured onset temperature for melting, 398 K, and the heat of fusion, 165 J/g, agree with values obtained from a commercial DSC apparatus for larger samples. With this same procedure, measurements for different heating rates are performed. Slow heating rates were performed to study the melting of the HDPE film to avoid possible thermal lags at higher rates which affect the calorimetric traces and to compare the behavior at the same cooling rate. The next figures show the melting transition of HDPE for 3 different slow heating/cooling rates. The transition melting point can be easily resolved even for the slower heating/cooling rate of 1 K/min. The sensitivity of the differential measurements is around $500 \pm 100 \text{ nW}$ which is obtained by equation 2.24 at a slow heating rate of 1 K/min.

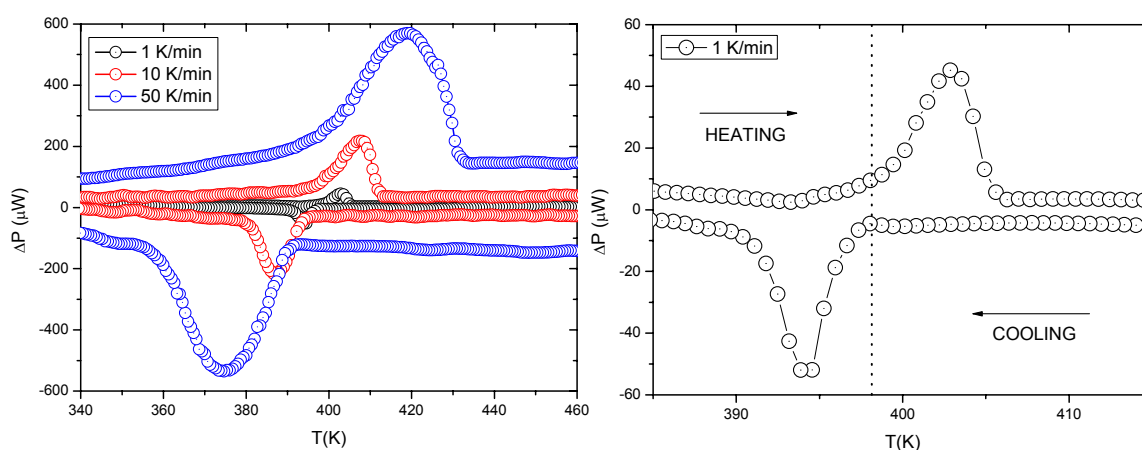


Fig. 2.22: Calorimetric traces showing the endotherm in continuous heating/cooling of the melting of a 10 μm thick HDPE film at various rates. The low mass involved ($\sim 4 \mu\text{g}$) and the slow heating/cooling rates demonstrate that the system is well suited for the characterization of small samples with power accuracy below 500 nW

Since Indium is a well established standard in calorimetry, with a melting transition at 429.75 K and a specific heat of fusion of 28.39 J/g; and considering the system limitations on power resolution, we chose to analyze first-order transitions like an In film with a nominal thickness of 150 nm ($m = 1 \mu\text{g}$) in order to test the controller with small perturbations. A pair of two identical calorimeters with a resistance difference below 0.5% (26Ω at 293 K) are mounted inside a specially design ultra-high vacuum chamber. The In sample is e-beam evaporated onto the active area of the sample cell membrane using an especially design shadow mask located 100 μm from the surface limiting sample growth. The value of the sample area can be obtained from an optical microscope after deposition with typical values around $0.87 \pm 0.04 \text{ mm}^2$. To diminish the time response of the devices, the experiments were carried out in the pressure range of $1 \cdot 10^3$ mbar. To prevent the complex behavior of the calorimetric traces due to radiation heat transfer the measurements are held below 550 K. Since the melting transition is reversible, no baseline subtraction of the second scan can be performed. The initial power difference ΔP_0 was determined by heating the calorimeters several times at different scanning rates prior to deposition. The sensitivity of the differential measurements is around $5 \pm 1 \mu\text{W}$ which is obtained by equation 2.24 at a maximum heating rate of 1000 K/s.

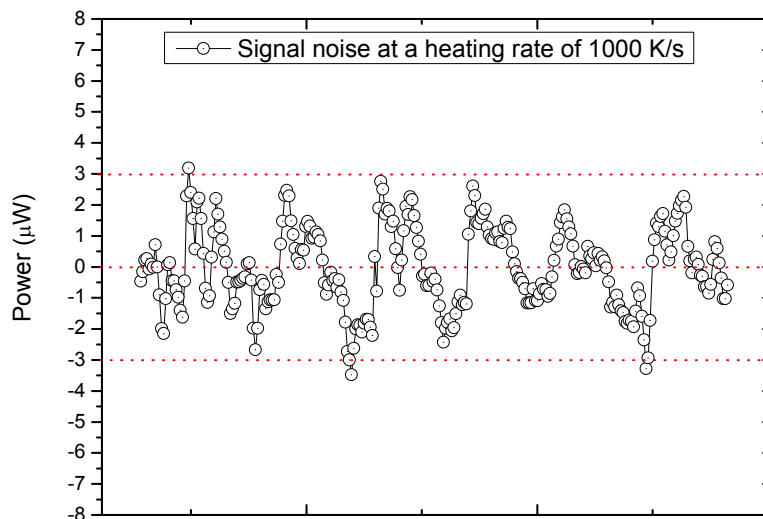


Fig. 2.23: Signal noise at a heating treatment with a rate of 1000 K/s.

Figure 2.24.a shows the data of the ΔP as a function of temperature for several heating rates. The melting transition during heating appears as an endothermic peak for all the heating rates. Although the achievement of the T_{onset} of the transition is clearly evident a dramatic enlargement of the melting area is present as the heating rates increase. Previous power compensation systems development in GNaM [6], show that for slow heating rates below 200 K/s the width of the melting transition remains narrow and constant achieving temperature differences (*width of the calorimetric peak*) of only 20 K which indicates the overall goodness of the system working below these heating rates. However, for higher heating rates the end of the melting peak moves to higher temperatures enlarging the peak with a $T_{\text{end}} - T_{\text{onset}}$ close to 100 K at 1000 K/s. These peak variations were explained by associating the broadening of the peak with temperature non-uniformities in the active area of the calorimetric cell and the non-zero error of the controller response during the phase transition. In our calorimetric traces we can observe temperature differences ($T_{\text{end}} - T_{\text{onset}}$) of 50 K at 1000 K/s and of 100 K for rates reaching the 4000 K/s. With this configuration we achieve minor improvements regarding the calorimetric traces and maximum heating rates.

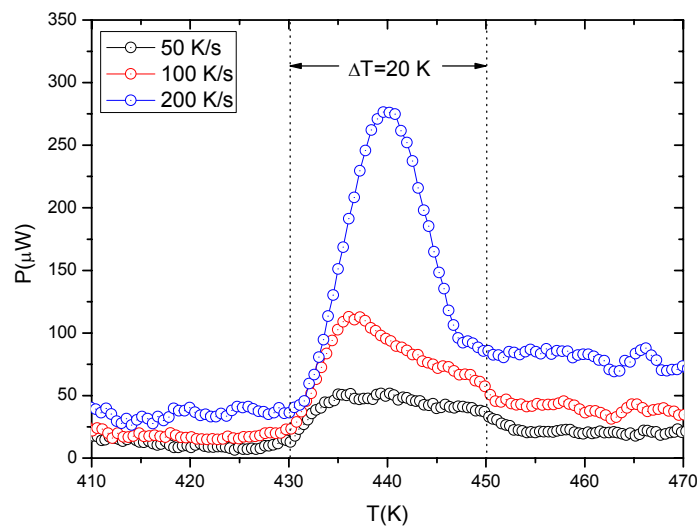


Fig. 2.24: $\Delta P - \Delta P_0$ curves as a function of temperature at low heating rates for a 100nm In thin film. The vertical lines mark the peak wide of the transition.

The control action cannot guarantee a constant error during the phase transition. In figure 2.25b we show the temperature error involved during the melting at the several heating rates. Power losses linearly depend on cell temperature, and the contributions to the apparent heat capacity are larger as the heating rate slows down. With heating rates above 200 K/s it is necessary to consider power loss corrections to analyze the phase transition as we will describe in the next section. For heating rates above the 1000 K/s the control algorithm does not respond adequately and will not achieve a zero temperature difference between sample and reference cell. We monitor higher temperature errors around 10 K for a 4000 K/s heating rate. With this high temperature errors involved during the transition it is difficult to acquire precise data of the energy of transformation. A more suitable electronic system with very low noise components, highly accurate integrated circuits and an accurate control loop with time responses below the 20 μ s are required. Also a redesign of microdevices can be considered to actually extend power compensated measurements at higher cooling rate since the time response of the calorimeter is dominant in a cooling process.

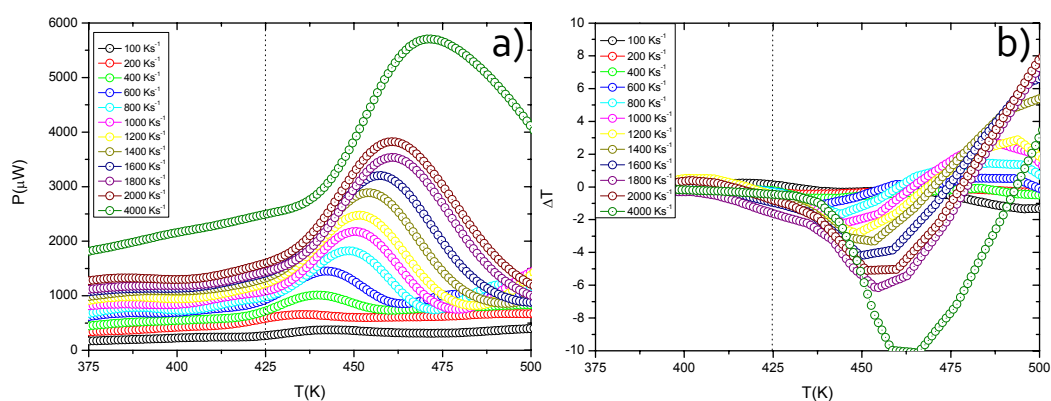


Fig. 2.25: Calorimetric traces of power and ΔT involved in the melting of a 150 nm In thin film. a) Differential Power curves as a function of temperature at several heating rates from low to high speeds (100-4000 K/s) with the Ar atmospheric pressure fixed at 1bar. b) Curve showing the temperature error signal as a function of temperature for the calorimeter loaded with the sample at the different heating/cooling rates. Higher speeds will involve larger errors in temperature due to system limitations.

2.3.3 Power Losses

One of the main variables in calorimetry is the power release by the system to reach certain temperature value. This main variable is affected directly by a term, power losses, that in most of the cases cannot be eliminated. Some systems in differential configuration are able to minimize differences between sample and reference and therefore heats of reaction can be easily determined. In cases of a well defined geometry subtraction of the power losses can also be accomplished, although, at the expenses of a reduction of absolute accuracy with respect to adiabatic calorimeters. The power losses of the calorimeter depend on the cell temperature and on the surrounding temperatures (T_0). At medium-to-high temperatures the nanocalorimeters have a non-ideal behavior and so the power losses become more relevant to the heat capacity evaluation. Corrections have to be performed in order to obtain a reliable measurement; these corrections depend on a proper estimation of the real P_{losses} term for each calorimetric cell in all scans. To visualize the P_{losses} effect we chose to analyze a first order transition of the melting of a high density polyethylene film (HDPE) of 10 μm thickness for comparison reasons with the total enthalpy necessary for a dehydrogenation process that will be discussed later on, a film of mass $\sim 70 \mu\text{g}$ was used corresponding to an enthalpy value of $11 \pm 1 \text{ mJ}$. This analysis is done with the use of the U-shaped microdevice since it present a more aggressive heat loss. HDPE is chosen as a reference material since it is well known and provides a severe test for microdevices in terms of both its relatively low thermal conductivity and poor wettability with the Ag layer that works as a heating plate. The crystallinity of the polyethylene thin film is 60% at room temperature, for a 10 μm thick film. The HDPE sample was placed with the aid of a micromanipulator on the Ag thermalization layer ($3 \times 3 \text{ mm}^2$), just above the heater and temperature sensors.

We have to identify the P_{losses} term in the equation of the calorimeter.

$$C_p(T) \cdot \frac{dT}{dt} = P_{heater}(t) - K_{th} \cdot (T - T_{frame}) - \varepsilon \sigma \cdot (T^4 - T_{room}^4) - h \cdot (T - T_{room}) \quad 2.25$$

where C_p is the heat capacity of the calorimetric cell, T is the average temperature in the calorimetric cell, P_{heater} is the power induced by the heater, T_{frame} is the temperature of the silicon

frame, T_{room} is the room temperature and Kth , $\varepsilon\sigma$ and h are the parameters which describe radiation and convection losses. So, we can possibly identify the term P_{losses} as:

$$P_{losses}(T) = Kth \cdot (T - T_{frame}) - h \cdot (T - T_{room}) - \varepsilon\sigma(T^4 - T_{room}^4) \quad 2.26$$

As already mentioned in the modeling section of chapter II, the thermal profiles play an important role not only in the sample deposition section but also in the rest of the membrane, since the conductive losses of the calorimetric cell depend on the surrounding boundary temperatures. Power losses linearly depend on the cell temperature, and the contributions to the apparent heat capacity are larger as the heating rate decreases.

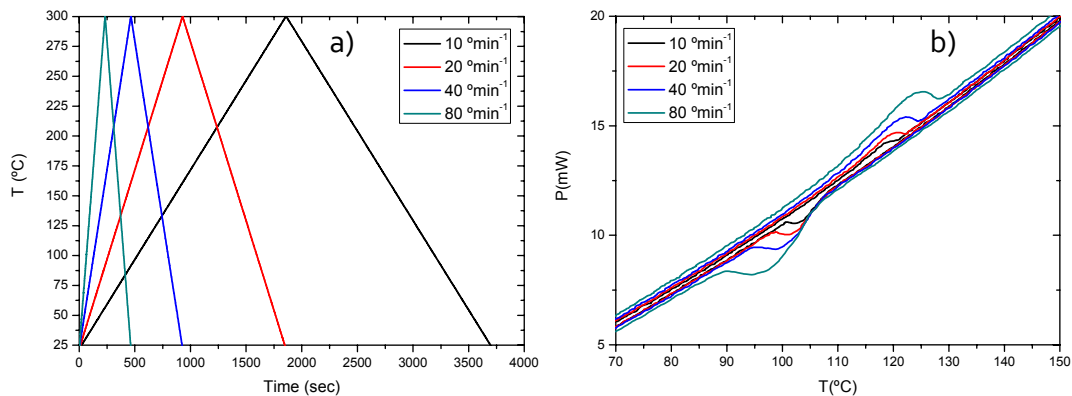


Fig. 2.26: a) Temperature profiles of the micro-calorimeter loaded with a 10 μ m thick HDPE thin film for various predefined linear set-points. Scanning rates ranges from 10 to 80 °C/min. b) Power signals as a function of temperatures for the calorimetric scans in heating/cooling experiments.

Heating and cooling measurements are made by simply fixing a temperature set-point with a positive and a negative ramp condition, for heating and cooling, respectively (Fig. 2.26). These conditions will generate the power induced by the heater eventually overcoming the melting transition of the HDPE thin film in the upper (*heating*) and lower (*cooling*) analysis. The smaller the current, the smaller the heating rate, and therefore the P_{losses} become larger and the measured heat capacity has a larger contribution from heat losses. In the limit of an infinite

heating rate, the P_{heater} should also grow to infinite while P_{losses} will remain finite. Then, if for a given temperature we plot the heat capacity values of the calorimetric cell measured at different heating rates as a function of the inverse of the heating rate, the points will be aligned and the heat capacity for an infinite heating rate, that is for P_{losses} equals zero. A linear fitting of these data can be used to predict the $Cp_{apparent}$ value for an infinite heating rate, which directly gives the real heat capacity at the given temperature, this is shown in figure 2.27. If the real Cp is known at several temperatures, the $P_{losses}(T)$ can be expressed as the following expression for each heating rate $\beta(T)$.

$$P_{losses} = [Cp_{apparent}(T) - Cp_{real}(T)] \cdot \beta(T) \quad 2.27$$

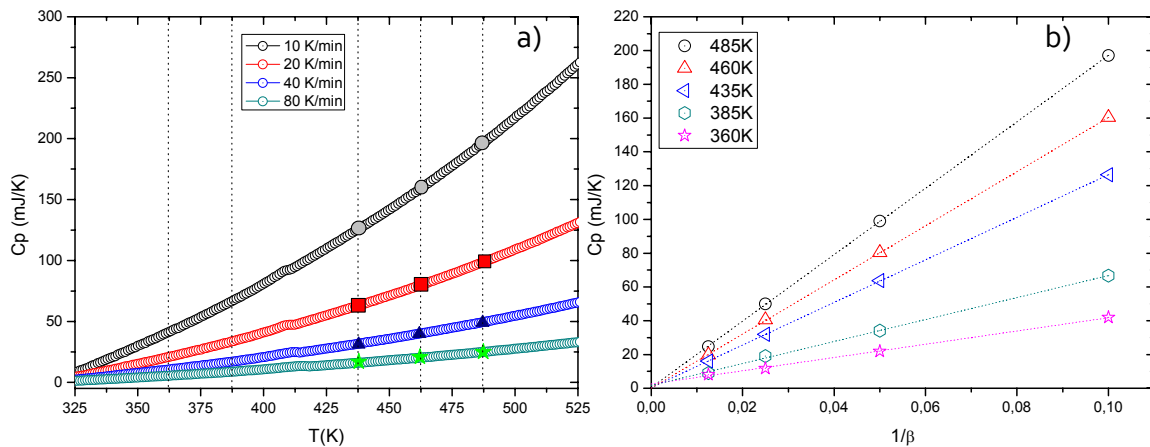


Fig. 2.27: a) Apparent heat capacity as a function of temperature for the calorimetric scans for several predefined set-points. Scanning rates ranges from 10 to 80 °C/min. b) Linear regressions of the apparent heat capacities measured at different heating rates at a given temperature value. The extrapolation to $1/\beta=0$ permits to obtain the "Real Heat Capacity" Cp_{REAL} which will be taken into account for the power losses estimation.

This method produces noisy functions. To eliminate the noise, these functions that are featureless can be fitted with a polynomial. The polynomial function will have the next appearance.

$$P_{losses}(T) = A + B \cdot (T - T_{frame}) + C \cdot (T^4 - T_{room}^4) \quad 2.28$$

The term A ideally should be zero. However, we have evidence that the linear fitting procedure introduces some errors in P_{losses} and the curves are slightly shifted to positive values at low temperatures. This error tends to zero at high temperatures when emissivity dominates. In order to consider the final losses we impose A equal to zero. At low temperatures, the value of P_{losses} is very small and the heating rates β are the largest in the scan. In the final correction of heat capacity, the P_{losses} term is weighted by the β , and therefore the error is minimized. Figure 2.28 shows the polynomial function extracted from the analysis, where we measure the melting of a high-density polyethylene (HDPE) 10 μm thick film.

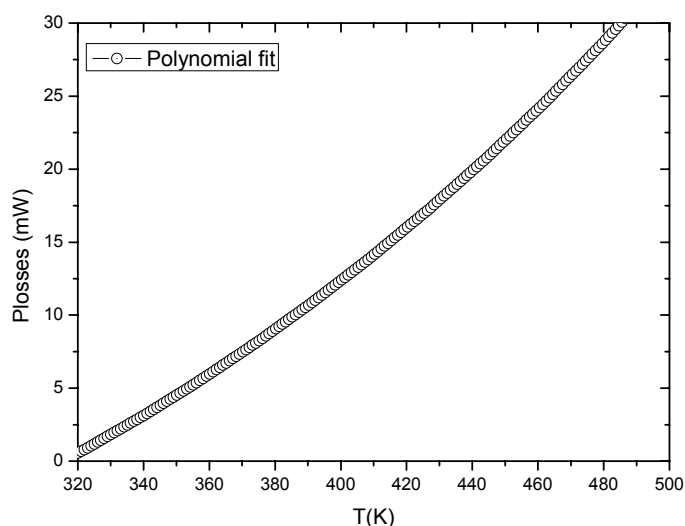


Fig. 2.28: Curve showing the Plosses values in mW as a function of temperature fitted with a low order polynomial expression.

The methodology outlined above is only applied to reversible transformations with a monotonic behavior of the different parameters. Irreversible reactions should be analyzed with a different approach, but this analysis may provide us with an idea of the P_{losses} effect under the same experiment conditions and for amount of energies of the same range. The main interest of this study was to check the capability of analyzing the effect of P_{losses} in the dehydrogenation behavior of metal hydrides.

Figure 2.29 shows the calorimetric measurement at different heating rates on the HDPE film after baseline subtraction and heat loss corrections. The baseline was taken of an empty calorimeter for each heating rate, since the thermal resistance, RT , between heater and surroundings do not change appreciable upon location of the sample on the centre of the membrane. With an empty microreactor, the temperature difference between the set-point and the measured temperature was below 100 mK independent of the heating rate. Measured enthalpies of $\sim 13 \pm 1$ mJ were obtained which correspond to the correct estimation for a ~ 70 μ g sample, this energy can give us an estimation of the P_{losses} effect in the calorimetric traces. These results are in agreement with the different analysis previously made at GNaMs group which yielded an onset temperature for melting, $T=394$ K and a heat of fusion of 165 J/g [19].

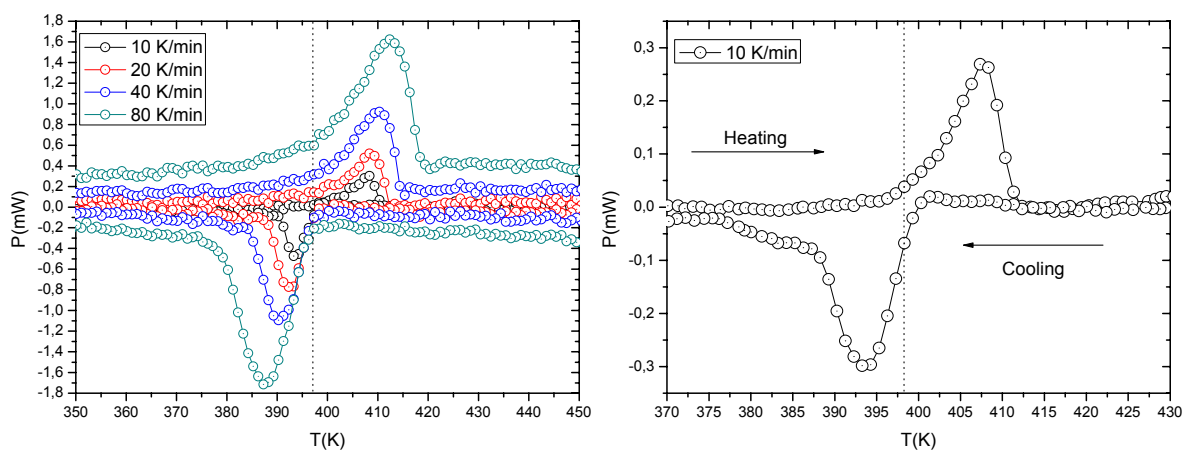


Fig. 2.29: Power signals as a function of temperatures for the calorimetric scans of a HDPE film a) at different heating/cooling rates b) For a heating of 10 K/min which will be the typical rates use for (de)hydrogenation analysis. The measured enthalpy is independent of the heating rate with a value of 13 ± 1 mJ for a sample of ~ 70 μ g.

Chapter III

Hydrogen Storage Materials

3.1 Introduction: Metal Hydrides

The development of effective hydrogen storage technologies is the object of intense research with the final goal to replace fossil fuel in transportation and reduce CO₂ emission to the atmosphere. For such purpose, the requirements dictated by the Department of Energy of the USA are being used as the goals to be fulfilled to achieve a cost effective competitive technology. Chemical and physical absorption are two possibilities which are being investigated.

Many metals and alloys have the ability to reversibly absorb hydrogen under moderate pressure and temperature, creating hydrides through chemical reactions. On these, molecular hydrogen is dissociated at the surface before absorption while two H atoms recombine to H₂ in the desorption process. In these materials, hydrogen is released when heat is applied through an endothermic reaction, which makes this process inherently safe. Metal hydrides have different thermodynamic properties depending on the particular composition. However, most of the metals known to form hydrides do not show appropriate desorption properties in the pressure and temperature range attractive for mobile storage (1-2 bar, 0–100°C), corresponding to an enthalpy change between 15 and 24 kJ mol H⁻¹ or they lack enough volumetric storage capacity to be used in real applications. New complex metal hydrides with large storage capacities have been recently synthesised and are receiving further attention [1-3]. Unfortunately, the hydrogen release is generally irreversible, and only some particular compounds have been found to be reversible (NaAlH₄ + TiCl₃) [4]. Another possibility of storage is physical absorption that has been largely studied in carbon-based structures, although in general due to the weak adsorption interaction the process of adsorption/desorption occurs below ambient.

The combined demands of reversibility of hydrogen loading, high capacity, low volume, low weight, price, safety and ease of operation make that, currently, no material meets the constraint for reversible hydrogen storage under near-ambient conditions.

Several alloys exist with promising properties for hydrogen storage like fast and reversible sorption kinetics with good cycling life and room temperature operation. For example $\text{LaNi}_5\text{H}_{6.5}$ which shows important features like astonishing volumetric hydrogen density at low pressures (2 bar) with the same operation temperature for hydrogen desorption. Storage in these intermetallics allows very safe hydrogen handling. But as lanthanum and nickel are large elements, the proportion of hydrogen in $\text{LaNi}_5\text{H}_{6.5}$ remains below 2 mass%. This is attractive for electrochemical hydrogen storage in rechargeable metal hydride electrodes, reaching a capacity of 330 mA h g^{-1} . For mobile applications the requirement of storage are to be within 4-6 mass %¹. The main drawback for scientist studying metal hydrides working near room temperature is the low mass density (Fig. 3.1). Although it is well known that many intermetallic compounds and alloys form hydrides with up to 9 mass % hydrogen they are not reversible within the required range of temperature and pressure.

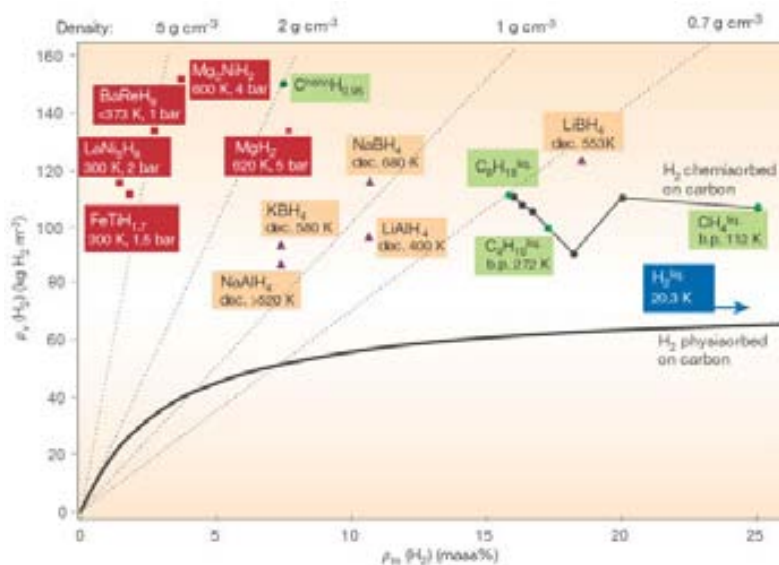


Fig. 3.1: Stored hydrogen per mass and per volume. Comparison of metal hydrides, carbon nanotubes, petrol and other hydrocarbons. Figure obtained from reference [27]

¹ 6.5 mass% and $62 \text{ kg H}_2 \text{ m}^{-3}$ are the targets of the US Department of Energy

Magnesium has probably attracted the most attention to the hydrogen storage field. Due to its properties Mg satisfies almost all requirements needed for storage in mobile applications except for its high stability and slow kinetics. Magnesium hydride has one of the highest reversible capacity, 7.6 wt.% H₂. This makes the material highly interesting for hydrogen storage purposes. A drawback of the material is the high enthalpy of formation of MgH₂, around -78 kJ/mol H₂, responsible for the high-temperature release of hydrogen (*552 K at 1 bar*). Magnesium also exhibits very slow hydriding and dehydriding reactions even for laboratory-size samples. The kinetics of the loading and unloading reaction is too slow during loading of hydrogen as a result of the formation of a closed shell of MgH₂ around a Mg metal core. Extremely long times are needed to overcome this diffusion barrier which inhibits hydrogen diffusion. The mobility of H in bulk MgH₂ is very low due to the lack of H vacancies. In Mg metal the mobility of a dissolved H atom is very high. Recent developments have shown the progress made in the past few years to improve Mg kinetics through a decrease in the grain size, however, element stability optimization still remains unsolved.

One strategy in the search for new metallic hydrides with improved performances is thus alloying magnesium with other metals with the aim to decrease the enthalpy of formation.

3.2 Metal Hydride Thin Films

Reduction of the material to the nanoscale by preparing nanostructured or nanocomposite bulk or thin films, has demonstrated improved hydrogen sorption and desorption kinetics [10-12]. In thin films hydrogenation/dehydrogenation is not significantly kinetically limited because of the short diffusion paths involved, and lower reaction temperatures can be used for an effective hydrogenation test of the system. In addition, thin films can be analyzed with high throughput screening techniques to foster the discovery of new hydrogen storing materials and associated catalyst/promoters. Another advantage of introducing the thin film approach for the research of new hydrides is the fact that metastable or amorphous phases, inaccessible by other techniques, can be synthesised and studied. Although thin films are envisioned mostly as test systems several industrial applications have been proposed as hydrogen sensors and switchable mirrors [5-8].

In order to decrease the thermodynamic constraints, various strategies for the development of Mg-based alloys for hydrogen storage have been analyzed and experimentally tested. In the last decade, several studies concerning hydrogen storage materials as thin films have been performed. In 2002, Leon and co-workers were able to store up to 7.5 % hydrogen in air exposed Mg thin films but the high temperatures of operation were not the ones of interest (350 °C) [9]. Recent developments to decrease hydrogen reaction enthalpy have been studied. Jian-Jie et al. have shown that magnesium hydride enthalpy can be lowered down to 58 kJ/mol H₂ when its grain size is reduced to 0,6 nm [10]. Also, another route to reduce the reaction enthalpies and achieve high storage capacities is by combining Mg with light-metal hydrides. These composites are often denoted as reactive hydride composites (RHC) since they react upon desorption in an exothermic reaction [11]. Attractive examples of Mg-based RHC are borohydride composites like, MgH₂ + NaBH₄, MgH₂ + Ca(BH₄)₂ which have very high storage capacity although high hydrogen pressures and high temperatures (500 K) are needed to reach reasonable fast absorption rates. When the Mg has started absorbing hydrogen a kinetic barrier appears, which may block further hydrogen uptake. Even though the surface kinetic barrier can be eliminated, with the addition of Pd to Mg surface, the barrier of the hydride to H₂ diffusion is still an unsolved issue [12]. Higuchi et al. [13] were able to reduce drastically the stability of MgH₂ by capping Mg thin films by Pd layers from both sides. Operating temperatures as low as 100°C were necessary to desorb hydrogen from the films under vacuum conditions. H. Akyildiz et al. reported the hydrogen storage in Magnesium thin films carried out in a constant volume apparatus (*Sievert-type*). They demonstrated the improvement of hydrogen uptake for Mg capped with Au-Pd compared for that in pure Mg [14]. Hydrogenation of pure magnesium and magnesium-aluminum thin films were studied in GNaM by R. Domenech-Ferrer and co-workers who performed hydrogenations at temperatures as low as 50°C in a few minutes. They characterized several Mg/Al films capped by a thin film Pd layer and proved that adding aluminum to Mg films improves its hydrogenation capacity. Also, they have confirmed that titanium is a better catalyst for the (de)hydrogenation of the Mg films [16]. Several studies on the (de)hydrogenation characteristics of MgSc have revealed excellent rate-capability and high reversible storage capacity [23]. Nevertheless, Sc high cost prevents this element from being used for any commercial application. A good alternative is to use Titanium instead; Ti atomic weight is nearly similar compared to Sc.

Ti also has a catalytic effect on the hydrogenation properties of magnesium. Griessen et al [15] have recently prepared an MgTiH ternary hydride from a vapor phase technique under

moderate conditions which is not accessible by other synthesis technique. Mg/Ti thin films have been demonstrated to be a well suited hydrogen storage material, with five times larger storage capacity than that of conventional metal hydride electrodes in NiMH batteries [13]. One of the most surprising properties of Mg/Ti-H films is their structural stability. An equality of the molar volume of TiH_2 and Mg is present. Very little is known about the stability, structure and electronic properties for these alloys. The binary phase diagrams for Mg with Ti indicates that no stable bulk compounds are formed. Investigations in the structure, optical and electrical properties have been made for $Mg_yTi_{(1-y)}H_x$ thin films showing that the crystallinity of the films is preserved during the hydrogenation process [14].

Studies show that $Mg_{0.8}Ti_{0.2}$ alloys have excellent rate-capability and high reversible storage capacity without the Ti forming stable compounds with Mg [24]. Increasing the Ti-content beyond 20 at.% induces the storage capacity to decrease slightly, which is solely dependent on the increasing weight of the corresponding alloys. Titanium is a lightweight metal, strong, corrosion resistant and abundant in nature. It does not form any alloy with magnesium. In contrast to the later transition metals, titanium does not form TiH_x . Also, Ti layers prevent the formation of Mg_xPd_y inter-metallics during thermal treatments. The incorporation of Ti enhances the hydrogenation process of magnesium films at the expense of inducing their partial detachment from membrane after adsorption. Results published by Song, Y et al. [25] suggested that the hydriding/dehydriding kinetics of magnesium hydride can be improved by the addition of titanium into the compound. The addition of a Ti thin film also lowers the onset temperature for dehydrogenating the sample compared to pure Mg and Mg-Al alloys [16]. D. M. Borsa et al. have analyzed the reflectivity of $Mg_yTi_{(1-y)}$ alloys with different values of y, highlighting the applicability of these films as smart solar collectors, in which all the films have a relatively high and featureless reflection that decreases with Ti content, reflection that diminishes after the hydrogenation process [8].

3.3 Thermodynamic characterization

The thermodynamic aspects of hydride formation from gaseous hydrogen are usually described with the Pressure Composition Isotherms or PCI (*Fig. 3.2*) [17]. The host metal initially forms the α -phase, solid solution. Increasing the pressure also increases the concentration of hydrogen inside of the metal. Afterward, for higher hydrogen pressure, the hydride β -phase

grows in the α -phase. While the two phases coexist, the isotherms show a flat plateau, the length of which determines the quantity of H_2 that can be reversibly stored with small pressure variations. In the pure β -phase, the H_2 pressure rises steeply with the concentration. At higher H_2 pressure, further plateaux and further hydride phases may be formed. The plateau or equilibrium pressure depends on temperature and is related to the changes ΔH and ΔS , enthalpy and entropy, respectively. A logarithmic plot of the various pressures at different temperatures gives access to the thermodynamic quantities of interest through the use of equation 3.1 [17], which is known as the Van't Hoff equation.

$$\ln\left(\frac{P}{P_0}\right) = \frac{\Delta H}{RT} - \frac{\Delta S}{R} \quad 3.1$$

Where ΔH and ΔS are the enthalpy and the entropy at P_0 , T is the absolute temperature and R is the gas constant. The knowledge of ΔH is also very important for the heat management required for practical engineering devices. As the entropy change corresponds mostly to the change from molecular hydrogen gas to the solid one, most of the metal hydride systems have entropies around $130 \text{ J.K}^{-1} \cdot \text{mol}^{-1}$. The enthalpy term will characterize the stability of the metal hydrogen bond. The ideal hydride should desorb at 1 bar of hydrogen and at temperatures around $80\text{-}100 \text{ }^\circ\text{C}$, which correspond from equation 3.1, to an enthalpy of approximately $40 \text{ kJ/mol } H_2$.

The potential utility of calorimetry is that it permits for a given pressure a direct estimation of the kinetic and thermodynamic reaction parameters from a single measurement making it a resourceful tool for the examination of phase transformations. Membrane-based calorimetry is relevant for the scientific community since with conventional differential scanning calorimetry its impossible to characterize the low amount of hydrogen present in thin film technology. The determination of the onset temperature and the enthalpy involved in kinetically limited phenomena requires slower heating rates than those achieved in pulse-heating mode under quasi-adiabatic conditions. This is the case of hydrogenation/ dehydrogenation reactions where the diffusion of hydrogen through the hydride is the limiting pathway; thus heating rates no higher than $10\text{-}20 \text{ }^\circ\text{C/min}$ are often required.

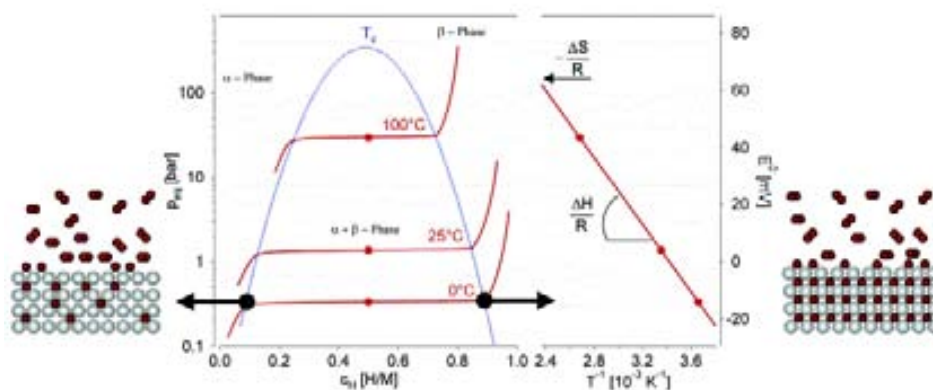


Fig. 3.2: LaNi₅ values. Pressure–concentration–temperature plot and a Van 't Hoff curve which corresponds to the logarithm of the equilibrium or plateau pressure against the reciprocal temperature. The vertical axes indicate the corresponding hydrogen pressure or the equivalent electrochemical potential.

3.4 Experimental Setup

The calorimetric experiments were performed inside a specially designed high-vacuum chamber, *Fig. 3.3a*, that is prepared for individual characterization and for future implementation for high-throughput screening permitting to carry over simultaneous calorimetric measurements on 8 different chips. More than 200 electrical connections to the on-chip bond pads were made using gold coated pogopins. *Fig. 3.3b* shows a part of the electronic pin plate that makes contact with the current pads of the membrane-based microcalorimeters. Each microreactor is contacted to four pogopins, two for the current signal and two for the voltage acquisition, obtaining a four-point probe measurement. The contact was performed by adjusting the microfabricated wafer to the probe card containing the pogopins; a four point symmetrical guide aid the downloading of the wafer. A homogeneous pressure is necessary for a simultaneously contact of all components. The pressure between pin-plate and the wafer was performed with a cross-form aluminum element placed in top of the wafer. Four screws help to regulate the pressure the more homogeneously as possible. Excess manipulation, higher pressure and improper handling may result in membrane or even wafer rupture. The experiments were typically carried out in the 10^{-2} mbar range to minimize convection heat losses and surface modification of the thin films during heating. In a typical calorimetric experiment on an individual microreactor, the Pt resistor served both as a heater and as a thermometer. The temperature in the center of the membrane was monitored by the variation in resistance with temperature as it has been explained in detail in chapter II.

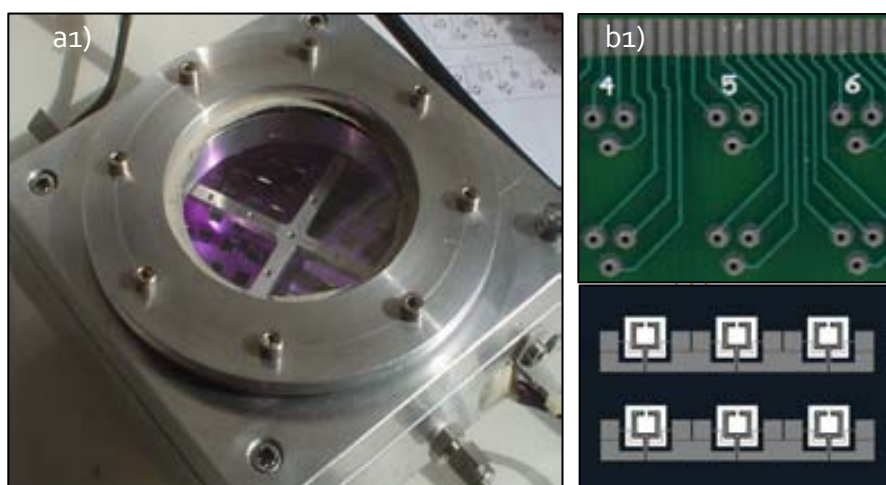


Fig.3.3: Experimental section for de/hydrogenation treatments. a) Specially designed high-vacuum chamber where the microcalorimeters are placed on top of a pogopin plate which makes connection to the external electronic hardware. b) Electronic pin-plate and current pads for the membranes. The electronic board was specially designed in parallel to the wafer containing the microdevices. Each pin is positioned on the bond pads to make voltage sensing and current feeding possible.

Since the output circuitry is performed with the aid of a Field Programmable Gate Array Card (FPGA) which can only deliver voltage values, the implementation of a voltage-to-current converter was necessary to induce a precise current value to the microcalorimeter throughout the current pads. The output current had to be charge-independent increasing the performance of electronic components. The XTR110 precision voltage-to-current converter/transmitter chip was used to provide high performance to the configuration. This integrated chip has selectable input/output ranges going from 0 to 40 mA and accepts a wide range of supply ranges from 13.4 to 40 V. The maximum current provided by the converter depends on the power supply and the load resistance value of the microreactor. By using a power supply of 24 V the current converter can supply up to 20 mA with a maximum load of 500 Ω . Considering that the microcalorimeter used in this section has initial resistance values around the 250 Ω we consider that it is sufficient and well suited enough to work with this operational values.

The circuit stage that gives current to the microcalorimeter is formed by a voltage-to-current precision converter joined with a MOSFET. This home-made circuit design offers a well suited electronic system performance for our experimental purposes (Fig. 3.4). An improvement of

the current output stage for this power compensation scheme has been detailed in section 2.3.2 of chapter II. The FPGA voltage output passes through a voltage-to-current converter. A potentiometer allows choosing the current range needed, which is proportional to the temperature range of the experiment. The current obtained is induced into the calorimeter creating a heating ramp that heats the microdevice to a certain temperature. The heating ramp is created by the controller action of a PI that acts over a ramp resistance which is proportional to the temperature following equation 2.5. The temperature present in the calorimeter can be calculated by determining the voltage and current values at each time following equation 2.17. A previous temperature calibration of the sensor resistance permits the calculation of the resistance at ambient temperature, R_0 at T_0 and the temperature coefficient of resistance, α .

Typically, the voltage measurements of the microdevices is small and the system requires an amplification stage for signal coupling in order to take the advantage of the FPGA input signal range. The maximum voltage obtained in the calorimeters is around 4 V, so it was normally amplified until 10V to use the maximum possible resolution of the FPGA's input range. The amplification stage is complete using an INA114 precision instrumentation amplifier integrated chip. The INA114 provides excellent accuracy for the microcalorimetric analysis and for other general purpose applications. It offers gain versatility from 1 to 10000 with only a 50 μ V low offset voltage. The gain of the amplifiers is set by connecting a single external resistor R_G and by following the equation 3.2. The 50 k Ω term comes from the sum of the two internal feedback resistors.

$$G = 1 + \frac{50k\Omega}{R_G} \quad 3.2$$

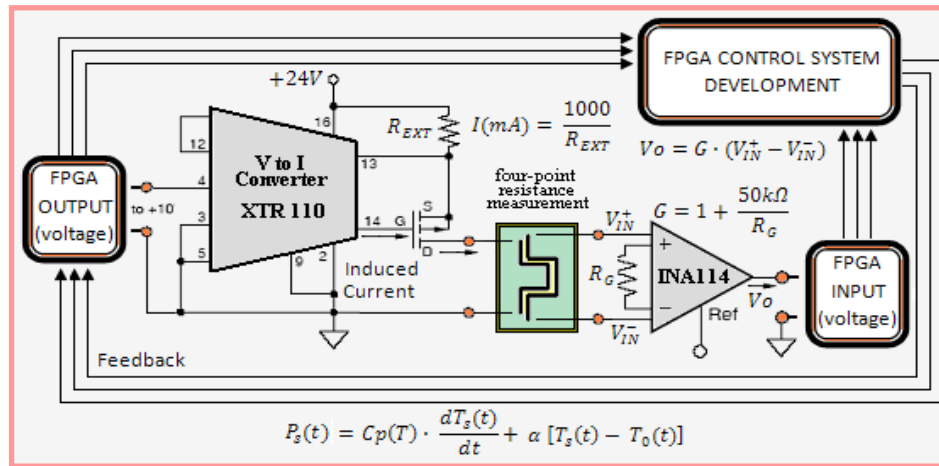


Fig. 3.4: Electrical configuration used in the power compensation calorimetry to study the behavior of the metal hydrides. This electronic circuit was designed to work with the U-shaped calorimeters. The high area of deposition increases the signal-to-noise ratio and reasonable calorimetric traces were acquired. Using a four point configuration resistance measurement and previous calibration the real temperature at which the device is operating can be determined. The voltage sensing passes to the INA114 amplifier, the amplified signal goes to the FPGA hardware functioning in the control loop. FPGA voltage output is converted by a XTR110 chip to current values. This current is supplied to the micro-device.

3.4.1 Control Development

Nowadays, devices with high screening characteristics are important in research environments for control applications, embedded processing and high-speed timing synchronization. LabVIEW® FPGA technology is ideal for applications requiring custom signals. Employing FPGA facilities with parallel operations can increase execution rates and improve determinism since executed tasks in processor-based targets are done over a common resource. Because the overall execution time in processor-based operations is dominated by the slowest operation task, the execution rate can be increased with a single hardware resource where the overall execution time for multiple operations is the sum of the execution times. FPGA is the short of Field-Programmable Gate Array, a semiconductor device containing programmable logic components and programmable interconnects. A hierarchy of programmable interconnects allows the logic blocks of an FPGA to be interconnected as needed by the system designer, so this programmable hardware allows to perform real concurrent processes. This type of logic programmable chip combines software flexibility with hardware speediness. The FPGA allows to

process eight I/O analog signals simultaneously, permits fast-time control with an internal clock at 40 MHz avoiding the errors that Windows-based programs can introduce in time.

With the FPGA module LabVIEW® programs can be built on a Windows development system. Then LabVIEW® compiles the code for FPGA synthesis on the device. Once downloaded to the NI PXI7833R target, the embedded LabVIEW® FPGA VI (Virtual Instrument) can execute in one of the following configurations:

- Autonomously (FPGA runs independently)
- Combines with a PC running LabVIEW® for Windows®
- Combined with a LabVIEW® Real-Time system

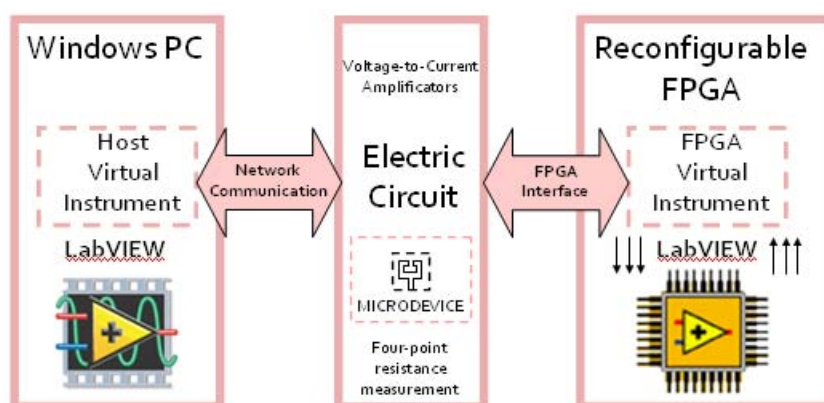


Fig. 3.5: FPGA configuration scheme with Host Computer and electronic implementation. Once the connections are made between the micro-devices and the hardware a link between software algorithms is necessary to execute an effective feedback to the calorimeters. The physical connections coming from the external electronics is attached to a PXI National Instruments® Windows®-based computer. The programming is done in LabView®. This computer-based program is called the host virtual instrument that communicates with the external environment and the internal Field Programmable Gate Array card which is the one in charge of executing the PI control loop.

It is worth noting that the mass of the analyzed samples are lower than 5 μg . This small value sets a compelling demand on the sensitivity of the calorimetric technique and more precisely on the controller and associated instrumentation. A software based digital proportional integral controller (*PI*) was developed in LABVIEW®. A detailed explanation on the controller configuration has been described in section 2.3.2 of chapter II. The control loop time, which

includes sensing, digital calculation, and control actuation is reduced to 20 μs , around three orders of magnitude faster than in GPIB-based controllers [18].

In the microcalorimetry system, the LabVIEW® Windows®/FPGA interface consists of two main programs. i) The FPGA target which is in charge of the data acquisition, I/O interaction, error estimation, reboot and mainly for the control operation loop. Once the controller calculates the correct control action, it provides the required power in form of voltage output. As the FPGA signals provides 16 bits of resolution (15 if working only with positive signals), the minimum step in temperature that can be achieved depends on the temperature range in which we are working, i.e., minimum step = [temperature range / (2^{15})]. ii) The Windows® environment consists mostly of visualization items for temperature, power, resistance, time and input parameters. This program interacts with the read/write functions directly from the FPGA program. This program has an interface palette in which the user can define values for the different constraints, mostly independent parameters regarding the behavior of each microcalorimeter: interval execution rate, R_0 resistance, temperature coefficient of resistance (TCR) and control PI variables. This software communicates with the FPGA allowing execution control of the various experiments.

The microcontroller is based upon a model that accounted for the power balance according to the equation:

$$(Cp_{calorimeter} + Cp_{sample}) \cdot \frac{dT(t)}{dt} + \frac{1}{R_T} \cdot [T(t) + T_0] + \varepsilon\sigma \cdot [T^4(t) - T_0^4] = P_{IN}(t) \quad 3.3$$

Where P_{IN} is the power introduced by the heaters, $1/R_T$ is the heat transfer coefficient in which conduction and convection losses are considered, T_0 is the constant temperature of the Si frame, T is the sample temperature, ε is the surface emissivity accounted for radiation losses and σ is the Stefan-Boltzmann constant. The heat capacity term contains the power needed to heat the sample $[(Cp_{calorimeter} + Cp_{sample}) \cdot dT(t)/dt]$ to a given temperature, whereas the second term accounts for the heat losses of the calorimetric cell to the surroundings. As described in the modeling section of chapter II, if assuming operation temperatures below 500 K we can neglect radiation losses. P_{IN} can be expressed as the power released by an electrical resistance and equation 3.3 can be reduced to the following

$$(Cp_{calorimeter} + Cp_{sample}) \cdot \frac{dT(t)}{dt} + \frac{1}{R_T} \cdot [T(t) + T_0] = R(T) \cdot I^2 \quad 3.4$$

We consider the calorimeter as a first-order system with a time constant τ . In the membrane-based calorimeter, the transient response time, τ , depends on the thermal characteristics of the membrane and on the environment pressure. The time constant τ , is defined as the time that the microcalorimeter takes to reach 63.2 % a final temperature for an input current step. τ is the main parameter to take into account in order to develop a digital controller. For the microcalorimeter designs, values for the time constant τ are around 50-150 ms working in vacuum conditions (Fig. 3.6). Working in other ambient gasses the convection losses increase and therefore τ will decrease. The stability of the control response can be increased and optimized by lowering τ values.

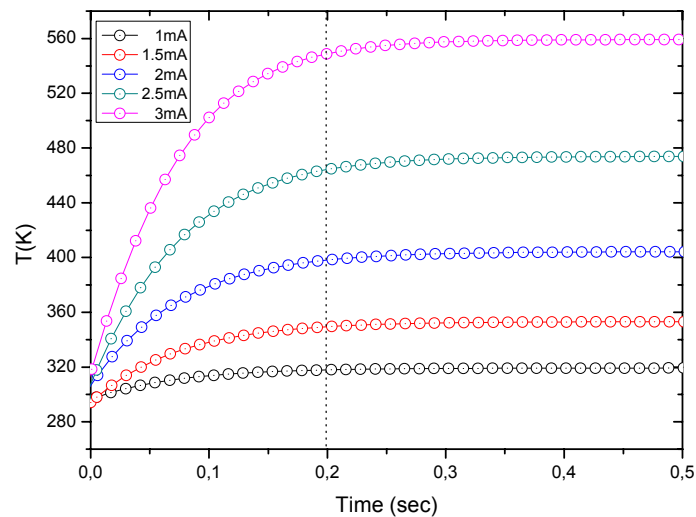


Fig. 3.6: Temperature response as a function of time for the different current input stops. The transient evolution of the temperature is observed and the time response τ can be deduced.

We chose a proportional-integral control to correct deviations during the calorimetric scans. The PI control offers important advantages over proportional or proportional-derivative controllers. The proportional controller actuates over the present errors and requires the additional contribution of the integral action (*which takes into account the previous error history*) to minimize errors in the steady state. Higher-order (*number of integrators*) controllers are typically preferred to minimize the steady-state error; in fact, to achieve zero steady-state errors during ramp set-points, the controller algorithm should include at least two integrators.

The viability of any controller can be tested by the error on temperature during the ramp and by the drift during the transformation. When a perturbation in the linear temperature ramp appears, the response of the system can follow different scenarios, such as oscillating, underdamped, critically damped, and overdamped, depending on the tuning parameters. To realize a quantitative determination of the heat involved during a transformation, it is preferable to keep the temperature error as small as possible while preventing a non-oscillatory transient response. Both conditions are difficult to attain; overdamped controllers may reduce oscillations, but the response speed to fast perturbations also decreases, and underdamped controllers may follow fast perturbations but can exhibit oscillations. A compromise between both is highly desirable to reduce the noise. The heating ramp is programmed in the FPGA by first measuring in a four point probe the resistance in t_o acting as a starting point of the ramp (R_o). Since we know that the resistance is proportional to the temperature at a given time from the equation 3.2, we can directly calculate the temperature of the calorimetric cell. To simplify the number of operations inside the FPGA, the internal set-point is calculated as the resistance value for each temperature. The calculation of the resistance is obtained from an internal digital division between the voltage and current (V/I). Two identical controllers have been implemented to calculate the control actions needed to attain the set-point with the process variable resistances. Some external parameters (K_P , K_I , R_o , R_T , C_P) are introduced to define and properly tune both control actions.

In calorimetry, one of the main variables is the power released to reach a temperature. The FPGA is used as a digital multiplier to generate a signal proportional to the power. During programming, it is necessary to take into account that the FPGA is limited to work with integer variables with a maximum resolution of 32 bits for internal computation and 16 bits for the I/O variables. To increase the resolution, internal variables are spread through scaling factors.

3.5 Sample Deposition and Results

The materials used in this work have been grown in the Laboratori de Capes Primes at the Universitat Autònoma de Barcelona using an e-beam evaporator facility or in MATGAS using a sputtering setup. To limit and locate the area of deposition in evaporated samples a Si microfabricated mask was designed, figure 3.7(c). The shadow mask is placed perpendicular to the beam close to the membrane where the deposition of the sample will be made. This ensures a small shadowing effect and therefore a good definition of the deposited area. Due to the high directionality of the electron beam compared to the sputtering process the shadow mask is more effective in the former case.

The use of thin films in hydrogenation studies offer significant advantages over more extended ball-milling techniques since stoichiometry, structural order, and grain size can be better controlled and characterized.

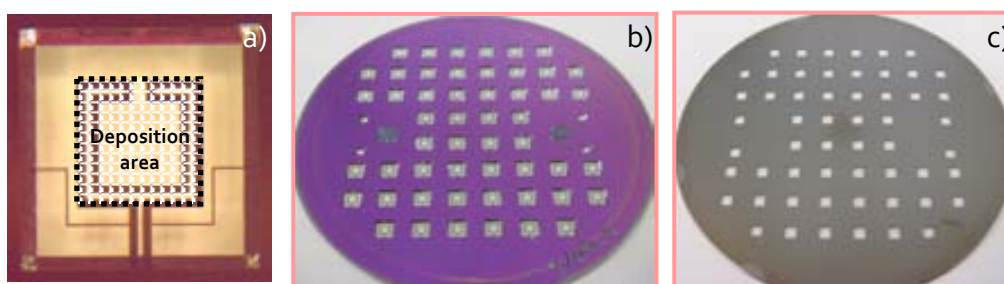


Fig. 3.7: a) Single chip micro-calorimeter distinguishing deposition area b) Entire Si wafer with the U-shaped micro-calorimeter array c) Si wafer which acts as a mask that delimits the deposition region to the active area of the heater as shown in the illustration a).

Most of the films are prepared in an e-beam evaporation set-up at a pressure of 4×10^{-6} mbar and room temperature. All analyzed samples have an overlayer of Pd, 10 nm thick, to facilitate fast hydrogen dissociation and permeation into the underlying metal as well as to avoid oxidation of the magnesium-based films during exposure to normal atmosphere. With this precaution, films can be exposed to air without adverse effects on the hydrogenation/dehydrogenation behavior. A thermalization layer of 50 nm of Ag was deposited

onto the SiNx membrane before the e-beam evaporation treatment to ensure sufficient temperature homogeneity within the sample region during the calorimetric scans (see modeling section of Chapter II). As a proof-of-concept three different compounds have been analyzed during the dehydrogenation process. i) pure 150 and 300 nm thick Mg films, ii) 350 nm thick Mg/Al alloy iii) 200 nm $Mg_xTi_{(1-x)}$.

3.5.1 Mg, Mg/Al and Mg/Ti depositions: individual and combinatorial

The combinatorial setting was made using a high-throughput synthesis methodology that combines the sequential deposition of pure elements, in this case, Mg and Al. This novel method of e-beam deposition was studied and described previously at GNaM [20], where a two shadow mask system, moving perpendicularly, was designed to prepare 4 identical libraries in a single wafer. A sequential deposition of the different metals coupled with a controlled programmable mask translation movement allowed to prepare 49 different members on each single library as well as 4 identical libraries in a single run. We can use this methodology to achieve a different composition and a direct intimate mixing of the elements in each $3 \times 3 \text{ mm}^2$ microdevice. Pure Mg and Mg/Al films were deposited onto the microcalorimeters at room temperature using an e-beam evaporation set-up at working pressures of 4×10^{-6} mbar. The evaporation temperature was optimized individually to fix the growth rate of the different metals using a quartz microbalance located inside the deposition chamber. The achieved growth rates were 0.2 and 0.25 nm/s for Mg and Al, respectively. A Palladium coating of 10 nm was deposited to ensure a fast dissociation rate and good transport properties for hydrogen as well as to avoid oxidation of magnesium from the atmosphere. It has been studied that no MgO is detected after a (de)hydrogenation treatment, confirming the utility of Pd layers as barrier for oxidation [21]. We deposited a multilayer Al-Mg system composed of 2 Aluminum layers (25 nm each) sandwiched by 3 Magnesium layers (100 nm each). For thicker magnesium layers, such as the 300 nm films studied in this work, the presence of PdH_x can be completely neglected.

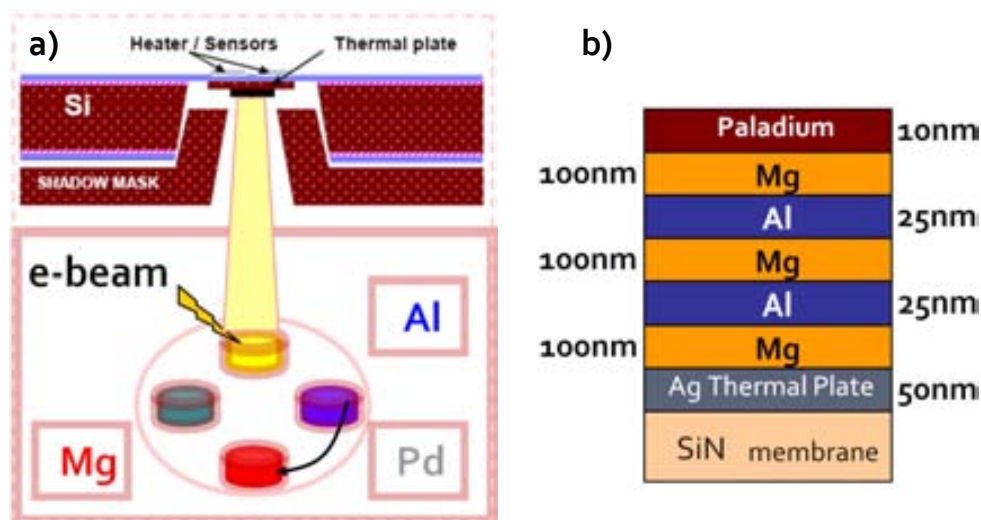


Fig.3.8: a) Illustration showing an e-beam evaporation system. The films were prepared in a Leybold UNIVEZ 450 e-beam evaporation set-up. Evaporation parameters are optimized individually to stabilize the growth rate of the different materials. The deposition rates are determined by a quartz micro-balance located inside the deposition chamber. b) A multilayer Al-Mg system composed of 2 aluminum layers sandwiched by 3 Magnesium layers that can be described as: Mg /Al/Mg/Al/Mg.

For the growth of the $Mg_yTi_{(1-y)}$ layers co-evaporation of Mg and Ti elements was achieved by simultaneous e-beam and thermal evaporation of Mg and Ti, respectively. Films were deposited on the active area of the microfabricated substrates at room temperature and the deposition pressure was kept at 10^{-6} mbar for rates of 0.4 - 0.5 and 0.1 nm/s for Mg and Ti, respectively. The growth rates were adjusted previously to achieve the desired $Mg_yTi_{(1-y)}$ compositions.

The as-deposited composition was characterized by Electron Scanning Microscopy (SEM), combined with energy dispersive x-ray analysis (EDX) in different points of the wafer to detect correct element composition. Only the reflections corresponding to the four metals were observed (Si, Mg, Ti, Pd). A JEOL JSM-6300 Electronic Microscope with a resolution of 3.5 nm with an EDX LINK ISIS-200 of a 138 eV sensitivity were used.

3.5.2 Mg and Mg/Al characterization results

Figures 3.9(a) and 3.10a show the calorimetric traces recorded at 10 °C/min from a 150 nm ($m \sim 2 \mu\text{g}$) and 300 nm ($m \sim 4 \mu\text{g}$) Mg films that were previously hydrided at 80 °C during 30 min in pure H₂ at 1 atm. The endothermic peak is characteristic of the hydrogen release from MgH₂ during the heating ramp and closely matches the results obtained with a commercial calorimeter, Perkin Elmer DSC7, with a sample mass around 1 mg, which is 500 times larger than the one used in our experiment (Fig. 3.9 b). The onset temperature of the desorption process is 130 °C, lower than values attained on nanocrystalline MgH₂ [22] which desorbs at 200 °C in dynamic vacuum. This value is comparable to previous results obtained on Mg/Pd films by Higuchi et al. [13]. Figure 3.9(a.1-a.3) shows the surface morphology observed by optical microscope of the membrane-based calorimeter active area after the different process stages: as-deposited, after hydrogenation and after dehydrogenation (*heated up to 275 °C*).

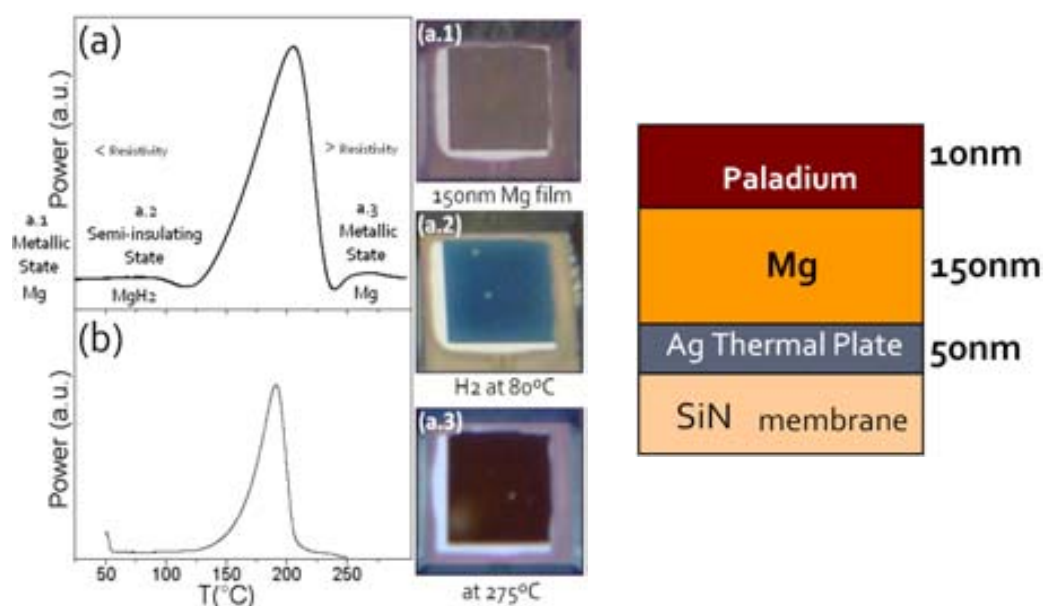


Fig. 3.9: (a) Calorimetric trace of the dehydrogenation of an MgH₂ film. The optical photographs (a1–a3) show the different sample stages throughout the process. (b) Identical sample with a much higher mass measured in a commercial DSC7 from Perkin Elmer.

A remarkable change in electrical properties occurs during the dehydrogenation. A metallic to a semi-insulating state transition becomes present upon hydrogenation directly affecting the electrical properties. Upon exposure to hydrogen, Mg metal transforms from the hexagonal closed packed structure to the tetragonal type (*MgH₂*) and thus switches from a

metallic to a semi-insulating state. It has been demonstrated that upon exposure to hydrogen the thin Mg film resistance increases sharply from values as low as 50 °C related to the metallic to semi-insulating state transition, which corresponds to a phase change from Mg to MgH₂. The resistance of the film also diminishes considerably and recovers values close to the as-deposited state, as has been previously shown [15]. The surface reflectivity of the thin Mg film also changes dramatically, as revealed by the surface color variation shown in the image of figure 3.9. During dehydrogenation the transmittance of the film recovers the low value of the metallic state. The resistivity variations occurring during the phase transformation have a pronounced effect in the heat exchange of the calorimetric cell with the surroundings, and therefore affect the calorimetric traces. When the thickness of the film is comparable to the thickness of the thermal plate and the supporting membrane, a standard procedure such as applying a baseline correction by simply subtracting the second scan to the first calorimetric trace is prone to large errors. In our case, we proceed by using an iterative function that describes the power losses in both the insulating (MgH₂) and the conducting (Mg) thermal states as show in section 3.4.2. However, according to the Wiedemann-Franz law the coupling between electrical and thermal conductivities in metals permits to infer the huge variation in the thermal conductance of the sample, which also affects the thermal link with the substrate. This fact remains an obstacle for a quantitative evaluation of the energy involved in the H₂ desorption and further work is needed to reliably account for those variations. Two possibilities can be foreseen: i) A redesign of the membrane reducing the thermal link with the substrate either by suspending the active area or by reducing the heated area. ii) A proper simulation may permit to appropriately correct for the variation in power losses before and after dehydrogenation.

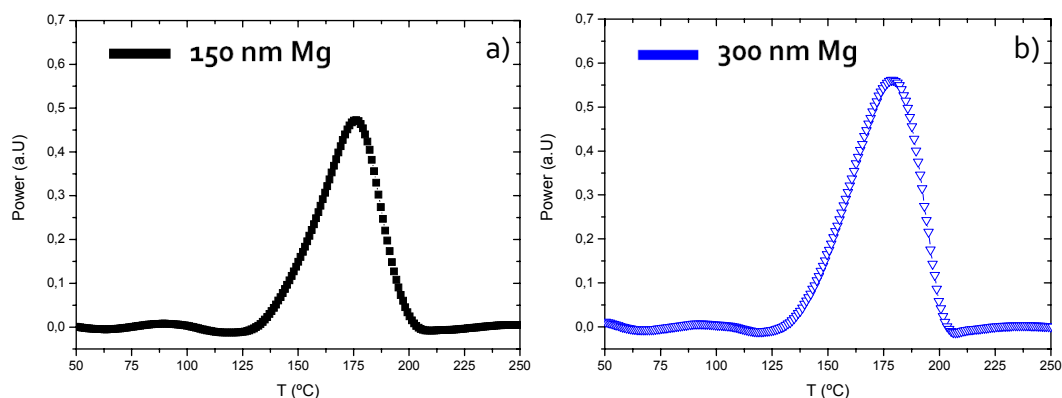


Fig. 3.10: Curves of the power evolution as a function of temperature for a) 150 nm b) 300 nm of pure Mg which has been previously hydrogenated. The calorimetric traces show an endothermic peak which is related to the dehydrogenation of the samples. The temperature for the dehydrogenation of the thin films remains practically identical

The reaction of hydrogen gas with magnesium metal is enhanced significantly by the addition of catalysts such as Al and by using nanostructured powders, which may result in compounds with lower formation enthalpy, as in the case of Mg_2NiH_4 [23]. Fig. 3.11 shows the calorimetric trace corresponding to the dehydrogenation of an Mg/Al thin film. In agreement with R. Domenech-Ferrer's research, a desorption action starting at ~ 130 °C is visualized. The dehydrogenation process was performed with a heating rate of 10 °C min^{-1} . According to several findings, the addition of Al to MgH_2 reduces the stability of the hydride leading to an improvement in the thermodynamics of the desorption process [16]. Other studies concluded that no significant difference in the desorption temperature was present compared for that in pure Mg [13]. In our case, the aluminum layer seems thus to act as an activator for the hydrogenation reaction. Higher peak area is present for Mg/Al compared with that in pure Mg, ensuring that the addition of Al in the thin films enriches the hydrogenation properties.

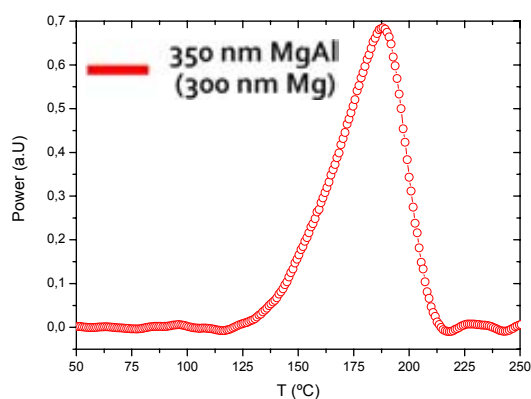


Fig. 3.11: Power vs. temperature curve for 300 nm Mg/Al sample. For the same amount of Mg a slightly larger peak area is measured for the Mg/Al sample compared with pure Mg, as shown in figure 3.9, assuming the enthalpy of desorption is similar, will indicate that the addition of Al in the thin films improves the hydrogenation of the material.

3.5.3 $\text{Mg}_x\text{Ti}_{1-x}$ characterization results

The importance of the co-evaporation is to obtain a homogeneous $\text{Mg}_{0.8}\text{Ti}_{0.2}$ composition. Average results given by EDX Spectrums of 9 different characterizations show an atomic percentage of 81.5 and 18.5 for Mg and Ti, respectively. The ~ 1.5 at. % error was due to the non-controlled parameters present in the thermal evaporator causing oscillations between the

rates of 0.4 and 0.5 nm/s. Nevertheless, considering system limitations, a good element composition was achieved by the selected deposition method.

Fig. 3.12a shows our power compensation system characterization of an $\text{Mg}_{0.80}\text{Ti}_{0.20}$ thin film dehydrogenation process. A desorption action starting at $\sim 75^\circ\text{C}$ is recorded. These results are in agreement with studies in which a lowering in the onset temperature is observed compared from those obtained in Mg/Al thin films. The sample was hydrogenated up to 75°C for 1.5 h at 1 bar of pressure in pure H_2 . The dehydrogenation process was performed with a heating rate of $10^\circ\text{C min}^{-1}$ during which the calorimetric trace was recorded. The study of the storage properties of Mg has been described electrochemically by P. Vermeulen et al. which were able to analyze the behavior by galvanostatically insert hydrogen to the sample. The experimental storage capacity of Mg was not in agreement with the theoretical findings. Only about 50 % of the thin film was fully hydrogenated due to the presence of poor permeability of MgH_2 for hydrogen, that in spite of the low-rate of current charging. Using high-rate of discharging, a poor 2.3 % dehydrogenating signal was obtained, demonstrating inappropriate properties of Mg hydride [18]. Hence, the dehydrogenation visualization enthalpies are dependent on heating rates. For slow heating rates is possible to completely dehydrogenate the sample. This phenomenon is sensitive to our calorimetric measurements.

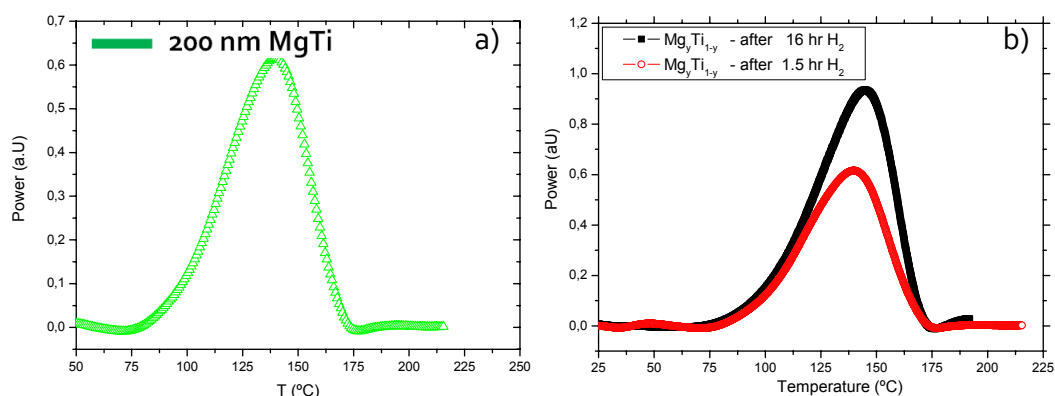


Fig.3.12: Calorimetric traces for 200nm MgTi b) Power vs. temperature curve for an $\text{Mg}_{80}\text{Ti}_{20}$ sample hydrogenated at 80°C during 1.5h (red curve) and 16h (black curve). We can assess that the kinetics of absorption/desorption is far superior for Ti containing thin films than for pure Mg or Mg/Al alloys as clearly revealed by the decrease in the onset of desorption temperature.

Figure 3.12b shows our DSC system measurement for the dehydrogenation of $\text{Mg}_{0.80}\text{Ti}_{0.20}$ thin films previously hydrogenated for 1.5 and 16 h at 1 bar in pure H_2 with a heating rate of $10\text{ }^\circ\text{C min}^{-1}$. Evidently, a higher percentage of peak area is present for the sample treated for 16 h than for the one hydrogenated for 1.5 h. The enthalpy calculation for the dehydrogenation processes yields a 30 % higher value for the sample treated for 16 h. A theoretical estimation of the enthalpy for a $\text{Mg}_{0.80}\text{Ti}_{0.20}$ thin film gives $\Delta H \sim 7.6\text{ mJ}$, assuming that the thin film was completely hydrogenated and dehydrogenated. The peak areas associated to fig. 3.12b are 0.825 mJ and 1.175 mJ for the 1.5 h and 16 h, which represent only 10.8 and 15.4 % of the total possible dehydrogenation, respectively. Two interpretations are possible: either the hydrogenation of the layer was not complete which is difficult to assume because of the short diffusion paths involved in these layers or power losses play a non-negligible role.

A comparison of the dehydrogenation behavior for the different Mg-based alloys utilized in this study (pure Mg, Mg_yAl_x and $\text{Mg}_y\text{Ti}_{(1-y)}$) is shown in Figure 3.13. It is clear that for pure Mg and Mg/Al samples the temperature for the dehydrogenation of the thin films remains practically the same, indicating no improvement for the dehydrogenation process. We believe the higher area of the MgH_2/Al system is mainly due to the shorter diffusion paths in the multilayer system which help easier hydrogenation. In $\text{Mg}_y\text{Ti}_{(1-y)}$ compositions it is clearly observed that a reduction in desorption temperatures is achieved. An onset temperature shift is registered compared to those resulted in pure Mg and Mg/Al films. A change of a $\sim 40\text{ }^\circ\text{C}$ shift to lower desorption temperatures is a very significant improvement.

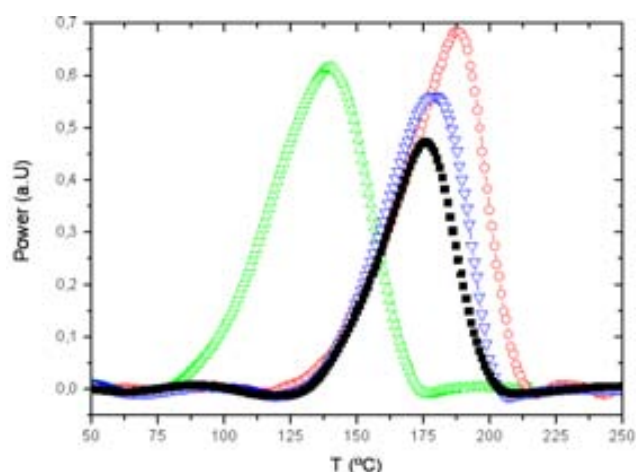


Fig.3.13: Comparison of the different calorimetric results showing the dehydrogenation peak of several compounds. Power vs. temperature curve for 150nm Mg (black), 300nm Mg (blue), Mg/Al sample (red) and $\text{Mg}_{80}\text{Ti}_{20}$ (green) samples previously hydrogenated.

3.6 Surface Micrography Analysis

3.6.1 Mg-based thin films

It is well established that due to volume differences between Mg and MgH_2 , magnesium-based alloys suffer a high level of deformation during the (de)hydrogenation processes. In the case of Mg thin films, upon hydrogenation, surface morphology changes and magnesium tends to delaminate due to volume expansion. This is especially important in thick films where high in-plane stresses can produce the detachment of the film from the substrate. Figure 3.14 shows the effect of hydride formation on a 300 nm thick Mg film surface in contrast to what was observed in the 150 nm thick layers (See figure 3.9) Upon hydrogenation the layer tends to buckle because of the volume expansion and for a sufficiently high hydrogen loading, the elastic energy contribution is too high and the buckles tend to wrinkle (Fig 3.14a). This phenomenon is accompanied by the formation of micro-cracks to further relieve the stress that act as micro-channels improving the hydrogen transport. At even higher hydrogen concentrations, the detachment of the layers can also occur. The dehydrogenation process partially releases the stress of the layers and the surface slightly flattens again (Fig 3.14c).

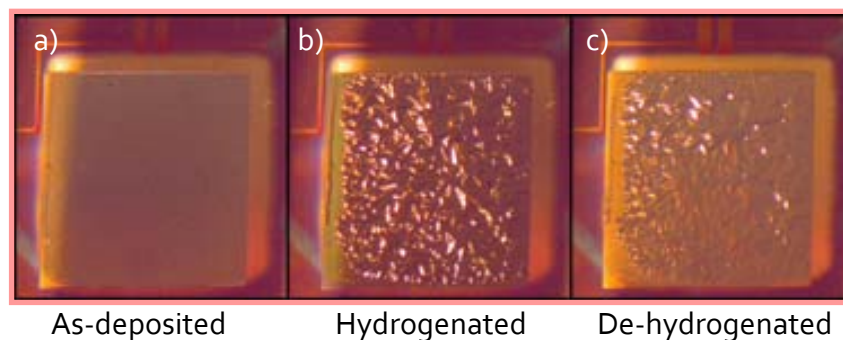


Fig. 3.14: Optical micrographs of a 300nm Mg film the effect of hydride formation is clearly observed. Upon hydrogenation the layer tends to buckle because of the volume expansion while the dehydrogenation process partially releases the stress of the layers (a) as-deposited, (b) after hydrogenation at 80 °C and (c) after dehydrogenation.

3.6.2 Mg/Al library compositions

It has already been seen by L.L.Pranevicius et al. [26] that in MgAl bilayer films (2-4 μm) bubbles nucleate and grow after a complete hydrogenation. While the hydrogen atoms tend to go out of the film it creates an expansion/contraction effect which produces micro fractures of the film and possible detachment. In our MgAl thin films the creation of bubbles in the films during the de/hydrogenation processes can be noticed in the micrograph (Fig. 3.15a). The reduced cycling in the films was not enough to generate a film detachment from the microcalorimeter sample area. A laser signal was acquired to demonstrate the phase transition caused by the removal of hydrogen from the MgAl hydride, the transition state from semi-insulating to metallic (Fig. 3.15b). The sample was hydrogenated up to 100 $^{\circ}\text{C}$ for 1.5 h at 1 bar of pressure in pure H_2 . The dehydrogenation process was performed with a heating rate of $15\text{ }^{\circ}\text{C min}^{-1}$.

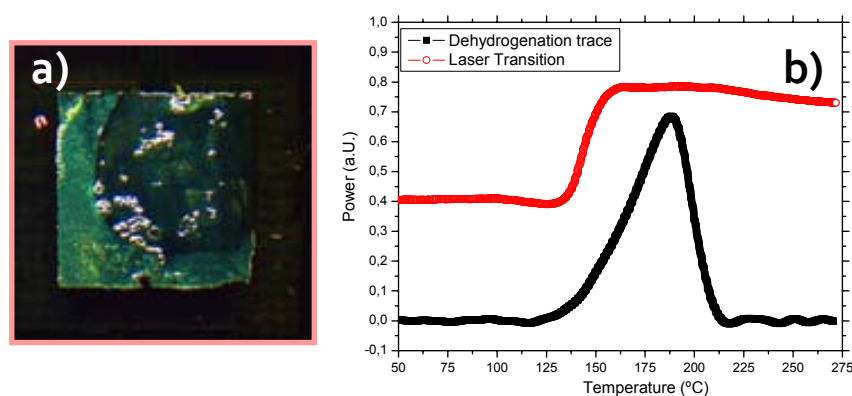


Fig.3.15: a) Micrograph of an MgAl thin film after de/hydrogenation process b) Calorimetric trace and laser signal transition of the dehydrogenation of MgAl.

3.6.3 MgTi coevaporated samples

It is likely that due to the large volume expansion of the $\text{Mg}_{0.80}\text{Ti}_{0.20}$ layer upon hydrogenation mechanical stresses are induced in the thin films. These stresses cause the thin film to slowly delaminate, effectively decreasing the storage capacity [16]. To visualize the effects of delamination and the influence of concentration we prepared several samples with different $\text{Mg}_y\text{Ti}_{(1-y)}$ compositions for examination. Using moving mask shutters in the e-beam set-up various compositional strips were grown on a single Si wafer. All the samples analyzed have a deposition of a Pd film over the samples to ensure fast hydrogen dissociation and diffusion rates as well as to avoid oxidation of magnesium from the atmosphere.

The four compositions corresponding to $Mg_yTi_{(1-y)}$ from $y = 1$ to 0.7 were then tested with the hydrogen loading in a specially design high vacuum chamber at 80 °C at 1 bar of pressure in pure H_2 for several hours. As already mentioned, the incorporation of Ti enhances the hydrogenation process of magnesium films at the expense of inducing their partial detachment from surface after adsorption. This phenomenon is sensitive to our calorimetric measurements since it can detach the sample from the membrane completely and is impossible to obtain a measurement with the dehydrogenation description of the sample. As we can see in the figure 3.16, $Mg_{70}Ti_{30}$ samples suffer a complete delamination and detachment from the surface which difficult the measurement and is consequently, not viable to work with membrane-based calorimetric techniques. A laser signal was acquired to demonstrate the phase transition caused by the change from semi-insulating to metallic state of the magnesium.

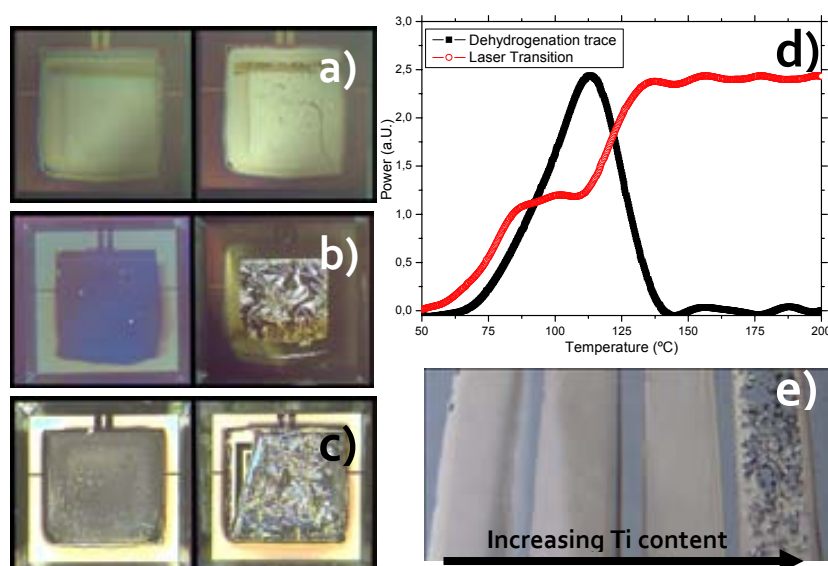


Fig.3.16. Optical micrographs of a) $Mg_{90}Ti_{10}$; b) $Mg_{80}Ti_{20}$; c) $Mg_{70}Ti_{30}$. The high level of deformation during de/hydrogenation processes on magnesium-based alloys is especially important in thick films where high in-plane stresses can produce the detachment of the film from the substrate. The increase in Ti content will produce higher hydrogen uptake and, in consequence, strong stresses will be present and will detached the sample from the surface. ;d) Power vs. temperature calorimetric trace of $Mg_{80}Ti_{20}$ alloy. The red line corresponds to reflectivity measurements. e) Several strip depositions of different MgTi stoichiometries to observe the relation between Ti content and detachment effects.

Chapter IV

Glass Forming Liquids

4.1 General Introduction

Glass forming liquids is the generic name of materials that undergo a glass transition temperature in their heating/cooling history. Glass is an amorphous (non-crystalline) solid that, unlike a crystal, lacks periodicity in its atomic structure. Glassy solids and related supercooled liquids have been the objects of studies of complex phenomena such as structure relaxation, glass transition, and crystallization [1]. The glass transition concept is very useful because it is a way to understand the molecular motion occurring over a wide variety of systems. By studying molecular motion one can describe different properties such as adhesion/cohesion factors in polymers [2]; ice crystal growth mechanism in frozen sugar solutions [3] and other assets. Several technologies have put much interest in the physical properties of glass forming systems. The glass transition has had an important impact in polymer science since thin polymer films are incorporated into device applications [4]. Understanding this phenomenon would be helpful in the future design of surface modification methods and biocompatibility applications. In the pharmaceutical sector, for certain drug molecules the glass transition is used to know how to modify the physical properties of such compounds. Pharmaceutics use physicochemical modifications in existing drug molecules and modified drug delivery technologies to reduce costs [5]. By knowing the T_g one can keep a material in the amorphous phase or play with viscous/rubbery parameters. The food industry has recognized the practical significance of the glass transition in food processing which can help establish product properties, quality, safety and stability [6].

The temperature dependence of a liquid structure plays an important role in organizing its thermodynamic and transport properties. If the existence of the liquid can be secured against unwanted crystallization, the temperature can be decreased rapidly from a temperature above its melting point T_m up to a point where it meets the dynamic glass transition; T_g^1 . Below the glass transition the system leaves equilibrium (we may consider the supercooled liquid to be a quasi-equilibrium structure) stage and forms a glass. When approaching the glass-transition

¹ T_g is the dynamic glass transition, where the relaxation time exceeds conventional experimental time of 10^2 - 10^3 s.

temperature, the dynamics of the liquid slow down drastically, the relaxation time increases sharply and the viscosity raises to values around 10^{13} poise to become progressively more heterogeneous. The glass is a rigid material in which the time-scale for relaxation required to achieve thermal equilibrium is extremely long compared to the observational or 'experimental' time-scale. Therefore, the glass transition observed in the laboratory is a purely kinetic effect and much debate exists in the scientific community whether or not a true phase transition is hidden beneath it.

The glass transition can be identified using scanning or AC calorimetric techniques. The main signature is the fast increase in specific heat C_p in a relatively narrow temperature range when a glass is reheated into the supercooled liquid state, as shown in figure 4.1. The temperature associated to the jump in C_p is known as the calorimetric glass transition temperature, T_g . The jump in heat capacity is also strongly related to the characteristics of the glass and depends on the 'fragility' of the liquid (in Angell sense) as will be discussed later on. Being a kinetic effect, the variation with temperature of the relevant thermodynamic properties such as enthalpy, entropy or volume across the glass transition, depends on the previous thermal history, i.e. cooling rate of the liquid, isothermal aging or heating rate [7,8].

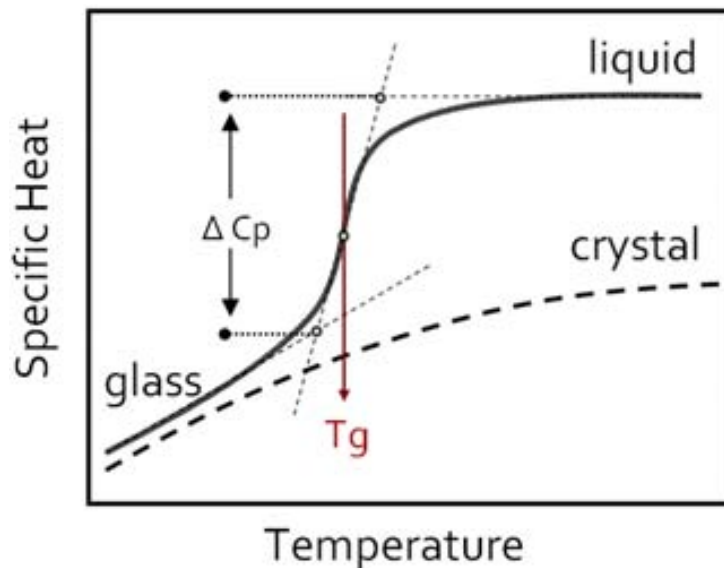


Fig. 4.1: Specific heat vs temperature at the dynamic glass transition. The specific heat drops in the liquid-to-glass transition to approximately the same value it has in the crystal phase. In general we can say that a glass is stuck in a single potential energy minimum for a long period of time, so that it loses all the configurational degrees of freedom.

Glass-forming liquids can be classified by the rate at which the viscosity changes with temperature on cooling through T_g . This is calculated by a term named fragility, expressed in equation 4.1, which measures the activation energy at T_g on a reduced temperature scale T_g/T . Close to the melting point the viscosity of the liquid is very small, whereas nucleation time is very large, thus it exists an abrupt increase in the viscosity of a liquid approaching glass transition temperature which has been an useful characteristic for the treatment of glass. If the viscosity rises enough as it is cooled further, it may never crystallize. The molecules then have a disordered arrangement, but sufficient cohesion to maintain some rigidity. This state is often called an amorphous solid or glass. Since important structure changes are present in the entire temperature history of glass forming liquids it is very important to understand the mechanical features of supercooled liquids which are given mainly by relaxation time and viscosity, η .

$$m = \left(\frac{d(\log \eta)}{d\left(\frac{T_g}{T}\right)} \right) \quad 4.1$$

4.1.1 Strong and fragile liquids

The fragility index of glass forming liquids was developed mostly by Angell who divided them in two categories: strong or fragile. The main features of the viscosity behavior are shown in Figure 4.2, where it is evident that “strong” liquids display an Arrhenius-type of temperature dependence. For the fragile liquid behavior the viscosity is low even in the undercooled regime, but increases sharply upon approaching the glass transition. These strong/fragile liquid patterns have become the basis for a classification of liquids, to indicate the sensitivity of the liquid structure to temperature changes. The crystallization of a system is given by two known processes: nucleation and growth. While nucleation basically depends on surface tension and free energy, the growth depends largely by the viscosity of the liquid in which the nucleus must develop. Viscosity has a tendency to prevent crystallisation.

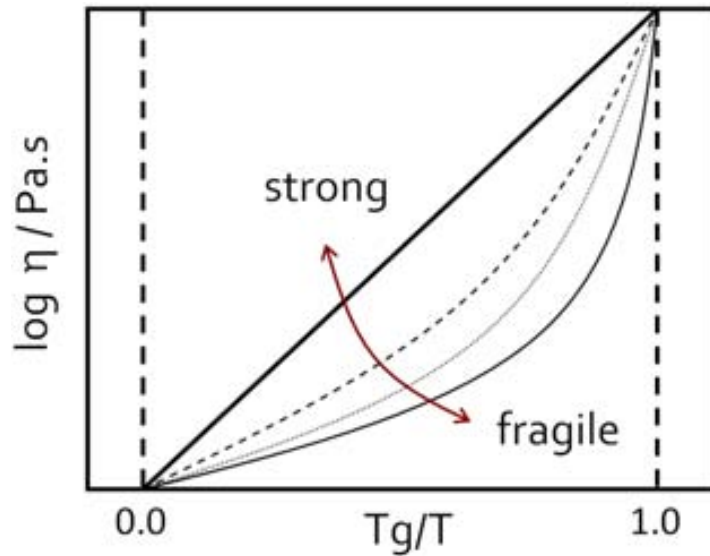


Fig. 4.2: A schematic of the liquid viscosity behavior vs. T_g / T for strong and fragile glasses. This representation is normally named Angell's plot. A purely Arrhenius behavior shows up as a straight line and it is the typical behavior of strong glass-formers. On the other hand, a behavior following the Vogel-Tamman-Fulcher (VTF) law will correspond to fragile glass-formers.

Until now the definition of a supercooled liquid is clear: a liquid that manages to get below T_m without suffering crystallization. The supercooled liquid and glassy states are considered metastable and unstable, respectively. Supercooled liquids may be stable for very long times depending on the cooling rate that has suffered, the purity of the liquid, the viscosity at T_m and some many other important factors. Strong liquids show an Arrhenius ($\eta \propto \exp(E / k_B T)$) dependence and in general have a three dimensional network structure of covalent bonds. Fragile liquids have a non-Arrhenius relaxation following the Vogel – Tamman – Fulcher (VTF) law and typically consist of molecules interacting through nondirectional, noncovalent interactions. The temperature dependence of relaxation times for supercooled liquids is described by:

$$\tau = \tau_0 \exp\left(\frac{B}{T - T_\infty}\right) \quad 4.2$$

If following Arrhenius behavior it is known that, $T^\infty = 0$, $B = E / K_B$ where E is the activation energy and K_B is the Boltzmann constant. When $T^\infty > 0$ a non-Arrhenius dependency arises and the relaxation time is predicted to become infinite at T^∞ . Normally supercooled liquids show more than one relaxation process at temperatures near T_g . Strong liquids approach T_g with a slowly varying viscosity while for fragile liquids the viscosity increases rapidly as the glassy state is reached. Fragile liquids have glassy state structures which are at the border of a collapse with little provocation from thermal excitation at their T_g 's and they reorganize to structures that fluctuate over a wide variety of particle orientations and coordination states. Strong liquids, in contrast, have a built-in resistance to structural change, and they show little reorganization despite wide variations of temperature, although, strong liquids can be converted to more fragile behavior by changing their densities. Strong liquids typically show very small jumps in ΔC_p at T_g , whereas fragile liquids show large jumps. This is considered to be the key experimental finding to understand thermodynamic/kinetic correlations over a wide range of substances [10]. For larger observed heat capacity changes, ΔC_p , at T_g , the higher the fragility index from the Vogel-Fulcher law.

Large quantities of different compounds have been studied. Figure 4.3 illustrates through an Angell plot the dynamic fragility performance for a series of small molecule materials. The thermodynamic response as the C_p liquid/ C_p crystal vs Temperature ratio is shown in the insert figure. By studying the fragility index for such small molecule glass-forming liquid compounds the tendency appears to be unambiguous, the strongly non-Arrhenius temperature dependence seen in the Angell plot is accompanied by a large value of C_p^l/C_p^c at the glass transition. As seen in the table (table 4.1) values for the C_p jump for hydrogen bonding liquids which are higher suggest those hydrogen bonds to have a special contribution to ΔC_p . According to Angell [11] the most fragile liquids that have been identified are polymers. The viscosity of a polymer liquid is largely controlled by its molecular weight and a modification is necessary for considering these compounds for fragility studies. Huang et al. [12] say that the behavior observed for inorganic liquids (positive correlation) not seem to follow for polymers (negative correlation).

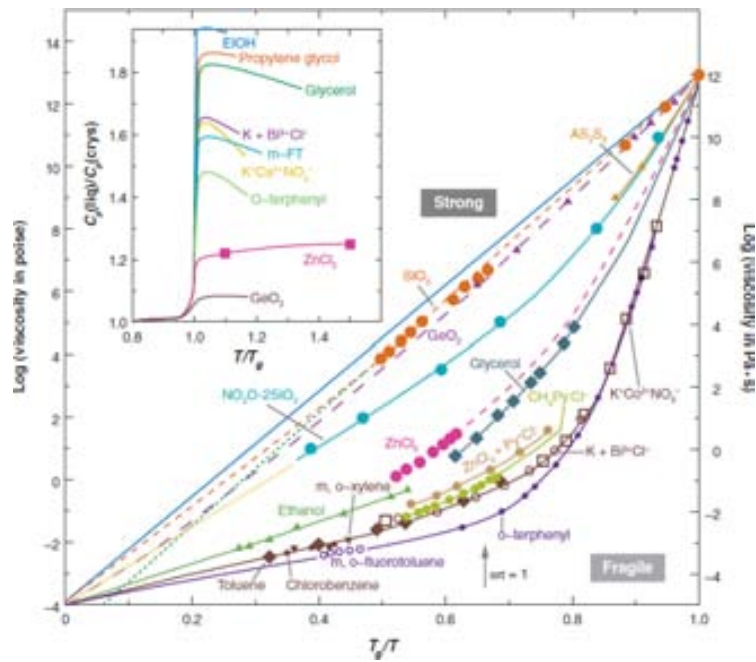


Fig. 4.3: Angell plot of viscosity for "strong" and "fragile" glass-forming liquids. The C_p jump is generally large for fragile liquids and small for strong liquids as shown in the inset figure.

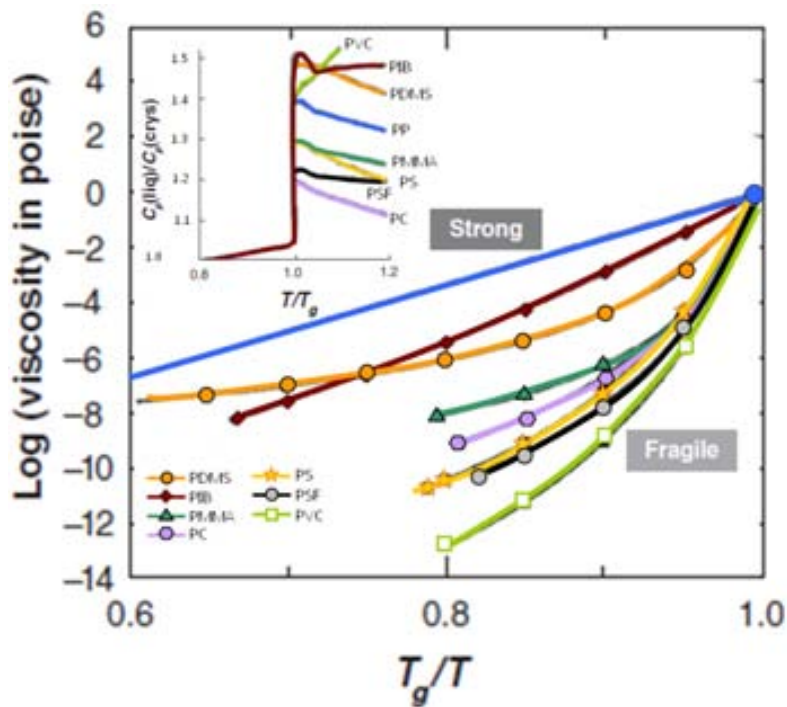


Fig. 4.4: Angell plot for segmental relaxation shift factors for different types of polymers. Here the C_p jump is larger for strong liquids and small for the fragile ones.

Compound	m	Tg (K)	Cp(l)/Cp(g,c)
Polymers			
<i>Polyetherimide</i>	214	478.5	1.100
<i>Polypropylene</i>	137	260	1.268
<i>Polycarbonate</i>	132	423.5	1.113
<i>Polystyrene</i>	116	373	1.188
<i>Polythylene (amorphous)</i>	46	237	1.538
<i>Poly (oxyethylene)</i>	23	232	1.928
Organic small molecules			
Triphenylchloromethane	93	243	1.402
Toluene	105	117.5	1.4699
Ethylbenzene	58	115	1.4683
Tri-2-naphthylbenzene	66	337	1.249
m-fluorotulene	45	117	1.935
Inorganic liquids			
BeF ₂	24	590	1.000
ZnCl ₂	30	370.5	1.279
SiO ₂	20	1446	1.005
GeO ₂	24	818	1.073
Se	87	307	1.498
Hydrogen bonding liquids			
Salol	63	218	1.714
Sorbitol	93	274	1.886
Ethanol	55	97	1.718
Propylene Glycol	52	167	1.848
Glycerol	53	190	1.847

Table 4.1: Fragility index m and the heat capacity change at the glass transition temperature for different glass forming liquids

4.1.2 Thermodynamics and kinetics

We can measure the glass transition temperature T_g of a glass in many different ways. Dilatometric techniques use the change in the thermal expansion coefficient in the transformation range of T_g . Thermal expansion of the glass and crystal are similarly dominated by atomic vibrations, but the thermal coefficient of the glass is lower than that for the liquid and supercooled liquid. In addition, it is essential to underline that the experimentally-observed glass transition is not a first-order transition and not even any kind of phase transition. It is a kinetic event which depends upon the crossing of an experimental time scale and the time needed for molecular rearrangements.

Stability is an important concept in defining the glass and the liquid state in glass forming liquids. In physics, the maximum stability is reached when the system achieves the lowest state of energy. Putting it in another way, the more energy it takes to modify a system the more stable it is. Below the melting point the only thermodynamic stable phase is the crystal. However, the supercooled liquid, which is metastable, is often considered as a true quasi-equilibrium structure whereas the glass is considered to be off-equilibrium and therefore an unstable phase [13]. When the system falls out of equilibrium, thermodynamic weaknesses reduce nearly discontinuously. This occurs across a constricted transformation regime where the characteristic molecular relaxation time becomes of the order of 100 seconds [14], and the rate of enthalpy change with respect to temperature decreases abruptly to a value comparable to that of a crystalline solid.

One of the most interesting thermodynamic parameters is the heat capacity. The heat capacity supervises the change of entropy (*enthalpy*) of a supercooled fluid. This change can be well approximated by subtracting the crystal heat capacity from the measured liquid C_p . This can be represented as in Figure 4.6. As we can observe in the laboratory experiments, the glass transition is to be a kinetic phenomenon and strongly depends on the experimental time-scales. The changes in the mechanical configuration are accompanied by changes in the thermal properties. Thermodynamics is necessary to relate the glass transition temperature, T_g , to the energies involved in supercooled liquids.

Once the specific heat has been obtained we can integrate the data in temperature to determine the part of the enthalpy that comes from the diversity of liquid configurations. In parallel with the dynamical changes on supercooling observed in the viscosity and relaxation times, there are apparent thermodynamic changes. In the liquid region, relaxation processes are

almost instantaneous compared to the observation or experimental time. In the glass transition region or supercooled liquid regime, relaxation times are comparable to the observation time. In the contrary, at the glass region the relaxation processes are so slow that they cannot be observed during experimental time. That is:

$$\tau_R^{liquid} \ll t_{observation} \ll \tau_R^{glass} \quad 4.3$$

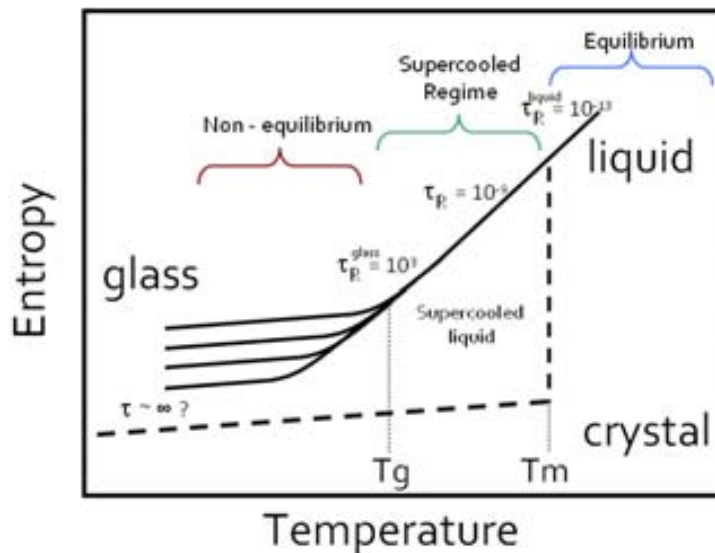


Fig. 4.5: Schematic representation of the entropy as a function of temperature in a liquid, the supercooled phase, the glass and the crystal. Where: T_m is the melting point, when a first-order phase transition between liquid and crystal occurs; T_g is the dynamic glass transition, when the relaxation time exceeds the conventional experimental time of 10^3 seconds; the longer the available experimental time, the lower the temperature where the system falls out of equilibrium forming a glass (different glass lines). We also denote the approximate relaxation times at the different regimes involved in a glass transition analysis.

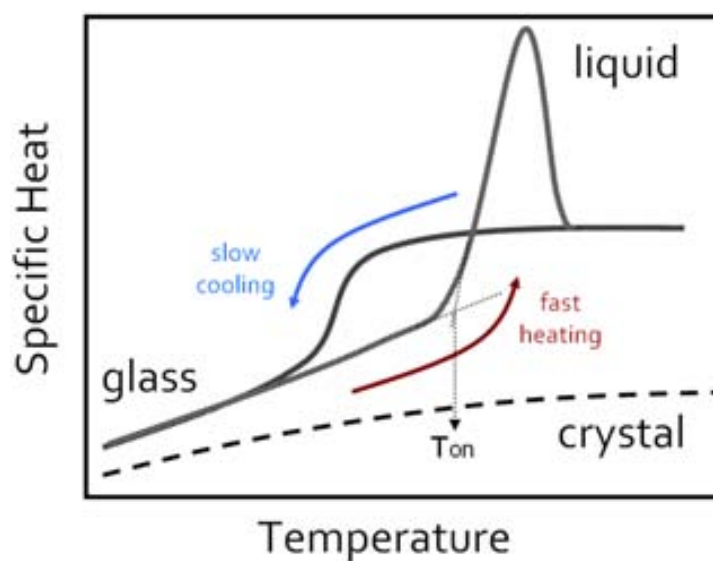


Fig. 4.6: General illustration of a calorimetric glass transition. The Specific heat drops at the dynamic glass transition to approximately the same value it has in the crystal phase. The excess enthalpy present in the glass appears as an overshoot in the specific heat.

Figure 4.6 illustrates the importance of the thermal history on the measurements of the glass transition. At the very fast heating rates ($\beta_h \sim 5 \times 10^4 \text{ K/s}$) that follow slower cooling rates ($\beta_c \sim 0.1\text{--}1000 \text{ K/s}$), such as the ones used throughout this work, the response of the system sets out to higher temperatures and an overshoot appears. The jump in the heat capacity is due to the calorimetric glass transition and the overshoot is related to the excess enthalpy that is suddenly released at T_g . Changes in the overshoot of the heat capacity associated with the glass transition are an indicator of the stability of the glasses. Bigger overshoots present in the sample analysis may specify the highly stable character of a glass. T_g is typically evaluated at the mid-point or at the onset of the C_p jump (*fig. 4.1 and fig. 4.7*). We will use throughout this work the onset temperature as the experimental measure of T_g at a given heating rate. The following figure describes these different definitions.

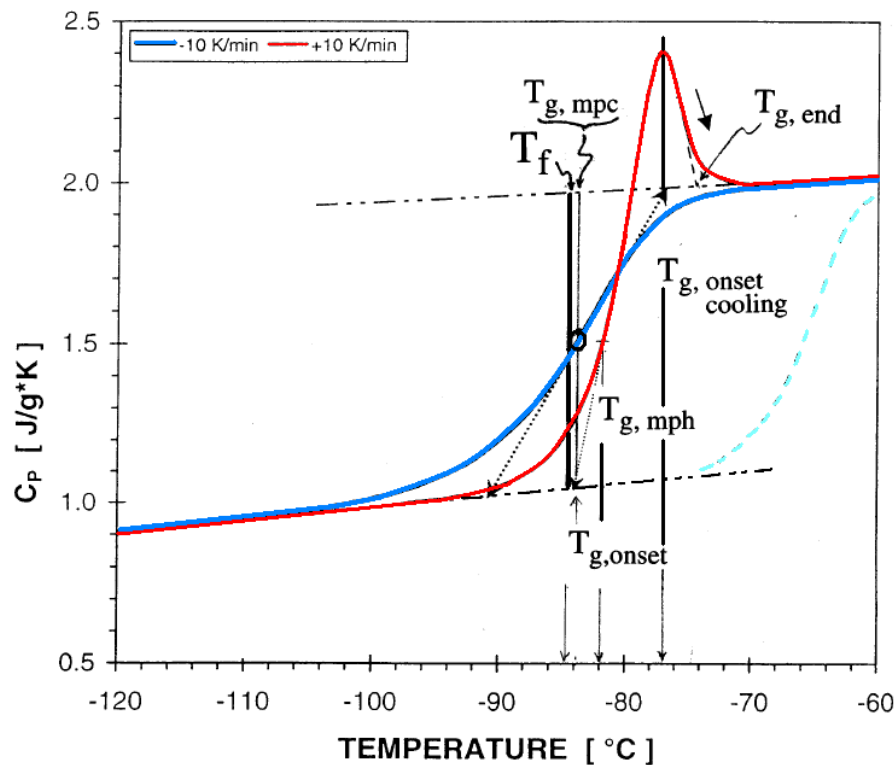


Fig. 4.7: Calorimetric glass transition for glycerol according to DSC in heating/cooling. The heavy vertical line illustrates the fictive temperature T_f . $T_{g,mpc}$ and $T_{g,mph}$ is the midpoint on cooling and heating definitions respectively. The onset cooling definition $T_{g,onset\ cooling}$ and the onset glass transition definition while heating, $T_{g,onset}$, which will be the one used in this work. Figure taken from [26]

The fictive temperature is defined as the temperature at which the structure of the glass is considered to be that of the equilibrium liquid. It can be obtained by extrapolation of the liquid and supercooled liquid lines in the enthalpy versus temperature plot (*figure 4.8*). The intersection of both lines determines the fictive temperature. Of course, T_f is highly dependent on the thermal history of the glass and therefore permits to quantify the difference in thermal history between two glasses. T_f is therefore a useful parameter for discussion of the effect of changes of cooling rate or any other thermal process on glass structure and properties.

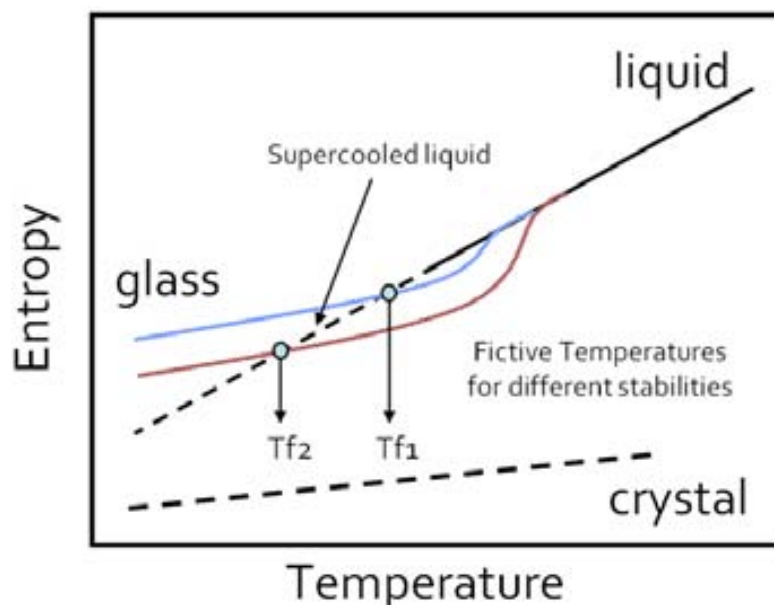


Fig. 4.8: Schematic representation of the entropy as a function of temperature. Enthalpy curves for different glasses obtained from integrating the specific heat curves. The temperature at which the extrapolated liquid line (black, dashed) intersects the enthalpy of the different glasses (color curves) defines the fictive temperature T_f as indicated by the vertical lines.

4.1.3 The Kauzmann entropy crisis

Quoting Kauzmann, *“The vitreous or glassy state of liquids evidently only exists because experiments performed by mortal beings must of necessity be of limited duration. It is interesting to speculate on the behavior which liquids would show at very low temperatures if enough time could be allowed in the thermodynamic measurement to avoid vitrification”* [19]

What Kauzmann stated is that if the entropy of a supercooled liquid is extrapolated to lower temperatures, it will equal the entropy of the crystal at a given temperature not far below T_g . This temperature is named, T_K , Kauzmann temperature. While visualizing that an amorphous state would have the same entropy as a well-ordered crystal is already alarming, if the entropy of a supercooled liquid were to become smaller than that of the stable crystal at T_K , its entropy will eventually become negative upon further cooling and would result in a violation of the third law of thermodynamics² giving rise to the entropy crisis. In this “far-away” scenario (*for not telling impossible*) the entropy of a supercooled liquid will be lower than that of the stable crystal.

² As a system approaches absolute zero, all processes cease and the entropy of the system approaches a minimum value.

In a general manner it is accepted that the entropy of a supercooled liquid cannot keep on lowering as the temperature is diminishing. Several resolutions have been proposed to avoid the entropy crisis [20]. One way is for the liquid to form an ideal glass³ at T_k by undergoing a second-order phase transition. Another way is to consider a first-order phase transition between T_g and T_k . Some, non-conclusive, support of the existence of such liquid-to-liquid transition can be found in the literature with experimental evidence and theoretical modeling [21,22]. Another alternative solution is a continuous behavior of the liquid with no phase transitions whatsoever. In figure 4.9 we illustrate the three possibilities.

The Kauzmann dispute is more significant for fragile than for strong glass-forming liquids. In fragile liquids the specific heat difference between the liquid and crystal is rather large and T_k often falls not far below the temperature range where experiments can still detect relaxation phenomena. For strong liquids, the specific heats between liquid and crystal are almost the same so that T_k is nearly identical from $T = 0$ K.

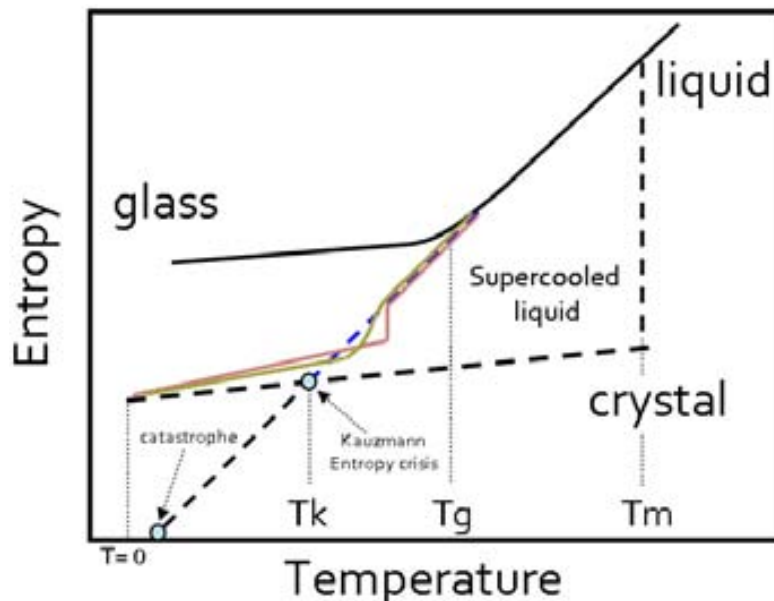


Fig. 4.9: Schematic representation of the Kauzmann entropy crisis and various possible solutions. The solid black lines designate regions that are currently accessible with experiments. Where: T_k is the Kauzmann temperature, T_g is the glass transition temperature, and T_m is the melting temperature. The blue-dashed curve illustrates the entropy of the supercooled liquid extrapolated to low temperature with a transition to an ideal glass at T_k . The red curve shows a possible first-order phase transition, and the green curve illustrates a possible resolution without any phase transition.

³ An ideal glass can be considered to have the same entropy as the crystal.

4.1.4 Aging and cooling rate effect on the glass

Aging is the process by which the physical properties of a material are relaxed towards more stable configurations as a result of thermal treatments below the glass transition temperature. This process is of extraordinary relevance in the field of polymers and other glasses which may undergo modifications after prolonged time exposures to a given temperature modifying the performance of the material. Manufacturing processes may be affected since physical aging can play an important role in the design and applications of amorphous materials. This will help prevent material failure in some commonly manufactured materials (*i.e. epoxies, engineering thermoplastics, optical materials*) [28,29]. The effects of physical aging are erased by heating the glass above its glass transition temperature, indicating a connection between aging and the glass transition. As glasses are non-equilibrium solids annealing them inevitably tend to a continuous change in their thermodynamic properties towards the equilibrium.

Many unsolved issues remain in dynamic phenomenology of supercooled liquids. While it is well established that the slow structural relaxation dynamics of many supercooled liquids present a non-Arrhenius behavior it is not known whether this conduct observed for fragile liquids results from a heterogeneous distribution or spatially homogeneous dynamics. In this manner, aging experiments are of relevant interest for finding a connection between heterogeneous/homogeneous dynamics and physical aging. In an aging process the structural enthalpy at a given temperature decreases with time which means that the structural state of a glass depends not only on thermal history but also on aging. In the last decades there has been an increased of interest regarding theoretical [23-25] and experimental [26,27] procedures of physical aging to well-understand the dynamic nature of glasses far below T_g . Experimentally, the progress of a glass towards the supercooled liquid state can be characterized through the evolution of the limiting fictive temperature T_f . As a glass ages for a very long period of time, T_f decreases until it is equal to the aging temperature.

As we have already briefly described the experimentally-observed glass transition being a kinetic effect depends on the thermal history. Therefore, during a cooling scan the temperature at which the specific heat drops (T_g) changes while varying the cooling rate at which the glassy state is formed. The slower the cooling rate involved the more time the sample will have to achieve equilibrium until lower temperatures. The dependence of the glass transition temperature T_g upon cooling may change by a few degrees (*3-5 K with an order of magnitude change in cooling rate*). Fast quenched glasses are not in thermal equilibrium due to the fact that

they are usually obtained by rapid cooling the system and they do not have the necessary time to reach thermal equilibrium [11]. Faster cooling rates produce higher fictive temperatures (*more unstable glasses*). Since the fictive temperature depends on the cooling rate, if you cycle a glass by cooling it at one rate and heating at another, it can present hysteresis effects (*Fig.4.6*) and an overshoot in heating will be present. When the heating and cooling rate are similar this excess enthalpy is minimum.

In other terms we can say that when the material remains in equilibrium, molecules maintain their immediate set of neighbors for hundreds of collisional or vibrational periods, this is called the α -relaxation. However, when α -relaxation becomes too slow and only a fraction of the interconversions have time to occur, the material is said to be a glass that ages. A glass may “densify” upon aging, as it moves to a more nearly equilibrium region (*lower enthalpy*). In the optical field, such treatment (*aging*) permits strains to be removed, making the glass more uniform, this is known as stabilization. Also, as mentioned before, the cooling rate has a direct influence in the glass transition. Some studies in glycerol have found that the cooling rate emerges as a crucial parameter at temperatures near T_g and appears to affect the structure and dynamics on the molecular level [32].

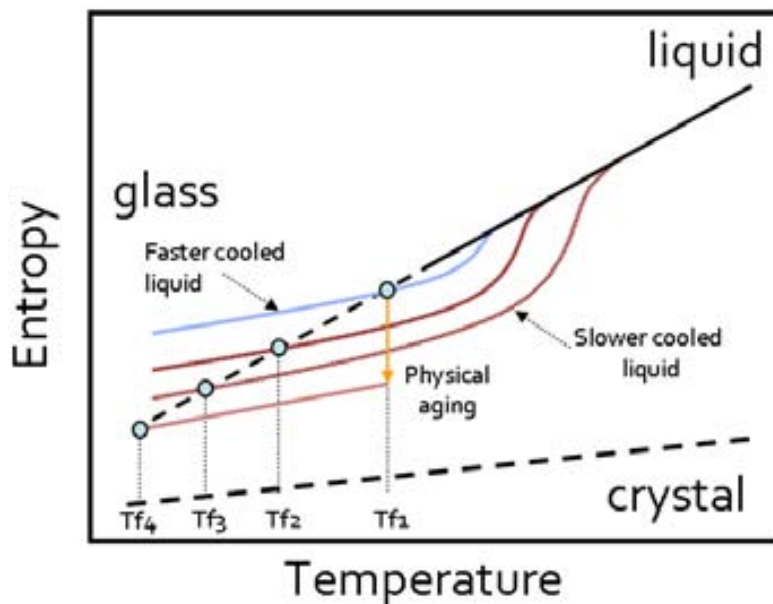


Fig. 4.10: Schematic representation of the entropy as a function of temperature. Entropy curves for different glasses with different stabilities are shown. The temperature at which the extrapolated liquid line (black, dashed) intersects the glass (color curves) defines the fictive temperature T_f as indicated by the vertical lines. A physical aging process will increase stability on very long time periods. This increase in stability will be reflected in the lowering of the fictive temperatures.

Confinement has a pronounced influence on the glass transition. Supported thin films of a variety of glasses show a depression of T_g when the interaction with the substrate is weak and an increase of T_g in the case of strong interaction [17]. Although less studied confinement also has a significant influence on aging as has been previously addressed by several authors [17,30,59,60]. Supported polystyrene films 18 nm thick undergo aging, however in chromophore-labeled poly(isobutylmethacrylate) as thin as 10 nm, no thickness dependent aging rate was observed. To our knowledge no aging behavior of ultrathin films below 10 nm has been yet addressed mainly because the experimental difficulties in accessing to thermodynamic parameters in such thin layers.

The potential energy surface of a supercooled liquid is expected to contain a large number of local minima. Each minimum is surrounded by a basin which is the set of all configurations that, using a local minimization of the potential energy, will end up in a particular local minimum. The configuration space can be uniquely partitioned into a sum of basins, among which one expects to find the absolute ordered minimum corresponding to the crystalline state, and the lower disorder state to the corresponding ideal glass state. It is found that the requirements of configurational space not only slow down the transition rates but also affects the apparent activation energy deduced from the variations of the final fictive temperature with the cooling rate.

The separation of fast and slow time scales in the dynamics of a supercooled liquid not only influences its equilibrium properties, but has also important consequences on its out-of-equilibrium behavior. The slow and fast degrees of freedom tend to reach equilibrium on their respective time scales. If a slow quenched treatment is used on a supercooled liquid it will have more time to find configurational spaces in the energy landscape to produce a higher stable glass than one produced by rapid cooling.

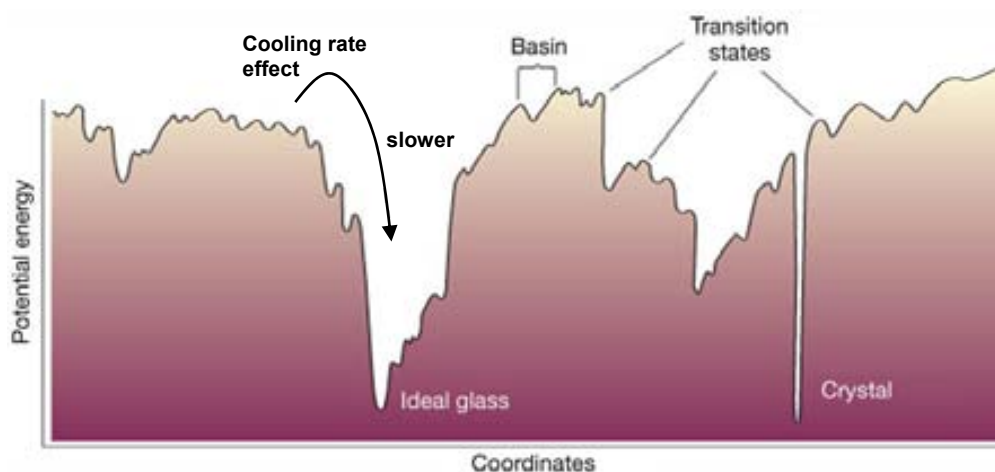


Fig. 4.11: Schematic illustration of an energy landscape. The stable phases (crystal and ideal glass) represent the lower potential energy. An unstable phase may lean towards low energetic positioning by changing the cooling rate. The x-axis represents all configurational coordinates. (Adapted from ref. [14])

4.1.5 Polyamorphism

At the moment there is evidence stating that certain glass forming liquids can exist in phases with identical compositions but different densities, and can undergo transition between the two phases as a function of temperature and pressure [11]. A substance that has the ability to exist in several different amorphous modifications it is known to suffer polyamorphism. Many amorphous substances can exist with different amorphous characteristics like polymers. However this phenomenon requires a clear phase transition between two distinct amorphous states. As amorphous solids are at times associated with liquid states⁴, polyamorphism is referred as well as a liquid-liquid phase transition. Polyamorphism is a comparable phenomenon with what happens in crystalline materials where structurally distinct phases of the same crystalline composition undergo transition⁵. For glasses, hydrostatic pressure is usually the thermodynamic variable used to induce polyamorphism. Such polyamorphic phase changes are often first-order transitions [34,35] and are reflected within the solid amorphous state, as rapid and often dramatic changes in the structure. There are several materials which have been reported to exhibit polyamorphism in the glassy state, such as amorphous ice, silica [36], silicon [37] and chalcogenide glasses [35].

⁴ A liquid-liquid transition however, is one that occurs only in the liquid state.

⁵ Polymorphism is the ability of a solid material to exist in more than one form or crystal structure.

The presence of a liquid-liquid transition has been also demonstrated in organic compounds like triphenyl phosphite (*TPP*). Ha et al. [38] reported the detection of a new amorphous phase in TPP. This new phase was called the glacial phase. The existence of this new phase opens the path of polyamorphism in organic compounds. It has been widely studied with numerous techniques such as calorimetry, X-ray diffraction, Brillouin scattering, dielectric and nuclear magnetic resonance spectroscopy [39]. Each method clearly provides information to conclude that the supercooled liquid of TPP transforms into a new phase which can be easily reproduced in most of the cases.

Some of the amorphous-to-amorphous transformations occur reversibly and are considered to be first-order transitions such as the case of water and triphenylphosphite. In some cases exothermic processes have been observed by calorimetry and attributed to a transition between an equilibrium liquid into the other. A recent example with vapor-deposited ethylbenzene has been reported [51]. Polyamorphism is still a matter of debate and various reports suggest that at least in some cases may be due to the presence of short-range order in the presence of minuscule nanocrystals. Studying polyamorphism can lead to the discussion of transformations from a fragile to a strong liquid. Dielectric relaxation measurements for TPP have suggested that the glacial phase is stronger than the ordinary liquid which is very fragile.

4.1.6 Toluene and ethylbenzene

Many organic liquids create a glass phase upon cooling, nevertheless few organic samples are considered to be simple enough until the point to ignore their intramolecular degrees of freedom [41]. Toluene is considered to belong to this type of simple molecule systems since the only low-frequency intramolecular vibration is that of methyl rotation. Toluene is a commonly used substance in the chemical and material industry. Chemically it is a mono-substituted benzene derivative used as a solvent for paints, silicon sealants, rubbers, adhesives, printing inks and polymers.

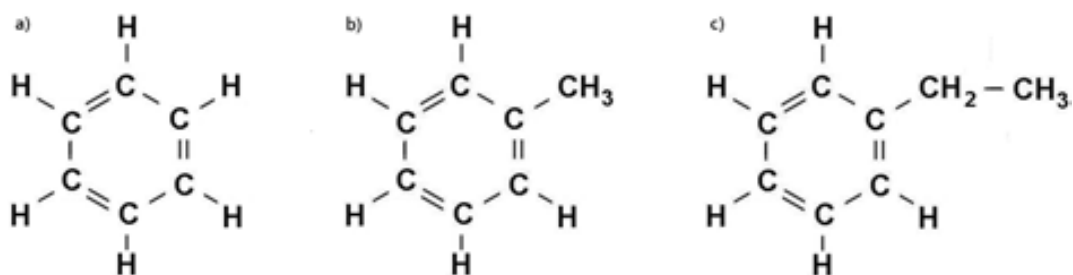


Fig. 4.12: Aromatics are a group of organic compounds characterized by the presence of a) benzene ring in their molecule. Benzene is the simplest aromatic organic compound, containing just the 'benzene ring,' that is 6 carbon atoms bonded to each other in a ring structure with each of the carbon atoms having a hydrogen atom attached to it. b) Toluene is one of the main aromatic organic solvents. It is one of the two (xylene is the other) simplest aromatics after the benzene. Toluene is made up of one hydrogen ion in the benzene ring replaced with a methyl group (CH₃). c) Ethylbenzene is an important aromatic hydrocarbon; it is used in the petrochemical industry as an intermediate in the production of styrene, which in turn is used for making polystyrene, a common plastic material.

Toluene shows high fragility with a fragility index $m = 105$ [42]. The super-Arrhenius dependence of the relaxation time when approaching the glass transition in supercooled toluene is well documented by several experiments including dielectric spectroscopy (DS) [42], deuterium spin lattice relaxation [43] and microwave spectroscopy [44]. The high fragility index of toluene is extraordinary in this same kind of benzene molecules since other alkyl-benzenes have significantly lower fragilities. An important aspect is that the other physical properties of toluene do not show any anomaly compared with those of these derivatives. Since Toluene is classified as a very fragile liquid it has been exploited in the study of dynamical heterogeneities in its supercooled liquid regime [61]. Many studies have demonstrated the existence of supramolecular heterogeneities using multidimensional nuclear magnetic resonance (NMR), light scattering, dielectric hole burning, small angle and double-axis spectrometry [75]. The density of small-size toluene could be comparable to the value in the bulk. Toluene resembles to a rigid molecule in which only the methyl rotation is the only low-frequency intramolecular vibration involved. Previous Differential Scanning Calorimetry measurements at heating rates of 10 K/min show evidence of the glass transition temperature at 117.5 K [45]. An ultrafast microcalorimetric study performed on micron thick toluene films obtained from the vapor has also been recently reported by Chonde et al. [46].

Ethylbenzene is an aromatic hydrocarbon which is an intermediate in the production of styrene, another organic liquid that is used for making the common plastic material, polystyrene. Ethylbenzene is flammable and combustible, naturally found in crude petroleum. It is used for the production of paints, solvents, resins, foams, inks, synthetic materials and insecticides.

Ethylbenzene shows fragility with a fragility index $m = 58$ [16]. The glass transition temperature T_g of the bulk ethylbenzene has been reported to be 115 K by Yamamuro and co-workers using calorimetry. Also, they have published the heat capacities of crystalline and stable liquid toluene and ethylbenzene and the configurational entropies of several glass-forming liquids [45]. The glass transition value has also been measured by Ishii et al. [52] for vapor deposited samples using reflected light intensity obtaining temperature values in accordance of those in the bulk sample.

Recently, Ishii and co-workers have reported the possibility of a liquid-liquid relaxation in the supercooled liquid of ethylbenzene. This supports the fact that the supercooled liquid which appears after the glass transition depends on the initial properties of the conformed glass and that is possible to convert between different stability glasses throughout different supercooled liquids through a liquid-to-liquid transition [51].

As a rule of thumb, the glass transition temperature is about two thirds of the melting temperature. Consequently, for the benzene derivatives like toluene and ethylbenzene, T_g must be positioned in the vicinity of 118 K. Calorimetric evidence of the glass transition in glassy organic films was first reported by Suga et al. [62].

4.2 Stable glasses by Vapor Deposition

Glasses are typically prepared by cooling the liquid and avoiding crystallization; other routes to create amorphous solids are vapor deposition, spin coating, freeze drying, and milling. Among these, vapor deposition has generally been regarded as a fast-quenching technique for vitrifying poor glass-formers and for trapping systems at high-energy configurations with a very high efficiency [52, 62]. Several studies have shown that glasses grown from vapor deposition are denser, less hygroscopic, and stronger than ordinary glasses [66, 67]. The formation of stable glasses by vapor deposition has been attributed to the surface mobility of molecules, which allows rapid equilibration of newly deposited molecules before they are locked in by later arriving molecules [67]. The behavior on the stability of organic glasses grown by vapor deposition has become somehow general through a couple of years. Zhu and coworkers [68] have managed to study the stability of organic glasses with exceptionally low energy and high kinetic stability. They were able to study up to four substances prepared by vapor deposition, most of them simple aromatic hydrocarbons, showing that they can produce high stable glasses with a very accessible setup indicating the generalization of this phenomenon and the high-availability of preparation conditions.

Up to very recently, vapor deposition at low temperatures below T_g was considered a very efficient approach to prepare glasses of a wide variety of substances, since crystallization was easily hindered. Most experiments were conducted at deposition temperatures around $0.6 T_g$ or even lower and the vapor molecules were very efficiently quenched into the non-equilibrium structure of a glass reducing their internal degrees of freedom which do not have enough energy to sample other more stable configurations in the energy landscape. This way, very unstable glasses (*with higher enthalpies than glasses cooled at normal cooling rates from the liquid*) were prepared. A number of examples confirming this behavior can be found in the literature [13,40,62]. A breakthrough was the recent discovery by Ediger and coworkers [15] that glasses vapor deposited close to T_g were in fact more stable than those obtained by freezing the liquid. Ediger's group has utilized the vapor deposition technique to create glassy materials with extraordinary thermodynamic and kinetic stability and high density [15,56,65]. They have prepared indomethacin and 1,3-bis-(1-naphthyl)-5-(2-naphthyl)benzene glasses by optimizing the stability obtaining higher onset temperatures of T_g for the vapor-deposited sample. This high onset for the glass transition indicates that the vapor-deposited material is kinetically much more stable, because higher temperatures are needed to dislocate the molecules from their glassy configurations. The integration of the heat capacity yields enthalpy curves that permit to evaluate the thermodynamic stability of a glass through the use of the concept of limiting fictive temperature. The stability of thick films grown from the vapor at $0.85 T_g$ was extraordinary and unreachable by simple annealing procedures of the glasses cooled from the liquid. In the case of Indomethacin it was roughly estimated that samples cooled from the liquid would require 10^7 years at the optimal aging temperature to reach identical values of the limiting fictive temperature than films deposited from the vapor phase. Other molecular glasses including toluene [57], ethylbenzene[52], nifedipine, felodipine, and phenobarbital [68] exhibit high stability after growth from the vapor at appropriate temperatures, so the phenomena seems quite general now.

More recently, Ishi et al. [52] measured the molar volume of ethylbenzene (EB) films, around $10 \mu\text{m}$ thick, grown from the vapor. The films grown at $\sim 0.85\text{-}0.9 T_g$ were denser and more stable than the supercooled liquid at the same temperature. The origin of the increased stability is thought to be based on the ability of the vapor molecules to efficiently sample different minima of the potential energy landscape before being buried by other molecules during the deposition process. These authors noted similar behavior for other alkylbenzene molecules, such as propylbenzene and isopropylbenzene, although toluene films behaved differently, displaying a

low reproducibility of the film density and in the assignment of the glass transition temperature. The authors explain this behavior by the small size of the methyl group compared to the functional groups on the other related molecules. In a previous publication, we showed an increased stability of vapor deposited thin films of ethylbenzene with respect to samples refrozen from the liquid at fast cooling rates of 2000 K/s. [66]. The increased kinetic and thermodynamic stability has been demonstrated in glasses of the large organic molecules indomethacin and trisnaphthylbenzene. A pronounced variation of the density and the glass transition with the deposition temperature was also observed. [15]

The kinetic destabilization of equilibrium solidification and glass forming ability are favored by the high-viscosity values achieved under continuous cooling, the slower the better. The atomic structure of a glass symbolizes the arrangement present in its liquid state which has been frozen in time and it is characteristic of the temperature at which the liquid thermally equilibrated for the last time. We can observe that more stable configurations have lower values of the fictive temperatures, which indicate a lower position in the energy landscape.

In an ordinary⁶ glass, molecular relaxation times become large in comparison to the time scale associated with the cooling rate. Since glasses are out of equilibrium, aging a glass for a significant long period of time below the glass transition T_g result in additional stabilization occurring with a very slow behavior. This has been observed in aged samples of poly(vinylacetate) below T_g for two months in which the system responded slowly [33]. The results of several studies have observed a significant reduction of the enthalpy associated to the glass state, a decrease of the fictive temperature and an increase of the onset of the calorimetric glass transition [15,52]. When an aged glass undergoes an annealing process above T_g , the transformation to the supercooled liquid can be considerably delayed.

The setup used in this work to deposit the glassy films has been reported in previous works done by E. León-Gutierrez et al. at GNaM [53]. It consists of a novel setup which combines a thermal evaporator in ultrahigh vacuum conditions with in situ measurements of the heat capacity of the thin films. This setup is being used for the analysis of the glass transition in ultrathin and/or thin organic glasses. The main advantage of this configuration with respect to conventional systems is the capability of allowing in situ treatments which can help explore a wide variety of glassy films by applying a large range of heating rates. The system comprises a high

⁶ An ordinary glass may be defined as a glass which is produced by cooling the liquid at a rate of a few K/min

sensitivity which allows the measurement of few nanometer thick films where size effects may become important. A more detailed explanation is described in the experimental section of this chapter and elsewhere [54]. Also, something relevant is that organic glassy films grown at low temperatures through the vapor phase have rarely been studied due to the difficulties inherent to in situ calorimetric measurements which are not the case with this development.

Toluene and ethylbenzene were chosen to study T_g kinetic effects since they are simple molecules that form transparent glasses by vapor deposition with good reproducibility [58]. The behavior of ethylbenzene as a glass is practically equal to that of toluene. We can manage to compare the results obtained with both molecules and support that this developed technique remains valid for many similar systems. Unlike other liquids, toluene and ethylbenzene (*EB*) have the heat capacity of the glass being considerably larger than that for the crystal below T_g . Ishii et al. have confirmed a stability increase for smaller molecules such as ethylbenzene [52].

The stability of the glass can be established by a relative comparison between the limiting fictive temperature, the Kauzmann temperature and the glass transition temperature. Eq. 4.4 provides a simple way to determine the position of a fragile glass on the energy landscape compared to an ordinary glass [15].

$$\theta_k = \frac{T_g - T_f}{T_g - T_k} \quad 4.4$$

The lowest position in the energy landscape would be when $T_f = T_k$, that is $\theta_k = 1$, indicating the lowest location in the energy landscape. When $\theta_k = 0$, the vapor-deposited sample has not improved any further down the energy landscape that can be reached by slow cooling the supercooled liquid. K. L. Kearns et al. have studied the enhanced stability of indomethacin (*IMB*) and 1,3,5-(tris)naphthylbenzene (*TNB*) by using the vapor deposition technique. [18]. They have obtained values of θ_k of 0.39 and 0.42 for IMC and TNB glasses prepared by vapor deposition and applying an aging process of the ordinary glass for several periods of time. By this measurement they conclude that, in the case of TNB ($\theta_k = 0.42$) the glass has progressed a 42% towards its lowest energy point in the landscape for amorphous arrangements.

4.3 Experimental description

Commercial Toluene and Ethylbenzene (*purity 99.5%*) were purchased from Sigma Aldrich and were placed in a pyrex container followed by several purifying sequences and by a repeated number of freeze-pump-thaw cycles and distillation with molecular sieves (*Sigma Aldrich*) before evaporation. After the container returns to room temperature, the vapor pressure of the sample liquid is high enough to be introduced into the UHV transfer prechamber using a needle valve. By carefully opening the high-precision leak valve connecting the prechamber with the main chamber, we control the leak rate into the main chamber and thus the quantity of vapor near the substrate. The vapor is injected through a glass micro-capillary connected to the leak valve. This system allows the deposition of organic films at very slow growth rates on cold substrates. A more detailed explanation of this configuration has already been reported [63].

Microfabricated calorimeters are used as sample support and heating/sensing devices. The microdevices consist of a 180 nm thick amorphous SiN_x membrane suspended on a silicon frame. Details on the development and calibration of these microdevices as well as of the thermomechanical stability and operation have been described in chapter II and elsewhere [70]. Once the calibration process is done two almost identical nanocalorimeters are selected and mounted on the copper holders and located inside the UHV chamber. The chamber holds pressures around 10⁻⁹ mbar using a turbomolecular pump which is connected through an oil-sealed mechanical roughing pump. On the selected nanocalorimeter working as the sample holder a shadow mask is placed on the bottom side. The shadow mask ensures selective film deposition only below the platinum heater region. The second nanocalorimeter is protected from any deposition and therefore serves as reference in the differential measurements. Previous examinations on changes in the Pt resistance were made upon deposition of various films. No changes were found in heater resistances, which could affect calorimetric traces.

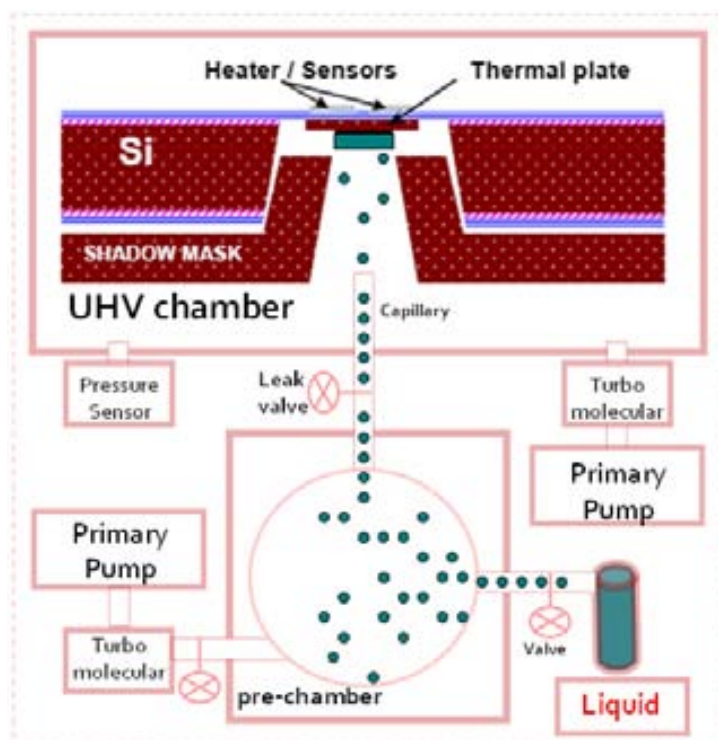


Fig. 4.13: Experimental configuration implemented on this work. Consisting of a main UHV chamber in which the thermal block containing reference and sample chips is localized. A pre-chamber where the vapor phase is generated which passes through a micro-capillary directly to the sample deposition region of the microcalorimeter

Before analyzing any type of samples, hundreds of calorimetric scans are performed by consecutively heating both nanocalorimeters up to the desired temperature, in this case 250 K followed by a self-cooling to 80 K. This procedure determines the initial difference between the two calorimetric cells, which will be used as the baseline to be subtracted from the final measurements. The raw data treatment has been explained in detail in section 2.3.1 of chapter II. After this internal calibration procedure, the selected vapor is introduced into the main chamber and rapidly condenses on the nanocalorimeter surface, forming a glassy film.

The deposition temperature can be tuned and maintained constant to any desired value above liquid nitrogen temperature by regulating the amount of current supplied to the Pt resistance using a proportional-integral-derivative controller. Deposition was carried out on substrates at temperatures from 90–120 K. The growth rates ranged between 0.001 - 0.1 nm s⁻¹. Films were grown on an amorphous SiN_x surface, the membrane of the calorimetric chip, with rms roughness of ~ 1 nm. Layer thickness ranges from 5-150 nm to analyze the effect of

nanoconfinement on aging. Samples 80 nm thick and above are considered to behave as bulk glasses as determined in a previous study [63]. Immediately after film deposition, scans are performed by heating the nanocalorimeter up to the desired temperature at heating rates of around 3.5×10^4 K/s. At such fast rates, the heat capacity of the sample can be evaluated from the measurement of the differential voltage between the two nearly-identical calorimetric cells, ΔV , as a function of time after applying baseline and time-derivative corrections during the heating [69] according to the expression 4.5. With the first data acquisition we determine the heat capacity of the as-deposited film. After the first fast heating treatment we use different cooling rates and analyze the heat capacity of films after various thermal histories.

$$C_{p_{sample}}(T(t)) = \frac{V_R(t)}{(dT/dt)^2 (dR/dT)_t} \frac{d\Delta V}{dt} \quad 4.5$$

where $V_R(t)$ is the reference voltage at a given time and (dR/dT) accounts for the TCR of the microchips. The final C_p value is obtained after several corrections are applied described in detail elsewhere [72]. To benchmark the calibration we grow *in situ* crystalline thin films (around 100–200 nm) of methanol and ethylbenzene and measure their melting points. The onset temperatures of the peaks are within 1 K of the bulk melting point.

4.3.1 Thermal treatments on thin film organic glasses

In the actual setup, the mass estimation relies on the measurement of the heat capacity above T_g , in the supercooled liquid region, and its comparison to the specific heat value of the conventional liquid at the same temperature, $C_{esp}(T)$, i.e., $C_p = 1.47013 \text{ J g}^{-1} \text{ K}^{-1}$ at 160 K [55,56]. This procedure yields $m = C_p(T)/C_{esp}(T)$. Because the deposition area is well characterized through the use of shadow masks in close proximity to the substrate, the thickness of the film can be inferred. The description of the different thermal treatments using fast heating rates is shown in figure 4.14. Every heating scan takes the sample far above the glass transition, i.e. into a proper liquid supercooled state. Therefore, the thermal history is erased after the upscan and every heating scan is representative of the previous cooling procedure.

Along this chapter, we will distinguish three main types of samples. Fast scans performed right after deposition are named as-deposited scans (AD) and provide information on the stability of the vapor-deposited samples. Samples that are re-frozen from the liquid at a rate close to 2000 K/s within the glass transition region are named fast-cooled (FC) samples, and heat scans performed after refreezing the film at $\sim 5\text{-}10$ K/min are named slow-cooled (SC). The heat capacity of AD and SC samples is evaluated from single upscans, whereas the C_p of FC samples represent averages of 50 consecutive measurements.

At temperatures below 180 K and using fast heating/cooling rates, sublimation is negligible. During data treatment we use a 75-point box averaging to all raw data (*acquired at 1.5 MSamples per second*) to improve the signal-to-noise ratio. Both EB and toluene layers can be fast heated back and forth many times without undergoing crystallization. Several annealing temperatures may be applied to study the stability of the cooled samples and to see whether or not the cooled samples can achieve the same stability with respect of the as-deposited ones. The heat capacity of the annealed samples is analyzed by applying the same heating rate applied for the as-deposited films.

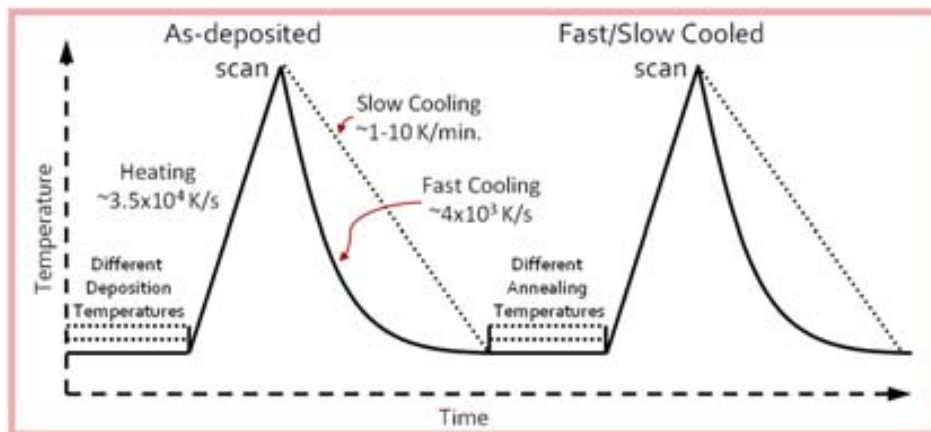


Fig. 4.14: Thermal treatments for the study of vapor deposited thin films. Fast scans performed at heating rates around $33\,000\text{ K s}^{-1}$ after deposition are named as-deposited scans (AD). Samples that are re-frozen from the liquid at a rate close to 2000 K s^{-1} are named fast-cooled (FC) samples, and heat scans performed after refreezing the sample at $\sim 5\text{-}10\text{ K min}^{-1}$ are named slow-cooled samples (SC).

4.4 Results and discussions

4.4.1 Influence of deposition temperature

Figure 4.15 shows the heat capacity data obtained from single scans of the as-deposited toluene thin films grown at various deposition temperatures [57]. The onset of the glass transition shifts to higher temperatures as the growth temperature is reduced from 115 K to 90 K. Also, the fictive temperature, T_f , moves to lower temperatures. This means that a higher stability is obtained when depositing at $0.8 T_g$ (90 K). This has been already observed by other authors [15]. This data confirms that the temperature of deposition highly influences the kinetic and thermodynamic stability. The experimental setup does not enable us to make deposition below 90K. However, is predictable that the stability will decay for lower temperatures since superficial mobility is hardly reduced.

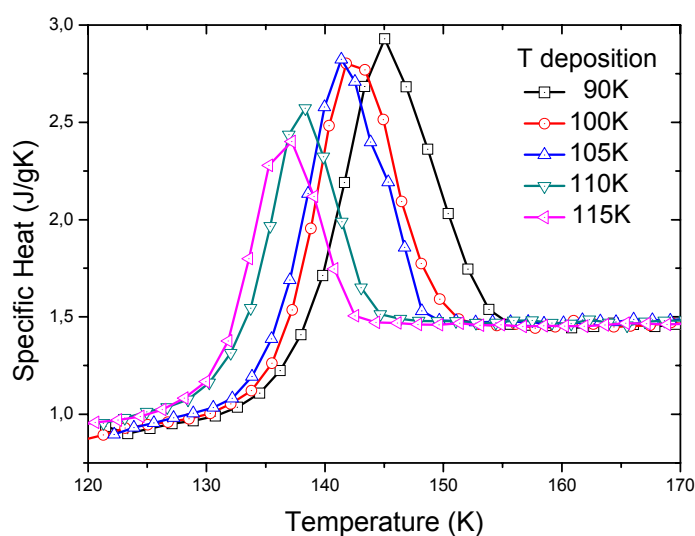


Fig. 4.15: Specific heat curves for toluene as a function of temperature. The different curves correspond for different deposition temperatures

A similar behavior is also observed for ethylbenzene, although the maximum stability appears to be located at a slightly higher temperature of 92 ± 2 K.

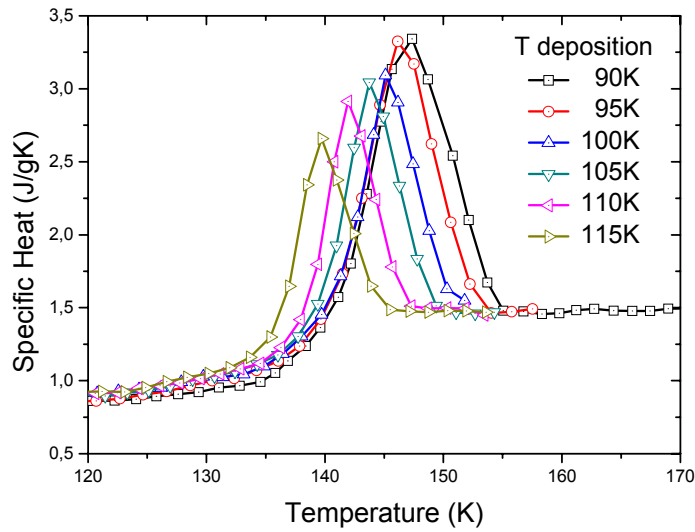


Fig. 4.16: Specific heat curves for ethylbenzene as a function of temperature. The different curves correspond for different deposition temperatures

4.4.2 Cooling rate effect

We first start with the influence of cooling rate on the onset and fictive temperatures of glasses refrozen from the liquid in comparison to those obtained from the vapor (AD layers). In figure 4.17 we represent the specific heat values as a function of temperature for Toluene and Ethylbenzene glasses cooled at different rates. Increasing the cooling rate leads to a reduced stability of the glass, which is traduced in a shift to lower temperatures of the T_{onset} during the fast heating scan.

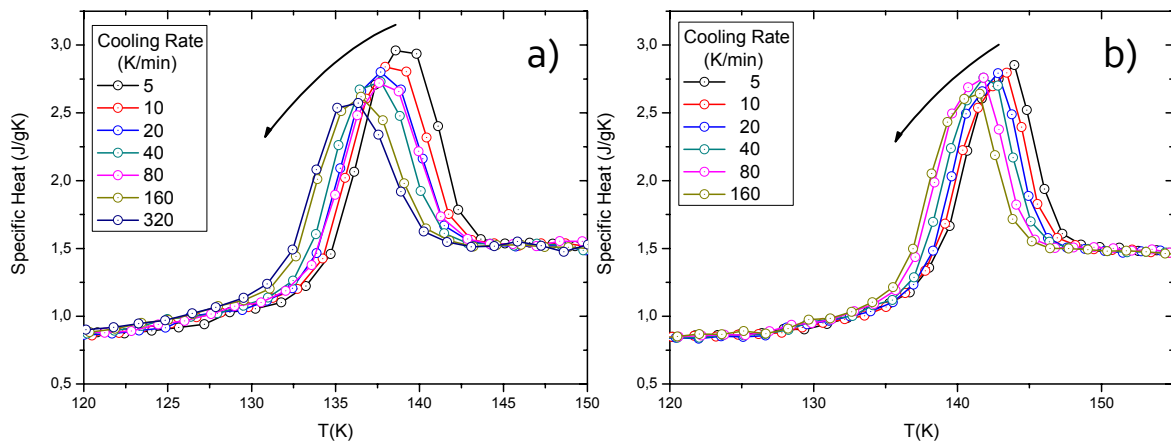


Fig. 4.17: Evolution of the onset temperature of the glass transition for a) toluene (85 nm) and b) ethylbenzene (100 nm) thin films

The next graphics show the specific heat and enthalpy values for the as-deposited (AD), fast-cooled (FC) and slow-cooled (SC) glasses at different cooling rates. The data correspond to a 85 nm toluene thick layer. The change in the cooling rate also has an evident effect on the fictive temperature T_f . If the stability of the film is deteriorated with faster cooling rates higher T_f will be observed.

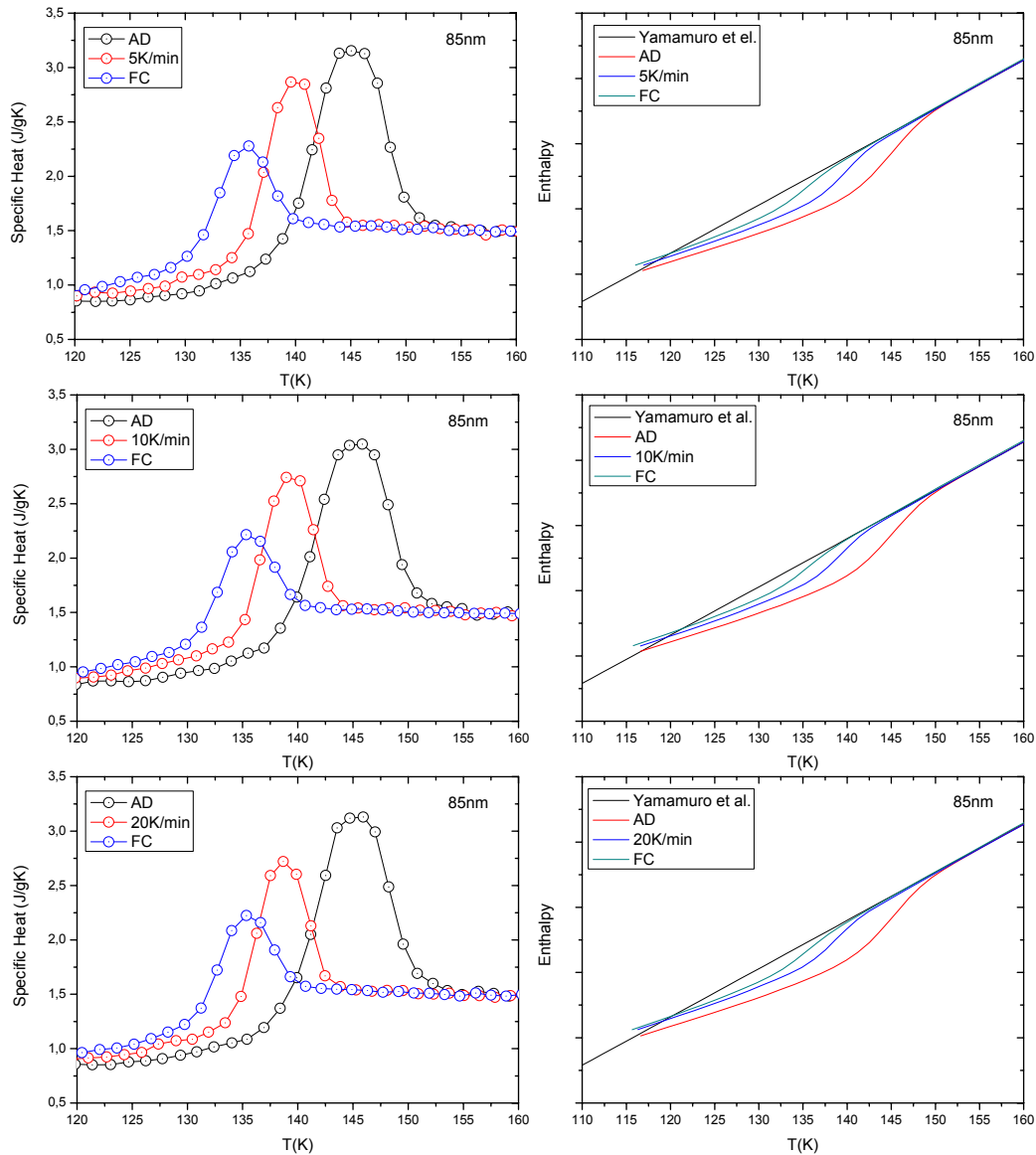


Fig. 4.18: Specific heat curves as a function of temperature for an 85 nm Toluene thin film deposited at 90 K. In black: the AD films scan corresponding to the immediate measurement after deposition. In blue: the FC films scan corresponding to the fast cooling of the supercooled liquid (~ 2000 K/s). In red: the SC films scan corresponding to the slow cooling from the supercooled liquid at various rates. Enthalpy curves as a function of temperature. In black: the enthalpy extrapolation for the supercooled liquid taking by Yamamuro et al. [45]. In red: the enthalpy extracted from the integration of the specific heat of the AD films. In blue: the enthalpy extracted from the integration of the specific heat of the FC films. In cyan: the enthalpy extracted from the integration of the specific heat of the SC films.

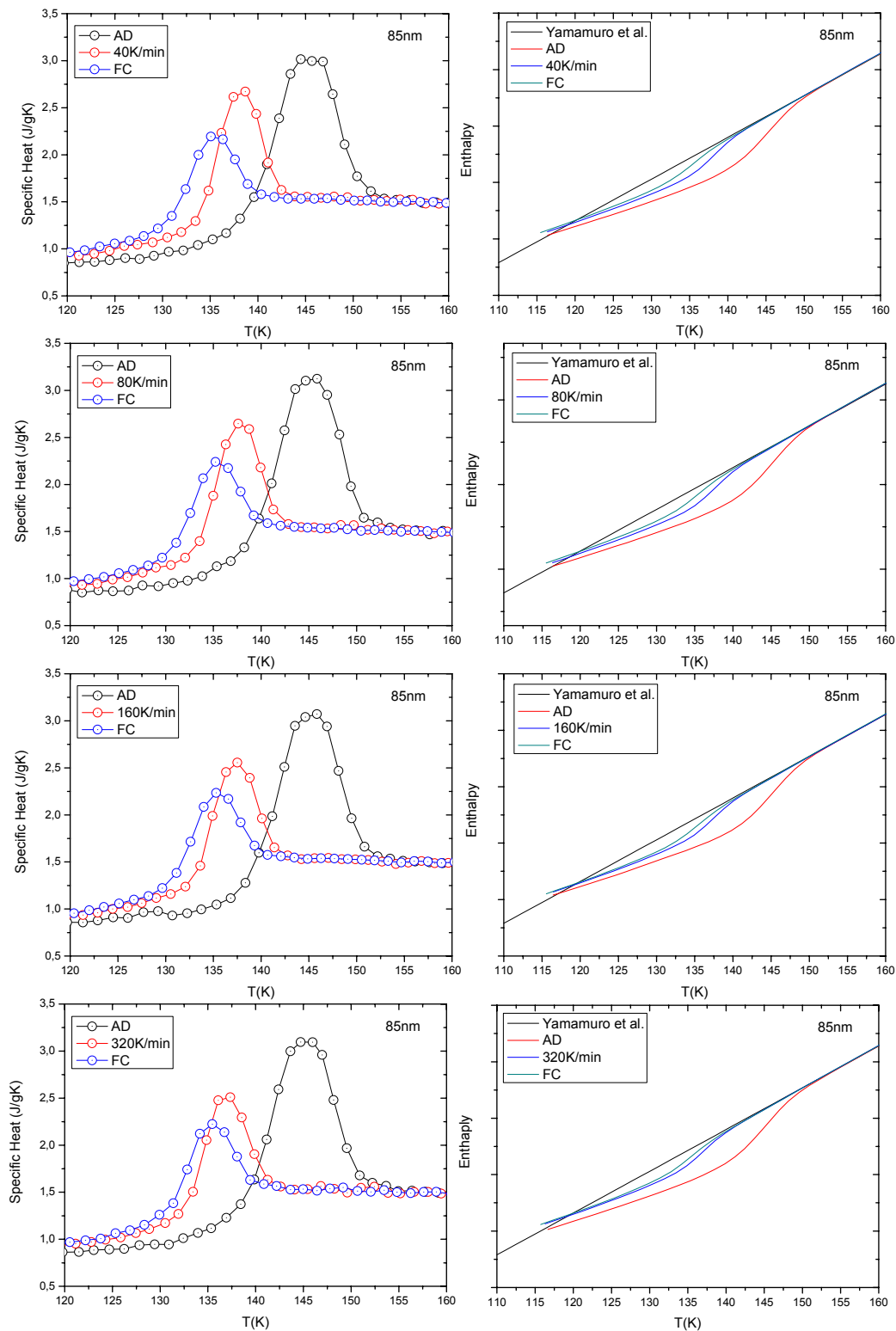


Fig. 4.19: Specific heat curves as a function of temperature for a 85 nm Toluene thin film deposited at 90 K. In black: the AD films scan corresponding to the immediate measurement after deposition. In blue: the FC films scan corresponding to the fast cooling of the supercooled liquid (-2000 K/s). In red: the SC films scan corresponding to the slow cooling from the supercooled liquid at various rates. Enthalpy curves as a function of temperature. In black: the enthalpy extrapolation for the supercooled liquid taking by Yamamuro et. al [45]. In red: the enthalpy extracted from the integration of the specific heat of the AD films. In blue: the enthalpy extracted from the integration of the specific heat of the FC films. In cyan: the enthalpy extracted from the integration of the specific heat of the AD films.

The onset of the glass transition and the limiting fictive temperature, both as functions of deposition temperature, are plotted in Fig. 4.20 for toluene AD films and FC and SC liquids. Every point is the average of 3–5 independent measurements and the error bars correspond to the standard deviation. For both molecules, films grown between 90–95 K, i.e. $0.77\text{--}0.82 T_g$, have the highest onset temperature and the lowest fictive temperatures. Our data confirm that the deposition temperature highly influences the thermodynamic and kinetic stability of vapor deposited films. At temperatures not far from T_g , growth from the vapor results in more stable material since the molecules at the surface have sufficient time and mobility to adopt the more stable configurations. It is not excluded that this very stable material differs structurally from a glass. However, such behavior is consistent with previous findings for the larger molecules indomethacin and trisnaphthylbenzene (*TNB*) as reported by Ediger et al. [15,18] and also with the results of Ishi et al. [73,74] for ethylbenzene. Since we are limited to deposition temperatures above 90 K, we have not measured the stability of films deposited far away from T_g . Below the maximum stability region, we expect the kinetic and thermodynamic stability would decrease.

Also in Fig. 4.20 (*red dots*) we have represented the evolution of the onset of the glass transition and the limiting fictive temperature with the variation of the cooling rate which indicates an evolution towards the AD values with a lowering of the cooling rate. The evolution of both onset temperatures of the glass transition and the limiting fictive temperatures as a function of the cooling rate used to quench the liquid of toluene is represented in Fig. 4.21.

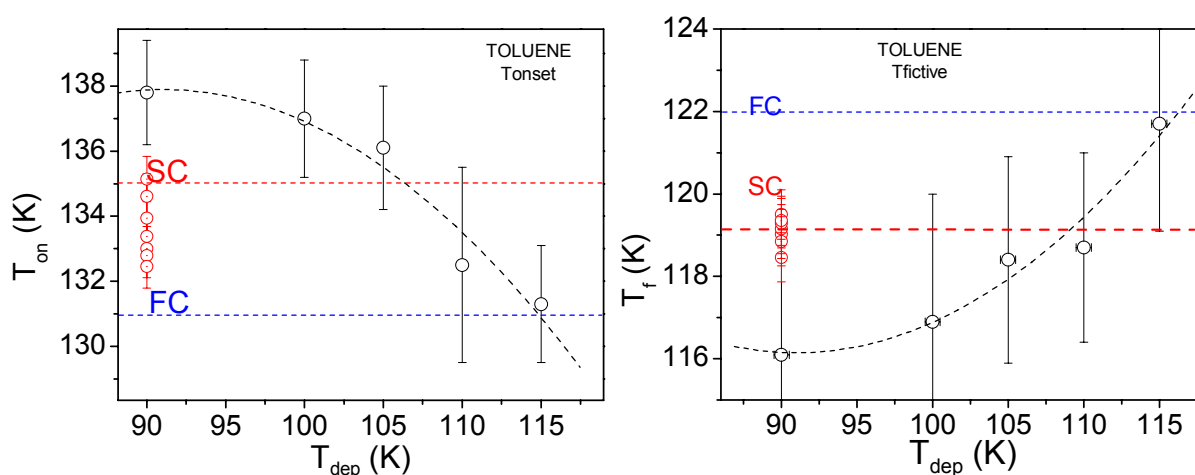


Fig. 4.20: T_{on} and T_f as a function of deposition temperatures between 90 K and 115 K for Toluene. In open black circles the representation of the As-deposited temperature values. The red line represents the slow cooled values for both temperatures and the blue line correspond to the fast cooled values. In red open circles we represent the evolution of different slow cooling rates for a sample deposited at 90 K.

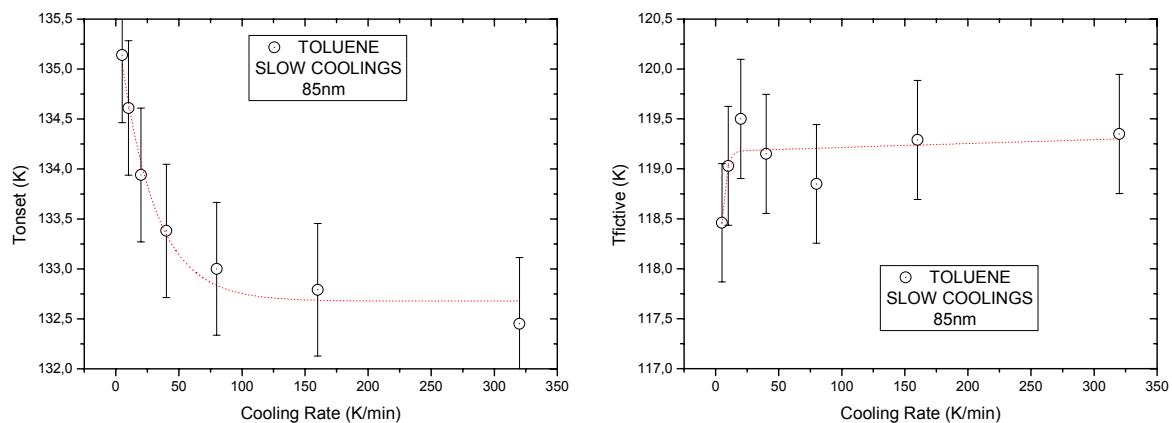


Fig. 4.21: Representation of the evolution of T_{on} and T_{f} as a function of cooling rate for thin films of Toluene of 85nm. Higher cooling rates will tend to temperature values near the fast cooled values.

The graphics represented in Fig. 4.22 and 4.23 show similar data than in 4.18 and 4.19 but for a 100 nm thick ethylbenzene thin film. The onset of the glass transition and the limiting fictive temperature, both as functions of deposition temperature, are plotted in Fig.4.24 for ethylbenzene AD films and FC and SC liquids. Every point is the average of 3–5 independent measurements and the error bars correspond to the standard deviation. The evolution of both onset temperatures of the glass transition and the limiting fictive temperatures as a function of the cooling rate used to quench the liquid of ethylbenzene is represented in Fig. 4.25.

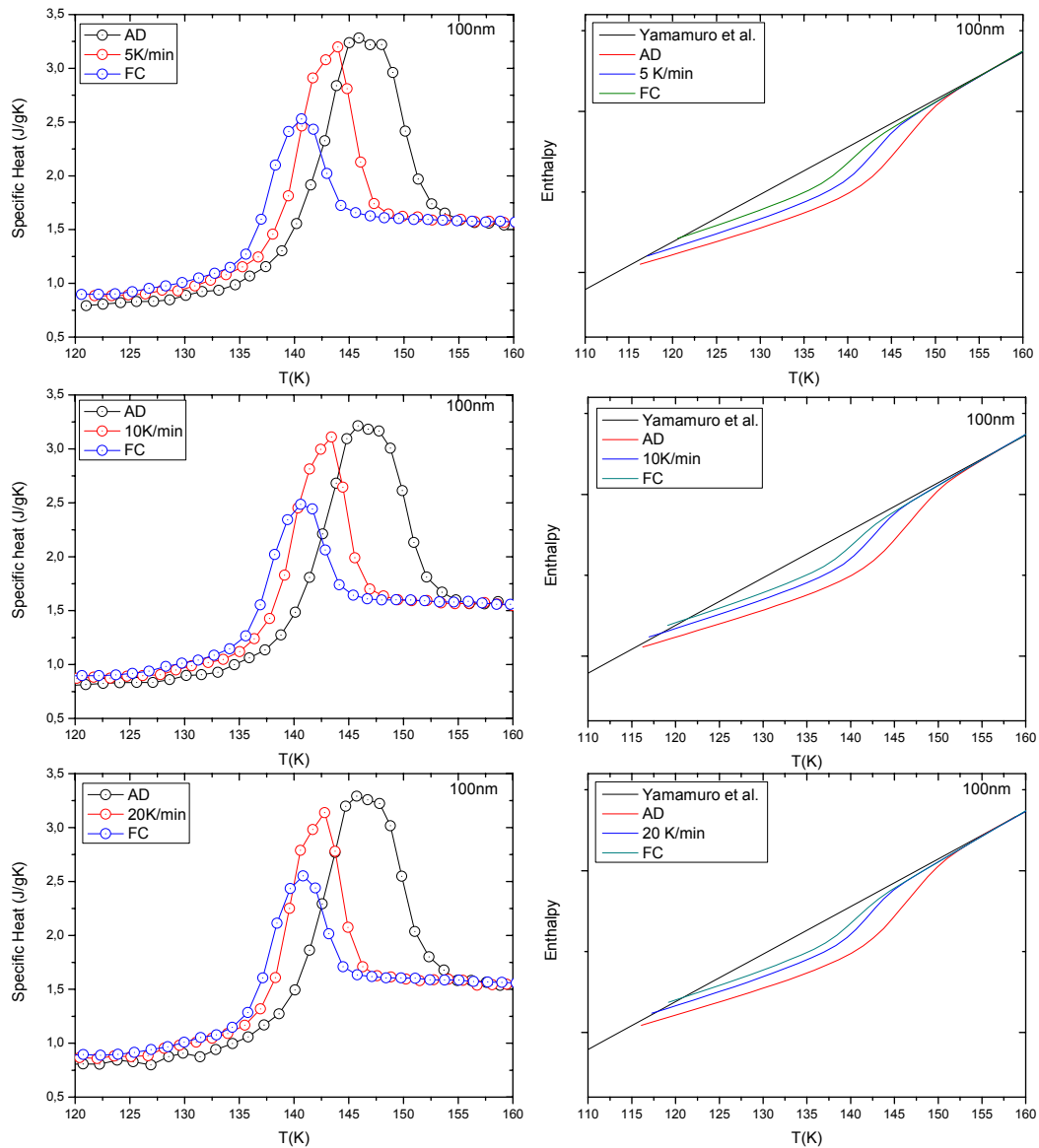


Fig. 4.22: Specific heat curves as a function of temperature for a 100 nm Ethylbenzene thin film deposited at 90 K. In black: the AD films scan corresponding to the immediate measurement after deposition. In blue: the FC films scan corresponding to the fast cooling of the supercooled liquid (~ 2000 K/s). In red: the SC films scan corresponding to the slow cooling from the supercooled liquid at various rates. Enthalpy curves as a function of temperature. In black: the enthalpy extrapolation for the supercooled liquid taking by Yamamuro et. al [45]. In red: the enthalpy extracted from the integration of the specific heat of the AD films. In blue: the enthalpy extracted from the integration of the specific heat of the FC films. In cyan: the enthalpy extracted from the integration of the specific heat of the FC films.

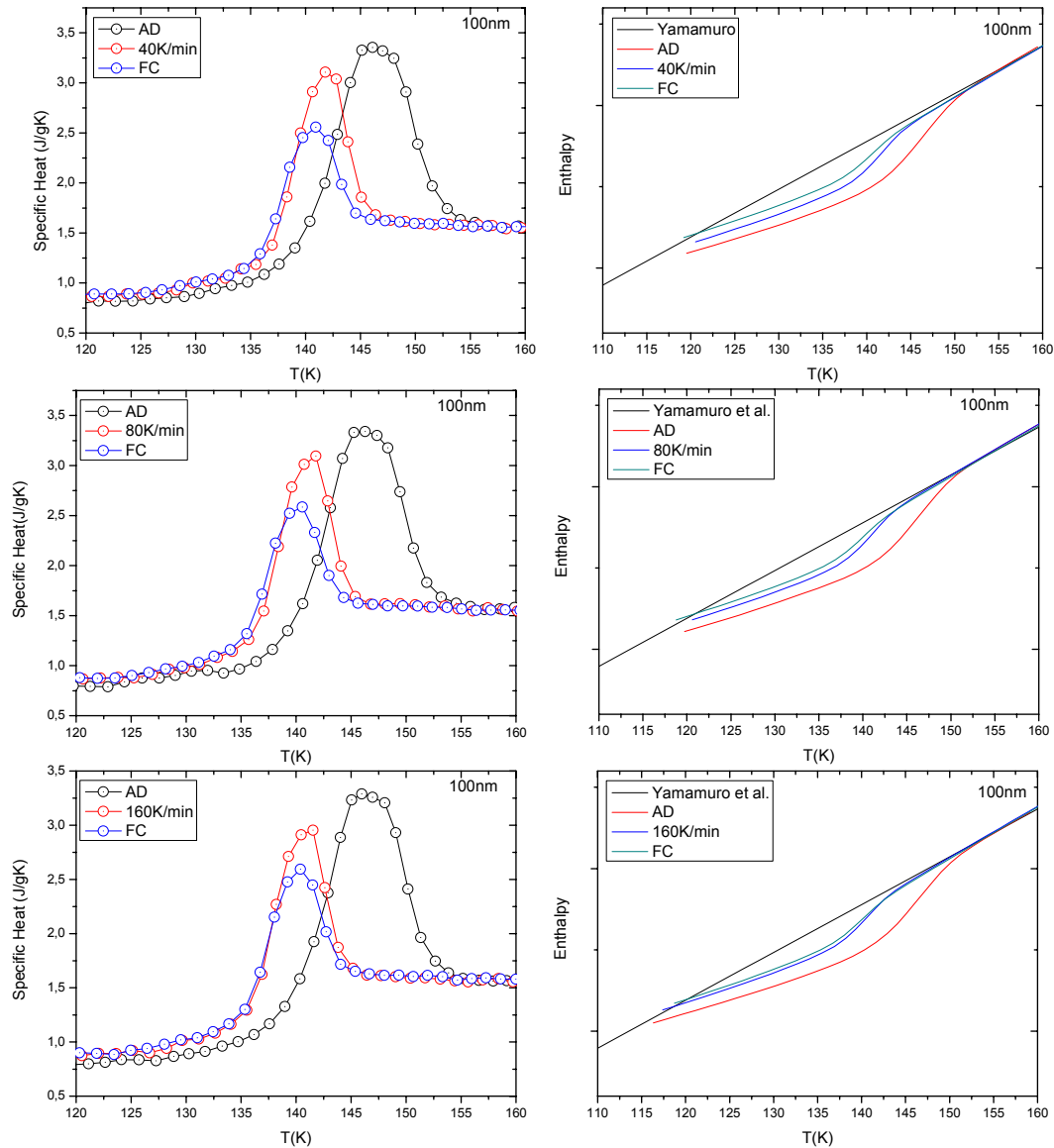


Fig. 4.23: Specific heat curves as a function of temperature for a 100 nm Ethylbenzene thin film deposited at 90 K. In black: the AD films scan corresponding to the immediate measurement after deposition. In blue: the FC films scan corresponding to the fast cooling of the supercooled liquid (~ 2000 K/s). In red: the SC films scan corresponding to the slow cooling from the supercooled liquid at various rates. Enthalpy curves as a function of temperature. In black: the enthalpy extrapolation for the supercooled liquid taking by Yamamuro et. al [45]. In red: the enthalpy extracted from the integration of the specific heat of the AD films. In blue: the enthalpy extracted from the integration of the specific heat of the SC films. In cyan: the enthalpy extracted from the integration of the specific heat of the FC films.

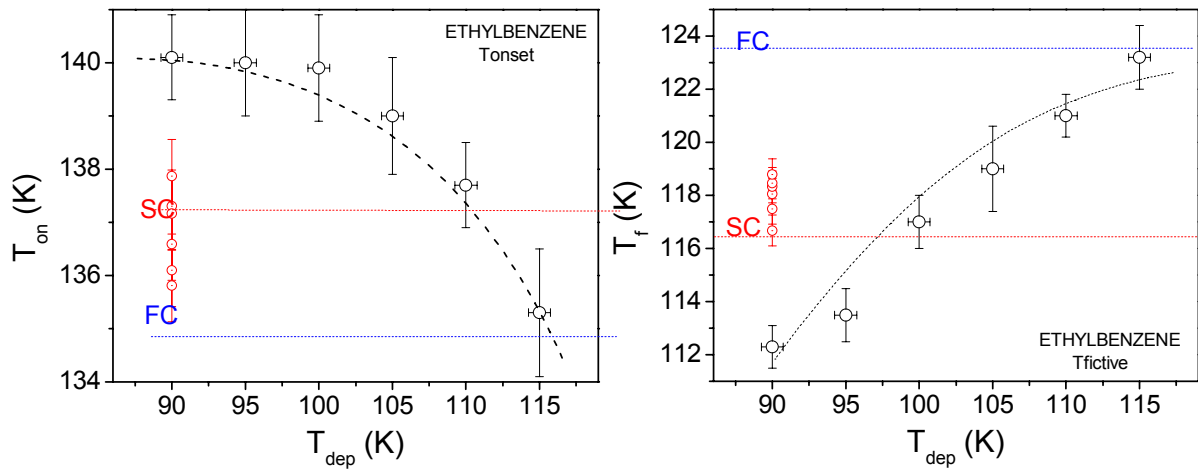


Fig. 4.24: Ton and Tf as a function of deposition temperatures between 90 K and 115 K for Ethylbenzene. In open black circles the representation of the As-deposited temperature values. The red line represents the slow cooled values for both temperatures and the blue line correspond to the fast cooled values. In red open circles we represent the evolution of different slow cooling rates for a sample deposited at 90 K.

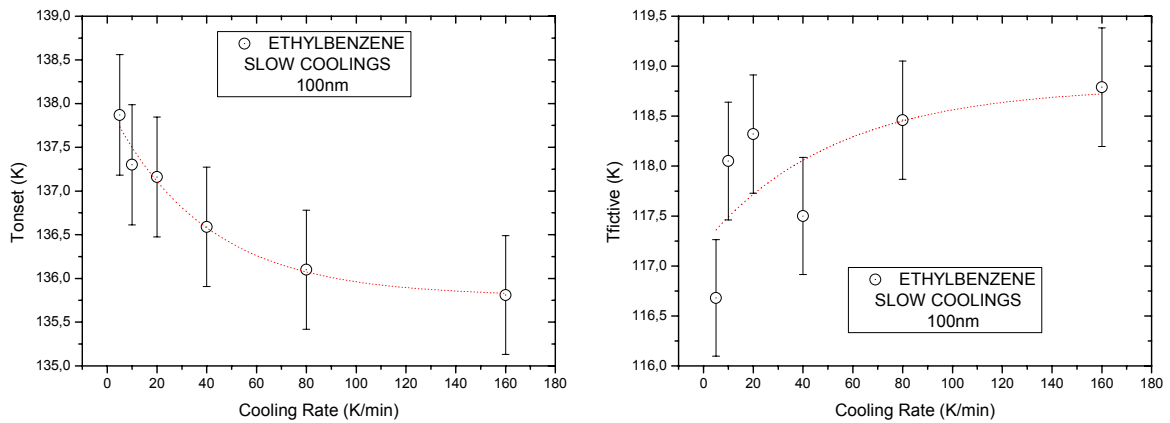


Fig. 4.25: Representation of the evolution of T_{on} and T_f as a function of cooling rate for thin films of Ethylbenzene of 100nm. Higher cooling rates will tend to temperature values near the fast cooled values.

4.4.3 Temperature effect on aging: Isochronal experiments

Several experiments were made in order to obtain the optimal aging temperatures at isochronal conditions for both toluene and ethylbenzene. A number of temperature values (90-120 K) were adjusted in the sample for a fixed time (15 min). Aging at a different temperatures below the glass transition T_g will affect the resulting stability of the sample. This can be monitored by analyzing the onset temperatures of the heat capacity. Finding an optimal aging temperature will result in an accelerated physical aging. In the following figure we represent the evolution of the heat capacity as a function of aging temperature for a 100 nm ethylbenzene thin film.

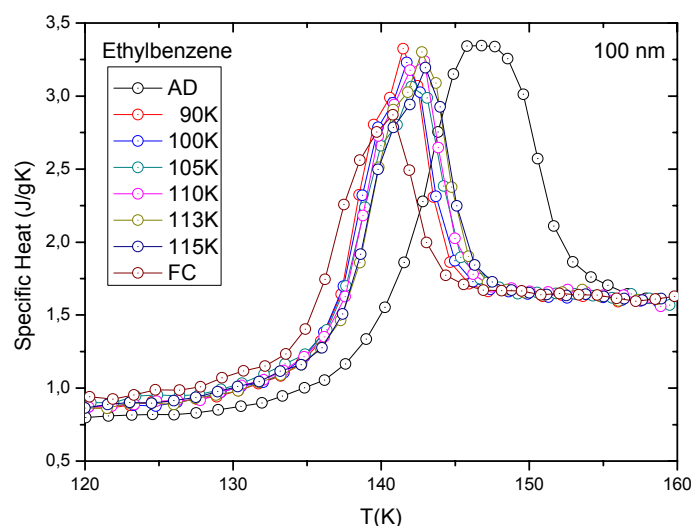


Fig. 4.26: Specific heat as a function of temperature for a 100nm ethylbenzene thin film. Several aging temperatures were analyzed in order to obtain the optimal aging temperature which yielded $T_a = 113$ K.

It seems that the required time to reach equilibrium increases as the aging temperature decreases. Optimal aging temperature of 115 K and 113 K, for toluene and ethylbenzene, respectively were achieved for a 15 min aging treatment, although the difference at these aging times is not remarkable. Typically, aging experiments are carried at the same distance from T_g to study the rate of physical aging. In this case, the aging experiments that will be shown in section 4.4.3 will be performed at the less-favourable (90 K) and optimal (115 K) aging temperatures.

Studies by Simon [63] on stacked ultrathin polystyrene films have demonstrated that the times required to reach equilibrium are significantly lower for ultrathin film samples compared with the bulk at a given aging temperature. The same behavior has been observed in our work on bulk (100 nm) and very thin (10 nm) toluene and ethylbenzene films. We can observe in figures 4.26 and 4.27 that for isochronal experiments (15 min) the ultrathin films have managed to achieve configuration closer to the higher possible stability than those in the bulk. Although nanoconfined samples may have different behavior compared for that in the bulk and the optimal aging temperature may depend on thickness since T_g temperature decreases for thinner films. The next figure shows the heat capacity of an ultrathin ethylbenzene film of 10 nm for several aging temperatures.

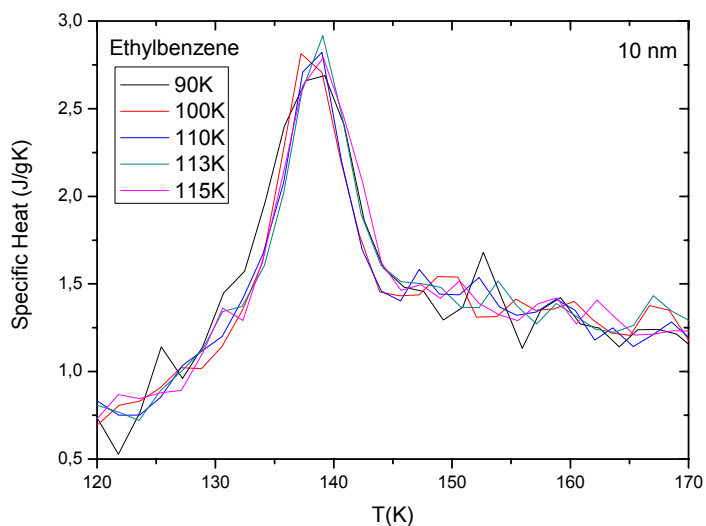


Fig. 4.27: Heat capacity as a function of temperature for a 10nm ethylbenzene film and for several aging temperatures at isochronal conditions.

Comparing the temperature effect on aging between the bulk and the ultrathin film samples, the evolution of the onset temperature of the heat capacity appears to be analogous obtaining very similar values for optimal aging temperatures (~ 115 K). This indicates that the aging will not strongly depend on the distance from T_g at which the aging treatment takes place. That may be explained by the fact that the onset temperature and the fictive temperature of the fast-cooled liquid does not change with thickness.

4.4.4 Aging of ethylbenzene and toluene glasses obtained from the liquid: Influence of thickness

In this section we analyze the aging behavior of toluene and ethylbenzene thin films down to 7 nm. The variation of the limiting fictive temperature is used as the major parameter towards quantification of the stability of the glassy films. We demonstrate that aging is heavily influenced by the thickness of the layers. The novelty of this work relies on the finding that the thinnest films formed by approximately 10-20 monolayers are extremely sensitive to aging. Samples aged at $\sim 0.8T_g$ for less than one day reach limiting fictive temperatures in close proximity to the vapor deposited films. In contrast, for thicker films around 100 nm aging is ineffective towards attaining a low configuration in the potential energy landscape compared to equivalent thick films obtained from the vapor and years are necessary to reach the fictive temperature of the bulk.

The calorimetric traces are obtained from fast scans after a specific thermal history as outlined in the experimental section (*Fig.4.14*). Figures 4.28 show the specific heat for toluene films of various thicknesses (115 nm, 50 nm, 7 nm) after isothermal aging at 90 K and 115 K from 1-to-600 min. In 115 nm films aging results in a noticeable shift of the overshoot with an increase of the onset temperature and a larger overshoot. However, the thinner films behave different since the onset temperature change only slightly, whereas the overshoot increases with aging. A similar behavior is observed for ethylbenzene layers, 100, 50 and 10 nm thick (*Fig. 4.29*) elaborated for 90 and 115 K. The results obtained for the AD and FC sample are in agreement with a previous report [63] where it was reported that the onset of the glass transition and the limiting fictive temperature of toluene films grown from the vapor at $\sim 0.8 T_g$ decrease with the thickness of the films. In contrast no change is observed for films obtained by refrozen the liquid at fast cooling rates where both T_{on} and T_f remain constant in agreement with other researchers [60, 64]. A similar behavior has been more recently observed for ethylbenzene layers. Figure 4.30 to 4.33 show the variation of the onset and fictive temperatures for toluene and ethylbenzene films of different thickness aged at 90 K and 115 K for times up to 30 min. Both figures clearly illustrate the general trend that as the thickness decreases the fictive and onset temperatures evolve towards the corresponding values of the stable glass. Every point shown in the results is the average of 5-7 independent measurements on equivalent thickness samples. The error bars correspond to the standard deviation. The main contribution of this work comes from the aging evolution of the thinnest films. It is clear from this figure that aging at $T_a=90$ K is remarkably

different depending on the thickness of the films. Accelerated aging has already been observed in a variety of thin film polymer glasses analyzed down to 10 nm [59]. However, in this work we investigate films that are below this thickness and where the observed effects are more noticeable. In fact, there is a remarkable decrease of the fictive temperature while the onset temperature remains nearly unchanged for the thinnest films of this study, 7 nm. The onset temperature which may be used as an indicator of the kinetic stability of the glass is nearly the same for the thinnest FC and AD glasses. This may be understood from the different dynamics of the molecules lying close to the outer surface with respect to those buried within the FC or AD glass. Since molecules at the surface have increased mobilities in both cases, FC and AD, and these molecules dominate the dynamics of the glass in the thinnest layers the onset of mobility should be closer. For the thickest films the evolution is markedly different: after prolonged aging up to 12 h both the onset and fictive temperatures remain mid way towards the value attained in the vapor-deposited stable glass. The aged FC glass has increased its thermodynamic and kinetic stability but it is still far away the values reached during growth from the vapor at the optimum temperature for 1 h.

We focus now our attention on the evolution of the fictive temperature with time at aging temperatures of 90 K and 113 K. Figure 4.34 shows the evolution of $T_f - T_a$ for $T_a = 90$ K as a function of aging time for films ranging in thickness from 7 to 100 nm. This figure illustrates the remarkable thickness influence on the aging properties of the glass. The superaging behavior is accompanied by a remarkable decrease of the fictive temperature as the film thickness decreases. In fact, aging dynamics is strongly influenced by layer thickness. Whereas a bulk film obtained from the liquid by a fast cooling procedure may need around 1 year to reach the low enthalpy of the vapor deposited glass, films of thickness 7 nm reach a much lower value of the fictive temperature, comparable to the highly stable vapor deposited glass, in only couple of hours. This behaviour reflects the importance of the outer surface layer on the dynamics of the films and helps to understand the mechanism of stabilization of the vapor deposited films. In effect, molecules at the surface have enough mobility to explore and attain lower configurational sites on the energy landscape picture. For bulk films aging of the glass obtained from the liquid is largely ineffective because the inner molecules are buried by other molecules and need extremely long times to find more stable sites. However, the thinnest films of this study, 7 nm, have many molecules within 6 molecular diameters of the surface (*~50% of the total number of molecules in the film*). In this environment mobility of the overall layer is largely enhanced and the molecules can sample more stable positions with a higher efficiency. The time needed to reach the stability

of the vapor deposited glasses is plotted as a function of thickness in the inset. 7 nm: 1.7 h (6000 s), 10 nm: 27.5 h (99000 s), 20 nm: 4.5 days, 106 h 3.8×10^5 s, 100 nm: 350 days (2.87×10^7 s)

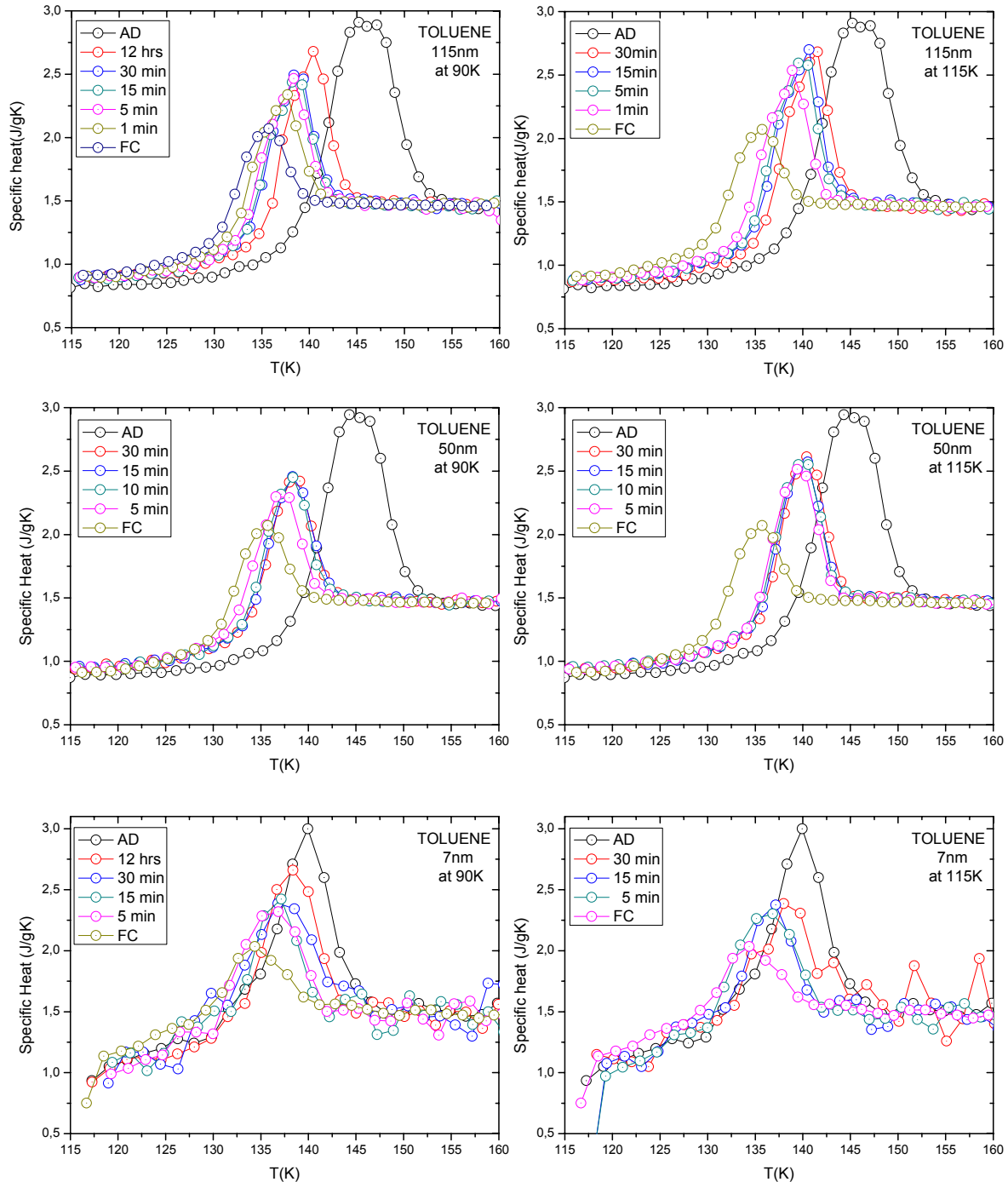


Fig. 4.28: Specific Heat curves as a function of temperature for Toluene thin films (7, 50, 115 nm) for the as-deposited at 90 K (AD), the fast cooled from the liquid (FC) and the aged for several times (1,5,15,30 min) at 90 K and 115 K

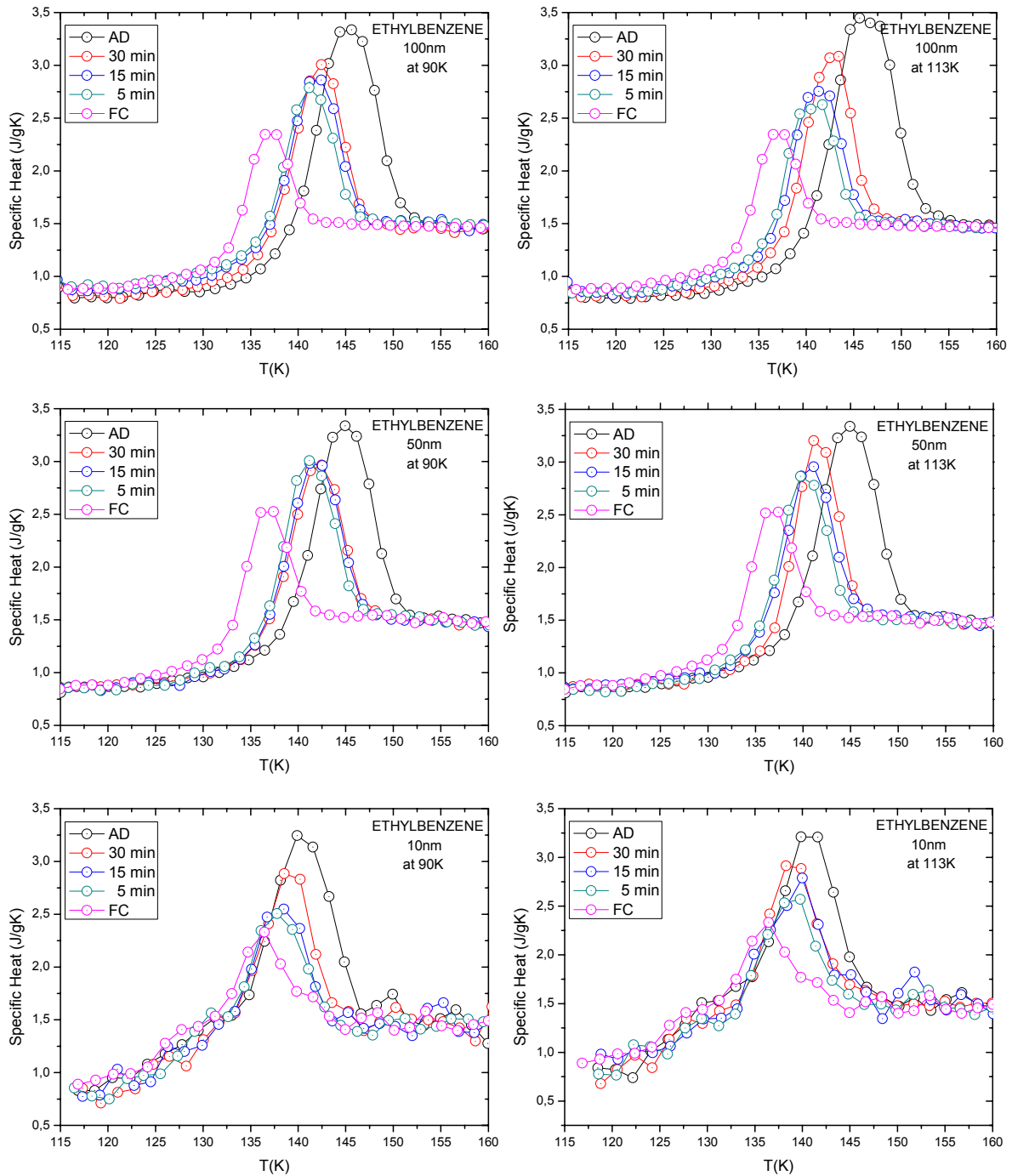


Fig. 4.29: Specific Heat curves as a function of temperature for Ethylbenzene thin films (10, 50, 100 nm) for the as-deposited at 90 K (AD), the fast cooled from the liquid (FC) and the aged for several times (1,5,15,30 min) at 90 K and 113 K

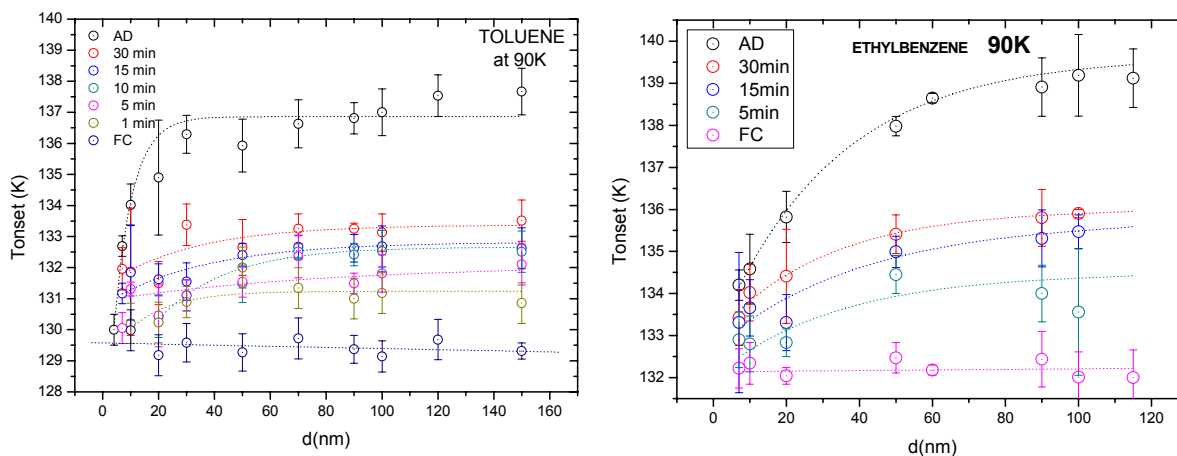


Fig. 4.30: Aging treatments at different times (5,15,30 min) for a 100 nm Toluene and Ethylbenzene films. Tonset as a function of thickness for an aging treatment at 90 K. A reduction for both Ton is observed while decreasing sample thickness. This provides information on the kinetic stability for these glasses as a function of thickness.

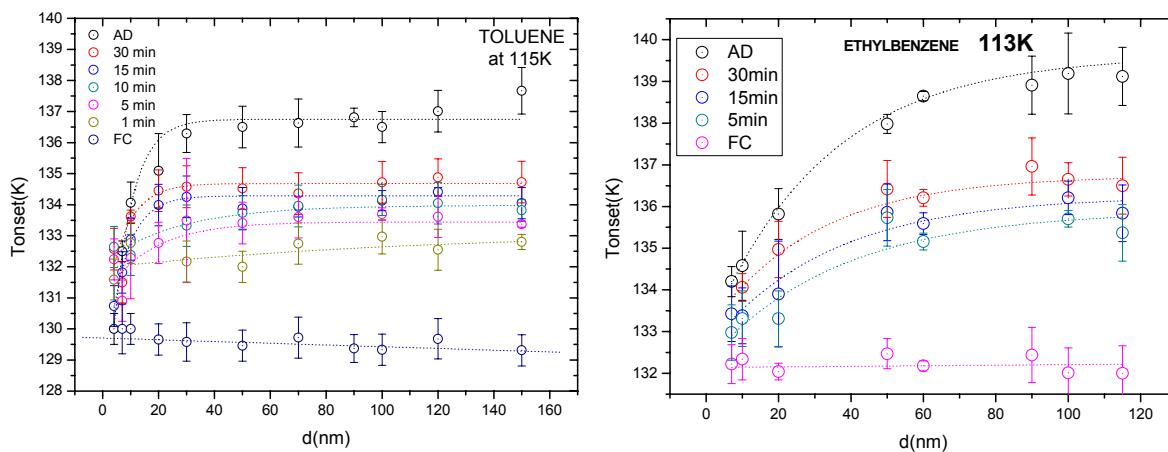


Fig. 4.31: Aging treatments at different times (5,15,30 min) for a 100nm Toluene and Ethylbenzene films. Tonset as a function of thickness for an aging treatment at 115 K and 113 K, respectively. A reduction of Ton is observed while decreasing sample thickness. This provides information on the thermodynamic stability for these glasses as a function of thickness.

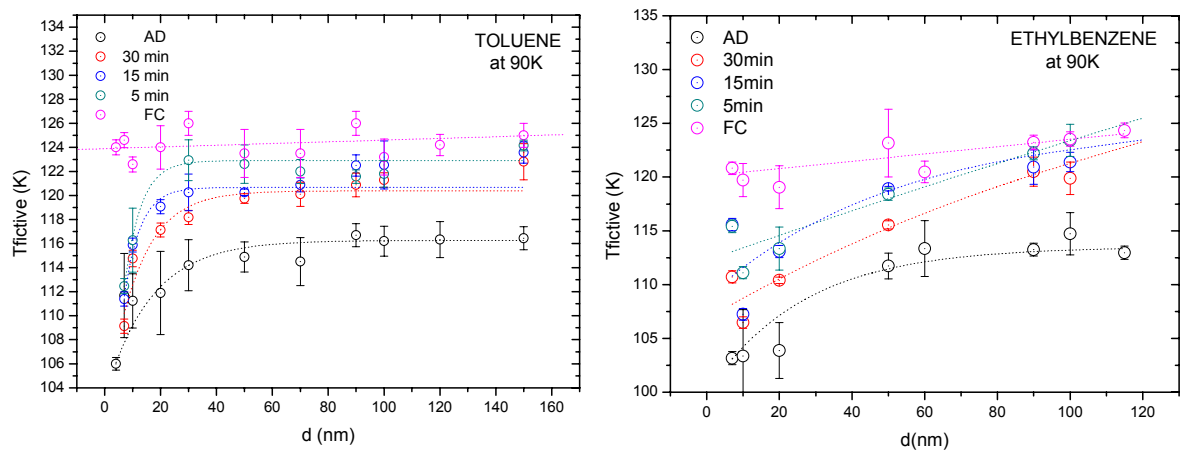


Fig. 4.32: Aging treatments at different times (5,15,30 min) for a 100nm Toluene and Ethylbenzene films. T_{fictive} as a function of thickness for an aging treatment at 115 K and 113 K, respectively. A reduction of T_f is observed while decreasing sample thickness. This provides information on the thermodynamic stability for these glasses as a function of thickness.

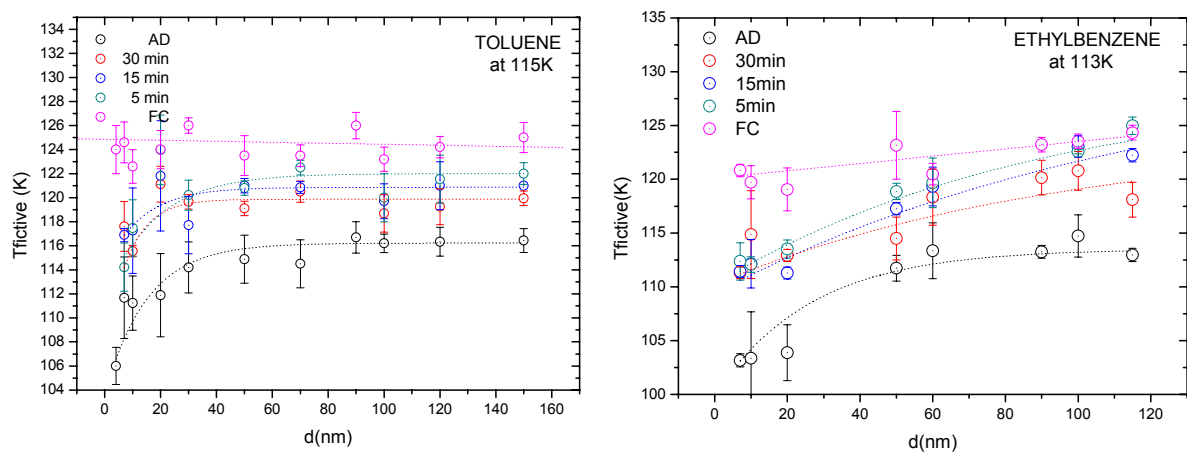


Fig. 4.33: Aging treatments at different times (5,15,30 min) for a 100nm Toluene and Ethylbenzene films. T_{fictive} as a function of thickness for an aging treatment at 115 K and 113 K, respectively. A reduction of T_f is observed while decreasing sample thickness. This provides information on the thermodynamic stability for these glasses as a function of thickness.

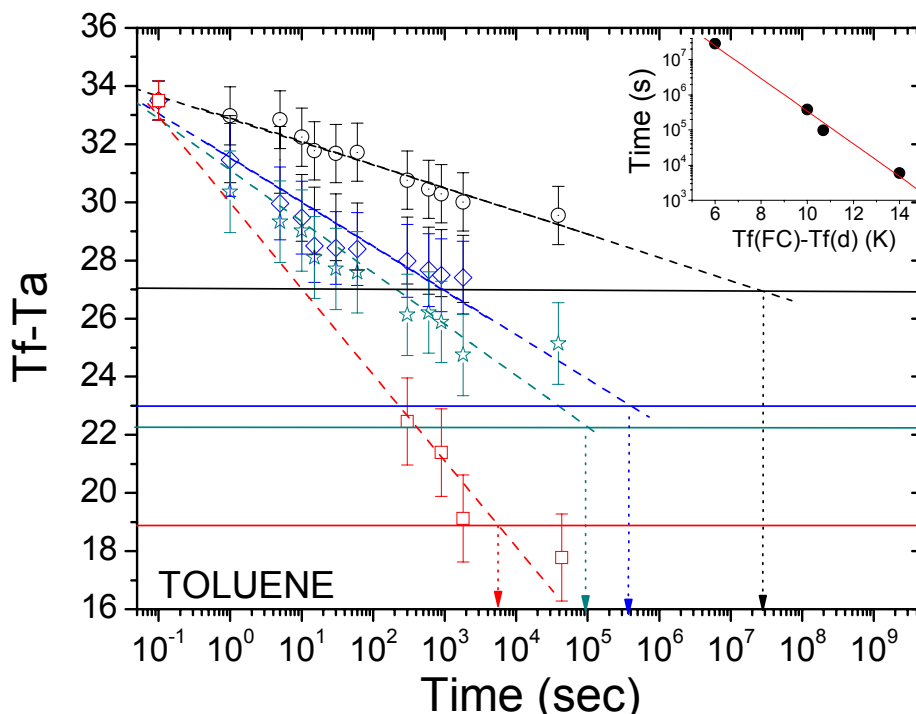


Fig. 4.34: T_f-T_a evolution for $T_a=90$ K as a function of aging time for 7, 10, 20 and 100 nm thick toluene films.

4.4.5 Isothermal aging of bulk organic glasses above T_g of the normal liquid ($T_g=117$ K)

Aging typically requires long times since the associated molecular rearrangements are very slow. Typically, aging of a glass does produce glasses with lower enthalpies, i.e. located in lower minima of the potential energy landscape as we have seen in the previous section. However, traditional aging procedures are unable to attain the high stability of glasses obtained directly from the vapor at temperatures close to T_g [15,57,63]. In this section we show that super-accelerated aging may occur when a seed of the stable phase is present in the initial glass. To our knowledge this is the first time that this mechanism of stabilization has been reported and may be important for the production of more enhanced glasses by fast quenching the liquid and further stabilization by a seed of the stable phase that will accelerate the transformation of the whole

layer. The results presented here are a first step towards this direction and further measurements will need to be carried out beyond this PhD work to exploit the full potentiality of this approach.

We perform annealing treatments at temperatures above the glass transition of the conventional liquid ($T_g=117$ K) to follow the kinetics of the transformation of the highly stable glass into the supercooled liquid. The thickness dependence of the transformation rate suggests a transformation mechanism that differs from what it is usually considered in normal glasses. More importantly, we show that it may be possible to recover the highly stable glass in a sample that has gone through a partial transformation in a reasonable time scale of hours. The kinetics is highly accelerated compared to aging a conventional glass in the same conditions. The remnant fraction of the stable glass in the mixed glass acts as a seed for subsequent growth of the stable phase.

Films of toluene and ethylbenzene are grown from the vapor at a temperature of 90 K and a growth rate of 0.2 nm/s. These conditions have been previously shown to produce very stable glasses with enhanced onset and reduced fictive temperatures, an indication of higher kinetic and thermodynamic stability compared to glasses obtained from the liquid [53, 66]. The thickness of all the glassy films analyzed in this report is around 100 nm, which is sufficient to neglect size effects since they behave as bulk glasses [63].

The thermal history of the samples undergoing structural recovery is the following: i) growth from the vapor at 90 K, ii) annealing at $T=122$, 124 or 128K for times ranging 1-600 min, iii) cooling down to 90 K by passive cooling, i.e. 1000 K/s, iv) fast scanning to record the calorimetric trace, i.e. the calorimetric traces reflect the state of the glass after partial structural recovery of the stable glass and fast cooling to 90 K.

Partially transformed glasses that have followed steps i and ii are aged below T_g , at 90 K, to analyze the evolution of the fictive and onset temperatures. Figure 4.35 shows heat capacity curves obtained by isothermal annealings performed at $T=122$, 124 and 128 K, above the nominal T_g of the normal liquid ($T_g=117.5$ K) and their corresponding mass transformed fraction represented by the area peak. This figure shows various remarkable aspects: 1) after annealing for sufficient time above T_g the calorimetric traces show a double overshoot which is reminiscent of a glass state formed by a mixture of two amorphous solids with different onset and even fictive temperatures. The relative area of both peaks after the calorimetric scan indicates the amount of

each local packing arrangement. This way the kinetics of the transformation is followed as a function of time and temperature. Interestingly, annealing at 122 K for 600 min (*fig 4.35a*) does produce a glass which is slightly more stable (higher overshoot and higher onset temperature) than the glass obtained by fast cooling of the supercooled liquid. Annealing at 128 K for few seconds (*fig 4.35c*) does produce a glass which is calorimetrically identical to our standard fast-cooled liquid.

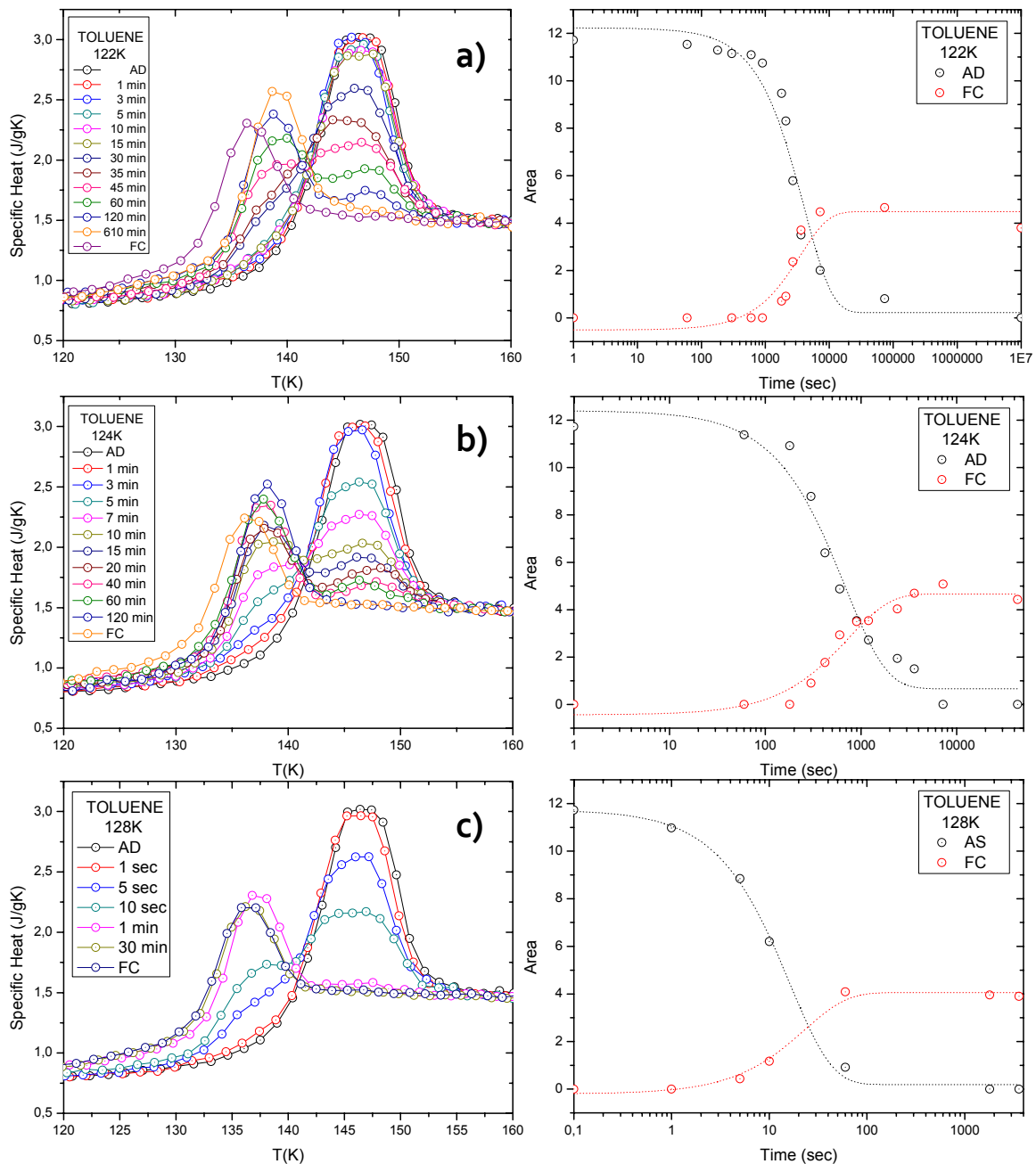


Fig. 4.35: Specific heat versus temperature following annealing at $T=122$ K (a), 124 K (b), 128 K (c) of stable vapor-deposited film. The lines are only guides to the eye.

Since the thermal treatments are performed under isothermal condition above T_g special caution should be placed on the various temperatures since the calorimetric traces are measured at fast heating rates around 30000 K/s. It is worth while to wonder what will be the onset temperature at relatively slow heating rates that permit to correlate with the isothermal measurements. For this purpose calorimetric measurements on both AD and FC thick films are performed at variable heating rates spanning few K/s to 10^5 K/s. In nanocalorimetry at medium-to-fast heating rates the residence time of the sample around the glass transition region is of the order of ms. For the rates used in the present analysis the time needed to go through the glass transition region, i.e. ~ 10 K, ranges from 0.25 ms (at 30000 K/s)-to-40 ms (at 100 K/s). Consequently, for a sample with identical thermal history higher temperatures are required to reach equilibrium at those heating rates. The onset of the glass transition for every given heating rate is plotted and fitted with the Vogel-Fulcher-Tamman equation, as shown in figure 4.36a. T_0 is set equal to 100 K, the Kauzmann temperature [19], and the value of D is 2.85 and 7.95 for the FC and AD glasses respectively. Using this value the estimated fragility for the vapor-deposited (if it can be defined this way) would be around 80, whereas 30 is found for the liquid, a value remarkably lower than those obtained by DS. We note that extrapolation to lower heating rates, 10 K/min, would yield onset temperatures around 114 and 125 K for the FC and AD sample, respectively. So, the annealing temperatures of 122, 124 and 128 K are at T_g+8 , T_g+10 and T_g+14 , respectively. In fact the highest temperature may be above the onset temperature of the vapor-deposited film.

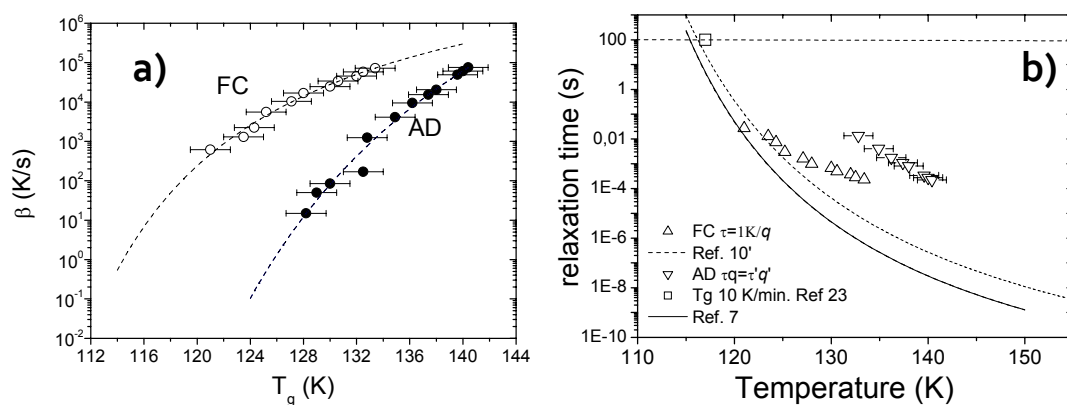


Fig. 4.36: (a) Heating rate as a function of the onset temperature of the glass transition. The dash lines represent fits with the VFT equation. (b) Plot of the relaxation time of toluene versus temperature for AD and FC samples. Continuous line corresponds to data from Döss et al. [7]. The square was obtained from calorimetry at a rate of 10 K/min [23]. Down (Up) triangles refer to AD (FC) samples with relaxation times calculated by the expression quoted in the graph.

A similar relationship, but now using the relaxation time is shown in figure 4.36b. This figure shows that under the present conditions of much faster heating than cooling the calorimetric relaxation times of the two glasses differ from those obtained by dielectric relaxation. The relaxation time is estimated using the relation $\tau q = 100 \text{ s} \cdot 10 \text{ K/min}$, where τ is the relaxation time associated to a heating rate, q . Whether it is certain that our samples show significant hysteresis due to the different heating/cooling conditions, the AD sample may be thermodynamically equivalent to a sample cooled from the liquid at an extremely slow rate.

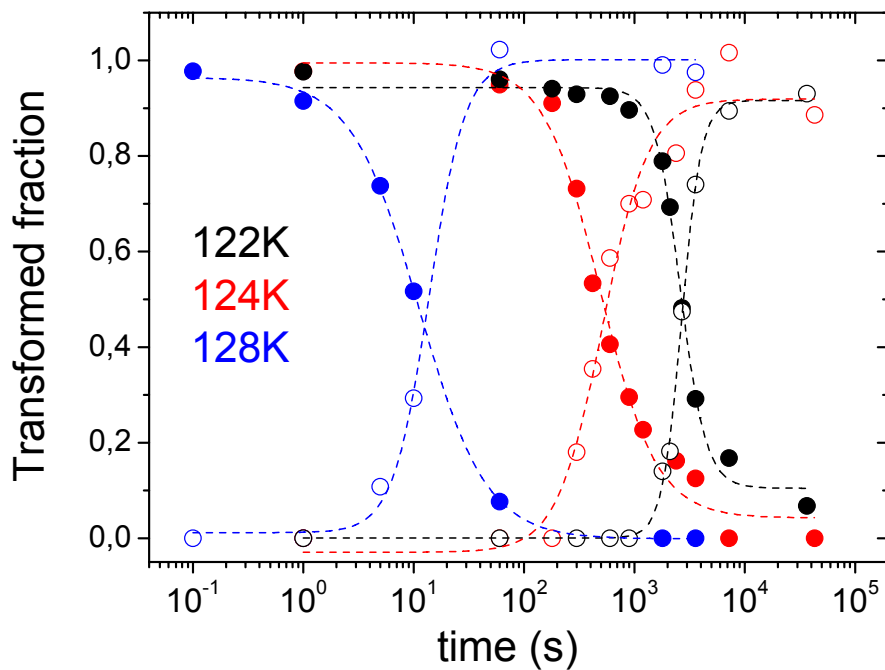


Fig. 4.37: Transformed fraction vs. time of the stable glass into the supercooled liquid (filled symbols) and the corresponding increase of the amount of glass obtained from the supercooled liquid after passive cooling (open symbols) at the three annealing temperatures.

The transformed fraction at the various temperatures and times is shown in figure 4.37. It is estimated from the area decrease of the heat capacity overshoot associated to the glass transition of the vapor deposited films and from the area increase of the peak associated to the sample cooled from the liquid. For sufficiently long annealing times the transformed fraction reaches almost 100 %, i.e. the AD sample transforms completely into a less stable glass through intervention of the supercooled liquid through the following path: Vapor deposited (*highly stable*) ----> SCL ----> Unstable Glass (*Fast-cooled like*). The amount of FC with respect to AD depends on the annealing temperature and time. The experimental data is fitted through the Avrami equation using $x=A*\exp(-(Kt)^n)$, where x is the transformed fraction and K , n are fitting parameters. The parameter n contains information about the transformation mechanism behind the change from the stable glass to the supercooled liquid. For most of the treatments values around 1.0 ± 0.4 are found which may be related to a one-dimensional mode of growth. The time needed to transform the glass is much larger than typically observed in normal glasses. For instance, using the relaxation times obtained by dielectric spectroscopy (*see continuous line below*): at $T=124$ K, $\tau_\alpha=5\times 10^{-4}$ s. The time to transformation of the stable glass is ~ 3000 s which is $10^7 \tau_\alpha$. At $T=122$ K $\tau_\alpha=5\times 10^{-3}$ s, and time to transformation of AD glass $t \sim 10000$ s which is again $\sim 10^7 \tau_\alpha$.

The partial transformation described above can also be very effectively accomplished by short annealings at higher temperatures. Figure 4.38 shows the evolution of the heat capacity curves obtained after 50 consecutive fast scans to every temperature for toluene and ethylbenzene. The total residence time at each temperature ($T-2$ K) is around 100 ms.

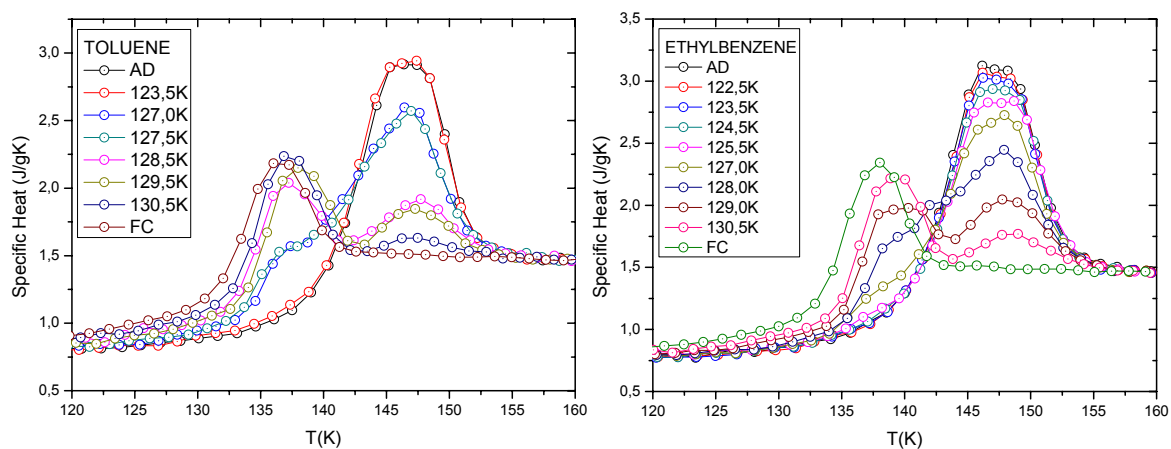


Fig. 4.38: Heat capacity vs. T after 50 consecutive fast scans to every temperature (a) toluene (b) ethylbenzene.

An important finding is that aging towards a highly stable local packing can be extremely accelerated in glasses with coexistence of two different packing arrangements. In fact, aging at 90 K for 11 h of a mixed glass that has undergone partial structural recovery by using pulsed scans to 129.5 K does produce a glass which is closer to the stable glass obtained by vapor deposition. Further aging for 2400 min does increase the amount of stable glass. This is shown in figure 4.39, where treatments of 660 min approaches the onset and the overshoot to the one of the ultrastable glass in comparison to aging of a FC or a SC sample that need months/years to be as effective. Aging for 40 h at 90 K yields the sample even closer to the highly stable vapor. The presence of regions with a more stable packing arrangement (*the one obtained from the vapor*) act as seeds for the transformation of the non-stable liquid. This transformation (*unstable glass --- --> stable glass*) does not involve the liquid and the mechanism may resemble the amorphous-to-crystal transformation in the presence of pre-existing nuclei. We speculate here that using more effective aging temperatures (*around 113 K*) would yield faster transformation kinetics. Finally, we point out that this methodology under the appropriate experimental conditions may provide the route to thermodynamically explore the intriguing existence of a true phase-transition below T_g between the non-stable glass and the more stable glass obtained by vapor deposition. This suggestive hypothesis needs to be confirmed by further measurements at various aging temperatures.

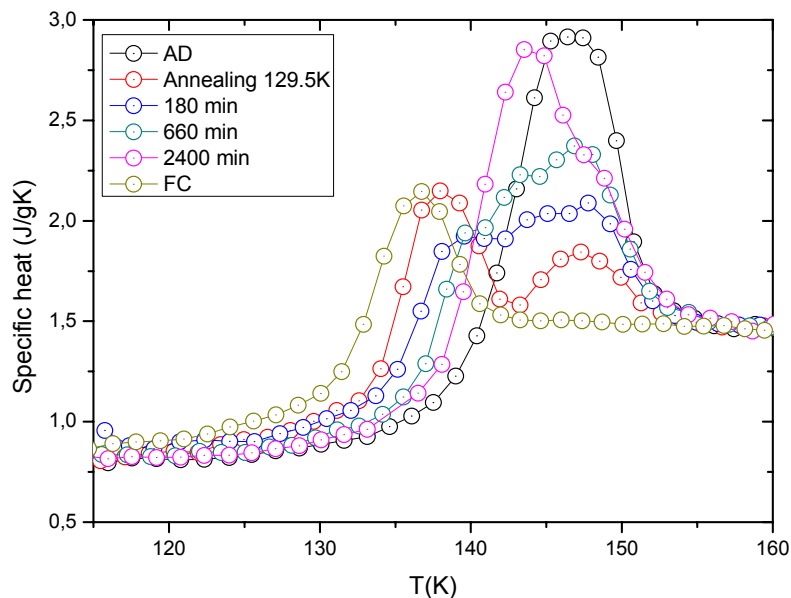


Fig. 4.39: C_p vs. T for i) black circle: as-deposited, ii) red circle: annealing of i) at 129.5K, iii) blue-circle: aging of ii) at 90 K for 180 min, iv) cyan circle: aging of ii) at 90 K for 660 min, v) magenta circle: aging of ii) at 90 K for 2400 min, vi) dark yellow circle: Fast cooled

Chapter V

Amorphous solid water

5.1 General Introduction

Water is one of the most important and omnipresent substances on Earth. Almost every aspect of our daily lives is influenced or controlled by water. Water is one of today's fascinating and important sources for physical scientist since it possesses very unusual properties. At the moment, several simulations and experiments have suggested that water can exist in at least two apparently distinct glass forms, presenting polyamorphism properties. It is also well known that water can exist in many crystalline forms. Up to date, 13 varieties have been identified, some of them stable at certain temperature ranges and other forms which are metastable [1,2,3].

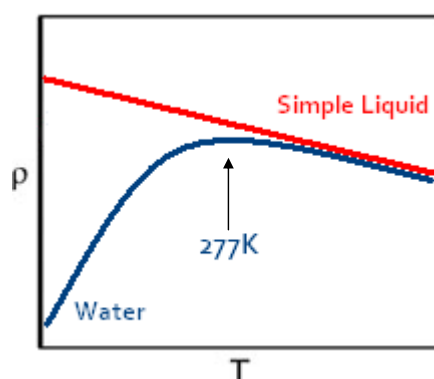


Fig. 5.1: A schematic comparison of the isobaric temperature dependence of the density ρ for water and a simple liquid.

Glassy water may be the most common form of water in the universe. The disordered state of water is formed by the slow accumulation of water molecules from the vapor state onto cold substrates such as interstellar dust which later will constitute the bulk of matter in comets, and plays an important role in planetary activity. [4] However, obtaining this state for further experimental analysis requires complex laboratory procedures. Water irregularities become more well-defined when it is cooled below its freezing point without the existence of crystallization, that is, supercooled water. The process of supercooling a sample is the cooling of a liquid or a gas below its freezing point without it presenting solidification. Pure water normally freezes at 273.15

K but it can be supercooled below this temperature to around 230 K by avoiding any presence of impurities, seed crystals or nucleus that may induce heterogeneous nucleation. However, even though extremely pure water is used homogeneous nucleation causes crystallization below 230 K during slow cooling. Hyperquenching onto very cold substrates can be used to bypass the crystallization barrier and reach the glassy state. This glassy state of water is known as Hyperquenched Glassy Water (*HGW*). Cooling rates above 10^6 K/s are needed to avoid crystallization since the water molecules can not form a crystal lattice due to the reduced amount of time involved in the treatment. Supercooled water exists in a state of uncertain equilibrium which means that minor perturbations can trigger the rapid manifestation of the stable crystalline phase. The basic anomaly of water with respect of other liquids is the anti-correlation between volume and entropy upon cooling [5]. In most simple liquids an increase in volume results in an entropy increase, which means that volume and entropy fluctuations are positively correlated. In water below 277 K the opposite action takes effect, an increase in volume decreases the entropy. The cause of this unusual property is the tendency of water molecules to attract each other strongly through hydrogen bonds forming tetrahedral symmetries in which bond strength and directionality impose a low local density and cause a loss of entropy [6]. Amorphous ice can be considered as the most famous case of polyamorphism. The various forms of amorphous ice are the following:

LDA - Low Density Amorphous Ice

It was the first type of glassy water formed. This type of glassy water is formed either by the accumulation of water vapor molecules onto a cold surface or by hyperquenching of the liquid (*HGW*). Amorphous Solid Water (*ASW*) obtained from the vapor was first produced in the laboratory in 1935 by Eli Burton and W.F. Oliver at the University of Toronto [7]. Today, vapor-deposited thin films of glassy water are typically grown, using molecular beams; on single-crystal substrates at temperatures between 10 and 120 K at deposition rates between 0.1 and 7 $\mu\text{m/h}$. Typical density value for this type of amorphous ice is around 0.94 g/cm^3 , although it depends on the growth conditions.

Direct vitrification of water following hyperquenching was first achieved in 1980 by Peter Bruggeller and Erwin Mayer at the University of Innsbruck using cooling rates of about 10^6 K/s [8]. The process of hyperquenching consists on the vitrification of liquid water by rapid cooling the sample. Both vapor-deposited thin films and hyperquenched samples, after suffering annealing treatments, relax to LDA. There is a consensus in

establishing that annealed ASW and HQW are the same material, called Low Density Amorphous Water (*LDA*).

HDA - High Density Amorphous Ice

This type of amorphous ice was obtained by Osamu Mishima in 1984 by pressure-induced amorphization compressing ordinary ice at 77 K to 1.0 GPa [9]. Typical density value for this type of amorphous ice is around 1.17 g/cm^3 . Notice the approximate 25 % density change between amorphous ice forms (*LDA to HDA*) sufficient enough to consider it an abrupt transition which can also be reversed [10]. In the case of High Density Amorphous Ice (*HDA*) at 77 K it does not relax to its expanded state, but when heated to 120 K forms LDA

VHDA - Very High Density Amorphous Ice

This form of amorphous ice has been proposed as a new form of glassy water due to its higher density value compared to HDA, around 9 % denser. VHDA is obtained by the same procedure for HDA by compressing ice I_h at 77 K up to 1.2 GPa. Once compressed, ice I_h suffers a transition to form HDA. High Density Amorphous Ice densifies further on heating at a constant pressure up to $\sim 165 \text{ K}$. It has also been shown that VHDA can be converted back to HDA after heating treatments to 140 K at starting pressures of 0.02 GPa [11,12]. Typical density value for this type of amorphous ice is around 1.26 g/cm^3 .

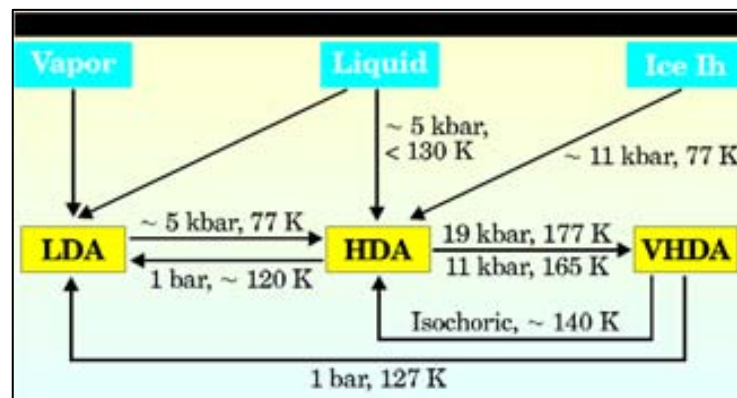


Fig. 5.2: Routes to the formation of low-density (LDA), high-density (HDA), and very-high-density-density (VHDA) amorphous ice. LDA is formed by rapid cooling of water vapour or liquid water, after annealing. It is also formed by heating decompressed HAD or VHDA. HAD is formed by pressure-induced amorphization of ordinary ice (ice I_h), compression of LDA, rapid cooling of emulsified liquid water at high pressure, or constant-volume (isochoric) heating of (VHDA). VHDA is formed by annealing HAD at high pressure. All of these processes are irreversible.

Different types of glassy water or amorphous ice can be obtained by different experimental procedures as shown in figure 5.3. The formation of the various polymorphs is accompanied by huge changes in basic physical properties, such as the density. That is why these different types of glassy water are distinguished principally by their densities. By pressurizing conventional hexagonal ice crystals to 1.6 GPa at 77 K of temperature they convert to HDA ice. Upon pressure release the phase becomes stable. By warming this phase up to 127 K at ambient pressure it converts to LDA ice. Or if the HDA ice phase warms up to 165 K of temperature at 1.6 GPa of pressure and then cooled back down to 77 K it forms VHDA ice. All those amorphous forms have very different vibrational lattice spectra and intermolecular distances. The glassy states differ in structure, as measured by neutron diffraction, x-ray diffraction, and Raman spectroscopy, and in bulk properties, such as density.

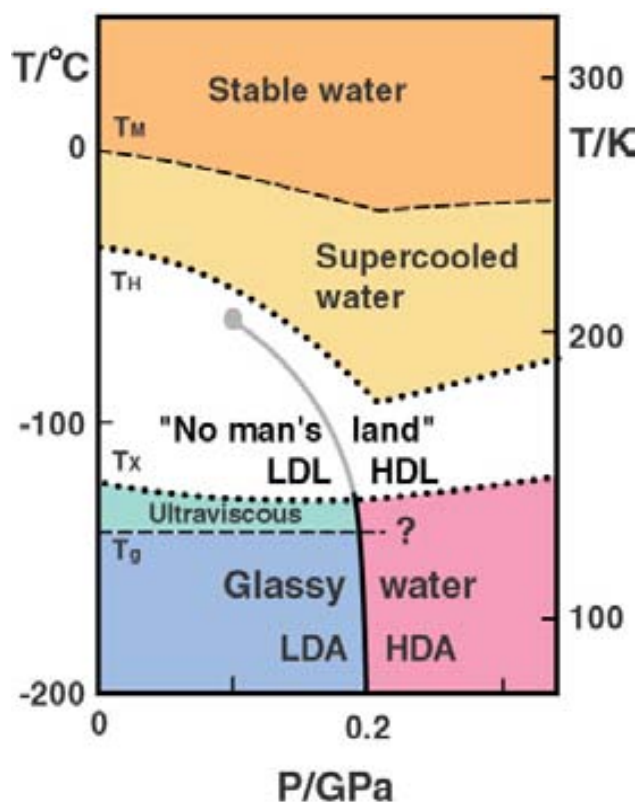


Fig. 5.3: Phase diagram of liquid water. Taken from O. Mishima from reference [10]

Although water has been studied extensively, many properties and processes are still far from being completely understood. The properties of vapor-deposited water films at temperatures below 200 K are still a case where many of the earlier results differ considerably regarding structural phases, phase-transition temperatures and sublimation rates. The large differences in the published data can be explained by the fact that the properties of vapor-deposited ice are very sensitive to the growing conditions including the type of surface used for condensation, nucleation and growth conditions, purity and also the technique in which these films are studied can lead to misinterpretation.

The polyamorphism in water is also yet to be completely understood. Although several studies reveal certain thermodynamic properties for this non-crystalline system, a vast description of water's low temperature thermodynamics does not yet exist. Nevertheless, a clear advance to comprehend glassy water has been developed [5] and turns out to be much closer than it was thirty years ago. Further investigation will require sophisticated combination of existing techniques.

5.1.1 Crystallization: nucleation and growth

Crystallization of amorphous materials is of wide interest from a fundamental and practical point of view. In particular, crystallization of ASW is of significant relevance in various fields. It plays an important role in the offgassing of volatiles trapped in cometary and interstellar ice. In cryobiology the stability of glassy water is also important since it is used as a cryoprotectant and an implanting material for electron microscopy where it is necessary to preserve the amorphous state to prevent damage to cells and tissues attendant to crystallization of the glass. However, water is not a good glass former and the crystallization of water is unavoidable unless the sample dimensions are undersized enough and the cooling rate is extraordinarily fast.

As the temperature of an ASW sample is raised above 150 K, the sample crystallizes to cubic ice [27]. We can state that the temperature obtained with conventional DSC or TPD¹ experiments of the fast crystallization of ASW ($T \geq 160\text{K}$) and the temperature of catastrophic freezing of supercooled water ($\sim 228\text{K}$) mark the borders of the temperature region denominated "No Man's Land" (see figure 5.3), where experimental analyses of amorphous water seem to be unreachable [3]. An important statement will be that the lower temperature boundary of the "No

¹ TPD = Temperature Programmed Desorption

Man's Land" region seems to be limited only due to experimental setup capabilities, that is, the heating rate applied by the instrumentation. The kinetics of crystallization of ASW has been investigated by several researchers. Crystallization is very sensitive to the specific experimental conditions used to obtain ASW, therefore studying the crystallization kinetics of thin amorphous ice has been considered a way to attack this conduct by analyzing temperature influence in desorption kinetics, deposition temperatures, variety of non-epitaxial surface substrates, water mobility, etc. The crystallization of ASW thin films can be initiated at the surface, in the bulk or at the interface with the substrate. The molecule interaction with ASW surface depends critically on the surface morphology (*crystalline or amorphous*). Many studies devoted to crystallization have concluded that the transformation proceeds through a homogeneous nucleation and isotropic growth of crystallites [16,33]. On the other hand, it has been proposed that the hydrogen bond rearrangement required for crystallization may occur more easily for the less coordinated water molecules at the surface [31]. Thermodynamic arguments also exist for nucleation occurring either at the water/vacuum surface or at the substrate/water interface. More recently Backus et al. [28] have demonstrated, by monitoring the water crystallization kinetics of the bulk and surface using Reflective absorption infrared spectra, that the crystallization of thin films starts at the surface (*water/vacuum interface*). For relatively thick films (*>100 ML*) the probability of bulk crystallization will be larger, simply because a large volume is available. Several studies have focused their attention on the nucleation and growth rates involved in this transition covering a wide range of sample thicknesses. The activation energies reported for the crystallization process are somewhat dissimilar. Dohnálek and co-workers [33] have studied the kinetics of thin ASW films deposited on crystalline ice and Pt(111) substrates. They have observed a dramatic acceleration of the crystallization rate in ASW thin films below 10 nm supported on crystalline ice. Activation energies for growth and nucleation were 56 and 140 kJ/mol, respectively. On the other hand, the activation energies reported for the crystallization ranges from 39 to 77 kJ/mol in other studies [33,34,35]. Lögfren et al. and Smith et al. have observed a slowing down of the transformation rate for samples below 6 nm and a thickness independent kinetics for films above 18 nm [29,32]. In contrast, the crystallization rate accelerates with increasing thickness on samples between 55 to 385 nm deposited on Ir(111) substrates. This study showed good agreement with a simple geometrical model of surface crystallization [31]. The disparity of results shows evidence of the uncertainty in the explanation of thickness-independent crystallization kinetics and the sensitivity in preparation conditions regarding deposition rates and substrate surfaces. Rapid deposition of water on very cold substrates (*< 120 K*) shows the possibility to obtain amorphous ice films with low density and high porosity [27].

Simulations may help to understand glassy water, however water is considered to be very challenging to simulate due to the fact that it is a molecular liquid. At present, there is no precise yet tractable intermolecular potential to be certain of. Some distinct advantages of simulations over experiments are somehow evident. Experimentally it is impossible to study the behavior in the “No Man’s Land”, but simulations have the advantage to provide structure and dynamical behavior in this particular region since nucleation does not occur on the time scale of computer simulations. Although, to pursue the development of good accurate models of structural and dynamic transformation in water to estimate crystallization kinetics, amorphous and crystal sublimation effects, glass transition, requires high-quality measurements that normally are proven to be of great challenge.

We consider that the measured heat capacity as a function of temperature can be written as:

$$C_{p_{experimental}}(T) = M_0 C_p(T) - |\Delta m(T)| C_p(T) + \frac{dm}{dt} \cdot \frac{1}{\beta} (T) L(T) \quad 5-1$$

where M_0 is the initial mass, $C_p(T)$ the specific heat of the ASW or crystalline ice, depending on the measurement scan; $\Delta m(T)$ the mass change from the initial state at a temperature T , (dm/dt) the instantaneous variation of mass, β is the heating rate and $L(T)$ the latent heat of sublimation. The following figure schematically describes the different contributions in the heat capacity of the sample.

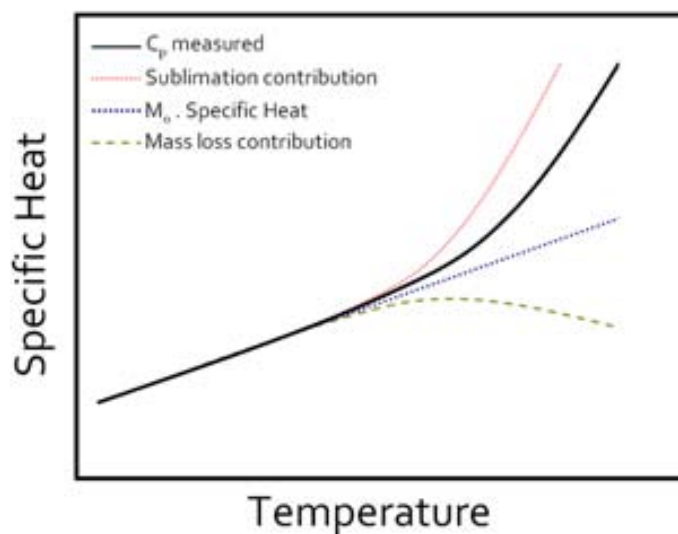


Fig. 5.4: Schematic representation of the different contributions for the C_p experimental data. The measured heat capacity as a function of temperature is expressed in equation 5.1.

This work is considered as an initial study of the crystallization kinetics of very thin film (< 150 BL) ASW samples with nanocalorimetry and also an attempt to explore the glass transition region in the search for evidence of its calorimetric signature. The temperature range to study ASW properties can be extended with adiabatic nanocalorimetry by rapid heating the sample before a significant fraction of ASW has crystallized, i.e. the onset of crystallization can be shifted from 150 K to around 200 K. Also, crystallization dependence with sample thickness can be tackled down to few nm due to the high sensitivity of the technique.

5.1.2 ASW and crystalline ice sublimation rates

Understanding water sublimation is essential to correctly interpret the experimental heat capacity data obtained by nanocalorimetry since sublimation is superposed to other relevant phenomena, such as relaxation, glass transition and /or crystallization. Sublimation rate is highly dependent on the nature of the surface. A detailed experimental work was conducted by Speedy et al. who investigated the evaporation rate of amorphous water and ice near 150 K calculating the residual free energy of the glass and entropy values [30]. Their studies were made on amorphous films, 30-1000 molecular layers (ML) thick, grown onto Ru (001) substrates at 85 K. The films were heated from 85 to 163 K and immediately cooled back to 85 K. Sublimation was monitored by desorption spectroscopy experiments (TDS) which are often the method of choice to determine sublimation effects as a function of temperature. These authors showed that the

crystalline phase sublimates at a lower rate compared to the glassy state at a given temperature, as illustrated in figure 5.5. The desorption rate from amorphous solid water is approximately twice that of crystalline ice. The activation energy of sublimation for the amorphous and crystalline phases are 46.15 and 48.15 kJ/mol, respectively.

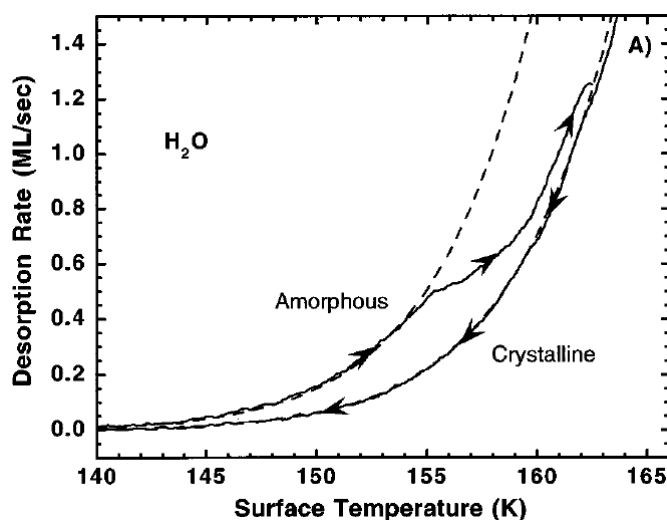


Fig. 5.5: Desorption rate from 100 ML thick films of amorphous water as they are heated and cooled at a rate of 0.6 K/s. The dashed lines are Arrhenius fits to the desorption rates. This figure is obtained from ref [30].

With the slow heating rates involved in Speedy study, the crystallization temperature was noticeable in the 155 to 165 K range. As the amorphous sample evolves with temperature its desorption rate will approach the one of the crystalline phase. In a previous investigation the sublimation rates of the amorphous and crystalline state were analyzed by Baragiola and co-workers who also showed that amorphous films have higher sublimation rates than crystalline ice [35]. They also demonstrated experimental and analytically that sublimation rates for both states are independent of the heating rate.

Modeling of the crystallization kinetics of the films depending on the thickness and heating rates require precise calorimetric scans to analyze that transformed fraction and understand the underlying mechanism that governs it. Since sublimation is highly endothermic

and becomes relevant around 170 K, it significantly affects the crystallization exotherm which develops at higher temperatures (200 K). Therefore, the precise determination of heats of crystallization for the different films requires previous careful analysis of the evaporation rate as a function of temperature.

5.1.3 The glass transition in water

Up to date, a debate is still open on whether ASW melts into a metastable liquid before crystallization or if it crystallizes directly from the amorphous phase. Figure 5.6 shows calorimetric traces for different amorphous water prepared by different conditions. The general view in the scientific community is that the onset temperature for the glass transition for vitreous water occurs at 136 K for ASW (*amorphous solid water*) and HQG (*hyperquenched glass*) analyzed by direct calorimetry and extrapolation of T_g data from glass forming binary solutions (SiO_2 , BeF_2 and $ZnCl_2$) [14,15] and from observed thermal effects [16]. Although this value can be considered to be somewhat suspicious since the glass transition has been either not found whatsoever [17,18,19] or evidently seen [20,21]. Although different values of T_g have been reported following distinct experimental procedures with resulting values fluctuating from 124 K to 129 K for LDA, the assignment of $T_g = 136$ K was affirmed by analyzing the amorphous phase of water in the temperature range of 140 to 150 K using blunt probe dielectric penetrometry [22] and with the combination with calorimetric studies. This value may be the one-value adopted by the scientific community to work as the basis for several studies; nevertheless there have been some findings which contradict these results [23] and some who demand further and accurate investigations linked to the correct and consistent assignment of T_g value. Angell has implied that water, above 136 K, is still in the glassy state and that remains so until crystallization occurs.

Johari and coworkers established the glass transition temperature in 136 K [36] by using Differential Scanning Calorimetry (DSC) on bulk samples of amorphous water. The crystallization peak was also obtained in the same experiment, with a temperature onset of 150 K. However, later experimental and theoretical works have opened the debate about the assignment of the temperature of the glass transition [26,36,37]. Angell and co-workers defend that the glass transition at 136 K observed by Johari is a "shadow transition" weaker than the real glass transition which would take place at higher temperatures and therefore water above 136 K is still in the glassy state remaining there until crystallization at 150 K. The new assigned T_g value occurs at 165 K, above the onset of crystallization (150 K) giving rise to practical experimental issues.

In order to clarify the real glass transition temperature, and confirming its difference from the so-called “shadow transition”, several indirect methods have been proposed. Angell’s group made a thorough comparative study between glassy water and hyperquenched inorganic glasses. [37] Comparing its behaviour Angell concluded that the glass transition necessarily occurs at a temperature greater than 136 K, and its C_p jump is also greater than the 1.9 J/molK experimentally obtained by Johari [36] (*see Fig. 5.6*) If the crystallization process starts at 150 K, it will prevent the direct determination of T_g , which means that a good strategy to avoid crystallization is necessary. This is the case of simulation studies. Computer simulations of water systems allows the prevention of a crystallization behaviour by applying extremely high heating/cooling rates, in order to observe the existence (or not) of the real glass transition. Giovambattista et al. [37] performed molecular dynamic simulations for a system of $N= 216$ molecules, with periodic boundary conditions and using extended simple point charge (SPC/E) model of water. The simulated heating rates of 3×10^{10} K/s prevent the crystallization of the glasses formed by ultrafast cooling ($\sim 10^{13}$ K/s); the glass transition has been observed at $T_g = 188$ K with a C_p jump of ~ 55 J/molK, which is more than one order of magnitude higher than the value determined by Johari at 136 K. The same simulation also demonstrates the presence of a small peak at 136 K which is assigned to the “shadow glass transition”. Up to this point, one of the main challenges in glass forming liquids is to experimentally observe the T_g of water.

It seems that spatial confinement can be the way to shift or avoid the crystallization. Some studies have been made in ultra thin films of amorphous water [31] and water confined into nano-pores [39]. Adiabatic nanocalorimetry may be a useful technique to analyze the possible existence of the glass transition in water. Due to the large heating rates involved in the experimental procedure (10^4 - 10^5 K/s) and the high sensitivity of the technique which permits to measure phase transitions in ultra-thin films (*only of a few monolayers*).

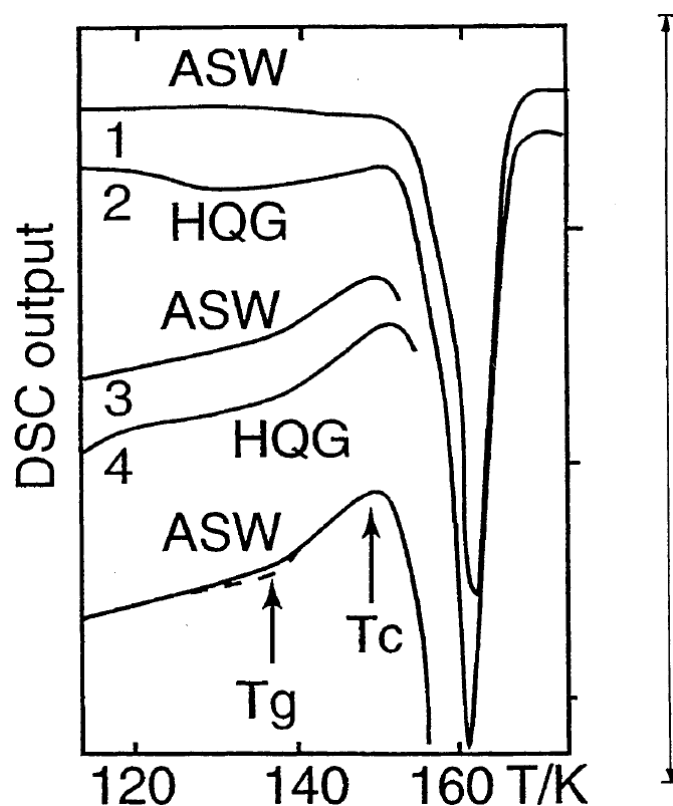


Fig. 5.6: Calorimetric effects on as-formed, and annealed, samples of amorphous waters used as basis for assigning the glass transitions for these materials. ASW (curve 3) is the vapor-deposited form, HQGW (curve 4) is the hyperquenched liquid form, after annealing while curves 1 and 2 are for the as-prepared materials. T_c is the crystallization temperature. Graphic obtained from reference [26]

5.2 Experimental procedure

The basic experimental procedure is analogous to our previous studies on organic glass forming liquids described in section 4.3 of chapter IV. ASW is formed by growth from the vapor at temperatures spanning 90-140 K in a specially designed high vacuum chamber at a partial pressure of 10^{-8} mbar. Amorphous solid water films were deposited on a 180 nm SiN_x support which makes part of the nanocalorimetric cell where heating treatments up to 230 K at 35000 K/s take place. Films from few nm thick up to around 50 nm were grown and subsequently studied by quasi-adiabatic calorimetry.

5.2.1 Thermal treatments on amorphous glassy water

We mainly distinguish two types of samples. The first fast heating scan up to 230 K is performed right after deposition and is named amorphous sample (AS) which provides information of the heat capacity of the amorphous sample obtained from the vapor and its crystallization behavior above 200 K. The heating rates are varied between 15000-35000 K/s. Second and subsequent scans measure the heat capacity of the crystalline state (CS). However, as sublimation starts to be significant above 170-180 K some mass loss is always present between consecutive scans. Therefore for the major part of the analysis only 1st and 2nd scans are considered. At temperatures below 135 K and using fast heating/cooling rates, the sublimation effect of both amorphous and crystalline states is negligible. During data treatment we use a 75-point box averaging to all raw data (*acquired at 1.5 MSamples per second*) to improve the signal-to-noise ratio. Several deposition temperatures were used to prepare ASW in the range of 90-140 K. The schematic illustration of the different thermal treatments using fast heating rates is shown in figure 5.7.

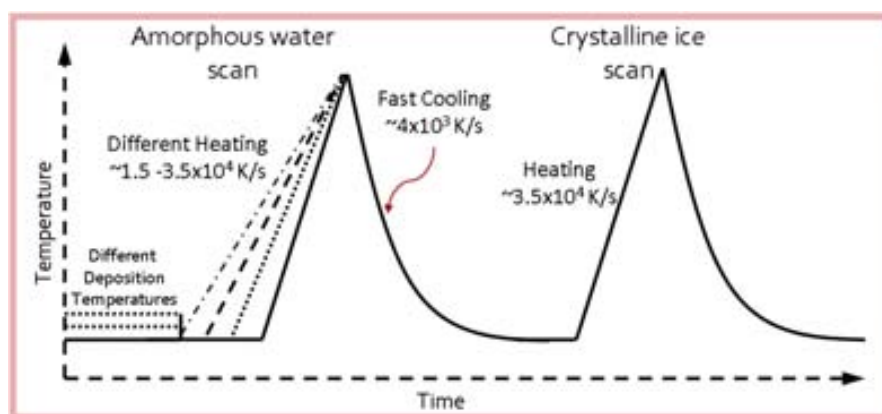


Fig. 5.7: Thermal treatments for the study of vapor deposited thin films. Fast scans performed at different heating rates around $33\ 000\text{K s}^{-1}$ after deposition are named amorphous sample (AS) scan. Samples that are crystallized are named crystalline state (CS) samples.

5.3 Results and discussions

The next figure shows the typical signal obtained from a nanocalorimetric scan of an amorphous water film (ASW) deposited at 90 K. The heat capacity as a function of temperature is determined from the first heat scan following the equation 4.9 (*Chapter IV*). We observe a clear heat capacity drop off at the crystallization region. The apparent increase in heat capacity observed above 220 K is recognized as being caused by the sublimation of the film.

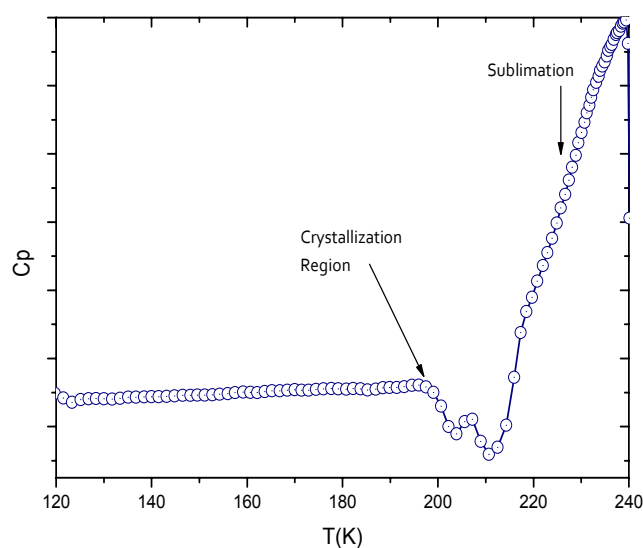


Fig. 5.8: Typical calorimetric trace for the crystallization of amorphous water films. At around 200K an exothermic peak indicating the crystallization is observed followed by the rapid desorption.

The onset temperature of crystallization is increased to near 200 K, as observed in Figure 5.8 much above the traditional value of 150 K. Therefore, the rapid heating rate permits to perform studies of the thermodynamic properties of ASW at temperatures as high as 200 K. It is also possible to study the crystallization kinetics of different films in a temperature range of only 30 K before sublimation effects become dominant.

5.3.1 Mass estimation

The mass/thickness estimation of the deposited sample is calculated by considering that the specific heat of the films is similar to the bulk, by simply dividing the heat capacity of a given T to the specific heat at this temperature (*equation 5.2*). Because the deposition area is well characterized through the use of shadow masks in close proximity to the substrate, the thickness of the film can be inferred from the mass estimation.

The clear evidence of these films is that they crystallize around 200 K which would clearly indicate an amorphous initial state of the sample. We assume that the initial state is 100 % amorphous. This value will be confirmed later. By experimentally measuring the heat capacity obtained for our samples at 125 K we estimate the thickness following the equation:

$$Thickness = \frac{Cp_{exp}(125K)}{Cp_{lit}(125K)} \cdot \frac{1}{\rho \cdot A} \quad 5.2$$

where A is the active area dimensions of the calorimetric cell (0.01 cm^2); the density ρ and the heat capacity Cp are obtained from the following table.

	Density gr/cm ³	Cp J/mol K
ICE	0.50	38
ASW	0.94	19.78

Table 5.1. Values used for the thickness calculations of the as-deposited samples.

5.3.2 Crystallization kinetics

Figure 5.9.a shows the heat capacity measurements of ASW samples with different thickness. The changes in the heat capacity data clearly indicate that crystallization behavior depends on film thickness. For films above 10 nm two exotherms are clearly resolved, however for films below 10 nm only one exothermic peak is visualized. Because the high heating rate (30000 K/s), the crystallization and desorption of water do not occur until above 200 K. The thinner the film, the crystallization peak shifts to lower temperatures while the second peak disappears. The onset of crystallization changes from 194 to 200 K, for thicker and thinner films respectively. These values should be analyzed with caution due to the different heating rates associated to every thickness (*see fig 5.9a.*) Figure 5.9.b shows the calorimetric traces for the corresponding crystalline samples in which only the desorption associated to the crystalline state is present. The absolute heat capacity of the crystalline sample may be somewhat lower than the one measured for the initial amorphous film, not only because their structural difference but mainly due to some mass loss during the first heating/cooling process.

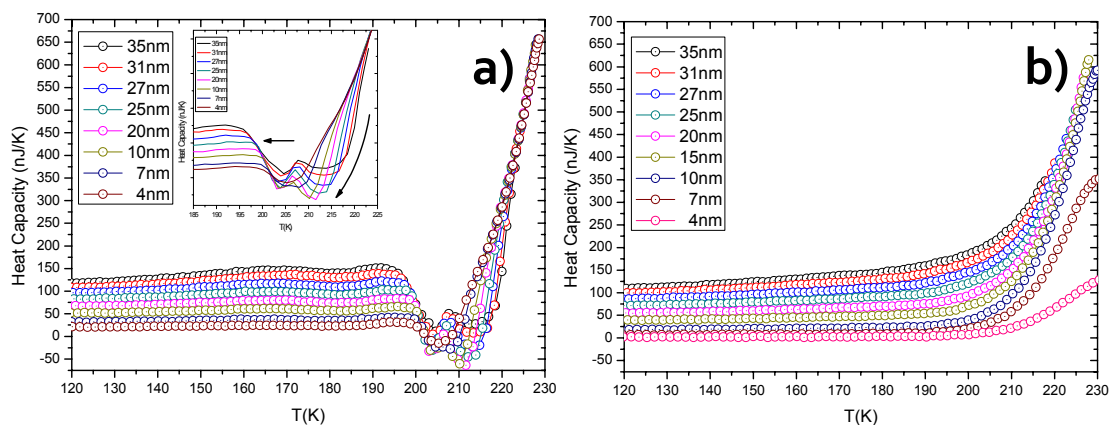


Fig. 5.9: (left) Heat capacity of the amorphous solid water obtained from the first calorimetric scan in which we observe a crystallization peak superposed to a heavy endotherm related to sublimation. (right) Heat capacity data of the crystalline phase obtained from the second calorimetric scan. The exponential rise of C_p is due to water sublimation.

The following figure shows the heating rates as a function of temperature for the different layer thickness. The heating rates vary because of the different sample masses. In fact, as will be shown later the variation of the onset temperature with thickness can be mainly attributed to the variation in heating rate at the onset of crystallization. Although a change in the

initial heating rate is observed, an approximately constant value of 32000 K/s was reached during the crystallization process.

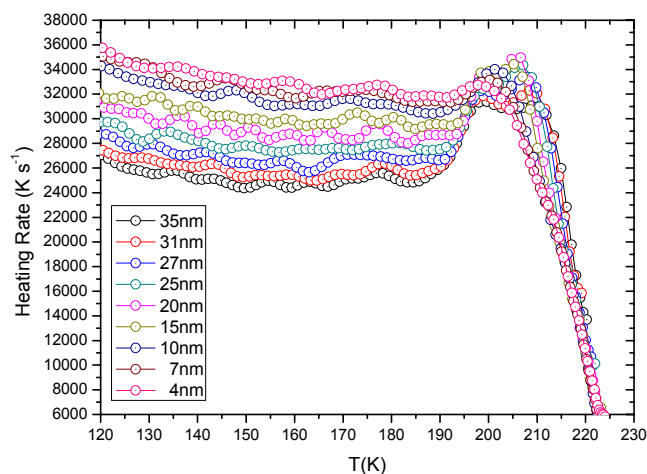


Fig. 5.10: Heating rates for different sample thicknesses as a function of temperature. An increase in heating rate is observed in the crystallization zone due to its exothermic reaction supplying heat to the calorimetric cell.

The heat capacities of the amorphous and crystalline phases are directly independent of the heating rate. In this case, they suffer an indirect correlation with this parameter since they are dependent of the sample mass at a time t , thus a change in heating rate, heat capacity and crystallization temperatures will be present and will have to be taken into account. The loss of mass in every scan also produces a change in the heating rate since for the same induced current the presence of a lower thermal mass is accompanied by an increase of the heating rate. Therefore, if the entire calorimetric scans are made at the same current pulse value (35 mA for $\sim 2\text{ ms}$) we will observe a sequence of heating rates that increases until the limit of the heating rate for an empty calorimeter.

Once the values of mass have been estimated we proceed to obtain the heat of crystallization involved in the transition for the various thicknesses. We first estimate the total mass of each sample and from it we evaluate the thickness by using the density and the surface area:

$$mass(g) = \rho(ASW) \cdot A \cdot d = 0.94(g/cm^3) \cdot 0.01(cm^2) \cdot d(cm) \quad 5.3$$

Using the relation of $1\text{mol}_{\text{H}_2\text{O}}=18\text{ g}$ we calculate the molar mass of the samples. To estimate the heat of crystallization we use a simplified procedure: the heat capacity of the 2nd scan (*crystal*) is subtracted to the 1st scan to remove the contribution of sublimation to the exponential rise of the heat capacity, as shown in the inset of figure 5.11. The heat of crystallization was easily obtained by integrating the crystallization peak in ΔC_p (nJ/K). Whereas this procedure works well for films above 10 nm, for thinner films the excess heat capacity shows some discrepancies. As shown in figure 5.12, in those films the heat capacity of the crystal (2nd scan) is much lower than that of the amorphous phase with large differences at temperatures above 210 K. It is important to remember that the films lose mass during the heating treatments due to sublimation at the surface and this effect becomes dominant in thinner films. The excess heat capacity ΔC_p (nJ/K) is illustrated in figure 5.11.

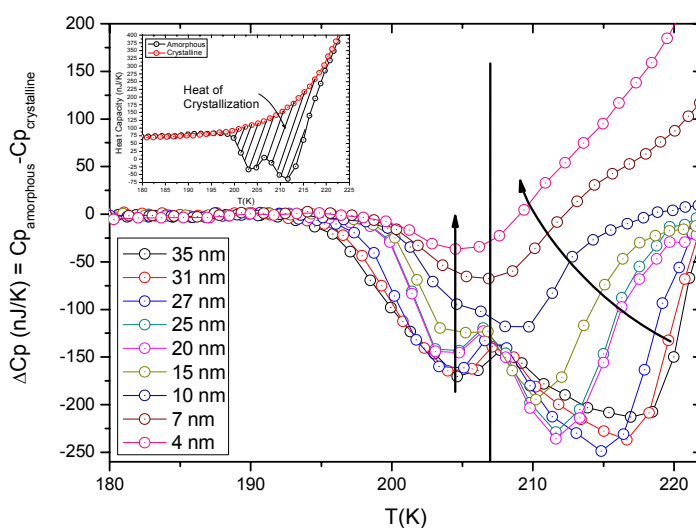


Fig. 5.11: Data analysis for determining the excess heat capacity values from our nanocalorimetric scans. The calorimetric trace of the crystalline sample was used as baseline for the subtraction to the heat capacity of the as-deposited film.

To avoid miscalculation the excess heat capacities for films below 10 nm are obtained by subtracting the scan of crystalline films grown directly from the vapor at temperatures around (160 K). The influence of deposition temperature will be further analyzed below. These measurements will therefore show the heat capacity of the thermodynamically stable, crystalline phase of the same mass proportions compared to that of the amorphous as shown in the next figure.

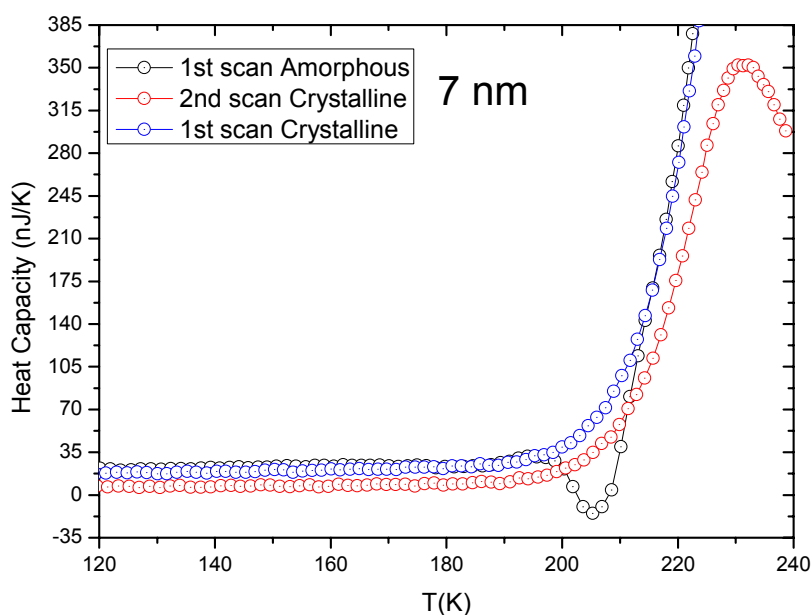


Fig. 5.12: Experimental heat capacity measurements for a) ASW deposited at 90K: 1st (amorphous) and 2nd (crystalline) scan b) Ice water deposited at 160K: 1st (crystalline) scan. Both films amorphous and crystalline grown from the vapour have a matched heat capacity below crystallization.

The measured heat of crystallization of ASW in the temperature range of 195 – 230 K of 2.34 ± 0.20 kJ/mol is consistent with the enthalpy release during crystallization of purely amorphous water grown at temperatures below 90 K [10]. This value is coherent with the fact that the heat of crystallization in this temperature range should be lower than that of liquid water (which is in the order of 4-5 kJ/mol). Figure 5.13 also shows that the crystallization enthalpy of our ultrathin films nicely fits linearly with values obtained for thicker films (above 1 μm) [38] demonstrating the absence of size effects for films down to 4 nm.

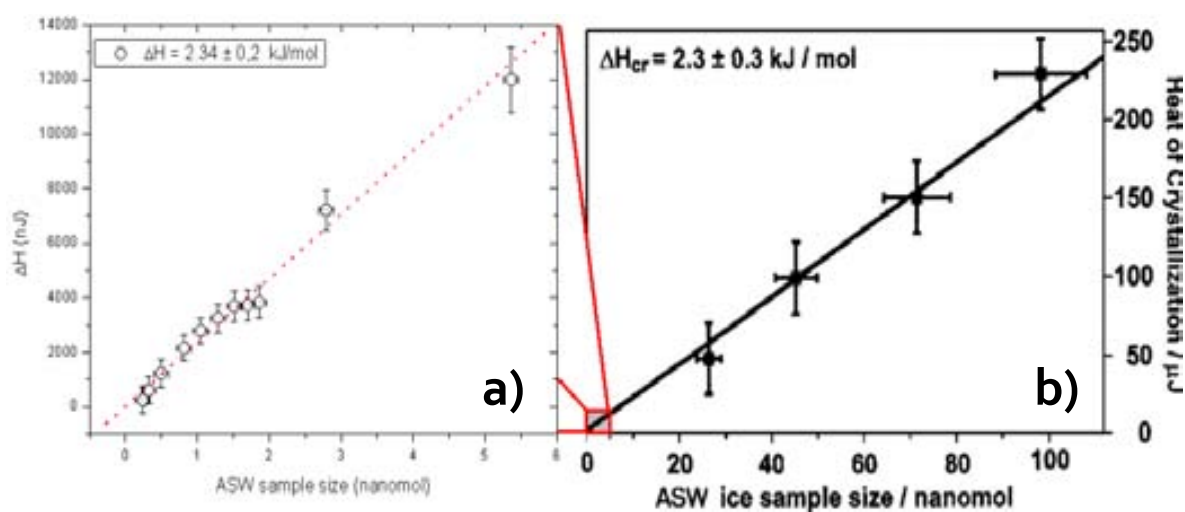


Fig. 5.13: Data resulted from the integration of the excess heat capacity between 195-230K previously obtained and shown in fig. 5.9. The total heat of crystallization is plotted as a function of ASW sample size. a) The resulting enthalpy of ASW crystallization is consistent with enthalpy release during crystallization of purely amorphous ice samples. b) Resulting enthalpy of crystallization for films 1-3 μm thick. Adapted from reference [38]

To gain insight in the crystallization initiation sites for the ASW films in the following figures (5.14 and 5.15) we show in more detail the heat capacity for films from 4 to 35 nm. We note here that these data represent the first thermodynamic set of data on ultrathin films of amorphous solid water. The heat capacity of the films obtained from the vapor at a substrate temperature of 90 K show three different phenomena: i) between 170-190 K an exothermic feature is associated to relaxation of the layer. This aspect will be further analyzed below when discussing the effect of the deposition temperature on the heat capacity curves. ii) At around 195-200 K depending on the heating rate the onset of an exothermic peak related to crystallization, iii) a continuous exponential rise of the heat capacity which is due to sublimation effects both in amorphous and crystalline water.

Concerning crystallization there is a clear change in the shape of the exothermic calorimetric peaks which strongly depends on thickness. Only one peak is observed in the thinnest films while two are clearly resolved for the thickest. The minimum of the first peak appears to be thickness independent but the second shifts to higher temperatures as thickness increases. It is tempting to attribute this behavior to a double nucleation and growth mechanism. A possibility

could be that the first crystalline nuclei appear at the substrate/surface interface and while growing perpendicularly towards the outer surface and laterally a second set of crystals nucleate on the open surface or in the bulk of the layer. This double process will only happen in ‘thick’ films, in the thinnest complete crystallization occur before the second nucleation stage. Extensive kinetic modeling is in progress to identify the nature of the two peaks and the thickness dependence. However, the process has revealed to be quite complex and we still have not a clear explanation.

Sublimation is basically a surface mechanism in which molecules at the surface abandon the solid towards the vapor phase due to the non-equilibrium conditions of the sample (*moderate T and ultra-high vacuum*). The complexity of the phenomena here is that sublimation strongly depends on the amorphous/crystalline nature of the sample as already shown in section 5.1.2, more specifically on the structural nature of the surface.

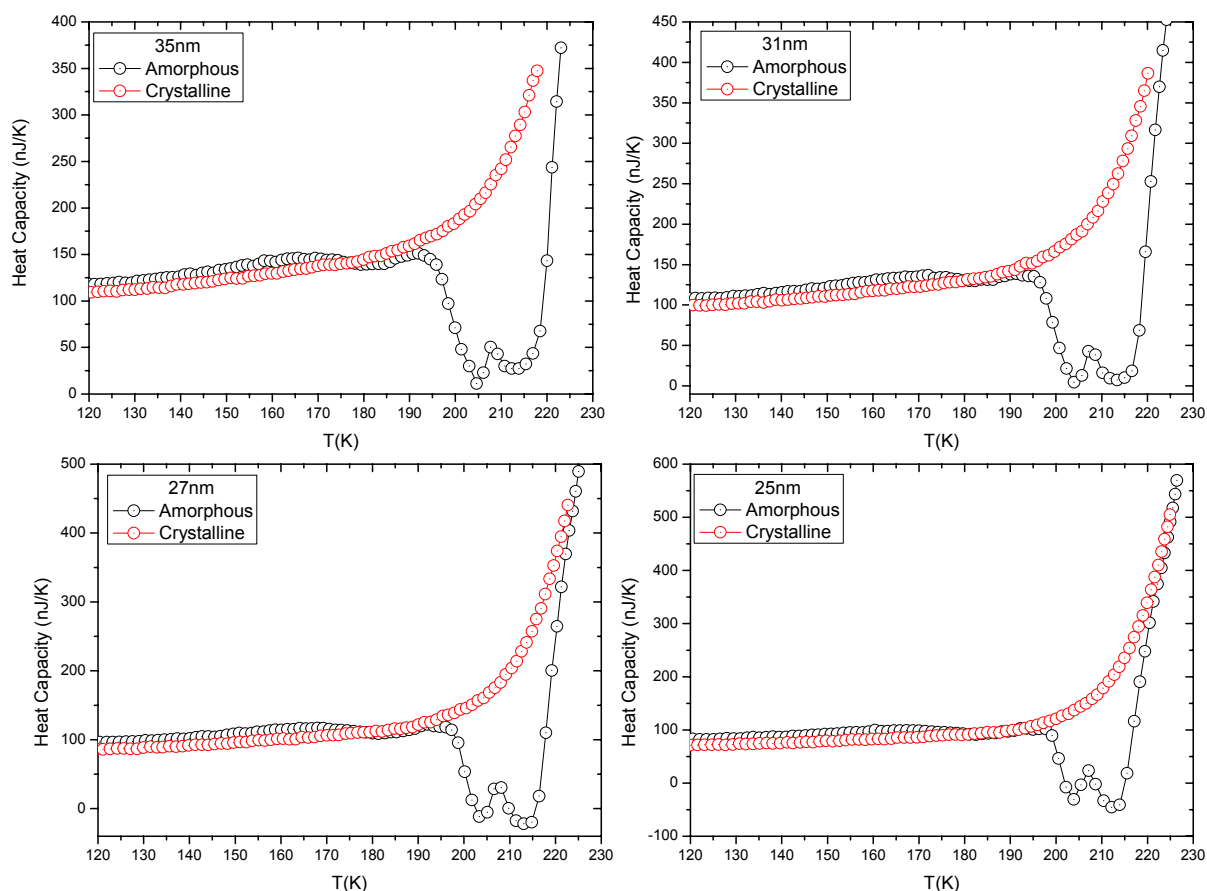


Fig. 5.14: Heat capacity data obtained from first and second calorimetric traces corresponding for the amorphous and crystalline states for samples of various thicknesses.

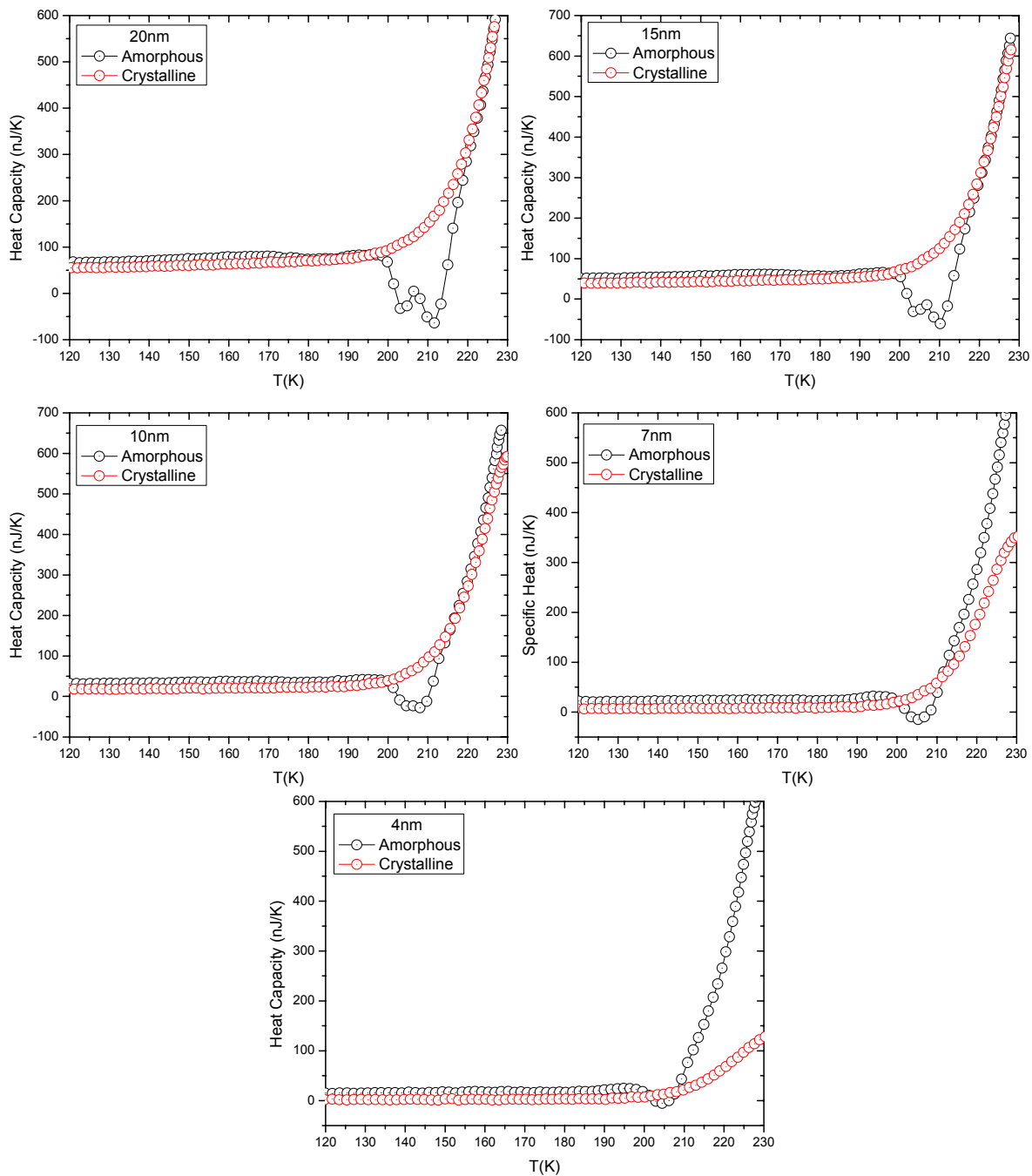


Fig. 5.15: Heat capacity data obtained from first and second calorimetric traces corresponding for the amorphous and crystalline states for samples of various thicknesses

The deposition temperature has a pronounced influence on the morphology of the layers. Growth temperatures were varied from 90 K to 160 K by applying variable current input into the resistive heater. The temperature is monitored by a PID controller, which applies the necessary corrections while the deposition process takes place to avoid any temperature oscillations. Depositing water vapor onto cold substrates below 120 K results in highly strained ASW, which presents a broad enthalpy relaxation peak in scanning calorimetry experiments at temperatures below the crystallization region [26]. Increasing the deposition temperature leads to noticeable changes in the heat capacity evolution of the amorphous sample. The ASW samples that were deposited at low temperatures showed the presence of the broad exothermic peak which preceded crystallization. This exothermic feature clearly evolves and vanishes at sufficiently high deposition temperatures. Figure 5.16 represents the heat capacity as a function of temperature for samples grown at several temperatures. It has been already demonstrated that strained ASW strongly depends on its thermal history and preparation conditions [27]. We can attribute peak A to the enthalpy relaxation of strained ASW nanometer films which appears in films grown below 120 K. When the deposition is carried out in the range of 120 - 135 K the molecules have enough surface mobility to improve its packing arrangement and no relaxation is apparent in the C_p data. Summarizing, thin films deposited between 90 - 120 K can be identified as non-relaxed glassy films whereas films grown between 120 - 135 K are relaxed ASW, i.e. LDA.

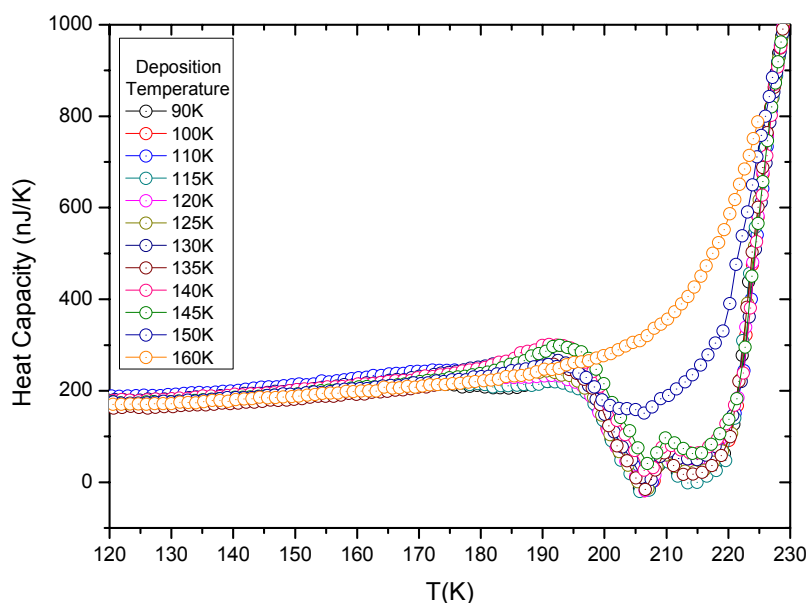


Fig. 5.16: Heat capacity as a function of temperature for a 25nm ASW sample deposited at different temperatures. A change in a first behaviour before crystallization is observed. This effect is designated to the relaxation of the film at temperatures around 150K

Films grown between 135 - 140 K exhibit an anomalous behavior. We consider that the samples are of similar thickness since the apparent heat capacity in the region below 140 K yielded a ± 1 nJ/K difference. This small disparity should not yield significant changes in the heat of crystallization for the samples. Similarly to films grown at slightly lower temperatures there is no evidence of relaxation effects, however interestingly an endothermic feature appears prior to crystallization. In figure 5.17 we show an enlarged heat capacity figure with values for films grown at 90 K, 140 K and 160 K; the change between the amorphous samples grown at 90 K and 140 K is made obvious. This effect will be further analyzed below in section 5.3.3. On the other hand, films deposited at temperatures above 145 K show a reduced crystallization exotherm. The higher the temperature of deposition the lower is the heat release, which is related to the amount of crystalline phase in the as-deposited layers. Above 160 K all the layers crystallize during growth from the vapor and no sign of crystallization is observed in the Cp curve.

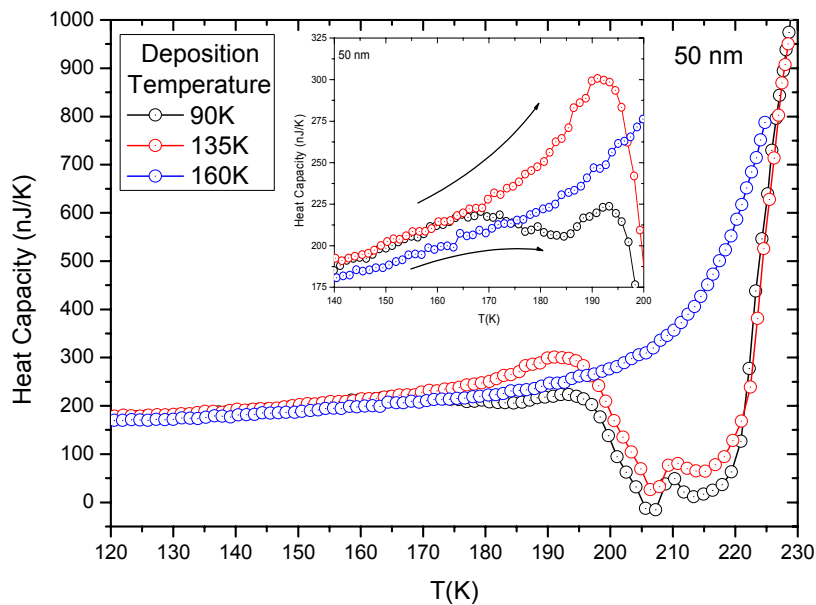


Fig. 5.17: Heat capacity as a function of temperature for a 25nm ASW sample deposited at different temperatures 90K, 140K, 160K. A change in a first behaviour before crystallization is observed. This effect is designated to the relaxation of the film at temperatures around 170K

With the aim to implement the modeling of the calorimetric signal various upscans at heating rates from 15000 to 38000 K/s for a 25 nm film deposited at 90K were realized. See figure 5.18. There are several points that deserve attention: i) The temperature onset of the crystallization is shifted to lower temperatures with slower heating rates as it may be expected

from any thermally activated process, (Fig. 5.19). ii) The crystallization region changes with the heating rate and more importantly for slower rates only one crystallization peak is observed while two peaks are visualized for faster heating rates. We have to note that the growth conditions and the deposition surface area are identical for all films. The only variable that changes is the heating rate. Unfortunately, a direct comparison with the crystallization performance of water at slow heating rates may not be possible to clarify the behavior at ultrafast heating rates.

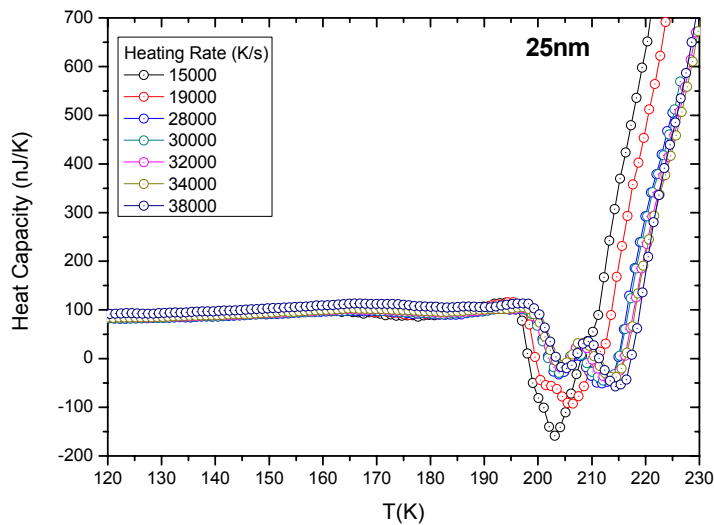


Fig. 5.18: Heat capacity as a function of temperature for a 25nm ASW sample deposited at 90K and measured at different heating rates. A shift of the crystallization peak to lower temperatures is observed. For slower rates the presence of a second peak in the crystallization is not observed.

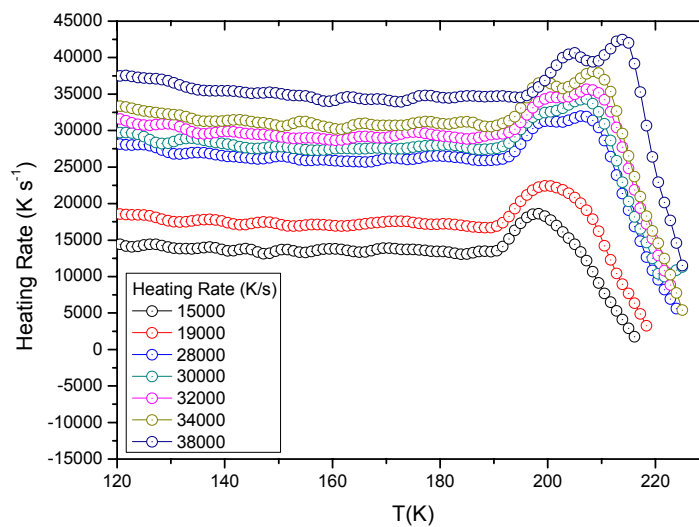


Fig. 5.19: Heating rates as a function of temperature for a 25nm ASW sample deposited at different temperatures 90K, 140K, 155K. A shift of the crystallization peak to lower temperatures is observed. For slower rates the presence of a second peak in the crystallization is not observed.

In figure 5.20 we illustrate the behavior of the films as a function of temperature for the different heating rates. We observe that the relaxation of the films is present independently of the heating rate employed for the upscan. The onset temperature of crystallization is reduced decreasing the heating speed. If we take into account the contribution of the heat capacity of the amorphous layer and the contribution of the sublimation to the experimental heat capacity all heating rates overlap giving the same curve within 10%. This behavior confirms that sublimation is independent of the heating rate as previously stated by other researchers in the field [35].

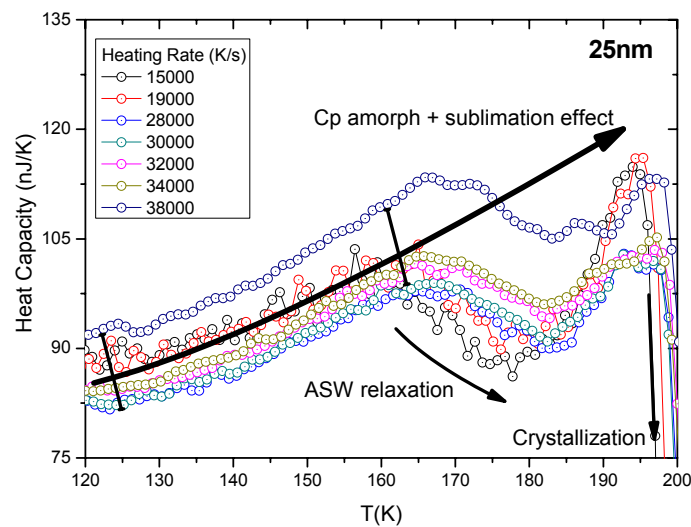


Fig. 5.20: Heat capacity as a function of temperature for a 25nm ASW sample deposited at 90K and measured at different heating rates. The representation of the sublimation effect of the amorphous state, the relaxation of the sample and the start of the crystallization is illustrated in the figure.

We use the Kissinger equation to estimate the activation energy of the first crystallization process. The Kissinger equation can be written as

$$\ln(T^2 / \beta) = \ln[E / (vR)] + [E / (RT)] \quad 5.4$$

where E is the apparent activation energy, R is the universal gas constant, v is the frequency factor, T is the characteristic temperature, and β is the heating rate. The equation shows a linear relationship between $\ln(T^2 / \beta)$ and $1/T$, whose slope is E/R . The equation is usually used to

estimate the apparent activation energy of glass transition and crystallization. Though the Kissinger equation was developed for the peak temperature, T_p , it is mathematically applicable to the onset crystallization temperature, T_x . The derived value from fig. 5.20b is 80 ± 2 kJ/mol, which is comparable to the activation energy value of 75 kJ/mol reported by Löfgren and coworkers [29] on thin amorphous water films deposited on Pt (111) substrates. The result that we have obtained is also close to the one published by Smith et al. [32] who yielded a value of 84 kJ/mol and also demonstrated Arrhenius-like behavior with a substrate independent activation energy for crystallization of thin films of ASW using Au(111) and Ru(001) substrates.

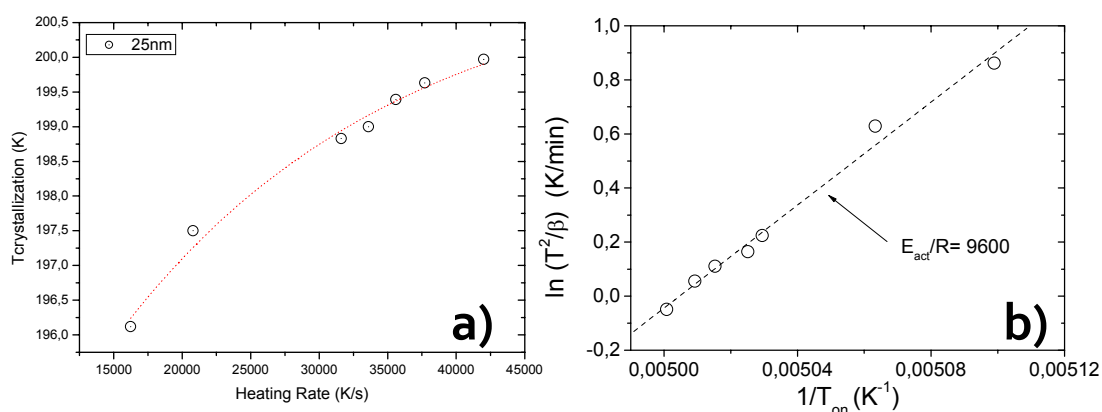


Fig. 5.21: (left) Temperature onset of crystallization as a function of heating rate. A shift to lower temperatures is observed while the heating rate is diminished. (right) Kissinger plot of the onset temperature.

A change of about 4 K of the onset temperature of crystallization was observed in the change of heating rate. This result confirms that the main temperature variation observed for the onset temperature in films of different thickness (*figures 5.9 and 5.11*) is attributed to the change in heating rate and not size-effects in relation to crystallization.

5.3.3 Glass transition in amorphous water

As briefly stated in the introduction the glass transition temperature in water is a matter of debate. In the case of the very thin films used in our study the presence or not of an endothermic feature that may be assigned to a transition between the glass and the supercooled liquid may be hindered by the appearance of the broad relaxation feature in some of the films and

by the superposition of the sublimation which is heavily endothermic. To find a clear path to distinguish the existence or not of the glass transition we will compare the nanocalorimetric data with analytical expressions that take account the sublimation process in the films.

For this purpose we use the ASW films deposited at 135 K in which we have previously demonstrated the absence of relaxation effects (*see figure 5.16*). Those glassy films can be considered a form of LDA.

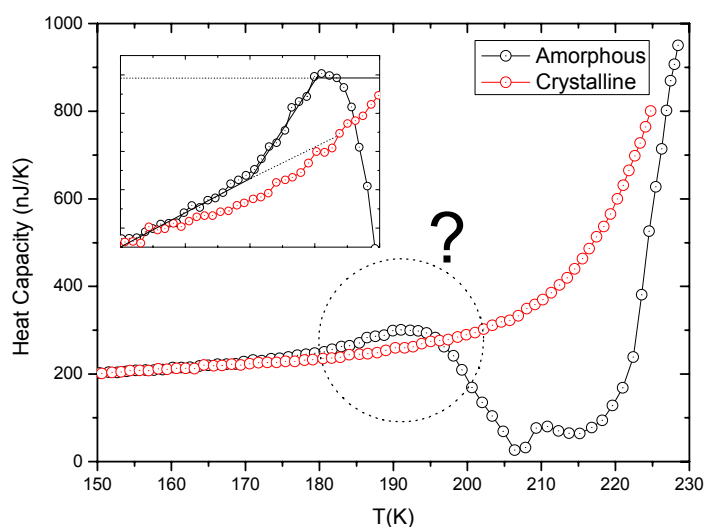


Fig. 5.22: Heat capacity traces obtained by fast heating the amorphous and crystalline samples. The samples are deposited at 135 K to avoid the relaxation of the film before crystallization. A question arises whether the C_p jump of the amorphous phase is due to the presence of a glass transition.

From figure 5.22 it is inferred that an upswing in the heat capacity trace just before crystallization may correspond to the glass transition. Since lots of discrepancies and arguments on the glass transition have arisen in the past decades it seems that this C_p jump is not that clearly obvious. Several reasons may account to this fact. It can be argued, if not a glass transition, that the heat capacity jump occurring on T_g is simply below detection limits of our nanocalorimetric technique.

The small variation in heat capacity is characteristic of a low temperature event and according to the theoretical predictions of Johari et al., the heat capacity of supercooled liquid water near 200 K must be at least 50% greater than the heat capacity of ASW. Thus, in case of an existence of the glass transition it is reasonable to think that ultrafast nanocalorimetry should be sensitive enough to detect such transition due to the ultra fast heating rates involved (35000 K/s).

Films of several thicknesses ($15, 50, 95\text{ nm}$) deposited at 135 K, will be analyzed to discuss if the heat capacity upswing observed before crystallization with onset temperatures around 170 K could be due to the possible existence of a glass transition in ASW. The several contributions (*Sublimation, Mass loss, $C_{p\text{amorph}}$*) making part of the experimental data will be analyzed in detailed.

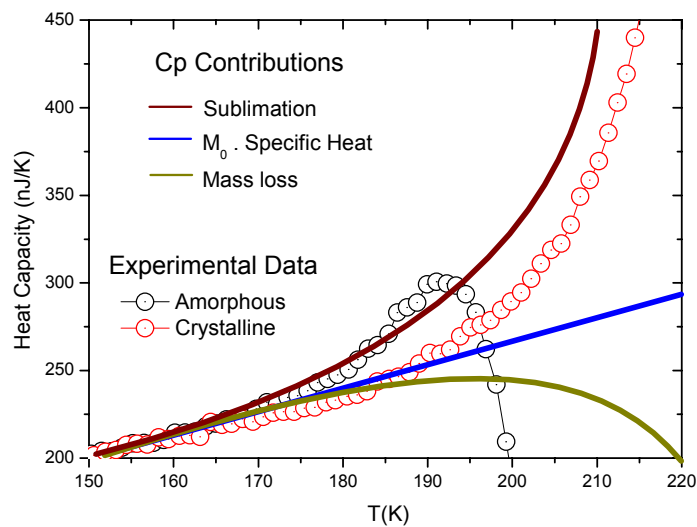


Fig. 5.23: Experimental heat capacities for the amorphous and crystalline phases with the contributions conforming the data.

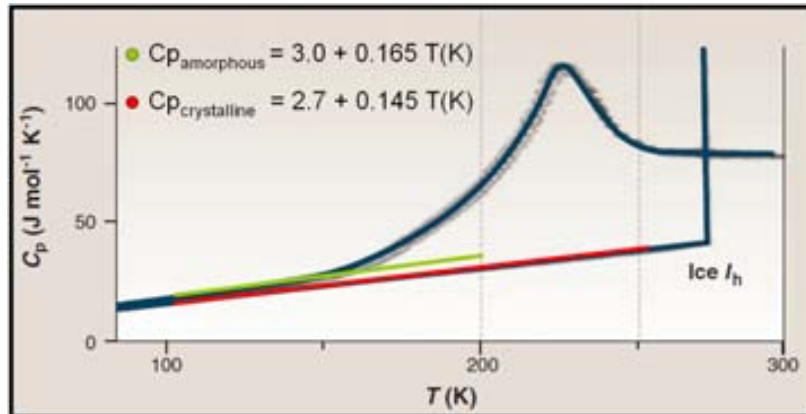


Fig. 5.24: Schematic representation of the amorphous and crystalline heat capacities used in this work. The original data is taken from reference [40]

Oguni et al. [40] have measured the heat capacities of mixtures of ordinary water and ice confined in silica gel. We use these experimental data to estimate the value of the heat capacity for the amorphous and the crystalline phases as a function of temperature (*figure 5.24*). The heat capacity of the amorphous phase can be represented by the linear equation:

$$C_{p_{amorph}} (J / mol \cdot K) = 3.0 + 0.165 \cdot T(K) \quad 5-5$$

By analyzing the samples in mol fraction we will have the following values for the different films:

Thickness (nm)	Mass (10^9 mol)
15	2.05
50	7.24
95	14.7

Table 5.2: mass values for the different samples taken into account in the glass transition study.

The evaporation rate which defines the mass loss is usually derived following an exponential relationship with temperature [41]. The sublimation information is contained into the terms $\Delta m(T)$ and $dm/dT(T)$ of equation 5.1. Thus we need to introduce a dependency of $\Delta m(T)$ which agrees with the experimental data. We can schematically observe this behavior in fig. 5.23 where the excess of heat capacity due to the sublimation rate is shown. The term is calculated as:

$$C_{p_{hyp}} = C_{p_{experimental}}(J/K) - C_{p_{amorph}}(J/mol \cdot K) \cdot M_{amorph}(mol) \quad 5.6$$

where $C_{p_{experimental}}$ is the heat capacity obtained from the experimental measurements, which will account to the contributions already mentioned (*figure 5.23*), $C_{p_{amorph}}$ is the heat capacity contribution of the amorphous phase and M_{amorph} is the mass in moles of the films deposited at 135 K taken from table 5.2. Since the glass transition overshoot is expected to be scalable with the sample mass we would expect a higher change for the thicker sample which is the behavior seen in figure 5.25 for films of 15, 50 and 95 nm.

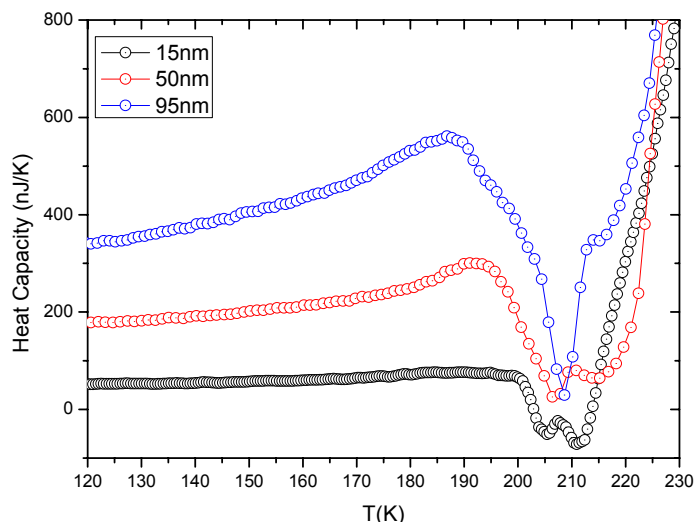


Fig. 5.25: Heat capacities as a function of temperature for different films of ASW deposited at 135K.

To quantitatively introduce the mass variation with temperature in the heat capacity curves we consider the effect of sublimation on the total mass of the film. The total mass at a certain t will be:

$$M(t) = M_{init} - A \cdot \int \left[\frac{X_{S,amorph} \cdot \phi_{amorph}(T) + X_{S,ice} \cdot \phi_{ice}(T)}{\beta(t)} \right] dT \quad 5.7$$

where M_{init} is the initial mass of the sample in moles, ϕ the sublimation rate of the amorphous or crystalline ice and X_S the volume fraction of the amorphous/crystalline phase. The mass of the amorphous fraction will be:

$$M_{amorph}(t) = M(t) \cdot x_{V,amorph} \quad 5.8$$

By using equation 5.6 we determine the heat capacity including the effects of the heat capacity of the amorphous phase and the mass loss as a function of temperature due to sublimation. At this point the latent heat contribution due to desorption of the film has yet to be considered. The resulting data derived from equation 5.6 is plotted in figure 5.26.

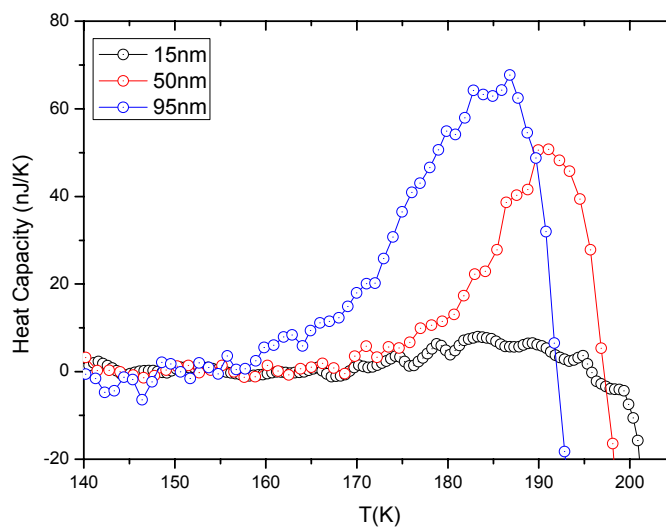


Fig. 5.26: Heat capacities as a function of temperature for the different films removing the contribution of the heat capacity of the amorphous proportion.

Once we have the heat capacity data without the contribution of the amorphous heat capacity and the mass change, we continue to analyze the effect that the sublimation has in the sample by studying the effect with two possible sublimation rates considered in all temperature regions of the treatment history (*from 90 to 230 K*). To consider the sublimation effect for the amorphous part we will have to represent the following contribution:

$$Cp_{glass-sublimation} = \phi_{am}(T) \cdot A \cdot \Delta H_{sub,amorph} \cdot X_{S,amorph}(t) / \beta(t) \quad 5.9$$

where $\phi_{amorph}(T)$ is the sublimation rate for the glass ($\text{mols.cm}^2.\text{s}^{-1}$), A the surface area of the film (cm^2) which is well known because of the use of a shadow mask during deposition, $A = 0.01\text{cm}^2$, ΔH is the sublimation enthalpy of the glass, $X_{s,amorph}(t)$ is the surface fraction that remains glassy and $\beta(t)$ is the heating rate. The sublimation rates of the amorphous and crystalline phases have been determined by Baragiola et al. [35] (*fig. 5.27b*). Temperature dependence of the sublimation rate curve follows Arrhenius dependence and can be fitted using the following expression:

$$\Phi(T) = f_a T^{3.5} \exp(-E_{sub} / kT) \quad 5.10$$

where E_{sub} is the sublimation energy in (J/mol), f_a is a pre-exponential factor derived by an areal factor which is equal to the ratio of the effective surface area to geometric area ($\text{mol/T}^{3.5}\text{cm}^2\text{s}$), T is the surface temperature, k is the universal gas constant expressed in (J/Kmol). Proper extrapolations to higher temperatures following the data presented in reference [35] where the possible sublimation effects considered in this work is shown in *fig. 5.27a*. Figure 5.27b corresponds to the data obtained in ref. [35].

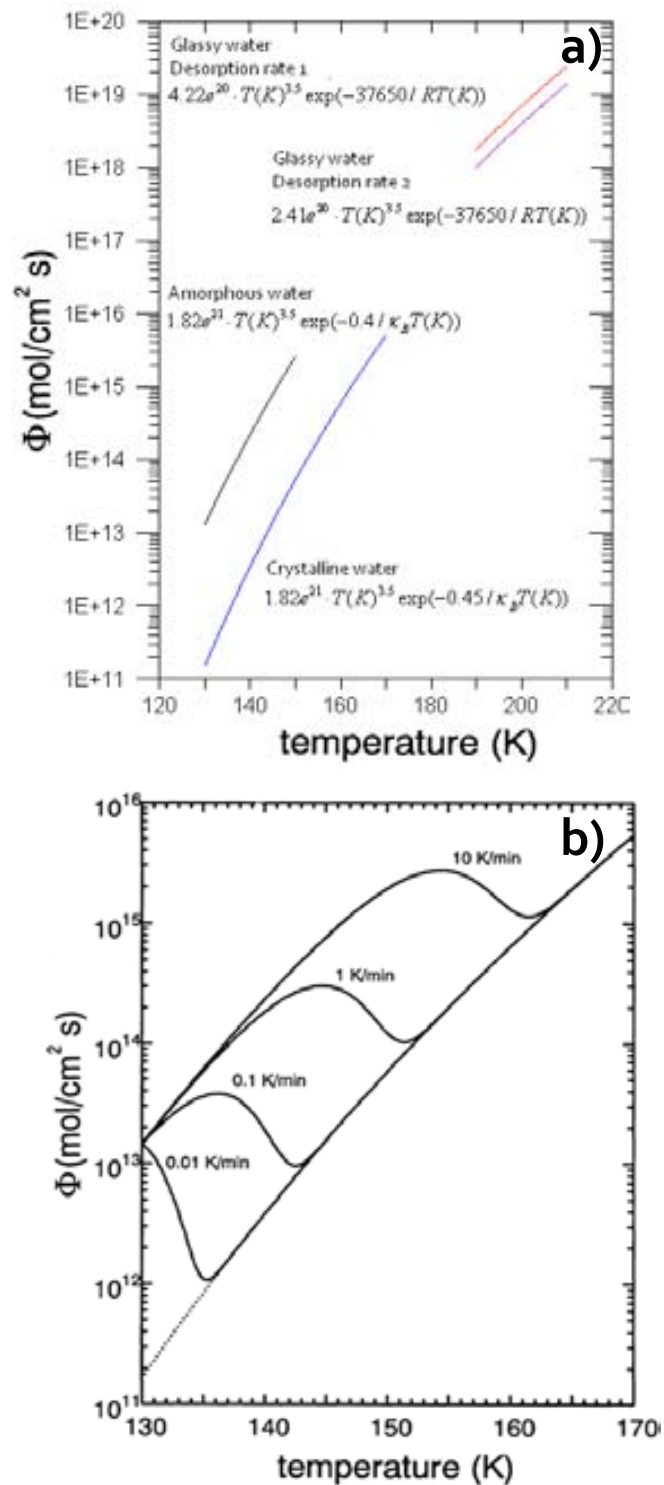


Fig. 5.27: Calculated sublimation rate as a function of surface temperature for an initially amorphous film heated at different rates. a) Calculated values considered in this work b) Values obtained in reference [35].

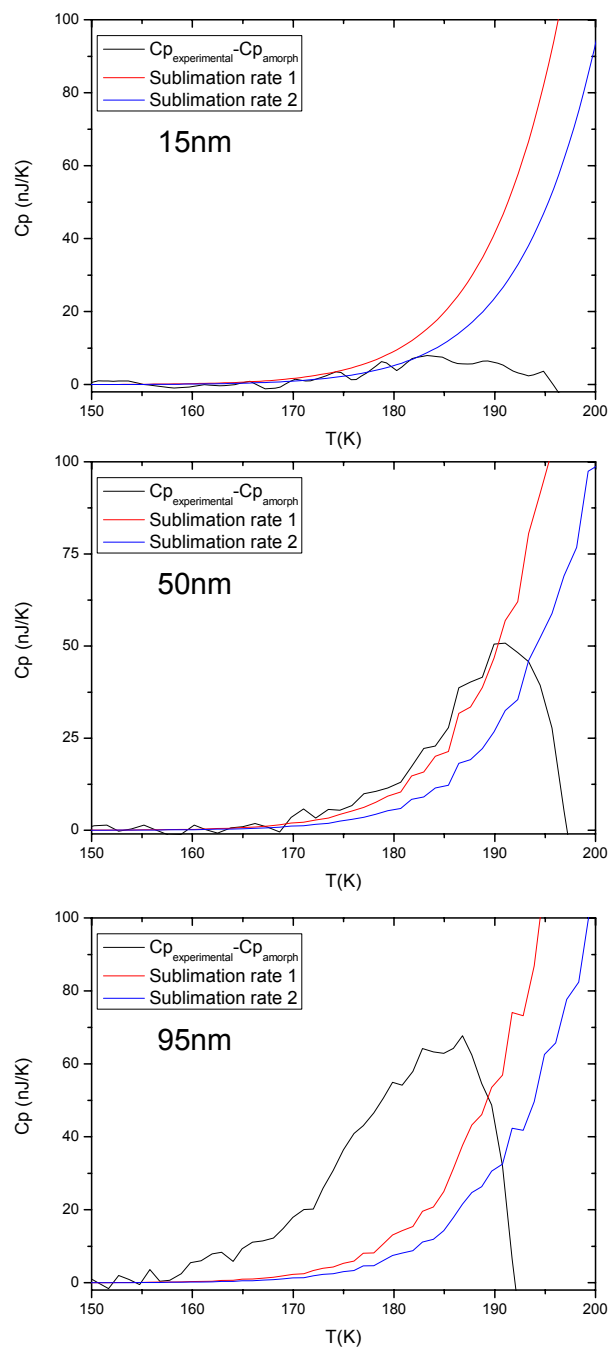


Fig. 5.28: Sublimation contributions for the different thick films. The black curves represent the data of C_p subtracting the effects of the amorphous heat capacity and mass loss. Two possible sublimation contributions with different rates will be taken into account (red and blue curves)

Figure 5.28 shows the effect of the two sublimation rates in the heat capacity of the films with different thickness. As apparent from this figure the endothermic rise may be followed by a plateau that is affected by the initiation of the crystallization regime between 190 – 200 K. In the following we discuss if sublimation in those films can lead to the observed increase in heat capacity above 170 K. We consider two possible sublimation rates with a factor ~ 2 for each ASW film. Figure 5.28 a,b,c clearly show that the same sublimation process can not account for the mass dependence of the observed heat capacity jump. Even in the unlikely case that the sublimation rates changed by a factor of two (*blue and red curves*) for different thickness sublimation could not alone explain the jump. The main reason is that the measured increment in C_p is proportional to the sample mass as it is shown in figure 5.29 whereas sublimation is mainly proportional to the surface area. Therefore, it seems possible that the jump in C_p can be attributed to the glass transition of amorphous solid water around 170 K.

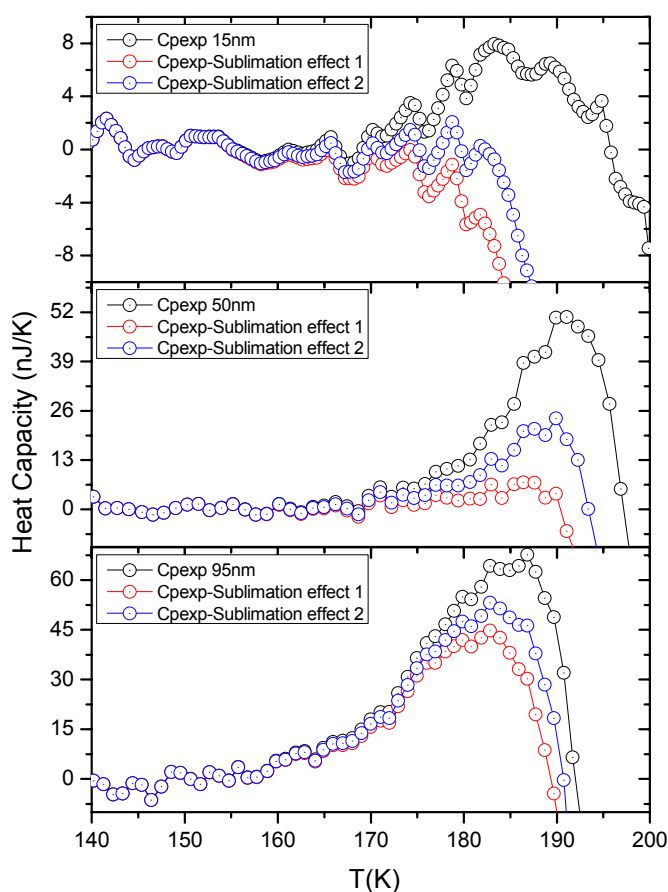


Fig. 5.29: Heat capacities as a function of temperature for the different films removing the contribution of the heat capacity of the amorphous fraction, the mass variation and of the sublimation. Results considering possible sublimation rates are shown.

Figure 5.29 shows the effect of removing the contribution for the various sublimation rates to the heat capacity according to equation 5.11

$$C_p = C_{p_{hyp}} - C_{p_{glass-sublimation}} \quad 5.11$$

Clearly the sublimation rates that are suited to explain the C_p jump in the 50 nm films (*red curve*) are unlikely to be reasonable for the 15 nm (*excessive sublimation rate that yields negative values of C_p not experimentally observed*) and for the 90 nm films where a considerable jump in heat capacity exists.

Considering that we have taken into account all possible processes affecting the experimental heat capacity data we infer that the observed heat capacity jump is related to the glass transition of ASW. We obtain approximate heat capacity jumps of 2.9 J/Kmol and 0.9 J/Kmol for the thickness of 95 nm and 50 nm respectively. These low values qualitatively compare to the ones obtained by Johari et al. for ASW (1.9 J/Kmol) and are much lower to the 55 J/molK suggested by Angell. Clearly, more experiments are needed to clarify the observed variation between the various film thicknesses.

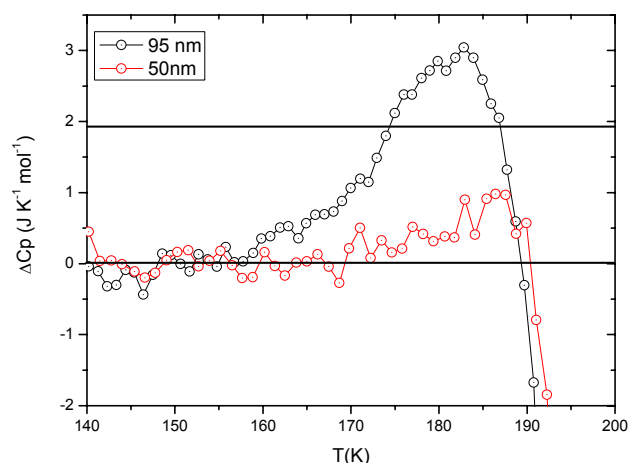


Fig. 5.30: Increase in heat capacity in the glass-to-liquid transition observed by nanocalorimetry taking into account computer processing for the amorphous heat capacity and sublimation rates.

Chapter VI

Conclusions

Standard microfabrication procedures have been utilized to fabricate 180-480 nm thick silicon nitride membrane calorimeters. Thermal profiles have been calculated analytically by finite modeling and experimentally by infrared technology to visualize the temperature distribution across the active area of the membrane. The S-shaped heater gives suitable profiles up to fast heating rates. The U-shaped design gives poor quality thermal profiles and a thermalization layer had to be used to reduce the temperature gradients across the sensing area.

We have developed scanning temperature controllers to be used for the heating of the microdevices at rates from ~ 1 to 1000 K/s in power compensation mode. We have analyzed several transformations of samples in the microgram range, opening the possibility to study kinetically limited processes not suited for ultra-fast heating, this is the case of the hydrogenation/dehydrogenation of metal hydride thin films. To show the feasibility of the technique, calibration tests were done in the calorimeters with a HDPE $10\mu\text{m}$ thin film. Different heating rates were performed in the analysis. The results are in good agreement relating the energies involved in the samples and the experimental values obtained. Hence, we have designed and developed a system that is particularly well adapted to measure the latent heat of first-order transitions occurring in thin film samples.

We have developed a power compensation technique based on membrane-based calorimeter capable to analyze the dehydrogenation process of metal hydrides. Among the several techniques employed for the preparation of metal hydrides, the thin film deposition technique presents several advantages in the search for new compounds. The use of vapor phase methods enhances the control of the compounds purity, stoichiometry, structural order and grain size in comparison with bulk methods such as ball milling. In addition, diffusion limitations are also minimized in thin films and therefore the sorption/desorption of hydrogen is not kinetically limited.

The dehydrogenation of Mg, Mg/Al and Mg_yTi_(1-y) hydrides thin films has been analyzed at heating rates of 10°C/min. The endothermic peak attributed to hydrogen desorption is well resolved. The addition of intercalated Al layers has a beneficial effect on the hydrogenation characteristics of the Mg films by increasing the hydrogen content. Calorimetric traces confirmed that the incorporation of Ti enhances the dehydrogenation behavior by lowering the onset temperature compared with pure Mg or Mg/Al films. The quantitative analysis of the dehydrating system is particularly troublesome due to strong variation of the thermal properties of the films during the phase transformation. The estimation of the thermodynamics involved during the hydrogenation/dehydrogenation remains a challenge and further work improving the calorimetric cell design.

Taking advantage of the use of vapor phase deposition techniques for the material preparation and a membrane-based microcalorimeter chip for the characterization, this work can be considered as the first step in GNaM for the development of a combinatorial deposition methodology coupled with a high throughput characterization technique based on the discrete deposition of selected composition on microchip arrays to discover new materials for hydrogen storage

We have developed a system working at heating rates in the order of 10⁵ K/s. Since the sensitivity of the calorimetric setup is very high and accurate it enables us to easily detect exo and endothermic transformations in thin films. It has been demonstrated that this technique can be used to study the stability of very thin film organic glasses (toluene and ethylbenzene) by analyzing the Cp jump related to the glass transition. Also, this system has the ability to analyze the crystallization kinetics and possible glass transition in amorphous solid water.

The stability of the films obtained by the vapor phase is dependent to the deposition temperature. A maximum stability for both toluene and ethylbenzene is accomplished at 0.8 T_g (90 K). These results are in agreement with previous findings of other authors.

Amorphous thin films of toluene and ethylbenzene between 5 and 100 nm have been deposited. The most stable As-deposited (*AD*) films reduce their onset temperatures (*T_{on}*) and fictive temperatures (*T_f*) simultaneously when reducing the thickness of the film, which implies a reduction in the kinetic stability and at the same time an enhancement in thermodynamic stability.

Stability values of the thin films obtained from supercooling the liquid (*FC*) is thickness-independent.

We have monitored the influence in organic thin film stability with the rate at which the liquid is quenched into the glass. The change in the cooling rate shows an influence in T_{on} and T_f . The stability of the film is worsened by using faster cooling rates since the molecules will have less time to rearrange and position themselves in a low potential energy site in the energy landscape.

Aging measurements below T_g have demonstrated that energetic recovery of the AD films by means of annealing treatments will require large time scales, out of reach for conventional laboratory time scales. The optimal aging temperature will correspond to fictive temperature (T_f) of the corresponding AD film, although the verification of this behavior would require larger time scales. It has been demonstrated that the minimum energetic level reached and aging efficiency depends on sample thickness. The stability will be more favorable when the thickness of the film is reduced.

Structural recovery has been studied in partially transformed glasses by aging experiments above T_g . The transformation towards highly stable local packing can be extremely accelerated by the presence of a stable phase seed in the initial glass. We have demonstrated that it may be possible to recover the highly stable phase in a reasonable time scale of hours. We have pointed out that this methodology under the appropriate experimental conditions may provide the route to thermodynamically explore the intriguing existence of a true phase-transition below T_g between the non-stable glass and the more stable glass obtained by vapor deposition. This suggestive hypothesis needs to be confirmed by further measurements at various aging temperatures.

Experiments regarding the crystallization of amorphous solid water show a clear modification in the shape of the exothermic calorimetric peaks which strongly depends on thickness. This behavior may be attributed to a double nucleation and growth mechanism. However, extensive and complex kinetic modeling will be necessary to identify the nature of the two peaks and the thickness dependence.

We have observe and important change in the heat capacity of amorphous solid water just before crystallization. Analytical data treatment was necessary to take into account all possible processes affecting the experimental heat capacity data. We have inferred that the observed heat capacity jump is related to the glass transition of ASW. We have obtained approximate heat capacity jumps of 2.9 J/Kmol and 0.9 J/Kmol for the thickness of 95 nm and 50 nm respectively. These low values are comparable to the ones stated by Johari et al. for ASW (*1.9 J/Kmol*) and are much lower to the 55 J/molK suggested by Angell. Clearly, more experiments are needed to clarify the observed variation between the various film thicknesses.

Appendix

Multiparallel dehydrogenation analysis: preliminary example

Introduction

With conventional methods of preparation/characterization of metal hydrides it is unreasonable to synthesize and screen numerous materials that could be considered as potential candidates for hydrogen storage testing one composition at a time, an enormous number of experiments would be required to map the structure-composition-property relations of a complete material system. Although important theoretical techniques have been developed [1], several of the complex systems are difficult to predict and so experimental investigations are necessary in the search of new materials. High-throughput procedures are nowadays coupled with the capability of producing large arrays of miscellaneous materials (*material libraries*) together with different measurement techniques of various physical properties (*multi-parallel characterization tools*).

In the field of hydrogen storage, different combinatorial methods have been used for study and discovery of promising candidates. S.J. van der Molen introduced a combinatorial approach based on the characterization of “matrix samples” to study the effect of Pd capping layers on Y thin films [2]. Olk et al. [3] characterized Mg-Ni-Fe alloys by monitoring the hydrogen sorption temperatures using a high-throughput infrared (IR) technique. They achieved to prepare 16 ternary compositions in one deposition step through combinations of mask positioning and substrate rotation. A novel and sophisticated high-throughput technique was developed by Gremaud and co-workers [4]. With this so-called “hydrogenography” method they were able to monitor the hydrogen absorption kinetics and optical properties of Mg-based compositional library samples (*i.e.* $M_yN_{(1-y)}$, $Mg_xAl_{(1-x)}$, Pd/Mg). This technique is based on the large optical changes of a metal upon hydrogen uptake.

In GNaM, a combinatorial synthesis method was developed by G. Garcia and co-workers [5] who prepared compositional spreads, as well as geometrically defined libraries of Mg/Al and MgTi using PVD techniques and specially designed moving shadow masks. The stoichiometry of the as-deposited films and libraries members were characterized by Energy Dispersive X-ray analysis (EDX). Taking advantage of this technique of material preparation developed at GNaM we proceed to elaborate a more sophisticated multi-parallel characterization technique based on the power compensation scheme described in section 3.5.2 towards a full high-throughput methodology (*deposition/characterization*).

We already devoted our work to develop a power-compensated membrane-based calorimetric technique suited for a single chip micro-device to study first-order transitions maintaining linear heating rate spanning from 1 to 1000 K/s. As it has been already described in previous sections, results were optimum at slow heating rates¹. Due to the system design, implementing a Differential Scanning Calorimetry with a high-throughput screening technology throughout multi-parallel characterization is one of the main goals of the research. To expand this technique further on to rapidly study different types of kinetic behaviors that can be consider time consuming we have designed and developed a multi-parallel sensitive power compensated scanning calorimeter for the use with microgram and sub-microgram samples in the temperature range from 77-900 K. This new system configuration allows us to analyze samples faster than the previous setting with the same accuracy and sensitivity since we can choose up to 8 calorimeters between a 52-array wafer and measure simultaneously different types of samples with the same ambient conditions.

¹ See section 2.3.2 and 2.3.3 of Chapter II

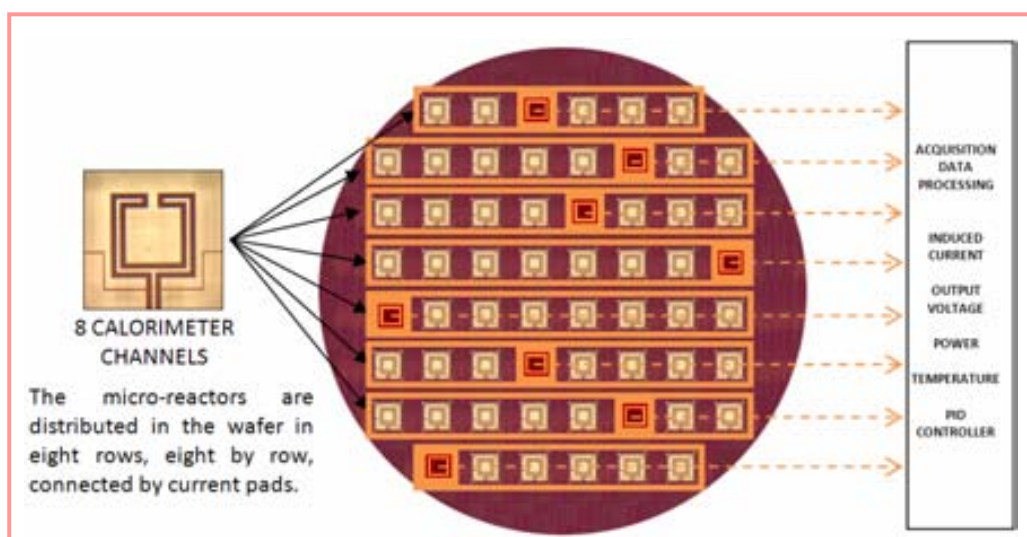


Fig. A.1: Multi-parallel micro-reactor Si wafer. It consists of 52 micro-devices fabricated in a Si wafer with their corresponding bond pads for voltage sensing and current feeding. The devices are connected in a row series. This configuration will need of 8 current sources to supply the necessary power to 8 independent micro-calorimeters simultaneously.

The channel configuration was made with more than 200 electrical connections to the on-chip bond pads used to make surface contact inside a specially designed high-vacuum chamber where the calorimetric experiments were performed (*Chapter III Fig. 3.2*). Each channel implements a multiplexor so the measurements can be done one at a time for every row, corresponding to 8 simultaneously real-time measurements. Hence, it is possible to acquire data of the entire 52 micro-reactor array. This configuration in combination with program facilities provides a great flexibility at the time of sample deposition, it is not necessary for every sample to be located in a specific calorimeter of each row.

For a Differential Scanning Calorimetric technique one empty calorimeter serves as a reference for the remaining micro-reactors. The advantage of this approach is the high throughput that could be obtained measuring simultaneously calorimetric data. Each device is contacted to four gold-coated pogo-pins, two for the current signal and two for the voltage acquisitions, obtaining the four-point resistance measurement. The parallel work of our system can reduce dramatically the time of measurement. Taking a typical scan rate of 20 K/min and a typical temperature range of 20-500 °C, in a conventional DSC system, the scanning of 64 samples, would

take more than one day, measuring daytime and night time. In the system we are presenting, the same work would be done in less than 3.5 h.

High-throughput material preparation

The Mg/Al e-beam evaporation was performed using moving shadow masks which allowed for the perfect selection of the deposition composition and thickness over each microchip. The films were deposited on the micro-fabricated substrates at room temperature and the deposition pressure was kept at 4×10^{-6} mbar for 0.2 and 0.25 nm/s thickness for Mg and Al, respectively. MgTi libraries were prepared using the co-evaporation process in a sputtering DC where the Ti gun faces the Mg gun. In order to ensure that the film to be characterised was only deposited over the chip sensing surface, we add a microfabricated shadow mask that perfectly fits the silicon wafer design. All the analyzed in-libraries were coated with a 10 nm Pd film to ensure fast hydrogen dissociation and diffusion rates as well as to avoid oxidation of magnesium from the atmosphere. The evaporation temperature was optimized individually to fix the growth rate of the different metals using a quartz microbalance located inside the deposition chamber. MgAl film samples were prepared using sequential individual deposition in order to perfectly control the thickness of each element, while 200 nm thick $\text{Mg}_y\text{Ti}_{(1-y)}$ films were coevaporated (simultaneous Ti e-beam and Mg thermal evaporation) to permit an intimate contact of both elements.

Once the ex-situ evaporation deposition is completed, the wafer containing the calorimeters is located in the particularly adapted high-vacuum chamber where the hydrogenation/dehydrogenation treatments take place. The experiments were held in two separate sections since one wafer was implemented to make the deposition of different thicknesses of pure Mg thin films and Mg/Al alloys. Another wafer was employed for the deposition of several Mg/Ti compositions. Different hydrogenation times were applied since the upper temperature boundary of the microdevice was limited due to hydrogen pressure and the current density supported by the device, thus experiments for a hydrogenation temperature above 100 °C were not accessible. Nevertheless, the formation of the hydride was then confirmed with calorimetric data for dehydrogenation which we have previously demonstrated in chapter III. Mg/Al were dehydrogenated in vacuum while pure Mg and Mg/Ti samples were heated up in air to increase heat losses through the gas.

Multi-parallel technique

The calorimetric experiments were performed inside a specially designed high-vacuum chamber. The same experimental setup was implemented as described in section 3.4 of Chapter III where a detail of the calibration can be found. The multi-parallel functionality of the system was tested under the same conditions by analyzing the melting behavior of different amounts of HDPE thin films ($\sim 40\text{-}80\ \mu\text{g}$). The measurements were made simultaneously on 7 calorimeters using one of them as reference for the differential data. The measured onset temperature for melting, 394 K, and the heat of fusion, 165 J/g, agrees with the values of the different thicknesses.

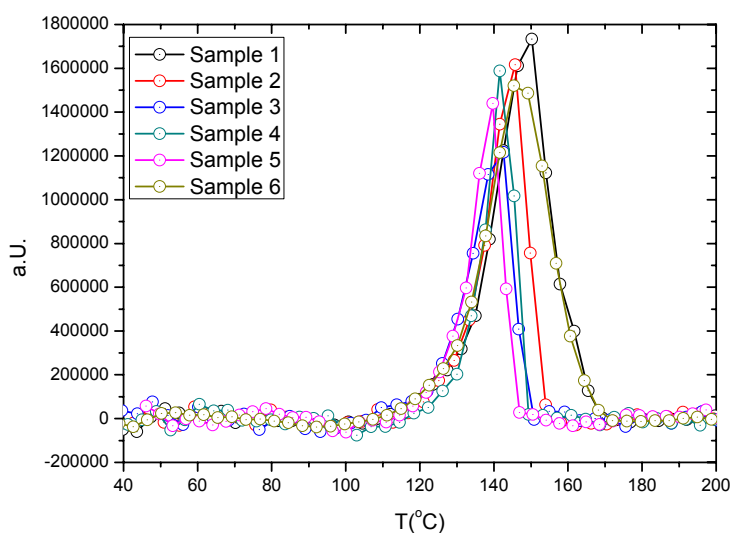


Fig. A.2: Multi-parallel measurement done on a $10\ \mu\text{m}$ thick HDPE film. This measurement was done simultaneously on 6 micro-devices. This is a first prototype towards a rapid-screening calorimetric tool. The system presented here allows simultaneous measurements on 8 different channels and sequential measurements on 54 individual samples hosted in a single wafer. Heating rates up to 1000 K/sec can be reached.

This first work was dedicated to specifically analyze the desorption temperatures for the different Mg-based compositions and expand the single chip technique and combine it with optical methods to confirm the calorimetric data. Once we have tested the multi-parallel design entirely by studying simple and understandable phase transitions and the interactions involved with our devices this technique can be considered being on an early stage for the study of metal hydrides. Several issues concerning power losses, thermal profiles and energy estimations still have to be

improved. Nevertheless, a parallel analysis of two types of samples was completed (Fig.A.3). Desorption temperatures were compared with our previous results where temperatures around 125 °C were obtained. The dehydrogenation treatment was done simultaneously by applying the same heating rate (10 °C/min) for both micro-calorimeters while one empty calorimeter served as the reference. Two synchronized measurements were considered the best approach to assure the most excellent performance from the controller algorithm in the FPGA and delete non-zero ΔT errors that could affect the calorimetric trace and the future quantitative energy estimation.

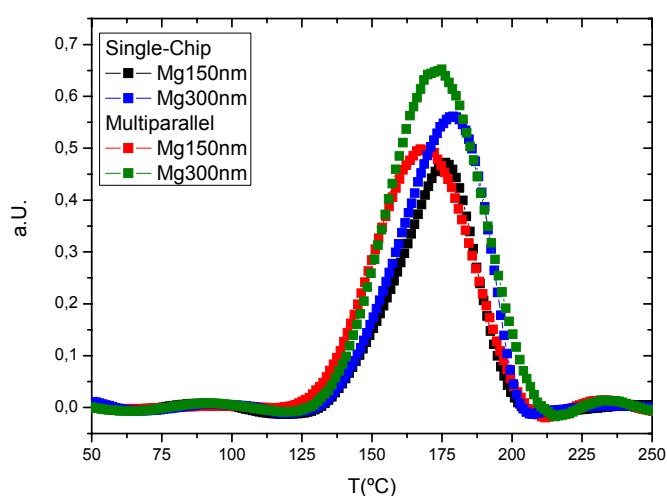


Fig. A.3: Dehydrogenation treatments were applied for two samples simultaneously

The quantitative estimation of the thermodynamics involved during the hydrogenation/dehydrogenation remains a challenge and further work improving the calorimetric cell design and the power loss analysis is under way.

Bibliography

Summary and Chapter I

- [1] Samuel Guerin, Brian E. Hayden, and Duncan C. A. Smith; *High-Throughput Synthesis and Screening of Hydrogen-Storage; Alloys*; J. Comb. Chem. 2008, 10, 37–43
- [2] P. J. McCluskey and J. J. Vlassak, *Parallel nano-differential scanning calorimetry: a new device for combinatorial analysis of complex nano-scale material systems*, Mater. Res. Soc. Symp. Proc. 924E, (2006).
- [3] A. F. Lopeandía, F. Pi and J. Rodríguez-Viejo, *Nanocalorimetric analysis of the ferromagnetic transition in ultrathin films of nickel*, Appl. Phys. Lett. 92, 122503 (2008).
- [4] Y. Miyoshi, K. Morrison, J. D. Moore, A. D. Caplin and L. F. Cohen, *Heat capacity and latent heat measurements of CoMnSi using a microcalorimeter*, Rev. Sci. Instrum. 79, 074901 (2008).
- [5] E. León-Gutierrez, G. Garcia, M. T. Clavaguera-Mora and J. Rodríguez-Viejo; *Glass transition in vapor deposited thin films of toluene*;Thermochim. Acta 492, 51 (2009).
- [6] A. A. Minakov, A. W. van Herwaarden, W. Wiend, A. Wurma and C. Schick; *Advanced nonadiabatic ultrafast nanocalorimetry and super-heating phenomenon in linear polymers*; Thermochim. Acta 461, 96 (2007).
- [7] A. F. Lopeandia, L. Cerdó, M. . Clavaguera-Mora, L.R. Arana, K.F. Jensen, F. Muñoz, J. Rodriguez-Viejo; *A sensitive power compensated scanning calorimeter for analysis of phase transitions in small samples*; Rev. Sci. Ins. 76 (2005) 065104.
- [8] A. F. Lopeandia, AF; Valenzuela, J; Rodriguez-Viejo, J; *Power compensated thin film calorimetry at fast heating rates*; Sensors & Actuators A –Physical Vol. 143 (2) P: 256-264, 2008
- [9] A. Sepúlveda, A. F. Lopeandia, R. Domenech-Ferrer, G. Garcia, F. Pi, J. Rodriguez-Viejo, F.J. Muñoz; *Microchip power compensated calorimetry applied to metal hydride characterization*; International Journal of Hydrogen Energy 33 (2008) 2729-2737
- [10] E. Leon-Gutierrez, G. Garcia, A. F. Lopeandia, J. Fraxedas, M. T. Clavaguera-Mora, J. Rodriguez-Viejo; *In situ nanocalorimetry of thin glassy organic Films*; The Journal of Chemical Physics 129, 181101 (2008)
- [11] Stephen F. Swallen, Kenneth L. Kearns, Marie K. Mapes, Yong Seol Kim, Robert McMahon, Mark D. Ediger, Tian Wu, Lian Yu, Sushil Satija; *Organic Glasses with Exceptional Thermodynamic and Kinetic Stability*; Science Vol315, 2007

- [12] Edgar Leon-Gutierrez, Alfonso Sepúlveda, Gemma Garcia, Maria Teresa Clavaguera- Mora, Javier Rodríguez-Viejo; *Stability of thin film glasses of toluene and ethylbenzene formed by vapor deposition: An in-situ nanocalorimetric study*; Phys. Chem. Chem. Phys. DOI: 10.1039/c0cp00208a
- [13] E. Zhuravlev and C. Schick; *Fast scanning power compensated differential scanning nanocalorimeter: 1. The device*; Thermochimica Acta 505 (2010) 1–13
- [14] L. H. Allen and S. L. Lai; MEMS-based Scanning Calorimeter for Thermodynamic Properties of Nanostructures; *Microscale Thermophysical Engineering* 2, (1998): 11
- [15] A. F. Lopeandia, J. Rodríguez-Viejo, M. Chacón, M. T. Clavaguera-Mora, F. J. Muñoz; *Heat transfer in U-Shaped microreactors for thin film calorimetry*; J. Micromechanics and Microengineering, 16 (2006) 965-971.
- [16] E. León-Gutierrez, G. Garcia, A.F. Lopeandía, J. Fraxedas, M.T. Clavaguera-Mora and J. Rodríguez-Viejo; *In-situ ultra-fast nanocalorimetry of thin amorphous organic Films*; Journal of Chemical Physics, 129, 181101 (2008)
- [17] Y. Anahory, M. Guihard, D. Smeets, R. Karmouch, F. Schiettekatte, P. Vasseur, P. Desjardins, Liang Hu, L.H. Allen, E. Leon-Gutierrez and J. Rodriguez-Viejo; *Fabrication, characterization and modeling of single-crystal thin film calorimeter sensors*; 510, 1-2, 2010, Pages 126-136
- [18] Bourgeois O, Skipetrov SE, Ong F, Chaussy J.; *Attojoule calorimetry of mesoscopic superconducting loops*; Phys Rev Lett. 2005 Feb 11

Chapter II

- [1] Höhne, G.W.H.; Hemminger, W.; Flammersheim, H-J.; *Differential Scanning Calorimetry: An Introduction for Practitioners*; Springer-Verlag; 1996
- [2] F.Spaepen; C.V. Thomson; *Calorimetric studies of reactions in films and multilayer's*; Appl. Surf. Sci. 38, 1-12 (1989)
- [3] M. Gonzalez-Silveira, M.T. Clavaguera-Mora, F.Pi and J. Rodriguez-Viejo; *Calorimetric evidence of assymetry in the nucleation of CuMg₂ in Cu/Mg multilayer's*; Phys. Rev. B 69, 113411 (2004)
- [4] A.F. Lopeandía, E. León-Gutierrez, G. Garcia, F. Pi, A. Bernardi, A.R. Goñi, M.I. Alonso, J. Rodriguez-Viejo; *Nanocalorimetric high-temperature characterization of ultrathin films of a-Ge*; Materials Science in Semiconductor Processing; 9, 4-5, 2006, 806-811
- [5] A. F. Lopeandia, J. Rodríguez-Viejo, M. Chacón, M. T. Clavaguera-Mora, F. J. Muñoz; *Heat transfer in U-Shaped microreactors for thin film calorimetry*; J. Micromechanics and Microengineering, 16 (2006) 965-971
- [6] A.F. Lopeandía; *Development of Membrane-based calorimeters to measure phase transitions at the nanoscale*. PhD. Thesis, Universitat Autònoma de Barcelona, 2007
- [7] A.F.Lopeandía, J.Valenzuela, J. Rodríguez-Viejo; *Power compensated thin film calorimetry at fast heating rates*; Sensors and Actuators A (2007)
- [8] Edgar Leon-Gutierrez, Alfonso Sepúlveda, Gemma Garcia, Maria Teresa Clavaguera- Mora, Javier Rodríguez-Viejo; *Stability of thin film glasses of toluene and ethylbenzene formed by vapor deposition: An in-situ nanocalorimetric study*; Phys. Chem. Chem. Phys. DOI: 10.1039/c0cp00208a
- [9] Madou, M; *Fundamentals of micro-fabrication. The science of miniaturization*; (CRC Press LLC. 2000)
- [10] N.E. Hager-Jr; *Thin heater calorimeter*. Thermochim. Acta 35, 618-624 (1964)
- [11] S.L.Lai, G.Ramanath, L.H.Allen, P.Infante and Ma, Z.; *High speed (10⁴C/s) scanning microcalorimetry with monolayer sensitivity (J/m²)*. Appl. Phys. Lett. 67, 1229-1231 (1995)
- [12] M.Y. Efremov, F. Schiettekatte, E.A. Olson, A.T. Kwan, S.L. Lai, T. Wisleder, J.E. Greene, L.H. Allen; *Discrete Periodic Melting Point Observations for Nanostructure Ensembles*; Phys. Rev. Lett. 85 (2000) 3560.
- [13] E.A. Olson, M. Yu, Y. Efremov, M. Zhang, Z.S. Zhang, L.H. Allen; *The design and operation of a MEMS differential scanning nanocalorimeter for high-speed heat capacity measurements of ultrathin films*; J. Microelectromech. Syst. 12 (2003) 355.
- [14] A.F. Lopeandía, J. Rodríguez-Viejo; *Nanocalorimetric analysis of the ferromagnetic transition in ultrathin films of nickel*; Thermochim. Acta 461 (2007) 82.

- [15] R. Karmouch, Y. Anahory, J.F. Mercure, D. Bouilly, M. Chicoine, G. Bentoumi, R. Leonelli, Y.Q. Wang, F. Schiettekatte; *Damage evolution in low-energy ion implanted silicon*; Phys. Rev. B: Condens. Matter Mater. Phys. 75 (2007) 075304.
- [16] S.A. Adamovsky, A.A. Minakov, C. Schick; *Scanning microcalorimetry at high cooling rate*; Thermochim. Acta 403 (2003) 55.
- [17] A.A. Minakov, A.W. Van Herwaarden, W. Wien, A. Wurm, C. Schick; *Advanced nonadiabatic ultrafast nanocalorimetry and superheating phenomenon in linear polymers*; Thermochim. Acta 461 (2007) 96.
- [18] M.Y. Efremov et al. *Thin Film differential scanning nanocalorimetry : heat capacity analysis*. Thermochimica Acta 412, 13-23 (2004)
- [19] A.T. Fiory, JOM 57 (2005) 21.
- [20] A. Sepúlveda, A.F. Lopeandía, R. Domenech-Ferrer, G. Garcia, F. Pi, J. Rodríguez-Viejo, F. J. Munoz, *Microchip power compensated calorimetry applied to metal hydride characterization*; International Journal of Hydrogen Energy, 33, 11, 2008, 2729-2737
- [21] M. Merzlyakov; *A method of rapid controlled cooling and heating of thin samples is developed*; Thermochim. Acta 442 (2006) 52.
- [22] E. Zhuravlev and C. Schick; *Fast scanning power compensated differential scanning nanocalorimeter: 1. The device*; Thermochimica Acta 505 (2010) 1–13
- [23] E. Zhuravlev and C. Schick; *Fast scanning power compensated differential scanning nanocalorimeter: 2. Heat capacity analysis*; Thermochimica Acta 505 (2010) 14–21
- [24] SRS Small Instrumentation Module, 2009. <http://www.thinksrs.com/products/SIM.htm>

Chapter III

- [1] Michael Felderhoff, Claudia Weidenthaler, Rittmar von Helmolt and Ulrich Eberle; *Hydrogen storage: the remaining scientific and technological challenges*; Phys. Chem. Chem. Phys., 2007, 9, 2643–2653
- [2] F. Schüth, B. Bogdanovic and M. Felderhoff; *Light metal hydrides and complex hydrides for hydrogen storage*; Chem. Commun., 2004, 2249 – 2258
- [3] J. Graetz, Y. Lee, J. J. Reilly, S. Park and T. Vogt; *Structures and thermodynamics of the mixed alkali alanates*; physical review B 71, 184115 (2005)
- [4] S. Singh, S.W.H. Eijt, J. Huot, W.A. Kockelmann, M. Wagemaker and F.M. Mulder; *The $TiCl_3$ catalyst in $NaAlH_4$ for hydrogen storage induces grain refinement and impacts on hydrogen vacancy formation*; Acta Materialia 55, 16, 2007, Pages 5549-5557.
- [5] I. Sayago, E. Terrado, E. Lafuente, M.C. Horrillo, W.K. Maser, A.M. Benito, R. Navarro, E.P. Urriolabeitia, M.T. Martinez and J. Gutierrez; *Hydrogen sensors based on carbon nanotubes thin Films*; Synthetic Metals 148 (2005) 15–19
- [6] Rakesh K. Joshi; Subramanian Krishnan; Mashamichi Yoshimura; Ashok Kumar; *Pd Nanoparticles and Thin Films for Room Temperature Hydrogen Sensor*; Nanoscale Res Lett (2009) 4:1191–1196
- [7] Young Tack Lee, JunMin Lee, Yeon Ju Kim, Jin Hyoun Joe and Wooyoung Lee; *Hydrogen gas sensing properties of PdO thin films with nano-sized cracks*; Nanotechnology 21 (2010) 165503 (5pp)
- [8] Borsa DM, Gremaud R, Baldi A, Schreuders H, Rector JH, Kooi B, et al. *Structural, optical, and electrical properties of $Mg_{y}Ti_{1-y}H_x$ thin films*. Phys Rev B 2007;75:205408.
- [9] Leon A A, Knystautas EJ, Huot J, Schulz R.; *Hydrogenation characteristics of air-exposed magnesium films*; J Alloys Comp; 2002; 345; 158-166.
- [10] Jian-jie Liang, *Theoretical insight on tailoring energetics of Mg hydrogen absorption/desorption through nano-engineering*, Applied Physics A: Materials Science & Processin, 2005, 80 (1), 173.
- [11] Dornheim M, Doppiu S, Barkhordarian G, Boesenberg U, Klassen T, Gut_eisch O, Bormann R.; *Hydrogen storage in magnesium-based hydrides and hydride composites*; Scripta Materialia; 2007; 56; 841-846.
- [12] Krozer, A.; Kasemo, B.; *Equilibrium hydrogen uptake and associated kinetics for the magnesium-hydrogen system at low pressures*; Journal of Physics: Condensed Matter; 1989; 1(8); 1533-8.

- [13] Higuchi K, Yamamoto K, Kajioaka H, Touyama K, Honda M, Orimo S, Fujii H.; *Remarkable hydrogen storage properties in three-layered Pd/Mg/Pd thin films*; J Alloys Comp; 2002; 330-332; 526-530
- [14] Akyildiz, Hasan; Oezenbas, Macit; Oeztuerk, Tayfur.; *Hydrogen absorption in magnesium based crystalline thin films*; International Journal of Hydrogen Energy;2006; 31(10); 1379-1383.
- [15] Robin Gremaud, Chase P. Broedersz, Dana M. Borsa, Andreas Borgschulte, Philippe Mauron, Herman Schreuders, Jan H. Rector, Bernard Dam, and Ronald Griessen; *Hydrogenography: An Optical Combinatorial Method To Find New Light-Weight Hydrogen-Storage Materials*; Adv. Mater. 2007, 19, 2813–2817
- [16] Doménech-Ferrer R, Sridharan MG, Garcia G, Pi F, Rodríguez-Viejo J.; *Hydrogenation properties of pure magnesium and magnesium-aluminium thin films*; J Power Sources; 2007; 169; 117-122.
- [17] A. Züttel; *Materials for hydrogen storage*; Materials Today 6 (2003) 24–33
- [18] A. F. Lopeandía, J. Valenzuela, J. Rodríguez-Viejo; *Power compensated thin film calorimetry at fast heating rates*; Sensors and Actuators A (2007)
- [19] A. F. Lopeandía, J. Rodríguez-Viejo, M. Chacón, M. T. Clavaguera-Mora, F. J. Muñoz; *Heat transfer in U-Shaped microreactors for thin film calorimetry*; J. Micromechanics and Microengineering, 16 (2006) 965-971.
- [20] Garcia G, Domenech-Ferrer R, Pi F., Santiso J, Rodriguez-Viejo J. *Combinatorial synthesis and hydrogenation of Mg/Al libraries prepared by electron beam physical vapor deposition*; J Combinatorial Chem ACS 2007;9:230_6.
- [21] Krozer, A.; Kasemo, B.; *Equilibrium hydrogen uptake and associated kinetics for the magnesium-hydrogen system at low pressures*; Journal of Physics: Condensed Matter; 1989; 1(8); 1533-8.
- [22] Rongeat C, Llamas-Jansa I, Doppiu S, Deledda S, Borgschulte A, Schultz L, et al. *Determination of the heat of hydride formation/decomposition by high-pressure differential scanning calorimetry (HP-DSC)*. J Phys Chem 2007;111:13301
- [23] Niessen RAH, Notten PHL. *Electrochemical hydrogen storage characteristics of thin film MgX (X=Sc,Ti,V,Cr) Compounds*. Electrochem Solid State Lett 2005;8(10):A534-8
- [24] H. Baker (Edt), *ASM Handbook – Alloy Phase Diagrams*, Vol. 3, ASM International 1992.
- [25] Y. Song, Z.X. Guo, R. Yang, *Influence of selected alloying elements on the stability of magnesium dihydride storage applications: A first-principles investigation*; Physical Review B 69, 094205, 2004
- [26] L. L. Pranevicius and D. Milcius; *Synthesis of Mg(AlH₄)₂ in bilayer Mg/Al thin films under plasma immersion hydrogen ion implantation and thermal desorption processes* Thin Solid Films 485, 135 (2005)

Bibliography

[27] Louis Schlapbach & Andreas Züttel.; "Hydrogen-storage materials for mobile applications" *Nature* 414, 353-358

Chapter IV

- [1] Angell, C. A.; Ngai, K.L.; McKenna, G. B.; McMillan, P.F.; Martin, S.W. J.; *Relaxation in glass-forming liquids and amorphous solids*; Appl. Phys. 2000, 88, 3113
- [2] Petrie, E.M., "The Importance of Glass Transition Temperature in Formulating Adhesives and Sealants", *SpecialChem4Adhesives*, 2003.
- [3] Steve Ablett, Chris J Clarke, Martin J Izzard and Dave R Martin; *Relationship between ice recrystallisation rates and the glass transition in frozen sugar Solutions*; Unilever Research and Development, Colworth House, Sharnbrook, Beds MK44 1LQ, UK
- [4] Interface and chain confinement effects on the glass transition temperature of thin polymer films; J. A. Forrest, K. Dalnoki-Veress, and J. R. Dutcher; *Department of Physics and Guelph-Waterloo Program for Graduate Work in Physics, University of Guelph, Guelph, Ontario, Canada N1G 2W1*
- [5] Jadhav NR, Gaikwad VL, Nair KJ, Kadam HM. *Glass transition temperature: Basics and application in pharmaceutical sector*. Asian J Pharm 2009;3:82-9
- [6] Hegenbart ; *Food Science and Technology on Characterizing food and its ingredients'. The food polymer science approach and the importance of glass transitions in foods have even become subjects of increasing discussion in recent food trade magazine articles*; 199 1; Best, 1992.
- [7] S.A. Brawer; *Relaxation in Viscous Liquids and Glasses*; American Ceramic Society, New York, 1985.
- [8] W. Scherer; *Relaxation in Glass and Composites*; Wiley-Interscience, New York, 1986.
- [9] Maxwell, J.C.; *On the Dynamical Evidence of the Molecular Constitution of Bodies*; Nature 1875, 11, 357-359,374-377
- [10] J.D.Stevenson; P.G. Wolynes; *Thermodynamic-Kinetic Correlations in Supercooled Liquids:A critical survey of experimental data and predictions of the random first-order transition theory of glasses*; J.Phys.Chem. B 2005, 109, 15093-15097
- [11] C. A. Angell; *Formation of Glasses from Liquids and Biopolymers*; Science, New Series, Vol. 267, No. 5206. (Mar. 31, 1995), pp. 1924-1935.
- [12] Huang, D., and McKenna, G.B. *New insights into the fragility dilemma in liquids*; *J. Chem. Phys.* 114, 5621-5630 (2001).
- [13] M. D. Ediger, C. A. Angell, S. R. Nagel; *Supercooled liquids and Glasses*; *J. Phys. Chem.* 100 (1996) 31 13200-13212
- [14] Pablo G. Debenedetti and Frank H. Stillinger; *Supercooled liquids and the glass transition*, Nature vol 410.

- [15] Swallen, S. F.; Kearns, K. L.; Mapes, M. K.; Kim, Y. S., McMahon R. J.; Robert, J.; Ediger, M. D.; Wu, T.; Yu, L.; Satija, S. *Organic glasses with exceptional thermodynamic and kinetic stability*; Science 2007, 315, 353-356.
- [16] Richert R, Angell; *Dynamics of glass-forming liquids. V. On the link between molecular dynamics and configurational entropy*. J. Chem. Phys. 108:9016-26
- [17] Rodney D. Priestley, Christopher J. Ellison, Linda J. Broadbelt, John M. Torkelson; *Structural Relaxation of Polymer Glasses at Surfaces, Interfaces, and In Between*; Science 15 July 2005; Vol. 309. no. 5733, pp. 456 - 459
- [18] Kenneth L. Kearns et al.; *Hiking down the energy landscape: Progress toward the Kauzmann temperature via vapor deposition*; J.Phys.Chem B 2008, 112, 4934-4942
- [19] Kauzmann, W.; *The Nature of the Glassy State and the Behavior of Liquids at Low Temperatures*; Chem.Rev. 1948, 43, 219
- [20] Gibbs, J. IL; DiMarzio, E.A. J. Chem. Phys. 1958, 28, 373
- [21] Poole, P. IL;Sciortino,F.;Essmann.U.;Stanley, IL. E.; *Phase behaviour of metastable water* ;Nature 1992, 360, 324.
- [22] Angell,C.C.;Moynihan, C.T.;Hemmati, M.J.; *Strong and superstrong liquids and an approach to the perfect glass state via phase transition*;Non-Cryst.Solids 2000, 274,319
- [23] Angelani, L.; Di Leonardo, R.; Parisi, G.; Ruocco, G. ; *Saddles in the Energy Landscape Probed by Supercooled Liquids*; Phys Rev Lett 2001, 87, 055502.
- [24] Sciortino, F.; Tartaglia, P.; *Extension of the Fluctuation-Dissipation Theorem to the Physical Aging of a Model Glass-Forming Liquid*; Phys Rev Lett 2001, 86,107.
- [25] Barrat, J.-L.; Kob, W. ; *Fluctuation-dissipation ratio in an aging Lennard-Jones glass*; EurophysLett 1999, 46, 63.
- [26] O'Connell, P. A.; McKenna, G. B.; *Arrhenius-type temperature dependence of the segmental relaxation below T_g* ;J Chem Phys 1999, 110, 11054.
- [27] O'Connell, P. A.; McKenna, G. B.; *Large deformation response of polycarbonate: Time-temperature, time-aging time, and time-strain superposition*; Polym Eng Sci 1997, 37, 1485.
- [28] Hampsch, H. L.; Yang, J.; Wong, G. K.; Torkelson; *Dopant orientation dynamics in doped second-order nonlinear optical amorphous polymers. 1. Effects of temperature above and below T_g in corona-poled films*; J. M. Macromolecules 1990, 23, 3640.
- [29] Hampsch, H. L.; Yang, J.; Wong, G. K.; Torkelson; *Dopant orientation dynamics in doped second-order nonlinear optical amorphous polymers. 2. Effects of physical aging on poled films*; J. M. Macromolecules 1990, 23, 3648.

- [30] R. D. Priestley, L. J. Broadbelt, J. M. Torkelson; *Physical Aging of Ultrathin Polymer Films above and below the bulk glass transition temperature: Effects of Attractive vs Neutral Polymer-Substrate Interactions Measured by Fluorescence*; *Macromolecules* 38, 654 (2005)
- [31] Turnbull, D. *Contemp. Phys.* 1969, 10, 473
- [32] M.E. Mobius, T.Xia, W. Van Saarloos, M.Ortiz and M. Van Hecke; *Aging and Solidification of Supercooled Glycerol*; *J. Phys. Chem. B* 2010, 114, 7439-7444
- [33] A. J. Kovacs, *Fortschr. Hochpolym.-Forsch.* 3, 394 (1964)
- [34] Katayama, T et al.; *A first order liquid-liquid phase transition in phosphorus*; *Nature* 403, 170-173 (2000)
- [35] Sen, S., Gaudio, S., Aitken, B.G and Leshner, C.E; *A pressure-induced first order polyamorphic transition in a chalcogenide glass at ambient temperature*; *Phys. Re. Lett.* 97, 025504 (2006)
- [36] Meade, C., Hemley, R. L. And Mao, H. K; *High pressure x-ray diffraction of SiO₂ glass*; *Phys. Rev. Lett.* 69, 1387-1390 (1992)
- [37] McMillan, P.F.; *A density-driven phase transition between semiconducting and metallic polyamorphs of silicon*; *Nature Mater.* 4, 680-684 (2005)
- [38] Ha, A.; Cohen, I.; Zhao, X.; Lee, M.; Kivelson, D. *J. Phys. Chem.* 1996, 100, 1.
- [39] J. Wiedesich, A. Kudlik, J. Gottwald, G. Benini, I. Roggatz, and. E. Rossler; *On Polyamorphism of Triphenyl Phosphite*; *J. Phys. Chem. B* 1997, 101, 5800-5803
- [40] K. Takeda, O. Yamamuro, H. Suga; *Calorimetric study of structural relaxation of 1-pentene in vapor-deposited and liquid-quenched glassy states*; *J. Phys. Chem.* 99 (1995) 1602.
- [41] G. Liu, M. Mackowiak, Y. Li and J. Jonas, *J. Chem. Phys.* 94 (1991), pp. 239–242.
- [42] A. Döss, G. Hinze, B. Schiener, J. Hemberger and R. Böhmer, *J. Chem. Phys.* 107 (1997), pp. 1740–1743.
- [43] G. Hinze and H. Sillescu, *J. Chem. Phys.* 104 (1996), pp. 314–319.
- [44] V.A. Santarelli, J.A. MacDonald and C. Pine, *J. Chem. Phys.* 46 (1967), pp. 2367–2375
- [45] O. Yamamuro, I. Tsukushi, A. Lindvist, S. Takahara, M. Ishikawa, T. Matsuo; *Calorimetry study of Glassy and Liquid Toluene and Ethylbenzene: Thermodynamic Approach to Spatial Heterogeneity in Glass Forming Molecular Liquids*; *J. Phys. Chem. B* 102 (1998) 1605
- [46] M. Chonde, M. Brindza and V. Sadtchenko, *J. Chem. Phys.* 125 (2006), p. 094501.
- [47] M.Y. Efremov, E.A. Olson, M. Zhang, S.L. Lai, F. Schiettekatte, Z.S. Zhang and L.H. Allen, *Thermochim. Acta* 412 (2004), pp. 13–23

- [48] A.F. Lopeandia, J. Rodriguez-Viejo, M. Chacon, M.T. Clavaguera-Mora and F.J. Muñoz, *J. Micromech. Microeng.* 16 (2006), pp. 965–971
- [49] M.Yu. Efremov, E.A. Olson, M. Zhang, Z. Zhang and L.H. Allen, *Phys. Rev. Lett.* 91 (2003), p. 085703.
- [50] M.Y. Efremov, E.A. Olson, M. Zhang, Z. Zhang and L.H. Allen, *Macromolecules* 37 (2004), pp.
- [51] K. Ishii, Y. Yokoyama, R. Moriyama, and H. Nakayama; *Liquid-Liquid Relaxation in the Supercooled Liquid State of Ethylbenzene: Thermal Studies Using a Prototype DTA Sensor for the Study of Vapor-deposited Samples*; *Chem. Lett.* 39, 958-960 (2010)
- [52] K. Ishii, H. Nakayama, S. Hirabayashi and R. Moriyama; *Anomalously high-density glass of ethylbenzene prepared by vapor deposition at temperatures close to the glass-transition temperature*; *Chem. Phys. Lett.* 459 (2008), pp. 109–112.
- [53] E. Leon-Gutierrez, G. Garcia, A.F. Lopeandia, J. Fraxedas, M.T. Clavaguera-Mora and J. Rodriguez-Viejo, *J. Chem. Phys.* 129 (2008), p. 181101
- [54] E. Leon-Gutierrez ; Ph.D. thesis, Universitat Autònoma de Barcelona, 2009
- [55] G.P. Johari, *J. Chem. Phys.* 127 (2007), p. 157101.
- [56] Kearns, K. L.; Swallen, S. F.; Ediger, M. D.; Wu, T.; Yu, L; *Influence of substrate temperature on the stability of glasses prepared by vapor deposition*; *J. Chem. Phys.* 2007, 127, 154702.
- [57] E. León-Gutierrez, G. Garcia, M.T. Clavaguera-Mora and J. Rodríguez-Viejo; *Glass transition in vapor deposited thin films of toluene*; *Thermochimica Acta* 492, (2009), 51-54
- [58] K. Ishii, H. Nakayama, T. Okamura, M. Yamamoto and T. Hosokawa, *J. Chem. Phys. B* 107 (2003), p. 876.
- [59] Brandon W. Rowe, Benny D. Freeman, Donald R. Paul; *Physical aging of ultrathin glassy polymer films tracked by gas permeability*; *Polymer* 50 (2009) 5565–5575
- [60] Sindee Simon; *Structural relaxation of stacked ultrathin polystyrene films*; *Journal of Polymer Science: Part B: Polymer Physics* DOI 10.1002/polb
- [61] V. Teboul and C. Alba-Simionesco; *Dynamical heterogeneity in glass-forming toluene: Comparison of bulk and confined conditions by quasielastic neutron scattering and molecular dynamics simulations*; *Volume 317, Issues 2-3, 2005, 245-252*
- [62] H. Hikawa, M. Oguni, H. Suga; *Construction of an adiabatic calorimeter for a vapor-deposited sample and thermal characterization of amorphous butyronitrile*; *J. Non-Cryst. Solids* 101 (1988) 90.
- [63] E. León-Gutierrez, G. Garcia, A.F. Lopeandia, M.T. Clavaguera-Mora and J. Rodríguez-Viejo; *Size Effects and Extraordinary Stability of Ultrathin Vapor Deposited Glassy Films of Toluene*; *The Journal of Physical Chemistry Letters* (2010) 1, 341-345

- [64] Zahra Fakhraai and James A. Forrest; *Probing Slow Dynamics in Supported Thin Polymer Films*; Physical Review Letters, 95, 025701, 2005
- [65] Kearns, K. L.; Swallen, S. F.; Ediger, M. D.; Wu, T.; Sun, Y.; Yu, L. Hiking down the energy landscape: Progress toward the Kauzmann temperature via vapor deposition. J. Phys. Chem. B 2008, 112, 4934- 4942.
- [66] Edgar Leon-Gutierrez, Alfonso Sepúlveda, Gemma Garcia, Maria Teresa Clavaguera- Mora, Javier Rodríguez-Viejo; *Stability of thin film glasses of toluene and ethylbenzene formed by vapor deposition: An in-situ nanocalorimetric study*; Phys. Chem. Chem. Phys. DOI: 10.1039/c0cp00208a
- [67] Kearns, Adv. Mater. 22 (2010)
- [68] Lei Zhu, Lian Yu; Generality of forming stable organic glasses by vapor deposition; Chemical Physics Letters 499 (2010)62-65
- [69] A. F. Lopeandia, J. Rodríguez-Viejo, M. Chacon, M. T. Clavaguera-Mora and F. J. Muñoz, J. Micromech. Microeng., 2006, 16, 965–971
- [70] A. F. Lopeandía, E. Leon-Gutierrez, J. Rodríguez-Viejo, and F. J. Muñoz, Microelectron. Eng. 84, 1288_2007
- [71] A. F. Lopeandía; Development of Membrane Based Calorimeters to Measure Phase Transitions at the Nanoscale; Ph.D. thesis, Universitat Autònoma de Barcelona, 2007
- [72] M.Y. Efremov, E.A. Olson, M. Zhang, S.L. Lai, F. Schiettekatte, Z.S. Zhang, and L.H. Allen, Thermochim. Acta 412, 13, (2004)
- [73] K. Ishii, H. Nakayama, S. Hirabayashi and R. Moriyama, Chem. Phys. Lett., 2008, 459, 109–112.
- [74] K. Ishii, H. Nakayama, R. Moriyama and Y. Yokoyama, Bull. Chem. Soc. Jpn., 2009, 82, 1240–1247.
- [75] Dawson, Kevin J; Zhu, Lei; Yu, Lian; Ediger, M. D.; *Anisotropic structure and transformation kinetics of vapor-deposited indomethacin glasses*; Journal of Physical Chemistry; submitted

Chapter V

- [1] F. Franks, *Water; A Matrix of Life*; 2nd ed., Royal Society of Chemistry, Cambridge, UK (2000)
- [2] P. Ball; *Life's Matrix: A Biography of Water*; Farrar, Straus, and Giroux, New York (2000)
- [3] O. Mishima, H. E. Stanley; *The relationship between liquid, supercooled and glassy water*; Nature 396, 329 (1998)
- [4] P. Jenniskens, S.F. Barnhak, D.F. Blake, M.R.S. McCoustra; *Liquid water in the domain of cubic crystalline ice I_c*; J. Chem. Phys. 107, 1232 (1997)
- [5] Debenedetti P.G. and Stanley; *Supercooled and Glassy Water*; H.E. 2003 Phys Today 56 (6) 40
- [6] Pauling L.; *General Chemistry*; 1970 (New York: Dover)
- [7] E.F. Burton, W.F. Oliver, Proc. R. Soc. London, Ser. A 153, 166 (1935)
- [8] P. Brügellier, E. Mayer; *Complete vitrification in pure liquid water and dilute aqueous solutions*; Nature 288, 569 (1980)
- [9] O. Mishima, L.D. Calvert, E. Whalley; *An apparently first-order transition between two amorphous phases of ice induced by pressure*; Nature 310, 393 (1984)
- [10] O. Mishima; *Reversible first-order transition between two H₂O amorphs at ~0.2 GPa and ~135 K*; J. Chem Phys. 100, 5910 (1994)
- [11] T. Loerting, C. Salzmann, I Kohl, E. Mayer, A. Hallbrucker; *A second distinct structural "state" of high-density amorphous ice at 77 K and 1 bar*; Phys. Chem. Chem. Phys. 3, 5355 (2001)
- [12] J.L. Finney, D.T. Bowron, A.K. Soper, T. Loerting, E. Mayer, A. Hallbrucker; *Structure of a New Dense Amorphous ice*; Phys. Rev. Lett. 89, 205503 (2002)
- [13] D.E. Brown, S.M. George, C. Huang, E.K.L. Wong, K.B. Rider, R.S. Smith, and B.D. Kay, J.; *H₂O Condensation Coefficient and Refractive Index for Vapor-Deposited Ice from Molecular Beam and Optical Interference Measurement*; Phys. Chem 100, 4988 (1996)
- [14] D.G. MacFarlane, C.A. Angell; *Glass transition for amorphous solid water*; J. Phys. Chem. 88, 759 (1984)
- [15] J.A. Ghormley; *Warming Curves for the Condensed Product of Dissociated Water Vapor and for Hydrogen Peroxide Glass*; J. Am. Chem. Soc. 79, 1862 (1957)
- [16] A. Hallbrucker, E. Mayer, G.P. Johari, J. Phys. Chem.; *Glass-liquid transition and the enthalpy of devitrification of annealed vapor-deposited amorphous solid water: a comparison with hyperquenched glassy water*; 93, 4986 (1989)

- [17] Y. P. Handa, D. D. Klug; *Heat capacity and glass transition behavior of amorphous ice*; *J. Phys. Chem.*, 1988, 92 (12), pp 3323–3325
- [18] J.A. Ghormley; *Enthalpy Changes and Heat-Capacity Changes in the Transformations from High-Surface-Area Amorphous Ice to Stable Hexagonal Ice*; *J. Chem. Phys.* 48, 503 (1967)
- [19] J.A. Pryde, G.O. Jones.; *Heavy Water Nature* 170, 635 (1952)
- [20] J.A. MacMillan, S.C. Los; *1,1-Dimethylhydrazine-Water Solid-Liquid System*; *J. Chem. Phys.* 42, 829 (1965)
- [21] M. Sugisaki, H. Suga, S. Seki; *Calorimetric Study of the Glassy State. IV. Heat Capacities of Glassy Water and Cubic Ice*; *J. Chem. Soc. Jpn.* 41, 2591 (1968)
- [22] G.P. Johari; *Liquid State of Low-Density Pressure-Amorphized Ice above Its T_g* ; *J. Phys. Chem. B* 102, 4711 (1998)
- [23] A.A. Tsekouras, M.J. Ledema, J.P. Cowin; *Amorphous Water-Ice Relaxations Measured with Soft-Landed Ions*; *Phys. Rev Lett.* 80, 5798 (1998)
- [24] Zh. V. Dobrokhotova, B.S. Zakharova, *Inorg. Mater.* 36, 191 (2000)
- [25] A.H. Narten, C.G. Venkatesh, S.A. Rice; *Diffraction pattern and structure of amorphous solid water at 10 and 77 K*; *J. Chem. Phys.* 64, 1106 (1976)
- [26] V. Velikov, S. Borick, and C. A. Angell; *The glass transition of water based on hyperquenching experiments*; *Science* 294, 2335 (2001)
- [27] R. A. Baragiola, *Water in Confining Geometries*, Springer Series in Cluster Physics, (Springer-Verlag, Berlin 2003), 359-395
- [28] Backus EH, Grecea ML, Kleyn AW, Bonn M. ; *Surface Crystallization of Amorphous Solid Water*; *Phys Rev Lett.* 2004 Jun 11;92(23)
- [29] Patrik Löfgren, Peter Ahlström, Jukka Lausma, Bengt Kasemo, and Dinko Chakarov; *Crystallization Kinetics of Thin amorphous Water Films on Surfaces*; 2003, vol. 19, n^o2, pp. 265-274
- [30] Speedy, Robin J.; Debenedetti, Pablo G.; Smith, R. Scott; Huang, C.; Kay, Bruce D.; *The evaporation rate, free energy, and entropy of amorphous water at 150K*; *The Journal of Chemical Physics, Volume 105, Issue 1, July 1, 1996, pp.240-244*
- [31] D. J. Safarik, R. J. Meyer, and C. B. Mullins; *Thickness dependent crystallization kinetics of sub-micron amorphous solid water films*; 2002, vol. 118, n^o10, pp. 4660-4671
- [32] R. Scott Smith, C. Huang, E. K. L. Wong and Bruce D. Kay ; *Desorption and crystallization kinetics in nanoscale thin films of amorphous water ice*; 367, 1, 10 November 1996, 13-18

- [33] Z. Dohnálek, Greg A. Kimmel, Ryan L. Ciolli, K. P. Stevenson, R. Scott Smith, and Bruce D. Kay; *The effect of the underlying substrate on the crystallization kinetics of dense amorphous solid water films*; J. Chem. Phys. 112, 5932 (2000)
- [34] P. Jenniskens and D. F. Blake; *Crystallization of amorphous water ice in the Solar System*; Planet. Space Sci. 44, 711 (1996)
- [35] NJ Sack, RA Baragiola ; *Sublimation of vapor-deposited water ice below 170 K, and its dependence on growth conditions*. Physical Review B 48:1414, 9973-9978 n
- [36] Andreas Hallbrucker, Erwin Mayer, and G. P. Johari; *Glass-liquid transition and the enthalpy of devitrification of annealed vapour-deposited amorphous solid water. A comparison with hyperquenched glassy water*; J. Phys. Chem., 93: 4986-4990, 1989
- [37] Nicolas Giovambattista, C. Auten Angell, Francesco Sciortino, and H. Eugen Stanley; *Glass transition temperature of water: A simulation study*; Phys. Rev. Lett., 93(\$), July 2004
- [38] M. Chonde, M. Brindza, and Vlad Sadtchenko; *Glass transition in pure and doped amorphous solid water: An ultrafast microcalorimetry study*; The journal of chemical physics 125, 094501 2006
- [39] Q. K. Jiang, L. H. Liang, and M. Zaho; *Modeling of the melting temperature of nano-ice in mcm-41 pores*; J. Phys.; Condens. Matter, 13:397-401, 2001
- [40] M. Oguni, S. Maruyama, K. Wakabayashi, A. Nagoe; *Glass Transitions of Ordinary and Heavy Water within Silica-Gel Nanopores*; Chem. Asian 2, 514 (2007)
- [41] K. P. Stevenson, Greg A. Kimmel, Z. Dohnálek, R. Scott Smith, and Bruce D. Kay; *Controlling the morphology of amorphous solid water*; Science, 283 (5): 1505-1507, March 1999

Appendix

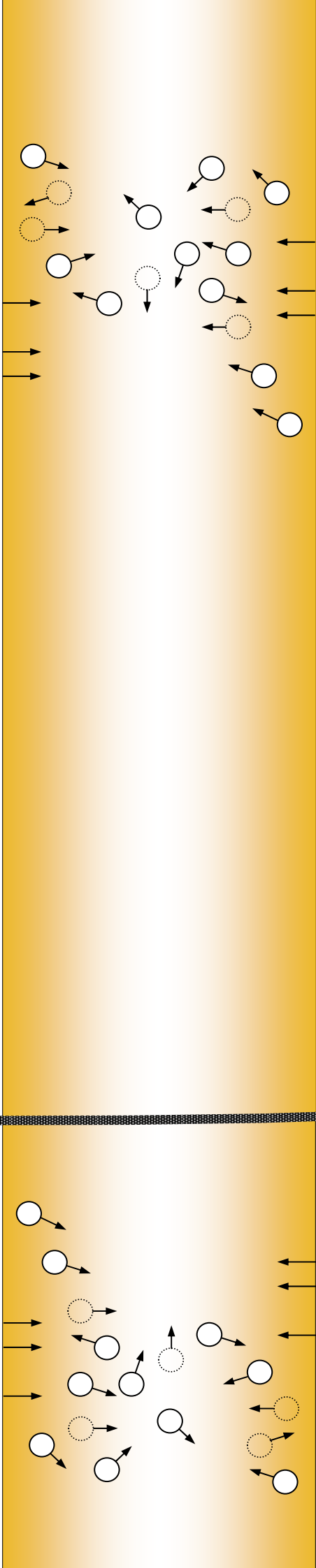
[1] Dornheim M, Doppiu S, Barkhordarian G, Boesenberg U, Klassen T, Gut_eisch O, Bormann R.; *Hydrogen storage in magnesium-based hydrides and hydride composites*; Scripta Materialia; 2007; 56; 841-846.

[2] S.J. van der Molen, J.W.J. Kerssemakers, J.H. Rector, N.J. Koeman, B. Dam and R. Griessen; ;*J. Appl. Phys.* 86 (1999), p. 6107.

[3] Olk CH, Tibbetts GG, Simon D, Moleski JJ. *Combinatorial preparation and infrared screening of hydrogen sorbing metal alloys.* J Appl Phys 2003;94:720-725.

[4] Robin Gremaud, Chase P. Broedersz, Dana M. Borsa, Andreas Borgschulte, Philippe Mauron, Herman Schreuders, Jan H. Rector, Bernard Dam, and Ronald Griessen; *Hydrogenography: An Optical Combinatorial Method To Find New Light-Weight Hydrogen-Storage Materials*; Adv. Mater. 2007, 19, 2813–2817

[5] Garcia G, Domenech-Ferrer R, Pi F., Santiso J, Rodriguez-Viejo J.; *Combinatorial synthesis and hydrogenation of Mg/Al libraries prepared by electron beam physical vapor deposition*; J Combinatorial Chem ACS 2007;9:230_6.



UAB
Universitat Autònoma
de Barcelona